

# **On Advanced Large-Field Photolithography**

**Thèse N° 9809**

**Présentée le 13 décembre 2019**

**à la Faculté des sciences et techniques de l'ingénieur  
Laboratoire de nanophotonique et métrologie  
Programme doctoral en photonique**

**pour l'obtention du grade de Docteur ès Sciences**

**par**

**Raoul KIRNER**

**Acceptée sur proposition du jury**

**Prof. C. Moser, président du jury  
Dr T. Scharf, directeur de thèse  
Prof. A. Herkommer, rapporteur  
Prof. U. D. Zeitner, rapporteur  
Prof. N. Quack, rapporteur**

**2019**





# Zusammenfassung

Das heutige Informationszeitalter wird durch den Einsatz von integrierten Geräten ermöglicht. Die Photolithographie stellt eine Schlüsseltechnologie bei der Herstellung dieser Geräte dar. Ständig wachsende Anforderungen an immer höhere Integrationsdichten treiben die laufende Weiterentwicklung photolithographischer Technologien an. Dies beschränkt sich nicht nur auf den sogenannten front-end-of-line-Bereich, wo immer feinere Strukturen realisiert werden. Im back-end-of-line-Bereich, wo Halbleiterchips kontaktiert und mit anderen Elementen verbunden, oder die Leiterbahnen von Flachbildschirmen hergestellt werden, äußert sich der Entwicklungsdruck nicht so sehr im Schrumpfen der minimalen Strukturgrößen, die aktuell bei 1-2  $\mu\text{m}$  liegen, sondern vor allem in der Strukturierung immer größerer Substrate. Dies ermöglicht es durch steigenden Durchsatz die Produktion insgesamt günstiger zu gestalten. Eine Untersuchung photolithographischer Systeme im Phasenraum liefert zwei Ansätze für die Verbesserung existierender Technologien. Die vorliegende Arbeit untersucht zunächst den Einsatz einer neuartigen Dauerstrich Laserquelle bei 193 nm als Lichtquelle für Proximity-Lithographie. Dafür wird ein Strahlformungssystem entwickelt und aufgebaut, welches die durch den Laser verursachten Kohärenzeffekte im Photoresist minimiert. Dieses Beleuchtungssystem ergibt im Zusammenspiel mit einem Präzisionstisch zur Substratpositionierung und einem Maskenhalter einen Mask-Aligner. Der Einsatz optischer Messtechnik zur Einstellung des Abstands zwischen Fotomaske und Substrat ermöglicht die Belichtung großflächiger Substrate. Mit diesem Aufbau werden geschriebene Strukturgrößen  $\leq 2\mu\text{m}$  bei einem Abstand von 20  $\mu\text{m}$  demonstriert. Der zweite Ansatz beruht auf einer mikrooptischen Multi-Apertur-Projektionsoptik zur photolithographischen Strukturierung eines Feldes von 100 mm x 100 mm. Eine laterale Verschiebung der Optik während des Belichtungsvorgangs ist nötig um das komplette Feld zu strukturieren. In dieser Arbeit wird eine solche Optik, sowie das dazugehörige mechanische System zur Realisierung dieser Verschiebung, realisiert. Diese Komponenten bilden zusammen mit einem Präzisionstisch zur Substratpositionierung und der Lichtquelle eines Mask-Aligners ein photolithographisches System zur Belichtung großflächiger Substrate. Der Ansatz sowie das optische Design werden durch die Demonstration von photolithographisch erzeugten Strukturgrößen von 2  $\mu\text{m}$  validiert. Dies wird jedoch nicht über das gesamte Schreibfeld erreicht. Eine umfangreiche Analyse der Fehlerquellen, sowie eine Diskussion möglicher Lösungsansätze und Lösungen, schließen diese Arbeit ab.

**Schlagworte:** Photolithographie, großflächige Belichtung, Phasenraum, Abstandsbelichtung, DUV Laser, Strahlformung, Kohärente Simulation, Microlens Projection Lithography, Wafer-Level Packaging, Mikrolinsenarray



# Abstract

The information age we live in today relies on highly integrated devices. They are fabricated with the help of photolithography, the patterning technique at the heart of their production. With the continuous demand for higher integration density to achieve ever growing performance levels, not only the front-end-of-line lithography, responsible for realizing the smallest structures, is under constant pressure for improvements. At the back-end-of-line, where ICs are interfaced, and elements like display panels are structured, this drive can be felt as well. The development here goes towards the processing of substrates of increasing size surpassing the wafer-level to increase throughput, thus becoming large-field photolithography. The current resolution requirements here are typically in the  $1\text{ }\mu\text{m}$  to  $2\text{ }\mu\text{m}$  for minimum feature size.

An investigation in phase-space identifies two possibilities for advanced photolithographic systems relying on different exposure mechanics. We combine a novel semiconductor laser light source emitting in the deep ultra-violet at  $193\text{ nm}$  with a beam-shaping system to enable proximity printing with sub- $2\text{ }\mu\text{m}$  resolution with a proximity gap of  $20\text{ }\mu\text{m}$ . The integration of this approach with optical exposure gap metrology and a high-precision substrate positioning stage demonstrates the possibility for large-field exposure. In a second approach we realize a highly integrated micro-optical multi-aperture projection lens to pattern an exposure field of  $100\text{ mm}$  by  $100\text{ mm}$ . A mechanical scanner to mount the projection lens, required to achieve uniform exposure of the entire field, is realized as well. Projection lens and scanner are integrated with a high-precision substrate positioning stage and a mask aligner illumination system to demonstrate the ability for large-field photolithographic printing. The optical design is validated by demonstrating printed minimum feature sizes of  $2\text{ }\mu\text{m}$ . Practical shortcomings of the system are investigated and strategies to overcome these issues are presented and discussed.

**Keywords:** Photolithography, large-field exposure, phase-space, proximity printing, DUV laser, beam-shaping, coherent simulation, microlens projection lithography, wafer-level packaging, microlens array.



# Contents

<b>Abstract (Deutsch/English)</b>	<b>ii</b>
<b>1 Introduction</b>	<b>1</b>
<b>2 Large-field photolithography</b>	<b>5</b>
2.1 Requirements of large-field photolithographic systems . . . . .	5
2.1.1 Resolution in photolithography . . . . .	8
2.2 Proximity printing in the deep-UV . . . . .	9
2.3 Multi-aperture imaging for photolithography . . . . .	10
2.3.1 A brief history of microlens projection lithography . . . . .	10
2.3.2 CTI project MURMELi . . . . .	12
2.4 The information content of an optical signal . . . . .	13
<b>3 Phase-space representation of photolithographic systems: an analysis</b>	<b>15</b>
3.1 Light and information in phase-space . . . . .	16
3.1.1 Plane waves in phase-space . . . . .	16
3.1.2 Diffraction in phase-space . . . . .	18
3.1.3 Diffraction under non-normal incidence illumination . . . . .	21
3.1.4 Information content of an optical signal and resolution . . . . .	23
3.2 Optical systems in phase-space . . . . .	25
3.2.1 The space-bandwidth product . . . . .	25
3.2.2 Space-bandwidth product and information transport in optical systems	27
3.2.3 Aberrations in phase-space . . . . .	29
3.2.4 Depth of field in phase-space . . . . .	31
3.2.5 Coherence in phase-space . . . . .	31
3.3 Photolithographic systems in phase-space . . . . .	33
3.3.1 Non-imaging system: mask aligner . . . . .	33
3.3.2 Imaging system: projection system . . . . .	35
3.3.3 Illumination for lithographic systems . . . . .	37
3.4 Possible enhancements for large-field lithographic systems . . . . .	40
3.4.1 Exploiting wavelength dependencies . . . . .	40
3.4.2 Temporal superposition: stepping and scanning systems . . . . .	41
3.4.3 Spatial superposition: multi-aperture systems . . . . .	43
3.4.4 Parallelization of projection systems: micro-optics as enabler . . . . .	44

## Contents

---

3.5	Intermediate conclusion . . . . .	46
<b>4</b>	<b>Mask aligner photolithography at 193 nm</b>	<b>47</b>
4.1	Photolithography at 193 nm . . . . .	47
4.2	Toptica's UV MOPA laser . . . . .	50
4.3	Illumination system for mask aligner lithography with a coherent source . . . . .	52
4.3.1	Beam-shaping with array optics . . . . .	53
4.3.2	Coherent sources and interference effects . . . . .	57
4.3.3	Ray-tracing of coherent sources: Gaussian-beam decomposition . . . . .	62
4.3.4	Simulation of randomized sources and validation of approach . . . . .	64
4.3.5	Coherent simulation of beam-shaping systems with temporal averaging . . . . .	66
4.4	Mask aligner lithography with DUV CW light source . . . . .	70
4.4.1	Methods . . . . .	70
4.4.2	Results . . . . .	72
4.4.3	Outlook on other mask aligner printing techniques . . . . .	76
4.5	Discussion of mask aligner lithography at 193 nm . . . . .	78
<b>5</b>	<b>Microlens projection lithography</b>	<b>81</b>
5.1	Design of a multi-aperture imaging system for photolithography . . . . .	81
5.1.1	Microlens projection lithography: a sum of many parts . . . . .	82
5.1.2	Microlens array technology for UV applications . . . . .	83
5.1.3	Image formation and achieving uniform dose and resolution . . . . .	85
5.1.4	Optics design and tolerancing . . . . .	89
5.2	Implementation of a prototype system . . . . .	93
5.2.1	Mask design . . . . .	94
5.2.2	Production of microlens array wafers in fused silica . . . . .	96
5.2.3	System simulation . . . . .	98
5.2.4	Wafer-level packaging for microlens projection lithography . . . . .	100
5.2.5	Mechanical scanner for microlens projection lithography . . . . .	105
5.3	System evaluation . . . . .	110
5.3.1	Mechanical system evaluation . . . . .	110
5.3.2	System integration and operation . . . . .	114
5.3.3	System verification . . . . .	117
5.4	System improvements . . . . .	123
5.4.1	Microlens array uniformity . . . . .	123
5.4.2	Wafer-level packaging process improvements . . . . .	126
5.4.3	Additional concepts for further improvement . . . . .	127
5.5	Conclusion on microlens projection lithography . . . . .	128
<b>6</b>	<b>Conclusion and Outlook</b>	<b>131</b>
<b>A</b>	<b>MPL optics sensitivity to axial misalignment</b>	<b>133</b>
<b>B</b>	<b>Improving the wafer-level microlens array uniformity</b>	<b>135</b>

<b>List of figures</b>	<b>138</b>
<b>List of tables</b>	<b>142</b>
<b>List of abbreviations</b>	<b>143</b>
<b>Nomenclature</b>	<b>146</b>
<b>Scientific publications and contributions</b>	<b>149</b>
<b>Bibliography</b>	<b>152</b>
<b>Acknowledgements</b>	<b>165</b>
<b>Curriculum Vitae</b>	<b>167</b>





It is well known that a vital ingredient of success  
is not knowing that what you're attempting can't be done.

— Terry Pratchett

To my parents,  
for their unwavering support of all my studies.



# 1 Introduction

Photolithography is at the heart of life as we know it today. If it is not the defining technology of the information age we are living in [1], then it is at least its enabler [2]. We rely on integrated circuitry and other integrated devices like light sources, antennas and sensors in nearly every aspect of modern life. Computers alone are ubiquitous, be it as PC, laptop, smartphone, in cars, TVs, or practically any other modern household appliance. They are also involved in the systems manufacturing all of these devices themselves, and a good part of everything else as well [3]. Photolithography is central to inscribing semiconductors and other materials with microscopic patterns required for their function as integrated circuit (IC), microelectromechanical system (MEMS) sensors, light emitting diode (LED) or laser diode (LD), and more [4]. It describes the pattern transport of a spatial structure to a substrate using light. On the substrate, the structure is recorded in a layer of photosensitive polymer, the photoresist. This layer then serves as mask in subsequent process steps [4].

The advent of modern photolithography dates back to the 1950s [5, 6]. It started with shadow printing. A photomask, containing spatial information in the form of openings in an opaque layer, was brought in close proximity or contact with the substrate and light was shone through the mask. In the early 1980s projection optics were introduced between photomask and substrate to transmit ever smaller features [7]. The next step forward was a reduction in the exposure wavelength [8]. Optical resolution depends on the wavelength, with shorter wavelengths offering better resolution [9]. The evolution continued, yielding some of the most complex optical systems ever created by man [10]. Today the highest resolving photolithographic systems rely on exposure wavelengths in the extreme ultra-violet (EUV) [11]. But this was only one path in the evolution of photolithography, as not all processes require the ultra-high resolution for the smallest structures at the heart of today's ICs [12].

At the back-end-of-line (BEOL), where the chips containing the ICs are interfaced, packaged, and connected to other devices, larger structures are required. Structure sizes are in the same range as for example the conducting structures on flat panel displays or the minimum feature sizes for MEMS devices. Photolithography for these structures relied as long as possible on mask aligners, being the least expensive option, as they do not require complex projection

lenses. Yet the growing resolution requirements in these segments as well as the introduction of ever larger substrates (display panels) led to a gradual transition to projection systems. Projection systems here differ from their highest resolution siblings in two aspects. They offer lateral resolution down to the single micron range, on exposure fields as large as possible. This is today's large-field photolithography.

At the same time as the most complex optical system were built for the front-end-of-line lithography in the 1990s, in Switzerland some people started looking into an idea for a novel BEOL projection system. They intended to combine the newly developed technology of manufacturing a large number of identical tiny lenses in parallel on flat substrates of Fused Silica by a dry-etch process [13,14] with the main design principle of insect eyes [15]. Their goal was to build a very thin projection lens yet with a large exposure field [16], which they called microlens projection lithography (MPL). The intended use-case was to build a thin projection system that could be integrated into an existing mask aligner to improve its performance and make it more competitive in terms of resolution, without heavily increasing its complexity. The initial results were promising, but required refinement of many of the involved processes. Yet the microlens array (MLA) technology developed for the project was sought after, and so the company, SUSS MICROOPTICS SA, started to sell such elements. The development of MPL systems continued slowly in parallel.

In 2015, 20 years after the initial idea, the latest attempt in realizing a MPL system was started in the frame of a collaboration between industry and academia. The Swiss commission for technology and innovation (CTI) funded a development project between SUSS MICROOPTICS SA and ÉCOLE POLYTECHNIQUE FÉDÉRALE DE LAUSANNE (EPFL) to develop a new MPL system. It should be capable of printing structures with 2  $\mu\text{m}$  minimum feature size over an exposure field of 100 mm by 100 mm with a working distance of 500  $\mu\text{m}$ . This systems should be able to expose 300 mm wafers, relying on typical BEOL photoresists for g-, h-, i-line illumination (436 nm to 365 nm). But instead of high-pressure mercury arc lamps, typical light sources for this spectral range, the system should incorporate a novel LED light source.

The presented work realized parts of this development project. A lens design has been realized in cooperation with the author of this thesis [MKN<sup>+</sup>19]. An optical system following this design is developed, produced and assembled at SUSS MICROOPTICS SA. A mechanical system required for the MPL process is designed, assembled and validated. Both parts are integrated with a high-precision stepping stage for wafer handling and a mask aligner light source to form a MPL system. The system is then characterized, validating the optics design by printing minimum feature sizes of 2  $\mu\text{m}$  in thin photoresist. Yet the system does not fulfill all specifications yet. An exhaustive analysis of the shortcomings, together with paths for future improvements is given. This work package is presented in chapter 5.

In another development project, funded by the German Ministry for Education and Research (DMBF), the German semiconductor laser specialist TOPTICA developed a novel continuous-wave laser light source in the deep ultra-violet (DUV) [17]. As SUSS MICROOPTICS SA was

---

application partner in this project, we gained access to this source. We used it to put another approach for advanced large-field photolithography to the test, an improvement of proximity printing. The DUV source is implemented in a mask aligner together with an optical gap-setting system. To enable successful printing, an illumination system is developed to deal with the high coherence of the source. This setup is capable of exposing theoretically arbitrary substrate sizes. In experiment, the lateral displacement range of the wafer positioning stage limits the substrate size to 300 mm wafers. Printing of minimum feature sizes of  $\leq 2\mu\text{m}$  is demonstrated for exposure gaps of  $20\mu\text{m}$  [KVO<sup>+</sup>18a]. In an outlook advanced proximity printing techniques are shown which would also benefit from this source [VKO<sup>+</sup>18]. Chapter 4 is dedicated to this subject.

In chapter 3 we introduce the concept of phase-space [18]. It allows the description of both imaging and non-imaging systems with the same methods. This makes phase-space ideally suited to investigate photolithography tools, as mask aligners and projection systems can thus be compared. Furthermore, phase-space allows to include the illumination into this analysis, as the same concepts can be applied in its investigation. As photolithography strongly depends on the illumination, this underlines the suitability of phase-space for this purpose. In the presented work we investigate mask aligners, projection systems and illumination systems for photolithography in phase-space. We will show how and why MPL and proximity printing at shorter wavelengths represent improvements on existing photolithographic systems.

Chapter 6 draws a conclusion on the presented work. We compare the results from both approaches for improving large-field photolithography. Furthermore we give an outlook to possible applications as well as paths forward for future improvements of the developed systems.

But let us begin with an investigation of large-field photolithography. In addition to carving out the resolution requirements we will introduce the different aspects of the presented work in more detail, and put them in the context of their respective state of the art.



## 2 Large-field photolithography

### 2.1 Requirements of large-field photolithographic systems

Photolithography is the patterning technology at the heart of today's integrated devices. The history of modern photolithography started in the second half of the 1950s, when the first semiconductor devices were manufactured with photolithographic processes [5, 6]. It started with shadow-printing in what we today call mask aligner. In the 1970s, the first projection systems were introduced to increase the distance between photomask and substrate, which was to be patterned, in order to decrease the possibility of mask damage and related effects during exposure [2]. Until the mid-1980s photolithography relied on high-pressure mercury arc lamps as light sources, with their spectral emission lines in the ultraviolet ( $\geq 365$  nm). In the 1980s two developments took place which ultimately shape the landscape of photolithography still today. Those were the introduction of reduction steppers [2], and the introduction of Excimer laser sources enabling shorter exposure wavelengths ( $\geq 193$  nm) [8]. The high-resolution systems were improved to realize constantly shrinking feature sizes, to today's front-end-of-line (FEOL) [19, Cha. 1] systems enabling features with critical dimensions<sup>1</sup> of 13 nm [20, 21], relying on even shorter exposure wavelengths (13.5 nm). The other development track was aimed at the BEOL, the part dealing with contacting the highly integrated circuits, connecting them to other elements, encapsulation and related process, in general known as packaging [22]. The requirements on feature critical dimension stayed well above the FEOL resolutions, and the photolithography systems for these applications were optimized towards large exposure fields to achieve high throughput.

Today, BEOL comprises not only packaging techniques like fan-out wafer-level packaging (FOWLP), through silicon vias (TSV), interposers, redistribution lines and the like, but also processes with similar critical dimension requirements like the exposure of large die formats without stitching, for example for image sensors, or for micro-electro-mechanical elements (MEMS). Substrate sizes also vary in size, from 150 mm wafers to large glass panels for display production or fan-out panel-level packaging (FOPLP). Large-field photolithography now refers

---

<sup>1</sup>A brief discussion of resolution in photolithographic systems will follow in section 2.1.1.

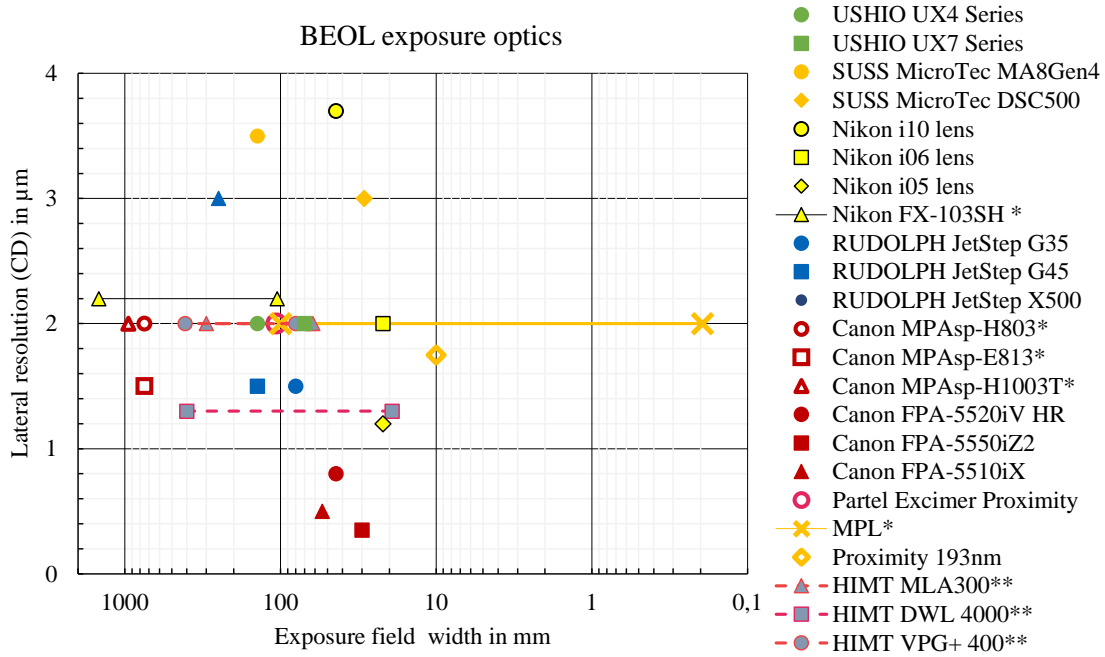


Figure 2.1 – Comparison of different commercial back-end-of-line (BEOL) exposure optics in terms of lateral resolution and exposure field size. No additional characteristics have been taken into account. Also listed are the two approaches investigated in this thesis (MPL, Proximity 193nm) and a similar work by Partel ET AL. [24].

\* Scan required during exposure.

\*\* Laser direct write tools with continuous scanning exposure.

to any exposure technology that is fit to expose substrates which exceed wafer-size. This definition can be found throughout different manufacturers of BEOL exposure tools, where it is used to differentiate between tools for wafer- and panel-exposure [23]. In this thesis we will use the term large-field photolithography to describe exposure technology fit for panel-size substrate exposure enabling BEOL critical dimensions in the printed structures.

To define BEOL resolution let us consider available exposure tools. Figure 2.1 shows a comparison of the exposure optics of commercial tools for BEOL applications, all with i-line illumination (365 nm). We neglect additional factors like depth of field<sup>2</sup>, and ignore the tools these optics are integrated in. Most are projection systems, some 1X lenses (both USHIO [23], Nikon FX [26], MPL from this thesis), some catadioptric 1X systems (SUSS MicroTec DSC500 [27], all Canon MPAsp [28–30]), some magnification lenses (RUDOLPH G45 [31], X500 [32]), and reduction lenses (Nikon i-series [33], RUDOLPH G35 [34], Canon MPAsp systems [28, 29, 35]). One commercial mask aligner is included (SUSS MA8Gen4 [36]), exemplary for these systems in general. Partel ET AL. tested outfitting a mask aligner with a KrF excimer laser source at 193 nm [24], which is also shown in fig. 2.1. Finally the mask aligner approach with a 193 nm

<sup>2</sup>As robustness and yield of the exposure process typically depend on the depth of field [4, Sec. 8.5] [25], it is clear that depth of field has to be investigated to judge the fitness of a tool for a given process.



## 2.1. Requirements of large-field photolithographic systems

---

continuous-wave (CW) laser light source is drawn as "Proximity 193nm" in fig. 2.1.

For the sake of completeness we also include 3 laser direct write photolithographic systems [4, p. 466] in fig. 2.1 (Heidelberg Instruments Mikrotechnik GmbH (HIMT), MLA300 [37], DWL 4000 [38], VPG<sup>+</sup> 400 [39]). Direct write lithography is a maskless approach, where the photoresist is locally and sequentially exposed via a directed beam. E-beam photolithography, where the direct write beam is an electron beam, is typically used for the production of photomasks, as it offers very high resolution, but with very low overall exposure speed [40, 41]. Laser direct write systems are faster, but offer exposed critical dimensions comparable to BEOL requirements. These systems typically rely on a spatial light modulator to steer the exposing beam [42–44]. This makes them ideal for the production of photomasks for BEOL application and they are typically advertised for this purpose. As all structures have to be individually written, throughput becomes the critical criterion [4, p. 106]. Throughput in photolithography typically describes the number of wafers or substrates which can be exposed by a given system during a fixed interval of time, typically one hour (typical unit: wafers per hour "wph"). Besides the exposure duration this metric also takes into account pre- and post-exposure processing times like alignment, wafer-handling and similar. The exposure time itself depends on the required exposure dose. Especially for the direct write tools these numbers are hard to come by, here typically only the write speed in  $\text{mm}^2 \text{min}^{-1}$  is given. This makes the comparison even more difficult.

Nevertheless we would like to give an idea how different systems compare in this respect. Direct write systems are advertised to expose up to  $6400 \text{ mm}^2 \text{min}^{-1}$  with  $2 \mu\text{m}$  resolution [39]. In comparison, mask aligners are typically specified to expose  $\geq 80$  wafers per hour. For 300 mm wafers, with an exposed area of 280 mm in diameter, this equals a size of  $\geq 5 \text{ m}^2 \text{h}^{-1}$ , or  $82\,100 \text{ mm}^2 \text{min}^{-1}$ . For 200 mm wafers (180 mm diam. exposed) this number is still  $33\,900 \text{ mm}^2 \text{min}^{-1}$ . Other systems, for example exposure tools from USHIO, relying on the UX7 Series lens, are specified to expose 120 300 mm wafers per hour, yielding exposed areas over  $120\,000 \text{ mm}^2 \text{min}^{-1}$  [23]. And systems for panel exposure achieve even higher exposure speeds. For example the Nikon FX-103SH is specified to expose one panel of 3370 mm by 2940 mm per minute, resulting in an exposed area of nearly  $10 \text{ m}^2 \text{min}^{-1}$ . This brief comparison serves as illustration and ignored the individual exposure doses the manufacturers based their throughput specifications on. The takeaway is that the significant differences in throughput achievable by the different systems limit direct write photolithography systems today mainly to the production of photomasks in industrial applications [45, Chap. 2].

As fig. 2.1 illustrates, the optical system of a BEOL photolithography system should combine a lateral resolution of  $2 \mu\text{m}$  (critical dimension (CD)) with a field of view (FOV) of 100 mm width to compete with currently available systems. Novel developments should aim at either increasing the resolution or the exposure field size.

By far the cheapest since simplest system in this comparison is the mask aligner (SUSS MicroTec MA8Gen4). Mask aligners typically use photomasks slightly larger than the exposed

substrate, and tactile gap-setting mechanics (proximity flags). In chapter 4 we will introduce a novel 193 nm CW laser light source into a mask aligner setup to improve resolution, and employ optical gap-setting metrology in order to realize a tool for exposing substrates of arbitrary size. Its performance is shown as "Proximity 193nm" in fig. 2.1.

A notable systems in fig. 2.1 is the Nikon FX system, which achieves its immense field size by arranging 14 smaller projection lenses in a line and scanning this arrangement during exposure [46], shown as two connected markers for single lens and full system. In chapter 5 we will investigate and implement an exposure system similar in function, but relying on highly integrated microoptical lenses instead of macroscopic projection lenses. This is shown as MPL in fig. 2.1.

The following sections will introduce basic concepts and considerations according to the two approaches for novel BEOL exposure optics identified before. Also we will provide background information on these systems, setting the stage for the in-depth treatment in the body of this work.

### 2.1.1 Resolution in photolithography

In the context of photolithography *resolution* is a term that is oftentimes wielded lightly. This also means that this term can be easily used too lightly, or implicitly requiring a large knowledge of the reader concerning the context in which it is used. This can be seen for example in Mack's comprehensive book on photolithography, where resolution in photolithography is defined as ([4, p. 484]):

"The smallest feature of a given type that can be printed with acceptable quality and control."

For this reason we will briefly discuss it here, to clarify its use throughout this work.

Resolution of an optical system can be defined in a physical sense as the capacity to transport spatial information with a certain contrast, to allow distinction between adjacent features [47, Sec. 8.6.3], and is linked to the diffraction limit. In photolithography the response of the photoresist is taken into account in addition. The optical resolution of the exposure system defines the minimum distance of adjacent features which can be printed in the photoresist [48]. For single, isolated features, exploiting the threshold behavior of the photoresist, the individual exposed and developed feature can be smaller than the optical resolution. The smallest realized feature size is referred to as critical dimension (CD). As structures for lithographic exposure typically consist not (only) of isolated features but of groups of adjacent features, a more strict definition can be applied, when periodic arrangements of lines are considered, closing the loop back to optical resolution. In this case, the minimum line-width is often referred to as *half-pitch* resolution, in relation to the period of the arrangement, and is in this case equivalent to the CD. Thus in photolithography the use of the term *resolution* can be ambiguous, especially if the definition used in a certain context is only implicitly stated.

Throughout this thesis, wherever not specified otherwise, we will use the term *resolution* typically as the half-pitch resolution as mentioned before. And we will use CD as synonym for the half-pitch resolution, thus always referring to the minimum feature size in non-isolated features.

For the sake of completeness, if the whole exposure process with all its variations and non-uniformities is taken into account, additional arguments have to be included in this discussion of resolution. This leads to so-called process windows [21, 25], yet their discussion is out of scope for this work.

## 2.2 Proximity printing in the deep-UV

Proximity printing is one photolithographic exposure mode in a mask aligner [4, 49–51]. To this end, a photomask is positioned in parallel to the substrate, with a separation of the exposure gap  $g$ . During exposure, the mask casts a shadow which is registered by the photoresist on the substrate. In contrast to contact mode, where photomask and substrate are brought into intimate contact, proximity printing greatly reduces photomask wear and increases yield by reducing resist damage [49, 50]. The achievable lateral resolution  $Res$  with  $\delta x_{\min} \propto \sqrt{\lambda \cdot g}$  depends directly on the exposure gap  $g$  and the exposure wavelength  $\lambda$ . Typical exposure gap values vary from 20  $\mu\text{m}$  to 200  $\mu\text{m}$ . The classical and prevalent light sources are high-pressure mercury arc lamps with emission lines in the ultra-violet (UV) at 436 nm (g-), 405 nm (h-) and 365 nm (i-line) [51]. The best resolution is typically found as 5  $\mu\text{m}$  critical dimension, that means equivalent to the smallest feature size, for a gap of  $g = 30 \mu\text{m}$  and exposure with i-line only.

If a certain exposure gap is to be maintained but better resolution is aspired, the only possibility is to reduce the exposure wavelength  $\lambda$ . Krypton-Fluoride excimer lasers emitting at 193 nm [52–54] are a typical light source for FEOL lithography tools [4], hence they are an obvious choice as light source for this approach. A study of this achieved lateral resolution of 2  $\mu\text{m}$  with an exposure gap  $g = 10 \mu\text{m}$ , using a 193 nm ArF excimer laser [24]. Yet the integration of such lasers is complex, as will be discussed in section 4.1, thus alternative light sources at these wavelengths would be of interest.

Garching, Germany, based semiconductor manufacturer TOPTICA just recently developed a novel laser light source with CW emission at 193 nm in the frame of BMBF<sup>3</sup>-integrated project *UVMOPA* [17]. Using CW laser sources for proximity printing requires specialized beam-shaping due to their typically high degree of coherence [55]. With SUSS MICROOPTICS SA, the employer of the author, partnering in the BMBF project, we investigated this light source towards proximity printing in a mask aligner in chapter 4.

---

<sup>3</sup> BMBF, the German Federal Ministry of Education and Research

### 2.3 Multi-aperture imaging for photolithography

The approach of distributing optical functionality over multiple channels can be found in many places as an evolutionary result in nature [15, 56–58]. All of these systems have in common the need to solve a vision problem efficiently with limited space and energy. Technical implementations of the different types of multi-aperture systems can be found from tiny integrated vision systems [59–61] over close-up vision systems [62] and everyday office appliances [63–65] to high-resolution vision systems [66, 67], and more.

Most of these systems share one common feature, their electronic sensor. This gives these systems a degree of freedom where the contributions of different imaging channels can be computationally combined [61, 66, 67]. Or, if the optical system is designed to accomplish the lateral recombination of adjacent channels, at least allow pixel-wise post-processing [60].

For a photolithographic application we do not have this degree of freedom. The photoresist, acting as analog sensor, requires a uniform exposure dose to achieve a uniform print [51]. In addition, photolithography as BEOL technology relies on exposure wavelengths in the UV, the aforementioned g-, h- and i-lines of the mercury emission spectrum. This severely limits the choice of lens materials significantly in comparison to the applications in the visible range listed above [68].

Yet the idea to introduce an integrated multi-aperture imaging system for photolithography dates back to the 1990s [69]. It was found that a scan of a multi-channel imaging system could overcome the dose uniformity requirements. Together with recent progress on the wafer-level production of uniform fused silica MLAs [70] and work on wafer-level packaging presented in this thesis this offered a unique opportunity to build a highly integrated imaging system with small build volume, yet high resolution and large exposure field. This approach was proposed as micro-lens array lithography [69], while the name MPL has taken hold in the following years [15].

#### 2.3.1 A brief history of microlens projection lithography

The realization of MPL systems has been an ongoing field of work since the early 1990s, when Hugle, Dändliker and Herzig presented the idea and started the development of such systems [16, 69]. They quickly found that systems built with commercially available microlens arrays [69] had severe limits in resolution. As these systems are intended for photolithographic exposure, their optical elements have to be transparent to the involved wavelengths. So they started investigating emerging technologies for the production of large MLAs in fused silica. Over the next 20 years they presented a steady progress not only in the production of larger and more uniform MLAs, [13, 14, 71] but also in MPL systems [72–74].

Manufacturing high precision MLAs in fused silica is not only of interest for MPL systems, so the company SUSS MICROOPTICS SA was founded in 1999, and the production of fused

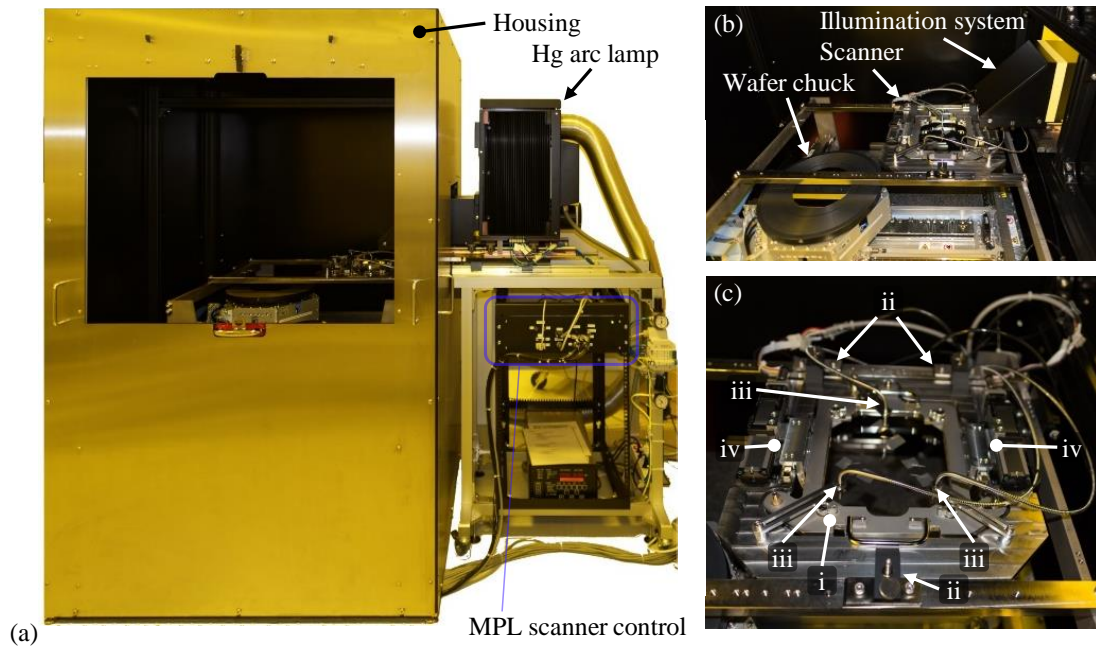


Figure 2.2 – MPL Alpha system as installed in 2015. (a) Total system view. The housing contains the stepping stage and the MPL scanner. (b) Photograph of the interior of the housing. (c) Close-up of the MPL scanner. **i** Mask holder, **ii** scanner leveling screws, **iii** optical gap sensors, **iv** scanner motors and linear bearings.

silica and silicon microlenses in general and other types of microoptical components was commercialized. Nevertheless, the development and improvement of both MLAs [70, 75] and MPL systems continued in the company [76, 77].

At this point, the technology to manufacture convex MLAs in fused silica on 200 mm wafer-level was mature and had been state-of-the-art for several years. The last MPL prototype system assembled at this point was intended for full-field exposure of 150 mm substrates. It was integrated into a modified SUSS MICROTEC MA150, an automatic mask aligner for 150 mm substrates. This MPL system consisted of a stack of 5 wafers, 4 containing microlens arrays and 1 additional wafer with an array of apertures, assembled on wafer-level with different bonding techniques [77]. The final system was able to resolve structures with  $\approx 10\mu\text{m}$  critical dimension with just over  $800\mu\text{m}$  working-distance. Working-distance describes here the space between the last surface of the MPL system and the substrate top surface. It had a depth of field of roughly  $50\mu\text{m}$ . The shortcomings of the systems were attributed to insufficient lens-to-lens uniformity of the individual microlens arrays, as well as problems in the system assembly or packaging process.

The development of MPL was put on hold at this point, as the assembled system performance significantly missed the design values. An analysis of the total system identified challenges in nearly all components, including the mechanics, the optics assembly process and even the

MLAs themselves.

In 2015 a new attempt at realizing a functioning MPL system was made. It was deemed secure that the manufacturing technology of MLAs had progressed enough to overcome the earlier problems in terms of lens-to-lens uniformity. Also, a different approach was chosen. Instead of producing MLAs spanning nearly the whole extent of 200 mm wafers, the exposure field was limited to 100 mm x 100 mm. This was enabled by the introduction of a high precision stepping stage. Now the photoresist-coated substrate could be positioned freely between exposures. This presented the transition from full-field to large-field exposure.

In 2016, with the start of this thesis, the first new MPL system had been realized, as shown in fig. 2.2. Both optics as well as mechanics were insufficient once again, and some useful but also painful lessons had to be learned. And with that the stage had been reached where the work in this thesis commenced.

### 2.3.2 CTI project MURMELi

The MPL development project of this thesis was carried out in the frame of CTI<sup>4</sup> integrated project MURMELi, a joint development project with SUSS MICROOPTICS SA as industrial partner and EPFL<sup>5</sup> as academic partner. The development project comprised the development of a full MPL system with a lateral resolution of 2  $\mu\text{m}$  critical dimension, a working distance  $\geq 500\mu\text{m}$ , that means a distance between optics and substrate, and an exposure field of 100 mm by 100 mm, as well as the investigation and development of novel light sources as replacement for the canonical high-pressure mercury arc lamps.

This project was split into work packages which have been realized by different people. Johana Bernasconi realized a novel exposure illumination system. It relies on light emitting diodes (LED) as light sources, with an emission wavelength of 405 nm [78].

Kevin Müller has realized the optics design for the MPL optics, the optical heart of the total system [MKN<sup>+</sup> 19].

The other parts of project MURMELi have been realized in this thesis. This comprises the technical implementation and realization of the MPL optics, the improvement of the scanner mechanics for the optics displacement during exposure, and the integration of the whole system with a stepping stage for substrate positioning and an exposure light source. Chapter 5 is dedicated to this topic.

---

<sup>4</sup>Formerly CTI, the Swiss commission for technology and innovation, has been transformed into *Innosuisse* in 2018.

<sup>5</sup>École Polytechnique Fédérale de Lausanne, Switzerland

## 2.4 The information content of an optical signal

All of the introduction so far described the technical work which has been carried out for the realization of this thesis. Yet one question has not been addressed, which is the question of the fundamental difference between proximity exposure in a mask aligner and projection printing with MPL. Both approaches rely on light as means of transport to transfer the spatial information of the photomask [4] to the photoresist on the substrate. To gain a deeper understanding of the differences of both techniques, but also to discuss what they have in common, we introduce the concept of phase-space [79] in chapter 3.

Phase-space is a concept to visualize the information content carried by propagating light [18]. It can be applied to understand the information content of an optical signal. Together with an analysis of the amount of information supported by an optical system, this allows for example to draw conclusions on the quality of imaging achievable with an optical system [80, 81]. As the concept of phase-space does not rely on the geometrical description of optical elements, but rather describes their behavior, it can also be applied to the description of illumination systems with the same terms [82].

Typically, phase-space is a description of the paraxial regime [82]. Still this does not exclude an enlargement of the concept to take into optical aberrations [80, 83]. This allows us to visually investigate realistic optical systems and their behavior. By introducing an extended phase-space [79], we can even investigate time-dependent systems like the scanning exposure required for MPL.

We employ thus this technique to investigate and compare the photolithographic systems which are object of this thesis, but without limiting the generality of the discussion to it.





### 3 Phase-space representation of photolithographic systems: an analysis

Photolithography is a patterning technique realizing information transfer relying on light.

Let us have a closer look at the implications of this statement.

Due to its wave-particle dualism light can be described both as electromagnetic waves of a certain spectral range and as photons of a certain energy [47, Chap. 1]. Light is emitted by different types of sources, which define many of its properties. In photolithographic application it is typically delivered via an optical system, the illumination optics.

In the context of two-dimensional patterning information is of a spatial nature. A pattern has to be transported and inscribed into the target. In most photolithographic applications the pattern is stored in a photomask. The information of the photomask can be transferred with one of two approaches, i.e. free-space propagation and imaging. Both rely on the propagation of light from the photomask, containing its spatial information, to a detector. In the case of imaging it is managed with an intermediate optical system relaying the light. Transfer of information is strongly defined by resolution meaning the smallest transferable structural dimension.

The typical detectors in photolithography are photoresists. These photosensitive compounds are applied in a uniform layer to the top of a substrate. They will change their chemical and physical properties on exposure with a certain wavelength and energy dose, thus storing the spatial information conveyed from the photomask for subsequent processes.

In this chapter we are going to discuss these parts that make up the initial statement. We will introduce the concept of phase-space as an illustrative tool offering insight into all aspects mentioned above. We will describe the propagation of light itself in phase-space and discuss the concept of resolution in this context. Then we will investigate different photolithographic systems in phase-space, and close with a brief digression on illumination systems. This will allow us to discuss possible improvements, which conclude this chapter.

Furthermore we will neglect polarization as additional property of light. This has to be taken

into account for the highest resolution photolithographic systems, and can cause problems if left unchecked, in general. Yet for the light sources as used throughout the applied part of this thesis, polarization is irrelevant because either the sources emit already unpolarized light (chapter 5) or the polarization of the source is scrambled with diffusers (chapter 4). This neglect does not invalidate the explanations and findings of this chapter and would on the other hand add another degree of complexity if taken into account.

## 3.1 Light and information in phase-space

In this section we introduce the concept of light as a propagating wavefront. Based on this we will discuss resolution in an optical sense. Also we will introduce the concept of phase-space as an intuitive way of graphically illustrating light in optical systems.

### 3.1.1 Plane waves in phase-space

A plane wave describes an ideal wavefront of infinite extent propagating under a certain angle. Its whole information content consists of its wavelength, direction and the amount of energy that is transported. Figure 3.1a shows two ideal plane waves  $E_1$  and  $E_2$ .  $E_1$  propagates parallel to the optical axis, in  $z$  direction, while  $E_2$  propagates under angle  $u_2$ . This graph sets the naming convention used throughout this thesis: the field lies usually in the  $xy$ -plane, while the optical axis is in  $z$ -direction. Thus propagation typically occurs in the positive  $z$ -direction as well. For simplicity most of the times only one field dimension, typically  $x$ , is drawn, for sake of simplicity but without limiting generality.

The characteristic information of those two wavefronts could be drawn in a different coordinate system, as is done in fig. 3.1b. This representation is the so-called phase-space representation. Here, a plane wavefront is limited to one spatial coordinate,  $x$  in our case, and the corresponding field angle  $u$ . This concept was initially introduced in the field of statistical mechanics to describe signals with both space and frequency dependence [84]. This representation in phase-space is also known as the Wigner distribution function after its inventor [18, 79]. For two ideal plane waves this is not very exciting, as a plane wave is represented by a single line under its corresponding angle. The phase-space representation is  $z$ -dependent, though, as becomes immediately visible when considering wavefront  $E_2$ . As it propagates the field-position of its vector changes, which is indicated in the displacement of the corresponding circle in fig. 3.1b, but the overall graph does not change as the extent of an ideal wavefront is infinite.

If one now considers finite plane waves, for example by limiting their lateral extent with an aperture of  $2a$  width, this lateral shear in phase-space as equivalent to free space propagation becomes much more visible. Figure 3.2a shows a schematic of this setup. One plane wave, indicated by the red ray, is propagating parallel to the optical axis, whereas another plane wave, indicated by the blue ray, propagates under the maximum field angle  $u_F$ . At the position

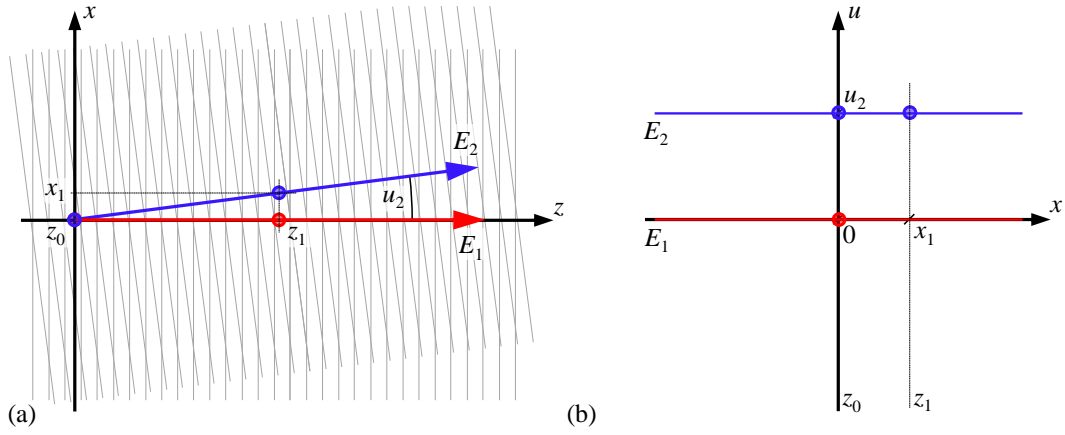


Figure 3.1 – (a) Schematic drawing of two propagating ideal plane waves  $E_1$  and  $E_2$ .  $E_2$  propagates under angle  $u_2$ , while the propagation angle of  $E_1$  is not shown as it is parallel to the optical axis in  $z$ -direction. (b) Phase-space representation of both wavefronts. The free-space propagation of off-axis points equals a lateral shear, indicated by the drawn dots.

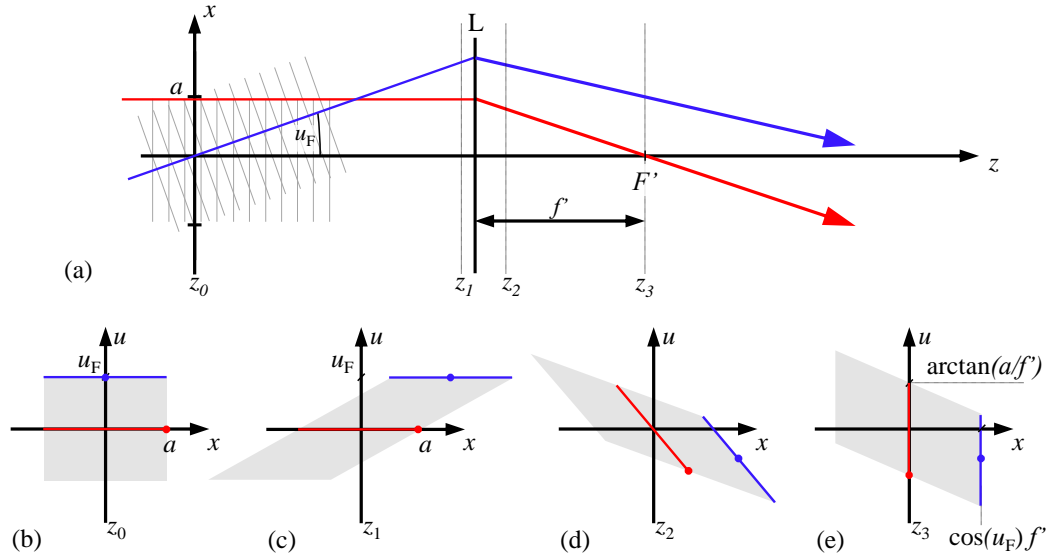


Figure 3.2 – (a) Two plane waves of diameter  $2a$  passing an optical system with a lens  $L$  of focal length  $f$ . Simplified paraxial representation. (b) The two plane waves in phase-space at  $z_0$ . The light gray area marks the plane waves that can pass the system if the blue ray is regarded as chief ray and the red ray as marginal ray. (c) The plane waves experience lateral shear as a function of their propagation angle, the phase-space equivalent to free space propagation. Depiction at  $z_1$ . (d) After passing the lens, spatial and angular domain are rotated by  $90^\circ$ . (e) In the image side focal plane  $z = F'$  of lens  $L$  the initial boundaries of the spatial and frequency domains are interchanged. This is equivalent to a Fourier transform of the initial signal.

of the aperture,  $z_0$ , the phase-space representation of the situation is depicted in fig. 3.2b. The just mentioned lateral shear in phase-space becomes immediately visible in fig. 3.2c, the situation at  $z_1$ . After passing a (ideal) convex lens  $L$  the two plane waves are deflected. A lens changes the propagation direction as function of the field height and incidence angle, transforming for example a plane wave under normal incidence into a spherical wave centered on the image side focal point  $F'$ . This is equivalent to a rotation in phase-space, as drawn in fig. 3.2d. In the image side focal plane at  $z_3 = F'$ , in combination with the lateral shear of the propagation to this plane, the situation presents itself in phase-space as drawn in fig. 3.2e. Now, the boundaries limiting the phase-space extent have been exchanged. The red ray, initially limiting the maximum field height, limits the maximum field angle, and the blue ray, initially limiting the field angle, limits the field height. This is equivalent to a Fourier transform, which is expected behavior from a convex lens.

#### 3.1.2 Diffraction in phase-space

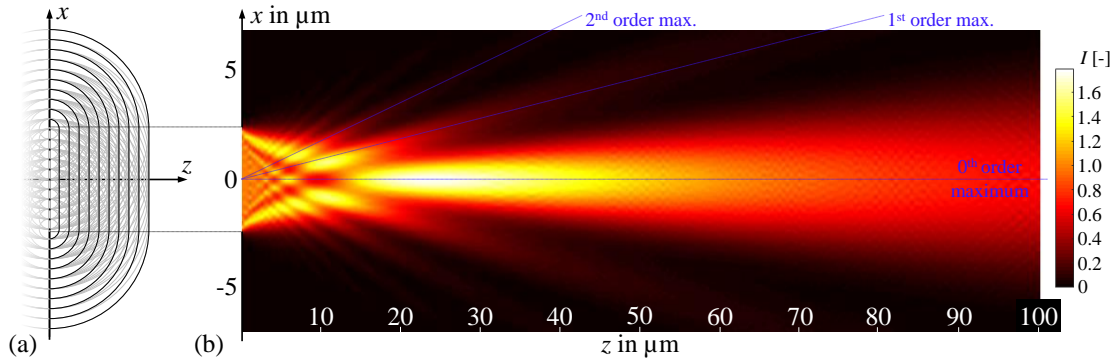


Figure 3.3 – Diffraction at a single slit of width  $2a = 5 \mu\text{m}$ , plane wave illumination at  $\lambda = 365 \text{ nm}$ ,  $\Delta\lambda = 5 \text{ nm}$ . (a) Sketch of Huygen's principle. (b) Simulation of the same situation. The  $0^{\text{th}}$ ,  $+1^{\text{st}}$  and  $+2^{\text{nd}}$  order maxima are highlighted.

Until now we stuck with a paraxial image, where lenses can be represented by a single plane (thin lens approximation), exhibit no aberrations, and plane waves can be simply limited in their lateral extent by an aperture. To get a realistic picture of what happens at an aperture limiting the lateral extent of a plane wave we need to consider diffraction.

Huygen's principle describes a propagating wavefront as the coherent sum of spherical wavelets emanating from every point of the source, compare fig. 3.3a. Coherent sum describes an addition of the complex wavelet, or an addition taking into account the phase relation between individual wavelets. If we consider the source as infinite plane, then the sum over these wavelets will, again, be an infinite plane. This is the propagation of a plane wave. When we now introduce an aperture, laterally limiting the plane wave, the lateral vectorial components of the wavelets start to propagate, or rather suddenly are no longer canceled out by corresponding opposite components of adjacent wavelets.

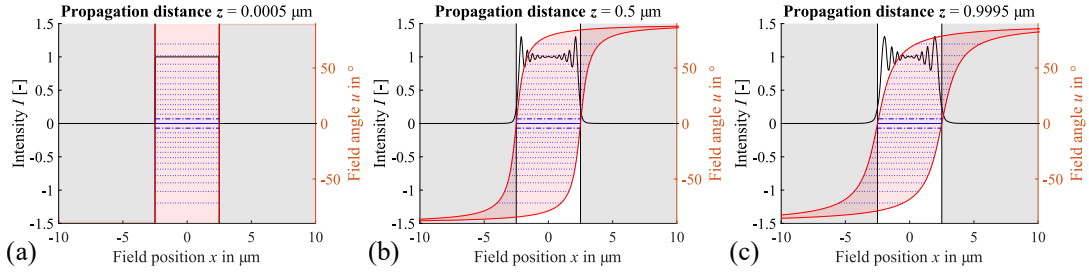


Figure 3.4 – Diffraction at a single slit of width  $2a = 5\mu\text{m}$ , plane wave illumination at  $\lambda = 365\text{nm}$ ,  $\Delta\lambda = 5\text{nm}$ , drawn in phase-space, in the optical near-field. The center white area between the gray areas represents the slit. The intensity (cross-section) is drawn as function of the spatial position. The red area is the phase-space representation of free space propagation in the angular half-space behind the slit. Intensity maxima caused by diffracted of different order are plotted in blue; the 0<sup>th</sup> maximum as line, the 1<sup>st</sup> order maximum as dash-dotted line and higher order maxima as dotted lines. (a)  $z = 0.0005\mu\text{m}$ . (b)  $z = 0.5\mu\text{m}$ . (c)  $z \approx 1\mu\text{m}$ .

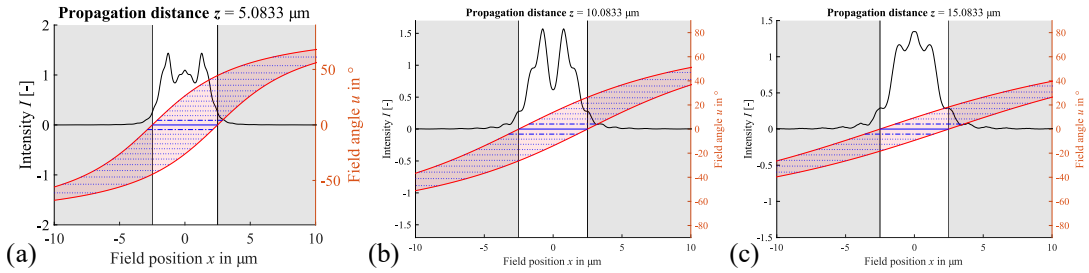


Figure 3.5 – Diffraction at a single  $5\mu\text{m}$  slit as in fig. 3.4. The propagation distance covers  $z = 5\mu\text{m}$  to  $15\mu\text{m}$ , a range that marks the transition from the near-field to the Fresnel regime. (a)  $z = 5\mu\text{m}$ . (b)  $z = 10\mu\text{m}$ . (c)  $z = 15\mu\text{m}$ .

The following simulations have been carried out with GENISYS LAB<sup>1</sup>, a simulation software, relying on the numerical Rayleigh-Sommerfeld solver implemented in this software, to calculate the diffraction integral [47, Sec. 8.11].

Figure 3.3 depicts diffraction for a slit of width  $2a = 5\mu\text{m}$ . While fig. 3.3a shows a schematic sketch of Huygen's principle for diffraction at the slit, as described in the previous paragraph, fig. 3.3b shows a simulation of the slit and subsequent propagation for illumination with a plane wave under normal incidence and  $\lambda = 365\text{nm}$ . The diffraction pattern behind the aperture is the result of the superposition of different orders of diffraction maxima, propagating under different angles. The blue lines in fig. 3.3b highlight three orders of diffraction maxima. These maxima are propagation directions, under which Huygen's wavelets constructively interfere. They are closely related to diffraction orders behind a periodic aperture, or grating. Yet they lack the discretization of diffraction orders behind a grating, as no effects of adjacent apertures contribute to narrowing the possible propagation directions.

<sup>1</sup>GENISYS GmbH, Taufkirchen, Germany. LAB common lithography technology simulation software in version 4.8.1.

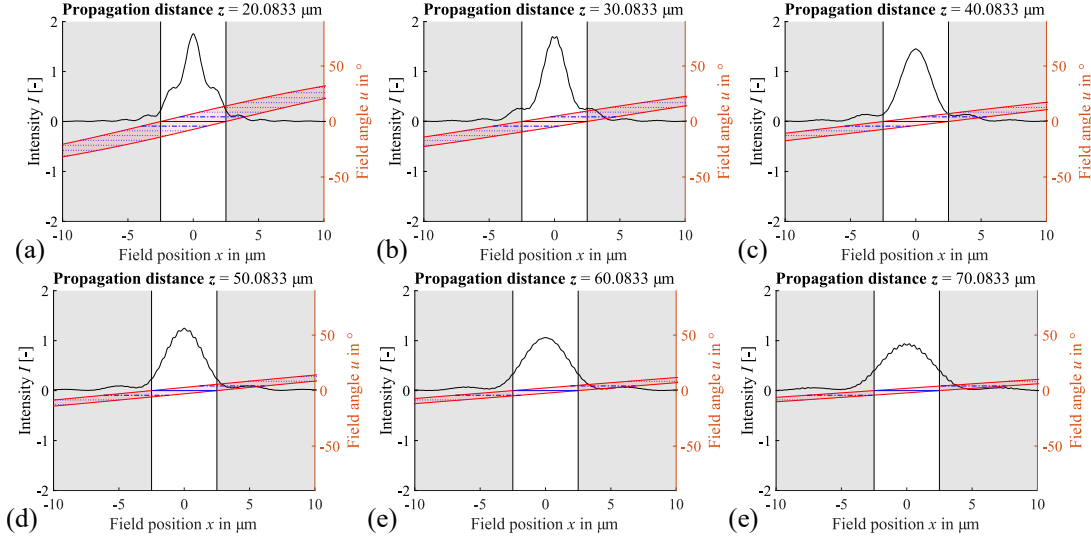


Figure 3.6 – Diffraction at a single  $5\mu\text{m}$  slit as in fig. 3.4. The propagation distance covers  $z = 20\mu\text{m}$  to  $70\mu\text{m}$ , a range over which the overlap of  $0^{\text{th}}$  and  $\pm 1^{\text{st}}$  order maxima decreases and vanishes. (a)  $z = 20\mu\text{m}$ . (b)  $z = 30\mu\text{m}$ . (c)  $z = 40\mu\text{m}$ . (d)  $z = 50\mu\text{m}$ . (e)  $z = 60\mu\text{m}$ . (f)  $z = 70\mu\text{m}$ .

As higher order diffraction intensity maxima may very well propagate under angles  $> 5^\circ$ , thus lie outside the paraxial region, the lateral shear of free space propagation in phase-space is no longer linear. Instead it follows a tangent relation in dependence on the field angle, as the angles are projected onto the observation plane [85, Sec. 19.4.6]. Figure 3.4 shows the propagation of the field from fig. 3.3b in three different propagation distances behind the slit,  $z = 0.001\mu\text{m}$ ,  $0.5\mu\text{m}$  and  $1\mu\text{m}$ . The slit of width  $2a = 5\mu\text{m}$  is depicted by the white area (transparent), whereas the aperture around is represented by the gray shaded areas. The intensity distribution over the field is plotted by the black line. The field angles are limited to the shaded red area, with the diffraction intensity maxima are drawn as blue lines. The  $0^{\text{th}}$  order maximum is drawn as solid line, the  $\pm 1^{\text{st}}$  order maxima as dash-dotted lines and higher order maxima as dotted lines.

When comparing the three graphs of fig. 3.4, one can draw several conclusions on the connection of diffraction and optical representation of the slit. After  $0.5\mu\text{m}$  propagation the highest order maximum visible already starts significantly wandering out of the region of the slit, and has left the slit to  $2/3$  already after  $1\mu\text{m}$ . This mutual lateral displacement of different orders of diffraction maxima is also visible in the intensity distribution over the slit. As long as all orders of diffraction maxima are aligned, the intensity distribution is nearly perfectly uniform, compare fig. 3.4a. As soon as the orders start to wander, their coherent sum no longer results in a rectangle, but in the typical diffraction pattern of a rectangular aperture, with the overshooting top edges and the foot protruding outside the aperture width. This can be found for example in [47, Chap. 11, Fig. 11.11].

For increasing propagation distance, the influence of the higher order maxima vanishes, as

they propagate out of the center region, thus no longer contribute to the shape of the main intensity peak. Figure 3.5 shows the development of the intensity distribution over a range from  $5\mu\text{m}$  to  $15\mu\text{m}$ .

As the propagation distance increases even more, the amount of diffraction order maxima overlapping in the center region decreases. This can be seen in fig. 3.6, where the same situation as previously discussed is shown, only for propagation distances of  $20\mu\text{m}$  to  $70\mu\text{m}$ , in steps of  $10\mu\text{m}$ . This range shows the development of the center intensity distribution for the transition where mainly only the  $\pm 1^{\text{st}}$  order diffraction maxima and the  $0^{\text{th}}$  order maximum contribute to the center intensity, and how this changes as the  $\pm 1^{\text{st}}$  order maxima move away from the center. After approximately  $40\mu\text{m}$  propagation distance, the  $\pm 1^{\text{st}}$  diffraction order maxima no longer overlap. After approximately  $70\mu\text{m}$ , mostly only the  $0^{\text{th}}$  order maximum defines the intensity distribution.

In the presented case  $z = 17\mu\text{m}$  marks the point where the *Fresnel number*<sup>2</sup>  $N_F$  is unity [86, Sec. 4.5.1]. This means that the graphs in fig. 3.5 show the transition from the optical near-field to the Fresnel regime. And fig. 3.6 illustrates the transition from Fresnel to Fraunhofer regime. The higher-order fluctuations on the intensity plots in fig. 3.6 are artifacts from the numerical simulation in GENISYS LAB.

A special case of diffraction at an aperture, which has wide application throughout optics, is for a circular aperture (instead of the slit we considered until now). For larger propagation distances, where  $N_F \ll 1$ , the intensity distribution follows the so-called *Airy pattern* or Airy distribution [86, Sec. 4.4]. Its minima separate the different orders of diffraction maxima. The first minimum encircles the  $0^{\text{th}}$  order maximum, and the energy transported in it is 83.9 % of the total energy in the aperture.

#### 3.1.3 Diffraction under non-normal incidence illumination

In the previous section 3.1.2 we investigated diffraction under normal incidence. What happens if we change the illumination angle? Figure 3.7 shows simulations for skew illumination of the already known slit aperture of  $5\mu\text{m}$  width. For the sake of completeness, fig. 3.7a again shows plane wave illumination under normal incidence. Figure 3.7b shows what happens when the plane wave illumination is tilted about  $2.5^\circ$ . Figure 3.7c shows how the intensity distributions for a whole range of angles would superimpose in case of incoherent superposition, as discussed in the previous section. This means that intensities for the different propagation directions are summed up.

---

<sup>2</sup>The *Fresnel number*  $N_F = a^2 / \lambda z$  can be used to distinguish between the different diffraction regimes in light propagation after an aperture of width  $2a$ . For  $N_F \gg 1$  the propagation takes place in the so-called optical near-field, and the Rayleigh-Sommerfeld diffraction integral [86, Sec. 3.5.2] has to be solved to calculate diffraction. This integral allows the calculation of propagating electro-magnetic waves. For  $N_F \approx 1$ , the Fresnel approximation [86, Sec. 4.2] can be used to approximate the Rayleigh-Sommerfeld diffraction integral. Here the propagating wavefront is approximated by spherical waves. For  $N_F \ll 1$  the propagating wavefront can be approximated by plane waves, which is the Fraunhofer approximation and the basis of Fourier optics [86, Sec. 4.3].

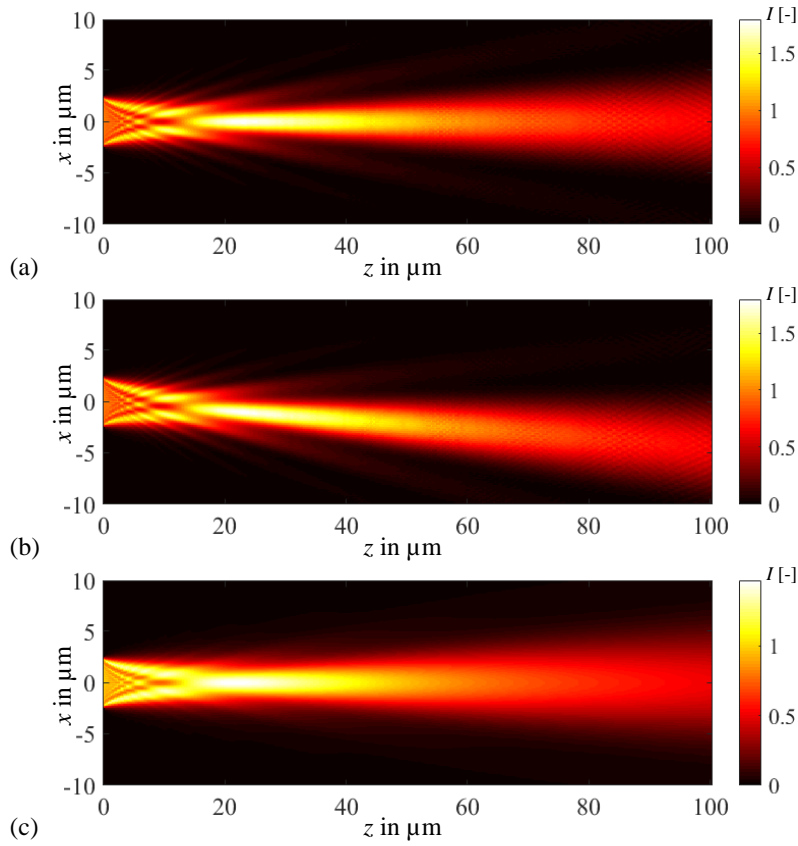


Figure 3.7 – Free-space propagation after a 5  $\mu\text{m}$  slit aperture with an illumination wavelength of  $\lambda = 365 \text{ nm}$ ,  $\Delta\lambda = 5 \text{ nm}$ . (a) Plane wave illumination under normal incidence. (b) Plane wave illumination under  $-2.5^\circ$  incidence. (c) Illumination with a uniform angular distribution over  $\pm 2.5^\circ$ .

To highlight the development of the intensity distribution in the different cases, fig. 3.8 shows cross-sections through the intensity distributions shown in fig. 3.7 for different propagation distances. It can be seen that the inclination of the plane wave illumination leaves the diffraction pattern practically undisturbed. This is at least true for small angles of up to  $2.5^\circ$  as shown here. If a continuous range of angles is incoherently superimposed, that means the intensities

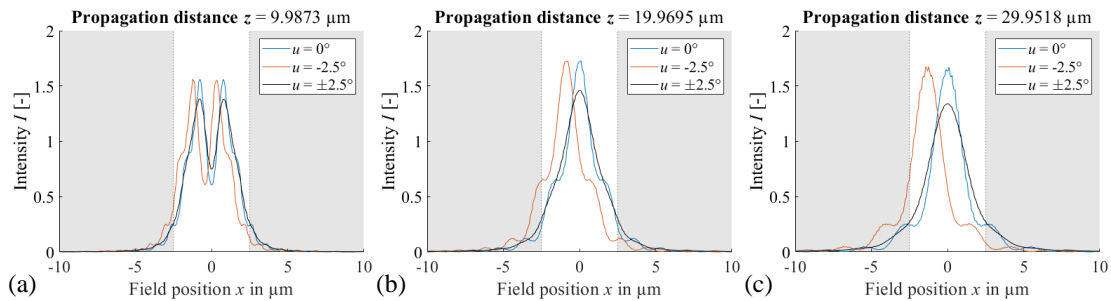


Figure 3.8 – Cross-sections through the intensity distributions shown in fig. 3.7 for different propagation distances, similar to fig. 3.4. (a)  $z = 10 \mu\text{m}$ . (b)  $z = 20 \mu\text{m}$ . (c)  $z = 30 \mu\text{m}$ .



are summed up, as shown in fig. 3.7c, the result is a slightly smaller peak (for a normalization to the original intensity) than compared to single plane wave-caused diffraction patterns, yet without distinct side-lobes, compare the distributions drawn in black in fig. 3.7. Also, as all angles have uniform weight and the angular range is centered around the optical axis, the resulting intensity distribution propagation direction is along the optical axis as well.

#### 3.1.4 Information content of an optical signal and resolution

As already stated in section 2.1.1, the topic of resolution has to be handled carefully in the context of photolithography. Let us begin with the physical resolution of an optical system. In his theory of image formation, Ernst Abbe considered a periodic object like a grating [47, Sec. 8.6.3] [86, Sec. 6.1]. He stated that for the transport of the basic spatial information, the period of the grating, an optical system has to collect the 0<sup>th</sup> and the  $\pm 1^{\text{st}}$  diffraction order of the grating, and bring them into superposition on an image plane<sup>3</sup>. This concept is at the base of image formation in Fourier optics, where an optical signal can be represented by its angular spectrum. The angular spectrum is the decomposition of the signal in plane waves, propagating in different directions away from the object [87, Sec. 3.10]. To reconstruct the object information from the plane waves or angular spectrum, they have to be collected by an optical system and brought into superposition. Thus the information content of an optical signal could be defined via the extent of the angular spectrum available for the transport of object features.

If not all plane waves are collected by the optical system, the entrance pupil of the optical system acts as spatial filter on the signal. Upon reconstruction of the thus limited signal, the low-pass characteristics of this filtering operation yield a complex field distribution which is equal to a Fourier transform of the system aperture. This field distribution is equal to the Fraunhofer approximation, that means the far-field representation of the diffracted field. For a circular aperture the typical intensity distribution of the diffracted field of an imaged point source is the Airy pattern [47, Fig. 8.12].

As an imaging system will not produce an ideal point, but an Airy pattern, we can ask what is the minimum separation of two adjacent points in an object, such that they can be perceived as two distinct points behind an optical system. One well known example of this 2-point definition of resolution was stated first by Lord Rayleigh [9], hence is called the *Rayleigh criterion* of resolution. He found that he could distinctly perceive two adjacent point sources only if the maximum of the Airy pattern of the first source was located not closer than in the first minimum of the Airy pattern of the second point source [86, Sec. 6.5.2]. This is schematically drawn in fig. 3.9. He expressed the minimum separation in an angle  $u$ , which can be found as  $\sin u = 0.61\lambda/a$ , for the illumination wavelength  $\lambda$  and diffraction at an aperture of the

<sup>3</sup>As the  $\pm 1^{\text{st}}$  diffraction orders are symmetrical, it suffices to transport only one of both together with the 0<sup>th</sup> order for the transfer of the spatial information. Yet, if only one of the 1<sup>st</sup> orders is transmitted, the image contrast, upon superposition of the two diffraction orders, will be lower compared to the case where both 1<sup>st</sup> orders are transmitted.

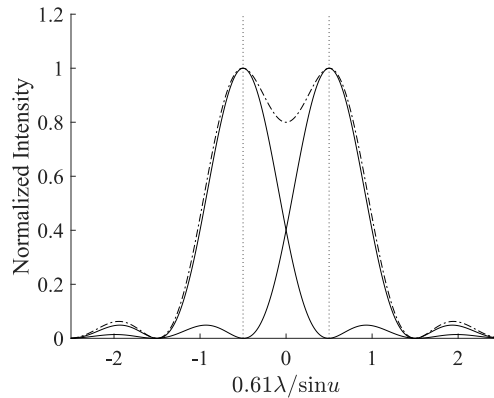


Figure 3.9 – Visualization of the Rayleigh resolution criterion. The minimum separation of two diffraction-limited spots of two point-sources is equal to the radius of the first minimum of the diffraction limited spot to allow clear distinction of both points. After [87, Sec. 6.5.2].

observation system of diameter  $2a$ . With his astronomic background it made sense for Lord Rayleigh to formulate this statement in this way, as his interest lied in resolving two adjacent stars upon telescopic observation.

When we explained the transport of spatial information above with the superposition of diffraction orders, we implicitly relied on a coherent process. What we did not mention until now is the influence of coherence on image formation in general. If light is spatially coherent then it can be described by a complex-valued field amplitude. In contrast, spatially incoherent light can be described by a spatial distribution of real-valued intensity [86, Cha. 2]. This means that for the superposition of mutually coherent light a vectorial addition of the complex amplitude has to be performed, whereas in the incoherent case a simple addition of the intensity distributions is sufficient. This naturally influences the image formation, hence how structures are resolved. An exhaustive treatment of this distinction and the consequences thereof can be found for example at Goodman [86, Cha. 6].

To return to the aforementioned Rayleigh resolution definition, it is obvious that this definition relies on the mutual incoherence of both adjacent point-sources, thus being viable only for incoherent image formation. If both point-sources were mutually coherent, the observation would result in an intensity distribution similar to the result of Young's double-slit experiment, where a fringe pattern was observed with fringe frequency governed by the slit distance [47, Sec. 7.3.1].

In reality, light is never fully coherent nor incoherent. Instead, its coherence properties are for example set by the source it emanates from, and exhibits so-called partial coherence. This describes the degree of coherence, or, for example, the spatial extent over which the light field would exhibit coherent effects upon superposition with itself, and above which an incoherent treatment is allowed [88, Sec. 7.4.3]. We will address the topic of coherence in phase-space in more detail in section 3.2.5.

Finally, as the topic of this thesis is photolithography, we need to address the additional limits and requirements photolithography adds to the discussion. We anticipate section 3.2.1, by taking into account the photoresist as the detector in a photolithographic system. Following Mack's definition of photolithographic resolution [89, p. 484], it is defined as the smallest feature that can be printed with acceptable quality and control. This statement implicitly expresses an indifference on the mechanism of image formation, whether coherent or incoherent, and instead installs the requirement of the application as criterion. When we talk about resolution in the following, we typically refer to a minimum feature size that can be transported into the photoresist, also referred to as critical dimension.

As closing remark we would like to state that in this thesis we rely on incoherent image formation, except for where expressly stated differently. Hence we can apply resolution criteria like the Rayleigh criterion.

## 3.2 Optical systems in phase-space

### 3.2.1 The space-bandwidth product

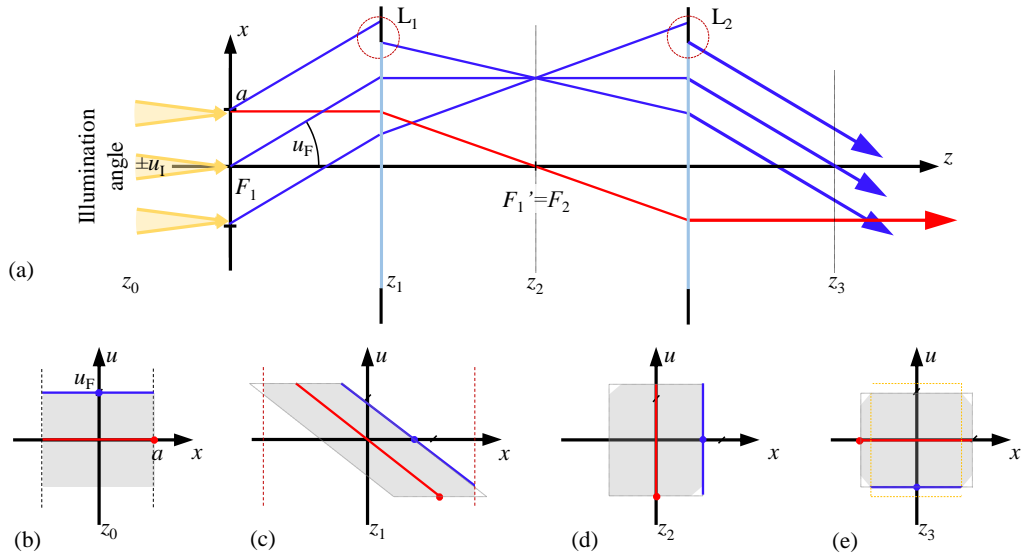


Figure 3.10 – Introduction of the space-bandwidth product, as means to evaluate the information content in an optical system. (a) Simplified optical setup, similar to fig. 3.2. (b) Maximum information content of the optical signal passing the aperture. (b) Propagated optical signal at  $z_1$ . (c) Optical signal after passing lens  $L_1$ . The outmost field points under large angles have been cut at the clear aperture of the lens, highlighted with red circles in (a). (d) Information content in plane  $z_3$ .

As discussed in section 3.1.4, the spatial information content of an optical signal can be described by its angular spectrum. This means, depending on the feature size, a minimum

angular spectrum is required to transmit at least the most basic spatial information of this feature.

Let us consider the example drawn in fig. 3.10a. An aperture of width  $2a$  is illuminated by light of wavelength  $\lambda$ , with an angular range of  $\pm u_i$ . The light is diffracted at the aperture, and the field propagating afterwards has the maximum field angle  $u_F$ . Then a lens  $L$  redirects the light. The largest angles are blocked at the border of the lens, highlighted in the drawing. Then the light passes another lens. In total the shown setup realizes a so-called  $4f$ -system, a simple imaging setup.

Let us now consider this example in phase-space. Figure 3.10b shows the maximum extent of the light field passing the aperture at  $z_0$ . It is laterally limited by the aperture, and its angular extent is defined by the maximum illumination angle plus the diffraction at the aperture. Up to the lens the light field undergoes the lateral shear of free-space propagation, as introduced previously. The lens transforms the spatial and angular distribution, as in the initial example fig. 3.2. But now we have a lens with a finite extent, blocking the largest angles in the corner of the field. In phase-space this can be visualized as an aperture limiting the maximum extent of the parallelogram representing our light field. This aperture thus cuts the corners of our light field representation, see fig. 3.10c. In the focal plane behind the lens the light field exhibits the same Fourier transform as in the original example, but the corners are still cut as drawn in fig. 3.10d. After passing the second lens  $L_2$ , an image of the original field distribution is constructed in plane  $z_3$ . Yet still the information that has been cut at the lenses is missing, see fig. 3.10e.

Now let us interpret this behavior. If the blue lines in fig. 3.10 represent the propagation angle of the  $+1^{\text{st}}$  diffraction order of the aperture at  $z_0$ , then blocking it only leaves the  $0^{\text{th}}$  order propagating, without the possibility to transport any spatial information about the aperture. This means that in  $z_3$  only in the area where both the red and the blue lines, thus  $0^{\text{th}}$  and  $1^{\text{st}}$  diffraction orders are present, spatial information on the aperture can be found. This area is highlighted by the yellow hatched rectangle in fig. 3.10e. In the area, where the blue line has been blocked, thus the largest field points, the system is not able to transport spatial information of the aperture.

If we generalize this picture by replacing the simple aperture in  $z_0$  by a more complex object, for example a photomask, with structures of different feature sizes, then the smallest feature size will define the maximum field angle required for successful information transport. This is schematically indicated by the horizontal light blue lines in fig. 3.11a. If now this largest field angle is partially blocked, then in the final reconstruction of the object information in plane  $z_3$ , the smallest features can be found only where no field angles have been cut. This is indicated by the yellow dashed rectangle in fig. 3.11a. In the area with limited angular extent, that means outside the dashed yellow rectangle, only larger features will be represented. Thus we have a loss in resolution.

After this discussion of fig. 3.10 we can now state that the gray area in fig. 3.10b to fig. 3.10e

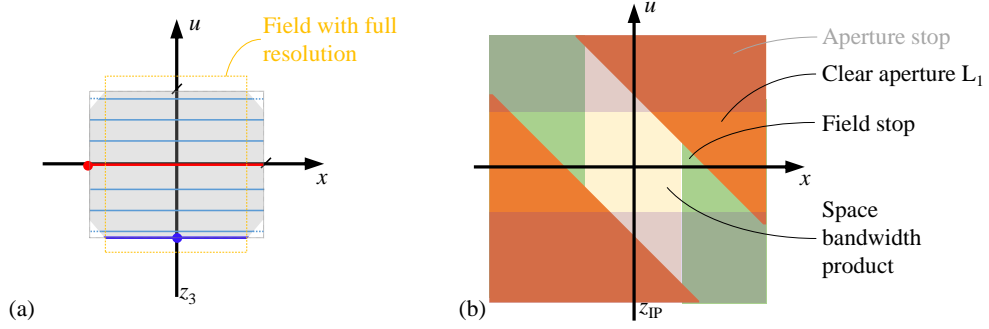


Figure 3.11 – (a) Space-bandwidth product illustrated with different diffraction orders, compare fig. 3.10e. (b) Schematic representation of the transfer function of an optical system in phase-space, and the influence of different apertures in the optical path.

and fig. 3.11a is equivalent to the information content the system can transport. This is the so-called space-bandwidth product [80]. It is a graphical representation of the Lagrange invariant, normalized to the illumination wavelength [90].

Considering fig. 3.11a we can imagine describing an optical system in phase-space by plotting the contributions of all apertures in the system to the space-bandwidth product in the output plane [91]. For an imaging system this output plane is the image plane. Figure 3.11b shows a schematic representation of the optical system previously discussed and drawn in fig. 3.10a. The yellow area in the center is the space-bandwidth product of the system, or the transmittable angles as function of the field coordinate. The shaded blocks around the space-bandwidth product represent apertures. Vertical limits (shaded green) represent the field stop. Inclined limits represent apertures outside the pupil planes of the system. In our case the limits imposed by the clear apertures of the lenses are represented by limits under  $45^\circ$  inclination, shaded orange. If the system had an aperture stop it would be located at  $z_2$ , the common focal point of both lenses ( $F_1'$  and  $F_2$ ). It would limit the angular spectrum passing the system, thus be represented by a horizontal limit in fig. 3.11b, drawn as partially transparent blocks. All apertures have symmetric influences, thus are mirrored at the origin of the phase-space representation. This representation of an optical system is also known as phase-space diagram.

### 3.2.2 Space-bandwidth product and information transport in optical systems

Following the discussion of the previous section we have yet another observation to discuss. In the discussion of fig. 3.10 we mentioned that an object placed in the object plane of the optical system might give rise to different 1<sup>st</sup> diffraction orders if different feature sizes are present in the object. This means that an object can be described by a necessary space-bandwidth product, containing the required angles to represent each field point. Also, as schematically shown in fig. 3.11b, an optical system can be represented by a space-bandwidth product, describing its full information transmission capacity in a phase-space diagram.

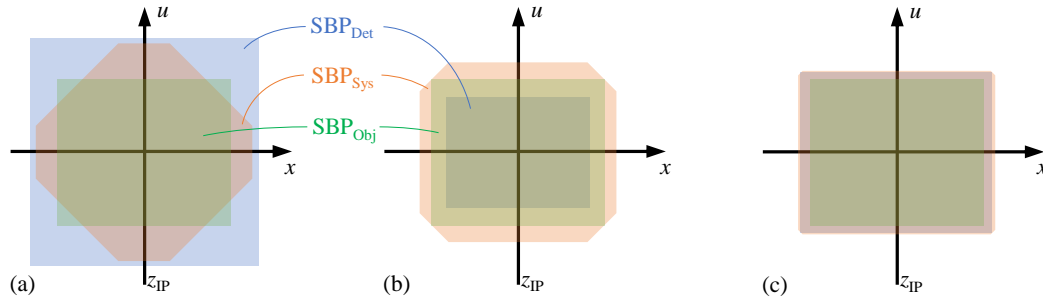


Figure 3.12 – Schematic representation of the concept of space-bandwidth support for the analysis of optical systems. The space-bandwidth products for object, optical system and detector are drawn and superimposed, to evaluate if successful information transfer is possible. (a) Sufficient detector but insufficient optical system. (b) Insufficient detector. (c) Well-optimized system.

Accordingly we can draw a similar conclusion on the detector, which we neglected until now. An optical system can only be as good as its detector allows, recording the information of the object, transmitted by the optical system. A simple example for this effect is a digital image sensor, with discrete pixels of a certain lateral pixel size. This detector is inherently incapable of capturing spatial information on a scale smaller than its pixel size. This is an adapted phrasing of the Nyquist-Shannon sampling theorem [92]. Thus we can also describe an optical detector by a space-bandwidth product, containing information on its maximum lateral extent and resolution. In addition, the detector might possess a maximum angle of acceptance, which would also be visible in phase-space. In the context of photolithography the sensor typically is a layer of photoresist adapted to the chosen exposure wavelength. It acts as analog sensor similar to photographic film. There are different exposure mechanisms which will be addressed in this thesis at the appropriate points when they are discussed for a given application.

To analyze whether an optical system is able to transport the full extent of information in a given situation can be investigated when overlaying the space-bandwidth products of its different components, object, transmission system and detector [80]. This concept of analyzing an optical system in phase-space and finding where full information transport is realized for a given situation is also known as the concept of phase-space support [91, 93]. Support describes here the capacity of the optical system to transport all required spatial frequencies of an object to the detector. And one could argue that this image needs to be enlarged by taking the detector into account as well, if it is not already included in the space-bandwidth product of the system.

Figure 3.12 shows a graphic representation of space-bandwidth product support. All three subfigures show the superposition of the space-bandwidth products of object, optical system and detector. Figure 3.12a shows a situation where the detector is large in comparison to the object. Yet strong clipping of higher field angles from the optical system limits overall

system performance for the largest field points. Figure 3.12b shows the inverted situation, where an optical system is fit to transport all object information, but the sensor is both too small regarding the necessary field extent as well as having too little resolution to fully resolve the object information (resolution here relates to resolution in the angular requirement as discussed with the Rayleigh criterion section 3.1.4). Figure 3.12c finally shows a well-optimized system, where the optical system as well as the detector offer slightly better performance over the whole field to fully transport the object information.

#### 3.2.3 Aberrations in phase-space

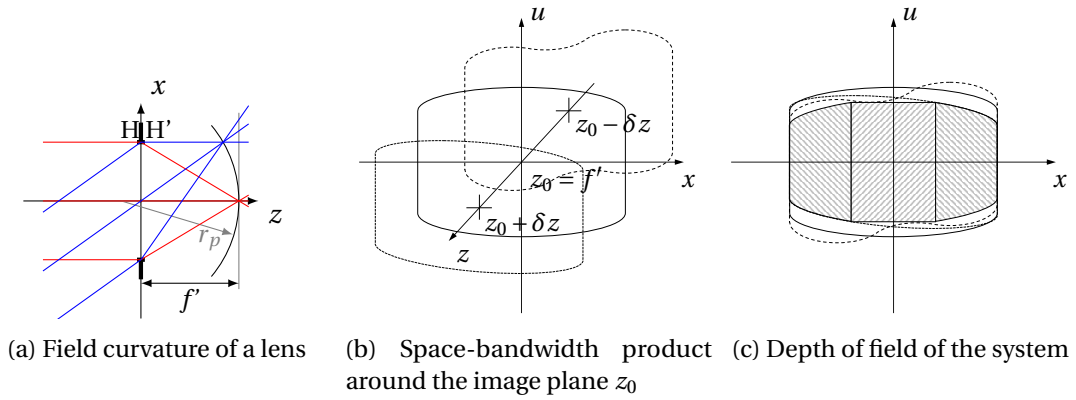


Figure 3.13 – (a) Field curvature of a spherical lens ( $HH'$ ) as simple example of an optical aberration. (b) Its influence on the system space-bandwidth product around the image plane, drawn in extended phase-space. (c) Usable system space-bandwidth product for a given depth of field  $\pm \delta z$ .

The investigation of optical transfer systems like imaging systems in the previous sections was implicitly done in the paraxial regime. This allowed the simplified treatment of apertures in the optical path as straight lines (first order approximation of the paraxial regime). What we did not touch until now is the topic of optical aberrations. They describe errors introduced by an optical systems, influencing the light passing the systems [85, Cha. 29]. Investigating imaging systems is incomplete without considering them. Here as well phase-space allows intuitive and graphical access. To do so we have to leave the geometric optical simplifications we have been applying until now, and consider higher-order terms. This introduces curves to the phase-space [91] [MKN<sup>+</sup>19]. The curvature serves as indicator of the severity of present aberrations, which can be also understood as an illustration of the field dependency of aberrations.

We would like to illustrate this with the example of Petzval field curvature. Other aberrations can be visualized similarly, even if for some cases a three-dimensional representation is advantageous [83, 94].

A spherical lens does not possess a focal plane, but rather a curved cap of best focus. This phenomenon is known as Petzval field curvature [85, Sec. 29.4]. A visualization of this property

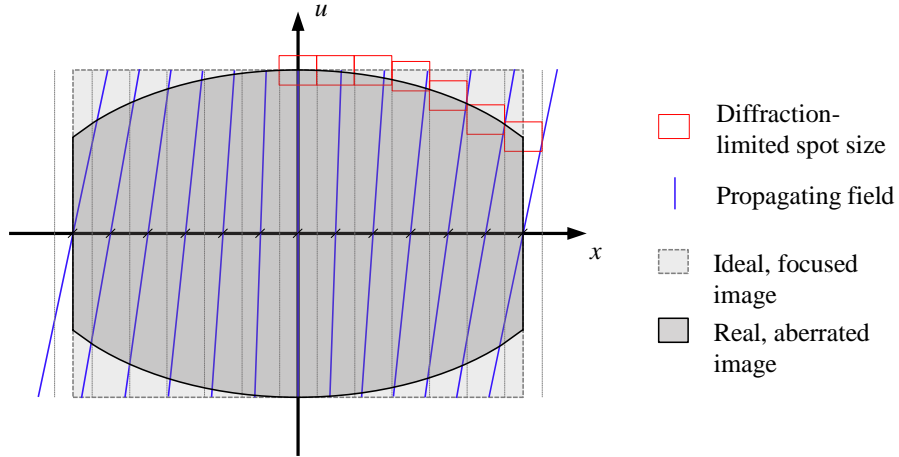


Figure 3.14 – Explanation to the shape of the space-bandwidth product in the image plane as shown in fig. 3.13b. Blue lines represent the optical signal, which is in focus on-axis (vertical line), whereas field points experience shear due to differential propagation in comparison to the on-axis field, as function of their field position. The dark gray area delimited by the black line evaluates the signal from a detector perspective, if the detector is positioned in the focal plane. The diffraction-limited spot-size illustrates the maximum angular extent per field point which still contributes to signal recombination on the detector.

is drawn in fig. 3.13a. In the presented case the image plane is equal to the focal surface. Figure 3.13b draws the space-bandwidth product of the lens for different propagation distances around the focal point. This view is an extended phase-space representation, as it includes an additional dimension, here the propagation direction  $z$ .

In the focal plane  $z_0$  behind the lens, on-axis the full resolution can be observed. For growing field points defocus decreases the maximum transmitted angular components, thus limiting the resolution. We can see this in the curve limiting the angular extent in the solid line in fig. 3.13b. For  $z < z_0$  the center is not yet fully focused, thus defocus here limits the maximum angle. But in the field positions can be found where the image is in focus, due to Petzval curvature, hence here the full resolution is visible. This situation is drawn as dashed line in fig. 3.13b. The dash-dotted line in this figure shows the general loss in maximum resolution due to defocus for  $z > z_0$ . In addition for planes outside  $z_0$  the lateral shear of free-space propagation in phase-space is present and visible.

For further illustration of this phenomenon in phase-space please consider fig. 3.14. Here the focal plane  $z_0$  of fig. 3.13b is drawn in more detail. On the optical axis the optical signal is in focus, thus the blue line crossing the  $x$ -axis at  $x = 0$  is vertical. This can be interpreted as all angles from the corresponding object point superimposing on the same field point, which is equal to image recombination with maximum available resolution. Field points outside the optical axis are not in focus. Thus the corresponding angles exhibit a skew distribution, drawn as the inclined blue lines. This is the shear we already encountered earlier for free-space propagation in phase-space. This is the signal-side interpretation of aberrations in phase-



space. If we now place a detector in the focal plane, this angular shear of field points translates to a position-dependent loss in resolution. On the optical axis all angles are available, thus the on-axis point offers the maximum resolution. For field points, the lateral shear of angles leads to the effect that higher angles will no longer overlap at the corresponding field position, thus limiting the resolution. The maximum lateral deviation angles can possess to still contribute to imaging of a given field point is defined by the diffraction-limited spot size of the optical system in question. This is shown by the red rectangles in fig. 3.14. Finally, if the maximum resolution for each field point is plotted, we find the horizontal lens-shape, drawn as dark gray area with black line, that is also visible in fig. 3.13b.

### 3.2.4 Depth of field in phase-space

The example of the field curvature, discussed in the previous section, leads to a connected topic, the depth of field. The concept of depth of field in optics describes the ability of an optical system to provide its function over an extended range in propagation direction, as opposed to only in its intended working plane. Or, differently put, depth of field describes the range in propagation direction over which its intended functionality is provided. In case of imaging systems the depth of field can be defined for example via their ability to achieve a certain desired resolution.

Figure 3.13 uses the field curvature of a single spherical lens to illustrate this situation. The optical system, schematically drawn in fig. 3.13a, exhibits a certain resolving power in its focal plane, visible as  $u_{max}(x)$  in (fig. 3.13b), which is dependent on the field position. For positions not at the focal plane not only is the space-bandwidth product sheared by the propagation after the lens, but also the resolving power of the lens changes. This can be seen by the change in the envelope of the space-bandwidth product for different values of  $z$ . To evaluate the depth of field, the system space-bandwidth product (SBP)s of the extreme image-plane positions  $z_0 \pm \delta z$  along the propagation direction  $z$  are superimposed. Their overlap equals the minimum accessible system performance inside the specified depth of field. Figure 3.13c shows the fully supported space-bandwidth product for a depth of field of  $\Delta z_{DOF} = f' \pm \delta z$  for a desired resolution (upwards hashed shaded area) as well as the outer field where image transfer with reduced resolution is possible (downwards hashed shaded area). This also illustrates why the depth of field is usually defined for a certain field of view.

### 3.2.5 Coherence in phase-space

Until now the discussion of information transport through optical systems in phase-space took place under the assumption that the propagating plane waves representing different field positions are mutually independent. This describes the ideal incoherent case, where one is effectively looking at a simple superposition of the intensity distributions of each individual plane wave, as already briefly introduced in section 3.1.4. To include the mutual phase relation of any two plane waves, i.e. to include coherence in the description, one

has to consider light as complex field. Also light is no longer propagating in plane waves but in wave fields with finite extent, representing the spatial degree of coherence. There are exhaustive treatments of this topic in literature, which is usually referred-to as partial coherence theory [88, Chap. 5] [47, Chap. 10].

Of importance for this work is the effect of coherence on image formation behind an aperture, for example structures on a photomask, if the propagation distances are not controlled<sup>4</sup>. In the context of this thesis, coherence has mainly two detrimental effects on photolithographic prints. Interference between adjacent features causes a loss in lateral resolution, and interferometric behavior from the optical system, e.g. from reflections in the mask gap, can modulate the maximum intensity over the exposure field. Both effects decrease the obtainable pattern fidelity in the photoresist, thus have to be avoided.

The representation of the partial degree of coherence of a propagating wave field in phase-space is no longer a dot or a line but an area. In this approach the degree of spatial coherence for a signal is encoded in the size of the area around each object (and image) point, which is called the support of said point, following *Castaneda* [93]. This support takes the form of a Wigner distribution function, the so-called marginal power spectrum, which, when drawn in a phase-space for both points, illustrates the state of mutual coherence both points are in. This holds true for propagation of both points to an image plane. This support allows to elegantly incorporate (partial) coherence in the phase-space representation. Considering two separated neighboring features (i.e. pinholes, lines on a photomask, ...), the image of both features is distorted with interference modulation as long as the separation of both points is smaller than the support of each point. This holds true no matter if the features are resolved (separated more than the Rayleigh resolution limits demands) or not resolved. If the separation is bigger than the support, it can be treated as spatially incoherent.

This is of interest for proximity printing, as it offers a straightforward approach to evaluating whether or not interference modulation will be visible in a print (which is to be avoided).

For imaging systems in microlithography, a different description of coherence has taken hold. A parameter  $\sigma$ , the so-called *coherence factor* [4, Sec. 2.3] to describe how close to coherent or incoherent a given case is, is defined as

$$\sigma = \frac{NA_c}{NA_{o+i}}. \quad (3.1)$$

Here the numerical aperture NA is defined as  $NA = n \sin \theta$ , with the refractive index  $n$  in the object space and the object-side half-angle of the lens  $\theta$ .  $NA_c$  describes the image-side Numerical Aperture (NA) of the condenser lens of the illumination system (read "source"),

---

<sup>4</sup>For FEOL photolithography systems coherence plays a central role, as these systems rely on coherent imaging. In these systems the optical path-length is precisely controlled to enable this. Also the photomask structures are typically of uniform dimension to enable coherent imaging. In the BEOL system discussed in this work feature sizes on photomasks can vary and the optical path-lengths are not controlled. Thus coherence has predominantly detrimental effects

whereas  $NA_{o+i}$  is the equivalent NA of the combined object spectrum and entrance pupil of the imaging optics, respectively;  $NA_{o+i} = n \sin(\theta_o + \theta_i)$  [88]. For usual systems and situations  $\sigma$  takes values between 0 (coherent case) and 1 (incoherent case), i.e. the usual case is some state of partial coherence [4, Sec. 2.3]. This coherence factor then allows to simply describe the influence coherence has on image formation in phase-space by limiting the maximum supported angle  $\nu_{max} = \sigma NA / \lambda$  [82, Sec. 19.2.2], with the wavelength-normalized angular extent  $\nu$ ,  $\nu = \sin u / \lambda$ . The straightforward interpretation of this relation is that coherence limits the maximum spatial frequency, thus the resolution obtainable by an imaging system. At the same time, as the extent in  $u$  is limited, also the possible influence of diffraction on the signal is limited, as diffraction is represented by lateral shear in phase-space.

Coherence plays also an important role in illumination for photolithography, as this is the part of a machine where usually the degree of coherence is set. Here the support-approach [93] discussed before is of interest, as will be elaborated on in section 3.3.3.

## 3.3 Photolithographic systems in phase-space

### 3.3.1 Non-imaging system: mask aligner

A mask aligner realizes information transport from a photomask to a photoresist-coated substrate relying on free-space propagation of light passing through and being diffracted at the photomask structures. The photomask is illuminated by a partially coherent source, with a certain angular spectrum. Also the source is usually telecentric [51], to achieve uniform image formation independent of position inside the field of view. This helps to render the exposure process robust against displacements in propagation direction, for example caused by warped substrates.

The image is registered in either a layer of photoresist on a planar substrate (which might already be structured by previous processes), or directly in a planar photosensitive medium (like photosensitive glasses, e.g. for micro-fluidic applications [95–97]). The diffracted light field, upon arrival on the photoresist, forms the so-called aerial image. This is the name for the light distribution formed on top of the photoresist in photolithography [4, Sec. 2.2.4]. The aerial image then exposes the photosensitive layer, and is thus registered via a thresholding process<sup>5</sup>.

The formation of the aerial image relies on the angular spectrum of the illumination, following the properties discussed in section 3.1.3. This enables the use of apodization and

---

<sup>5</sup>The exposure of photoresist requires turning to photochemistry, and the exposure mechanisms. In the scope of this thesis we limit ourselves to the following general statement: photoresist requires a certain exposure dose. This means that only with a certain amount of irradiated energy during exposure enough photo-activated processes have been able to take place inside the resist to change its chemical composition such that it becomes visible upon development. The simplest approach describes this process as a binary threshold process. In reality this is a whole topic of studies by itself, and we suggest the interested reader to turn to Mack's exhaustive book on photolithography [4].

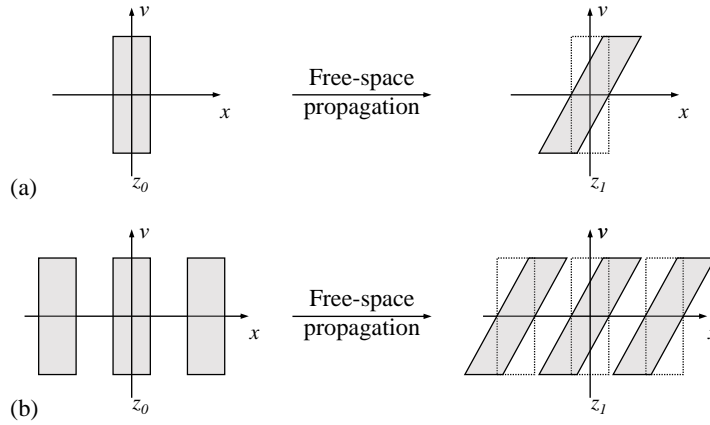


Figure 3.15 – Object space-bandwidth product of a mask aligner in phase-space for an exemplary feature with small critical dimension. In (b) the mutual influence of neighboring features can be seen (spatial overlap of adjacent angular components), hinting at a superposition of diffraction tails [93] and possibly interference effects (Talbot effect and similar) [79, Cha. 9].

similar techniques, to enhance the fidelity of the transported image, as will be discussed in section 3.3.3.

To evaluate the resolution we can obtain with this approach, we need to consider the propagation kernel and evaluate its influence on the object and system space-bandwidth products. With propagation kernel we mean here the transformation of the space-bandwidth product due to free-space propagation of the diffracted light field behind the photomask, hence the lateral shear in phase-space, as introduced in sections 3.1.1 and 3.1.2.

Figure 3.15 shows image formation in a mask aligner in phase-space. It is necessary to evaluate both object and system space-bandwidth products separately as the field of view is so large that a single structure (e.g. a line of line-width  $5\text{ }\mu\text{m}$ ) would not be visible due to several orders of magnitude in difference. To even better represent the limitations in image formation in mask aligner lithography, one has to not only use the geometric-optical propagation kernel, but to include higher orders, as introduced in figs. 3.4 to 3.6.

For an interesting investigation on the mutual influence and/or the separation of adjacent features together with the influence of coherent illumination in the formation of the aerial image in phase-space we invite the reader to turn to Waller [98].

As the lateral shear of the object space-bandwidth product due to free-space propagation is a function of the propagation distance ( $x' = x + z \cdot \tan u$  [85, Eq. 19-139]), it is immediately visible that the best representation of the object (photomask) in the detector (photoresist) can be found for a propagation distance  $z = 0\text{ }\mu\text{m}$ . This is so-called contact printing, realizing lateral resolution of  $0.5\text{ }\mu\text{m}$  to  $2\text{ }\mu\text{m}$  [99].

Contact printing suffers from one severe drawback for industrial applications, which is the

physical contact between photomask and the photoresist layer on the substrate. This can lead to mask contamination when photoresist sticks to the mask upon separation, and at the same time causes yield problems. Even more severe is the possibility of damaging the photomask [100].

The other printing mode, typically realized in industrial environments, is proximity printing. Here the photomask is positioned in a plane parallel to the substrate, with a separation of typically 20  $\mu\text{m}$  to 200  $\mu\text{m}$ . Now the free-space propagation governs the formation of the aerial image, and the minimum resolved feature size  $Res$  can be found as [49]

$$\delta x_{\min} = k_3 \sqrt{\lambda g}, \quad (3.2)$$

with the exposure wavelength  $\lambda$ , the exposure gap, the separation between mask and substrate,  $g$  and a constant factor  $k_3$ . The definition of resolution follows the Rayleigh-criterion, as introduced in section 3.1.4. The  $k_3$ -factor incorporates not only the minimum required separation between adjacent point sources from the Rayleigh-criterion (in which case  $k_3 = 1.4$ ), but also the resist response including influences of subsequent processes involved in the photolithographic process and the influence of typical source partial coherence for mask aligners. Thus in practice  $k_3$  can be found to be about 1.6 [49]. The factor is called  $k_3$  in proximity printing due to a naming convention in photolithography.  $k_{1,2}$  are resolution factors for projection printing, discussed in the following section.

#### 3.3.2 Imaging system: projection system

Projection systems are a group of imaging systems with a very specific task under closely controlled conditions. This makes them some of the most or best corrected optical systems in existence. The task, as for mask aligners, is the transport of geometrically similar structures (lines and spaces, dots and similar geometrically simple basic features) of uniform critical dimension with the least possible aberrations onto photosensitive substrates. Two types of projection lenses with distinct properties exist. Reduction lenses, typically found in combination with stepping capability of the substrate, allow the structuring of a field of view which is small in comparison to the substrate. The exposure field is then sequentially stepped over the substrate to entirely pattern the substrate. 1X lenses, where an erect image with a magnification as close to unity as possible is desired in the image plane, exist in different shapes and sizes, with single field of views of up to 200 mm for systems relying on refractive optical elements only [101]. Catadioptric systems with field sizes of nearly 1 m exist for specific applications [35]. As their field is wide but narrow, they only image a small part of the object and require a scan for full-field printing. Reduction systems, while being some of the most advanced and corrected optics in industrial large-scale fabrication [20] (as opposed to specialized astronomical telescopes or others), are excluded from our discussion. While offering lateral resolution down to the some tens of Nanometers in the latest generations, these systems are not suitable to enable large field of views, thus they are out of scope for the

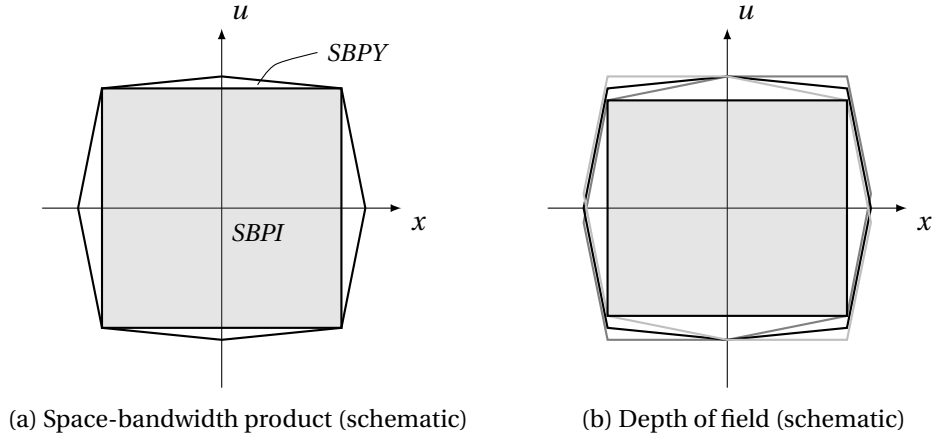


Figure 3.16 – (a) Projection system in phase-space. The system pupil is limited by all system apertures and distorted by lens aberrations. The system space-bandwidth product  $SBPY$  and object or signal space-bandwidth product  $SBPI$  are highlighted. (b) For a well-corrected system these aberrations are minimal, thus not easily visible in the focal plane. But when considering the depth of field they become a limiting factor for the  $SBPI$ .

presented work.

Projection lenses all battle the same problem. A certain depth of field has to be maintained for ever increasing the field of view. The larger the field the larger the aberrations, thus the smaller the depth of field, and the effort to correct these optical systems. This is a conundrum that drives cost for larger systems, and effectively limits the diameter of single 1X lenses (relying on refractive lenses) to about 200 mm circular field of view.

Figure 3.16 shows the representation of a projection system in phase-space, where both a large field requirement is combined with large angles, to achieve high resolution.

To characterize the resolution of projection systems we can again turn to a resolution criterion like the one introduced by Lord Rayleigh section 3.1.4. From the discussion of image formation there, we remember that an optical system has to allow the 0<sup>th</sup> and a 1<sup>st</sup> diffract order from the smallest structure in the object plane to pass to enable representation of this smallest structure in the image plane. This defines a required opening angle  $u$  of the optical system, typically referred to as Numerical Aperture  $NA = \sin u$ . The resolution of a projection lithographic system can thus be found as [49]

$$\delta x_{\min} = k_1 \frac{\lambda}{NA}, \quad (3.3)$$

again with the exposure wavelength  $\lambda$ . The  $k_1$ -factor again incorporates not only the resolution criterion but also the resist response and connected influences, analog to proximity printing in the previous section. As the coherence of the source plays a much bigger role in projection lithography than in proximity printing, the  $k_1$ -factors also differ widely. According to Rai-Choudhury [49],  $k_1 = 0.7$  is a typical value found in praxis.

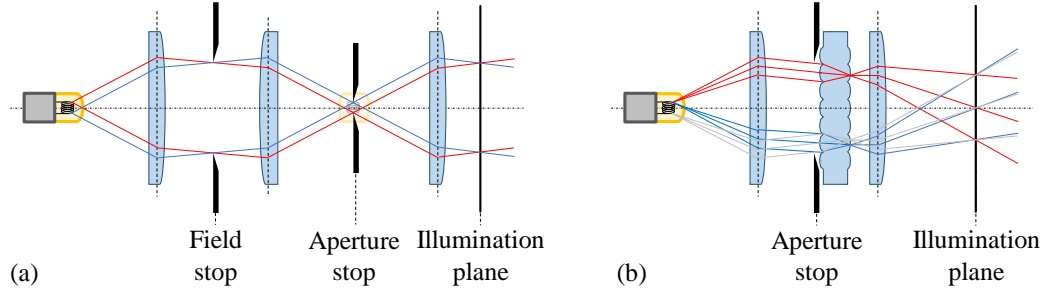


Figure 3.17 – Koehler illumination setup, schematically drawn. (a) Classical Koehler illumination [103]. A source is imaged into an intermediate image plane which is then Fourier transformed into the illumination plane. Field and Aperture stops allow independent control over illuminated area and illumination angular spectrum. (b) Microoptical implementation of the Koehler illumination principle [51]. Here a double-sided microlens array is introduced to achieve beam-mixing to improve the intensity uniformity in the illumination plane.

For projection systems a second characteristic plays an important role in printing as well, the depth of field DOF [49]:

$$\text{DOF} = k_2 \frac{\lambda}{\text{NA}^2}. \quad (3.4)$$

As it scales with Numerical Aperture<sup>2</sup>, it is immediately visible that as resolution decreases, the depth of field decreases even more rapidly. The depth of field sets requirements on the positioning accuracy of both photomask and substrate in respect to the projection lens. As introduced in section 3.2.3, aberrations in an optical system limit the useful depth of field even more, or impose limits on the useful field size (which is equivalent). Thus the second  $k$ -factor  $k_2$  is equally important than  $k_1$  in application, and can be found close to 1 in praxis [49].

### 3.3.3 Illumination for lithographic systems

Photolithographic systems rely on a precise control of the illumination angular spectrum. This is equally important for both non-imaging and imaging systems, as precise source-control allows to implement not only uniform photolithographic printing but also certain resolution enhancement techniques. On such technique is for example the adaptation of the illumination angular spectrum as function of the structures on the photomask. If only structures of similar critical dimension are to be printed, it can be advantageous to allow only certain illumination angles, required for the transport of the respective spatial frequencies [102]. At the end of this section we will briefly discuss one interesting aspect of this technique, because it highlights an application of the phase-space investigation of illumination systems. Further than that we will not dive deeper into the field of these enhancement techniques, as they only allow a gradual improvement mainly of the feature fidelity in the printed structures, and also these techniques represent a whole field of studies by themselves.

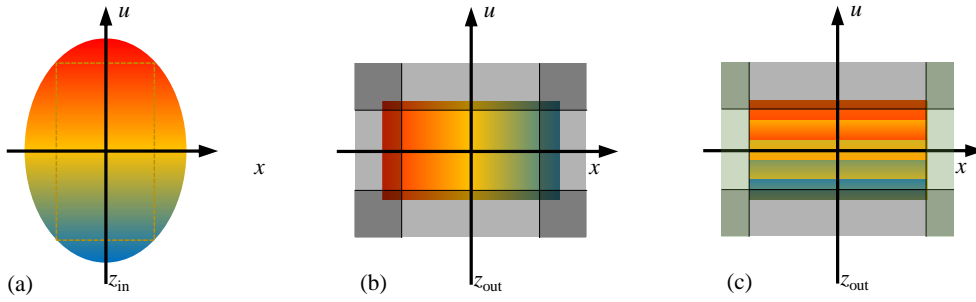


Figure 3.18 – Phase-space representation of Koehler illumination fig. 3.17a. The input from a light source, i.e. an iridescent lamp (a) is limited by a beam-shaping system such that the aperture stops are represented by vertical (field stop) and horizontal (aperture stop) lines in phase-space (b) (compare fig. 3.10). In addition the system is constructed such that the entrance pupil is imaged to infinity, to avoid a visible source representation in the illumination plane. (c) Representation of the field mixing realized with a fly's eye condenser. The field aperture is no longer controlled by an aperture stop but by the focal lengths of the fly's eye condensor's lenses and the Fourier lens.

One important type of illumination system is the Koehler illumination, named after its inventor [103]. Originally devised for microscopy, it has found adoption in many fields, photolithography being one of them. A schematic representation can be found in fig. 3.17a. It consists of a beam-shaping system that is constructed such that the entrance pupil of the system is imaged to infinity in the output plane. This prohibits a visible representation of the source in the illuminated output plane. This can also be understood as a Fourier transform of the input plane, which means that the angular spectrum of the source becomes the spatial distribution of intensity in the output plane and vice versa.

Aperture and field stop in the system are positioned such that each one ideally limits the spatial or angular extent, to allow a precise adjustment of the illumination properties in the output plane. Figure 3.18 shows a schematic representation of this illumination in phase-space, with the input plane shown in fig. 3.18a and the output or illumination plane shown in fig. 3.18b. Here the limiting apertures are shown as gray shaded areas, indicating how they limit the illumination space-bandwidth product, the brightly colored area. The rainbow gradient is used to highlight the distribution in input and output planes. The Fourier transform relation between input and output plane is indicated by the  $90^\circ$  rotation of the distribution in the space-bandwidth product in fig. 3.18. For the sake of completeness we would like to point out that in literature the illumination space-bandwidth product is known under the term *Étendue* [82, Sec. 20.5.1], and defined in terms of direction cosine and solid angle.

One remaining problem of Koehler illumination is the dependency of the illumination uniformity on the uniformity of the source. An important advancement of the Koehler illumination is its implementation with fly's eye condensers [104, 105]. A fly's eye condenser consists of two identical lens arrays separated by their mutual focal length. If implemented in a Koehler



illumination setup it replaces the second lens, as drawn in fig. 3.17b [106]. The input light is separated by the microoptical element into smaller parts, and each part is then used to illuminate the whole illumination plane. This is realized with a Fourier lens recombining the contributions of all microoptical channels. This will be investigated in more detail in section 3.4.3. The illumination plane is drawn in phase-space in fig. 3.18c. The illumination uniformity has been increased, as it is no longer dependent on a specific part of the angular spectrum of the source, but on an average over the angular spectrum. The aperture stop, setting the illuminated area of the fly's eye condenser, controls the angular spectrum. But the illuminated field is now set by a combination of the focal length of the lenses of the fly's eye condenser and the Fourier lens.

The illumination homogenization directly depends on the amount of channels on the fly's eye condenser, which makes microlens arrays ideal for this application [107]. One commercially available illumination system realizing this type of Koehler illumination relying on microoptical fly's eye condensers for mask aligner lithography is MO EXPOSURE OPTICS [51, 108]. It is a state-of-the-art illumination system for mask aligners manufactured by SUSS MICROTEC<sup>6</sup>. Here two of such microoptical Koehler illuminations are staged subsequently to not only achieve uniform intensity but also a uniform angular spectrum.

We would like to briefly discuss the topic of off-axis illumination. This is a technique commonly applied in photolithography, to improve the resolution of the photolithographic print. As hinted at in the beginning of this section it highlights the value of phase-space investigation of illumination systems for photolithography.

If the photomask features uniform structure sizes they require the support only of specific angles by the optical system transporting the spatial information from photomask to substrate. In such a case one can adapt the illumination to specifically support this structure size, as shown in fig. 3.19. Figure 3.19a shows the case for illumination normal to the photomask plane. Here, as expected, we will find the  $\pm 1^{\text{st}}$  diffraction orders symmetrical to the  $0^{\text{th}}$  order. As we only need two diffraction orders according to Abbe's theory of image formation section 3.1.4, by realizing off-angle illumination we can enlarge the effective accessible numerical aperture of the system, thus improve resolution, compare fig. 3.19b [4, Sec. 3.2.1], [104]. This is equivalent to the pupil representation [4, Sec. 2.3.2], if partial coherence is taken into account as well. As stated before in section 3.2.5, partial coherence can be included in the phase-space representation by representing signals through extended surfaces in phase-space, with an overlap of signal surfaces representing mutual coherent interaction.

---

<sup>6</sup>SUSS MICROTEC SE, Garching, Germany

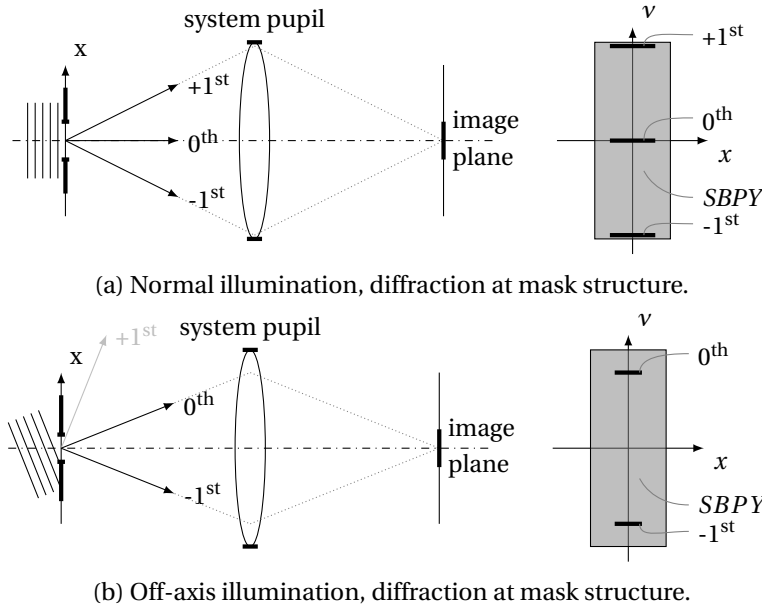


Figure 3.19 – Off-axis illumination in phase-space. Exploiting image formation theory (compare *Rayleigh criterion*), the transmission of two diffraction orders is sufficient for imaging. By careful illumination design, and also by introducing apertures blocking the center angles of the illumination, the achievable resolution can be improved.

### 3.4 Possible enhancements for large-field lithographic systems

Now that we investigated photolithographic systems in phase-space, let us discuss possible improvements in regard to photolithographic systems with large exposure fields.

#### 3.4.1 Exploiting wavelength dependencies

Until now we only stated the influence of the wavelength of light on the information content of the optical signal (compare section 3.1.4), but did not discuss what this implies.

When we consider the resolution of mask aligners (eq. (3.2)) and projection systems (eqs. (3.3) and (3.4)), we find a direct influence on the achievable resolution. For mask aligners the resolution scales with the square root of the exposure wavelength ( $R \propto \sqrt{\lambda g}$ ), whereas the resolution of projection systems even scales linearly with the exposure wavelength.

Figure 3.20 shows a comparison of the simulation of how the aerial image of a single line with width  $2a = 2\mu\text{m}$  would look like for an exposure gap of  $g = 20\mu\text{m}$  for two different wavelengths. Figure 3.20a shows the simulation with standard mask aligner exposure wavelength  $\lambda = 365\text{nm}$ , or i-line (a spectral width of  $\Delta\lambda = 1\text{nm}$  was chosen for this comparison), calculated after the same fashion as fig. 3.4. The intensity distribution is very broad, as can be expected if one considers the lateral spacing of the  $\pm 1^{st}$  diffraction orders (drawn in the blue dash-dotted lines). The Fresnel number for this case is  $N_F = 0.14$ , thus we are in the transition zone

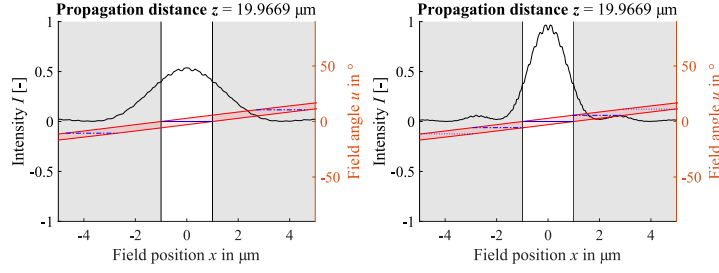


Figure 3.20 – Simulated diffraction at a single slit of width  $2a = 2\mu\text{m}$  after a propagation distance of  $g = 20\mu\text{m}$ , with plane wave illumination for two different wavelengths (a)  $\lambda = 365\text{nm}$  and (b)  $\lambda = 193\text{nm}$ .

from Fresnel to Fraunhofer regime. As can be seen from fig. 3.20a, if we apply the threshold simplification to resist image registration with a contrast requirement of 0.3, we would expect a printed feature width larger than  $2\mu\text{m}$ , and one that is very susceptible to dose variations. Also, when considering the spread of the intensity distribution, for lines and spaces patterns with  $2\mu\text{m}$  critical dimension we don't expect to be able to resolve this at all.

In contrast, choosing the exposure wavelength  $\lambda$  as  $193\text{nm}$ , as shown in fig. 3.20b, would result in an intensity distribution with which a photolithographic print of  $2\mu\text{m}$  critical dimension should be possible.  $193\text{nm}$  is a typical exposure wavelength usually emitted by excimer<sup>7</sup> laser sources [24], hence there are photoresists readily available for this wavelength. A discussion of this type of sources and other possible sources at this wavelength will follow in section 4.1.

For projection systems this shorter wavelength is advantageous as well, considering the linear scaling of resolution (see eq. (3.3)).  $193\text{nm}$  is the typical exposure wavelength of FEOL projection lithographic systems [109] (besides the  $13.5\text{nm}$  of the latest EUV tools).

In the scope of this work we will investigate the improvements this shorter exposure wavelength offers for mask aligner lithography, especially for proximity printing, together with the introduction of a novel semiconductor laser light source at  $193\text{nm}$ , in chapter 4.

#### 3.4.2 Temporal superposition: stepping and scanning systems

As we investigate photolithographic systems with large exposure fields in this thesis, the following investigation is centered on 1X systems, which typically offer the largest field sizes for projection systems in photolithography. Still this does not limit the findings to these systems in general.

1X projections systems all have the projection lens realizing erect 1X imaging in common.

<sup>7</sup>Excimer is a neologism from a shortening of *excited dimer*, describing the working principle of these lasers: a molecule or complex is formed by excited monomers which only exists in excited state. The energy released on bond breaking equals the emission wavelength. The name excimer is in most cases a misnomer as it describes an excited dimer, whereas most deployed lasers of this principle use either argon fluoride (ArF) or krypton fluoride (KrF) as active material, forming *excited complexes*, and should thus be named exciplex.

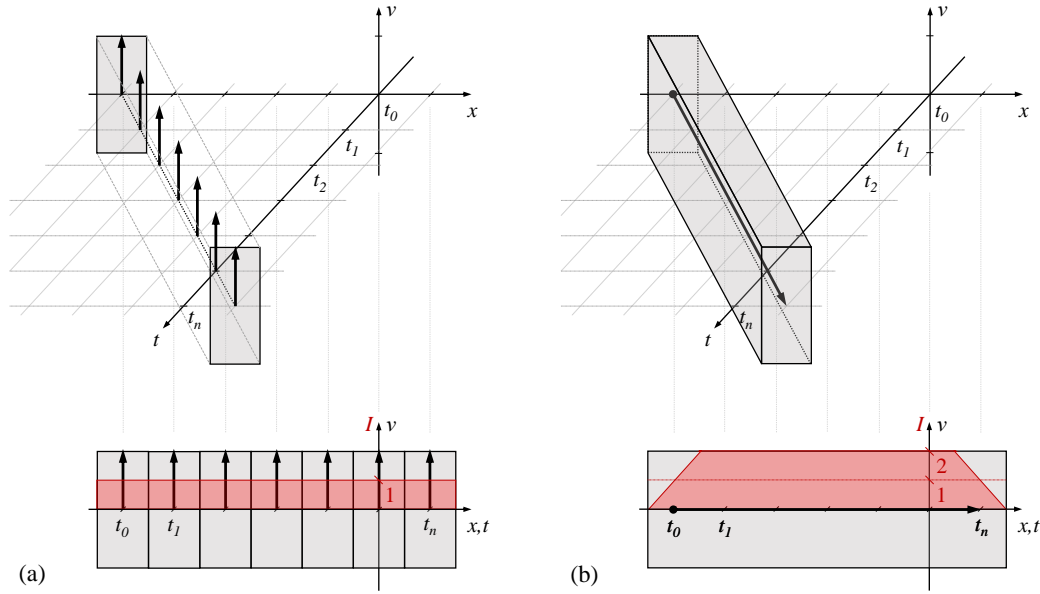


Figure 3.21 – Temporal superposition in phase-space: (a) Stepping system - signal transfer at temporally varying yet spatially discrete positions. (b) Scanning system - signal transfer at temporally varying spatial positions with continuous image capture. Stepping requires high lateral position accuracy, scanning requires a longer scanning distance to ensure uniform exposure dose throughout the scan. The intensity in the superposition image is shown in red in the bottom graphs.

Projection lenses exist with up to 200 mm (circular) FOV [101] or wider but more narrow exposure fields [30]. If the substrate becomes bigger than this there are two possible ways forward, employing stepping or scanning mechanics, or a combination of both, to synthetically enlarge the field of view of the system.

Both techniques rely on the possibility to (virtually) subdivide the photomask into different parts, each such that it fits into the field of view of the projection lens. The photomask is aligned to the substrate and kept at a constant relative position to the substrate throughout the exposure process. The projection lens is then subsequently positioned at different lateral positions and the local information of the photomask is transferred to the substrate. The key here is the temporal superposition of the image in the photoresist. This means that the synthetic enlargement of the projection lens field of view comes at a cost of processing time.

Stepping systems rely on a static lens during each exposure, and a displacement of the lens between exposures. Scanning systems rely on a constant displacement of the lens during one long exposure, where only the local part of the photomask, where the lens is currently located, is transferred. This is drawn in extended phase-space in fig. 3.21. Figure 3.21a shows the stepping superposition with discrete exposure fields, while fig. 3.21b shows the scanning superposition with constant displacement of the projection lens.

Mathematically this temporal recombination of the exposure field can be understood as a convolution of the projection lens space-bandwidth product with a temporal comb function in case of the stepping system, with the lateral spacing of the Dirac pulses equal to the lateral extent of the field of view, and with a continuous and constant function over time in case of the scanning system.

Both approaches come with certain drawbacks. Stepping superposition requires high-precision lateral displacement, as any misalignment of the exposure field will lead to artifacts in the print - either non-exposed areas if the spacing is too large, or overexposed areas where adjacent exposure fields overlap. This is suggested by the red area in fig. 3.21a, a representation of the overall exposure intensity (and, for uniform exposure times for each print, the dose). Scanning systems do not have the stitching problem (at least for linear scans; if two-dimensional displacements are necessary then stitching of adjacent line scans is a potential problem as well). Instead they require a projection lens displacement with constant speed. Any fluctuations in scanning speed would lead to dose fluctuations, as the photoresist integrates over any exposure light it sees. In addition starting and stopping of the scanning process leads to dose gradients, which requires overscanning of the mask size to avoid. The dose distribution is highlighted in red in fig. 3.21b.

Another requirement both approaches pose on the projections lens is distortion-free imaging. Otherwise either adjacent images will not line up properly, or, for scanning systems, distortion will lead to a blurring of the image in the photoresist.

#### 3.4.3 Spatial superposition: multi-aperture systems

Similar to the temporal superposition of spatially displaced exposure fields as discussed in the previous section, a parallel spatial superposition of exposure fields can be realized. This leads to the topic of multi-aperture or multi-channel optical systems. There are basically two types of multi-channel optical systems (which are also found in nature, in the eyes of insects and other related species): apposition and superposition compound systems [15]. Figure 3.22b shows the apposition compound system in phase-space. An enlargement of the field of view is realized by arranging multiple imaging channels in parallel. In an ideal case the individual channel has uniform imaging characteristics over the whole field, and the channel spacing is equal to the lateral extent of the individual field of view. This is equal to the convolution of a single-channel space-bandwidth product with a spatial comb function. Figure 3.22c shows the superposition compound system in similar fashion. Here an angular multiplexing is realized by adjacent channels. We consciously did not write resolution, as this would be true in reality only for an aberration-free system with a perfectly coherent illumination. Otherwise different optical path-lengths between adjacent channels and non-ideal information arrangement would be detrimental to much of the gain in resolution one would expect. For this reason this kind of multiplexing system mainly finds its application in illumination optics, as discussed in section 3.3.3.

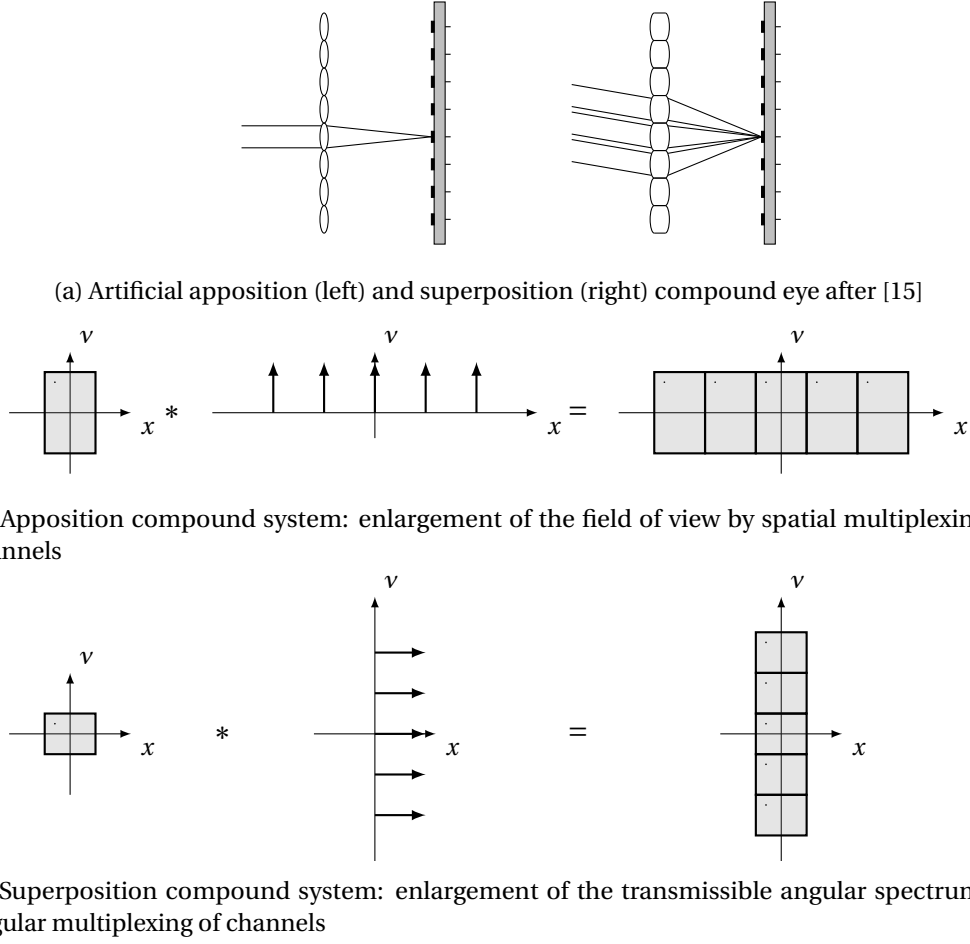


Figure 3.22 – (a) The two main types of multi-channel systems in phase-space.  
 (b) Apposition compound eye - spatial multiplexing (i.e. parallel imaging channels) to enlarge the field of view without changing the dimensions of a single imaging channel.  
 (c) Superposition compound eye - angular multiplexing for an increased accessible angular range per detector / angular spectrum per detector.

#### 3.4.4 Parallelization of projection systems: micro-optics as enabler

Turning to microoptics as manufacturing technique of a large amount of identical lenses, readily integrated on a substrate [70] allows us to combine several of the previously discussed aspects in a single system to realize large-field photolithography.

Microoptics allow us to make use of certain scaling laws of optical systems [107]. An imaging system can be characterized by its stop number  $F = f/2a$ , also known as f-number [107]. If we rewrite the diffraction-limited resolution and depth of field eqs. (3.3) and (3.4) using the stop number, we find  $Res \approx \lambda F$  and  $DOF \approx 4\lambda F^2$ . Both are independent of the lens scale. However, down-scaling of the lens will reduce wavefront aberrations [72]. One of the biggest hurdles in constructing large-aperture 1X projection lenses is the field curvature.

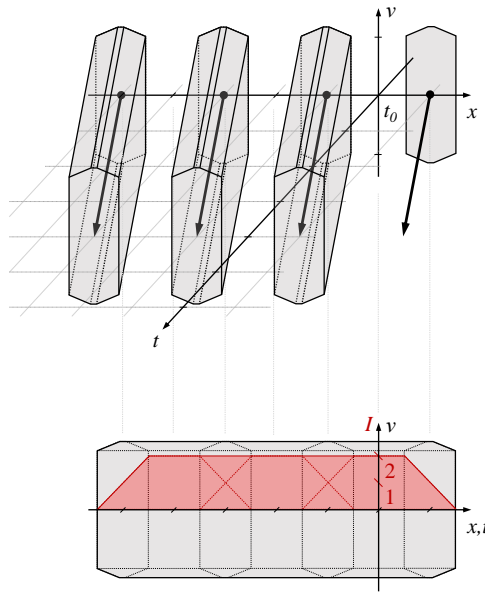


Figure 3.23 – Schematic phase-space representation of a MPL system. Each channel has similar imaging characteristics. A scan of the whole system is performed during exposure, such that adjacent channels overlap. This can be seen in the bottom graph, where the initial and final positions of the individual channels are indicated by the dashed shapes of the individual channel. The intensity representation in this plot, drawn in red, illustrates how, in the field, uniform intensity is achieved with the scan.

Discussed in section 3.2.3, field curvature scales with the square of the field extent. Thus it becomes increasingly hard to compensate, making 200 mm-field of view 1X projection lenses the probably largest field of view projection lenses to be built [110].

We propose thus an integrated microoptical imaging system with  $2\mu\text{m}$  critical dimension resolution, with an exposure field of 100 mm by 100 mm. This compares favorably to the exposure field of 1X projection systems with similar resolution [23]. The proposed imaging system follows the MPL configuration [69, 72], yet with better resolution. The concept of MPL requires a scan of the projection lens during exposure to achieve imaging channel superposition, thus the system approach combines both spatial and temporal superposition. This is shown in fig. 3.23. Here the individual imaging channels are shown similar to fig. 3.22b, which then are scanned in unison similar to fig. 3.21b until adjacent channels overlap. Thus uniform imaging of the whole object can be achieved, with uniform transmitted dose. This is shown in the lower half of fig. 3.23.

In addition, we propose to integrate this exposure system with a stepping stage to allow the exposure of substrates of arbitrary size, following fig. 3.21a.

For a detailed phase-space investigation of an individual imaging channel of the system please consult section 5.1.4, as this investigation fits better in the context of the optical design of the implemented system, discussed there.

### 3.5 Intermediate conclusion

In this section we have discussed the transport of information in optical systems. We have introduced the concept of phase-space as an accessible and intuitive way of representing information transported by light. Building on this we introduced the concept of the space-bandwidth product, a means to evaluate the information in either an optical signal, or supported by an optical system, and have illustrated and discussed the requirements for successful transport of information using light.

We then investigated photolithographic systems in phase-space. As photolithography relies on the transport of spatial information using light, this concept readily suggests itself for this purpose. We also examined an illumination system for photolithography, demonstrating that the same concept applies for both the examination of imaging and non-imaging systems. We limited our investigation in the scope of this thesis to 1X systems with large exposure fields.

Finally, we investigated possible ways to improve photolithographic systems relying on the previous phase-space analysis. We found two possible paths ahead. One is to exploit the exposure wavelength dependency of proximity printing in mask aligners. This will be implemented and examined in chapter 4. The other is a complex highly parallelized integrated microoptical imaging system. In the following sections these two principles will be implemented, investigated and evaluated. Chapter 5 is dedicated to the implementation and investigation of this approach.



## 4 Mask aligner photolithography at 193 nm

In this chapter we investigate the reduction of the exposure wavelength in mask aligner lithography as an approach to enhance the resolution in large field photolithographic patterning. This has been discussed as a first approach in section 3.4.1. As opposed to the excimer laser sources deployed for this purpose by another group [24], we resort to a novel laser light source emitting at 193 nm provided by TOPTICA<sup>1</sup>: a semiconductor CW laser with two subsequent second harmonic generation stages.

This chapter is based on the original work [KVO<sup>+</sup>18a, KVO<sup>+</sup>18b, KVN<sup>+</sup>] and contributions [VOS<sup>+</sup>18a, VKS<sup>+</sup>18, VOS<sup>+</sup>18b, VKO<sup>+</sup>18, OSG<sup>+</sup>18, LSN<sup>+</sup>18] from the author.

### 4.1 Photolithography at 193 nm

Lasers are the light source of choice for photolithography with wavelengths shorter than i-line (365 nm) of mercury high-pressure arc lamps. The first lasers leveraged transitions between different states of excitement of valence electrons of existing elements or molecules to emit light at wavelengths corresponding to the energy difference of those states [111]. This makes them great for long wavelengths (i.e. Helium-Neon lasers from visible range (VIS) (380 nm to 750 nm) to mid-infrared(3.4  $\mu$ m)). The short end of the achievable wavelength range is limited by the ionization energy of the valence electrons of the active material. Semiconductor light sources show similar limits. Here the transition of electrons over a band gap from conduction to valence band defines the emission wavelength. Such sources are light emitting diodes (LEDs), superluminescent diodes and laser diodes (LDs). Technological improvements have made LEDs and LDs available in the UV just below 300 nm [112].

Towards the DUV, a wavelength range with vague definition, in the field of photolithography usually applied for wavelengths from 248 nm to 193 nm, one has to resort to different approaches. Historically the shortage of DUV light sources was overcome by the development of excimer lasers [111]. For photolithographic applications two laser systems with characteristic

---

<sup>1</sup>TOPTICA Photonics AG, Lochhamer Schlag 19, 82166 Gräfelfing, Germany

Table 4.1 – Important wavelengths and the corresponding light sources for photolithography [8, 85]. Wavelengths for Hg lamp refer to emission lines in the emission spectrum. "Color" lists the respective wavelength range. NUV refers to near UV, DUV to deep UV, outside photolithography also often called far UV.

$\lambda$ in nm	Emitter / source	Color	Fraunhofer line
436	Hg high pressure arc lamp	blue	g-line
405	Hg high pressure arc lamp	violet	h-line
365	Hg high pressure arc lamp	NUV	i-line
248	KrF excimer laser	DUV	
193	ArF excimer laser	DUV	

wavelengths have taken hold: KrF and ArF excimer lasers emitting at 248 nm and 193 nm, respectively. Table 4.1 shows an overview of typical photolithographic wavelengths.

The introduction of excimer laser light sources into photolithographic equipment started in 1985, with the implementation of a LAMBDA PHYSIK EMG LAMBDA 248 L excimer laser into an industrial mask aligner from KARL SÜSS [8]. In the mid-1990s excimer lasers were adopted as light sources for wafer steppers, starting with KrF excimers. The demand for ever smaller structures lead to the adoption of ArF excimer light sources by the end of the 1990s and in the early 2000s.

As photolithography not only requires a light source but equally important relies on materials with a photosensitivity at the desired exposure wavelength, so-called photoresists, it is easily understandable that only a few wavelengths with corresponding resist chemistry have prevailed. So the introduction of novel light sources to photolithography not only requires the development of a light source but usually is hindered by the non-compatibility of existing photoresists. The easiest approach is to make use of existing photoresists.

The use of an ArF excimer laser as light source for mask aligner photolithography was investigated by Partel *et al.* [24]. While possible, the actual integration of excimer sources is complex and expensive. For high-power operation they require voltages exceeding 40 kV and large volumes of corrosive gas mixtures at high pressures [113]. Frequent maintenance, including gas and electrode exchange, adds to complexity and cost of such systems. Additionally, the choice of feasible optical materials is limited to calcium fluoride ( $\text{CaF}_2$ ) and UV-grade fused silica in the deep ultra-violet. High peak power in pulsed operation can lead to the formation of color centers, degrading the material transmittance over time [114]. In fused silica, the high peak energy of the pulses leads to a compaction of the optical material, changing its refractive index, thus its optical properties [115, 116]. From an optical perspective their multimode and pulsed operation have to be taken into account and dealt with. These characteristics also weigh in on the efficiency of light collection for illumination purposes [117]. For efficient beam-shaping it would be advantageous if the number and shape of laser modes could be controlled. From an Étendue perspective monomodal operation of the laser would provide the most freedom.

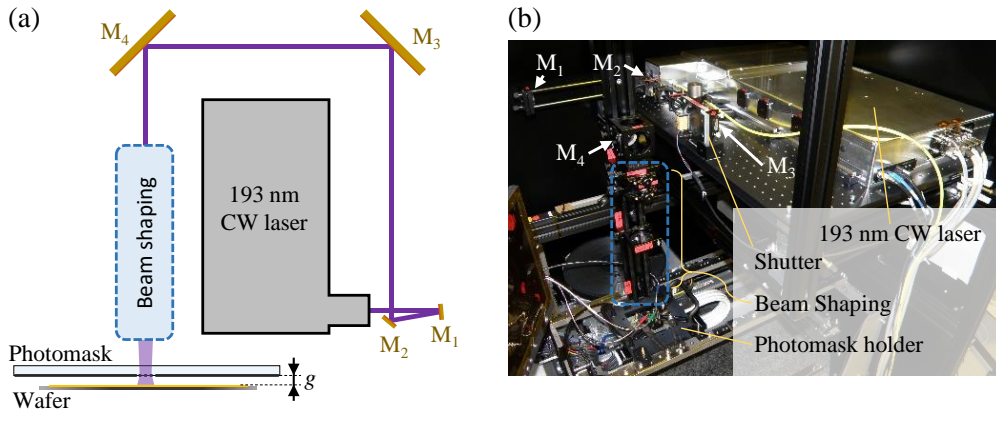


Figure 4.1 – Mask-aligner setup with TOPTICA's 193 nm CW semiconductor laser light source. (a) Schematic: the beam is guided from the laser output via 4 mirrors ( $M_{1-4}$ ) to the photomask and wafer stack. Beam-shaping was investigated with both a non-imaging and an imaging homogenizer setup. The exposure gap  $g$  was set and controlled using a single micron-precision 6-axis movement stage with optical gap metrology. A mechanical shutter enabled the control of exposure times. (b) Photograph of the implemented setup.

For these reason the development of a novel CW semiconductor laser source by TOPTICA emitting at 193 nm is intriguing. It circumvents the necessity of developing novel photoresist families by enabling the use of existing chemically amplified photoresist chemistry<sup>2</sup> for 193 nm. It is enabled by a crystal material for frequency up-conversion to the desired wavelength, which only recently became available in the required grade [17]. Photolithography with frequency up-converted lasers leveraging non-linear optical effects in certain materials has been demonstrated before [55], but not for 193 nm. This was only enabled by the recently developed laser by TOPTICA.

To investigate mask aligner photolithography at 193 nm we implemented the laser source into an experimental mask aligner setup, shown in fig. 4.1. Multiple mirrors are used to deliver the laser beam to a beam-shaping setup, transforming the monomodal beam with Gaussian irradiance profile to a flat-top profile, to enable uniform exposure of the full field. The beam-shaping setup consists of a rotating diffuser setup to introduce multiple illumination angles, and a subsequent beam homogenizer setup featuring microoptical multi-aperture elements for beam mixing. Literature suggests non-imaging homogenizers for most effective beam-shaping of monomodal sources, but the use of diffusers suggests better results with imaging homogenizers. Both non-imaging and imaging beam-homogenizer setups have been investigated, together with different diffuser setups. We present photolithographic prints realized with these illumination setups, illustrating the viability of this laser source for mask

<sup>2</sup>Chemical amplification refers to a technique where the exposure not directly changes the bulk photoresist. Instead, it frees an acidic component, which in turn catalyzes a chemical reaction in the photoresist during post-exposure bake. This reaction may implement either a positive or negative resist behavior, but the crucial point is that the acidic component is not used-up during this process. This allows to expose photoresist with comparatively low exposure doses. [89]

aligner lithography.

The following chapter aims to answer the following questions:

1. Can we simulate the whole illumination system as implemented, including interference effects?
2. What beam-shaping approach is best suited for the task?
3. Is this novel 193 nm CW laser light source suited for mask aligner lithography?

### 4.2 Toptica's UV MOPA laser

As it is important for the following original work to understand the workings of the laser light source by TOPTICA, in the following we review its setup and working principle, together with some key parameters with regard to our application. This section is based heavily on work from TOPTICA's Matthias Scholz [17], as well as additional work where the author of the presented thesis contributed (but not on the development of the laser source itself) [OSG<sup>+</sup>18, LSN<sup>+</sup>18].

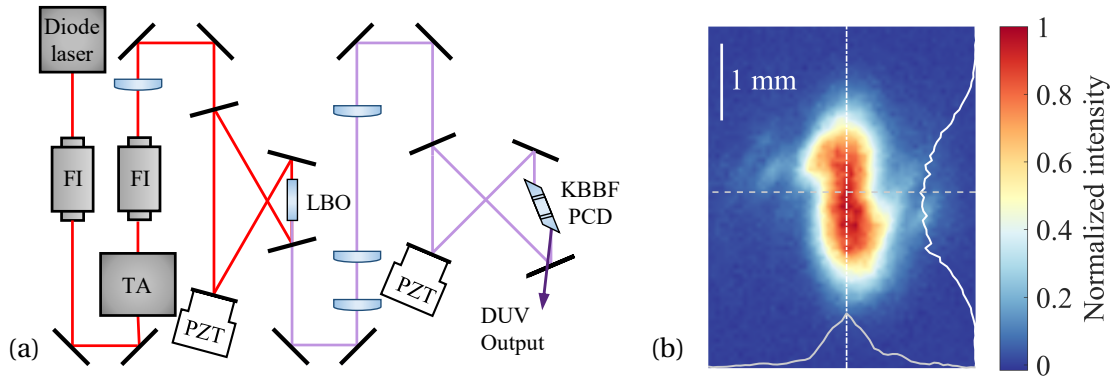


Figure 4.2 – (a) TOPTICA's 193 nm UV master oscillator power amplifier (MOPA) semiconductor laser. The output of a frequency stabilized open-cavity diode laser is routed through a Faraday isolator (FI) and magnified in a tapered amplifier (TA). Frequency upconversion takes place subsequently in a lithium triborate (lithium triborate (LBO)) and potassium fluoro-beryllate (potassium fluoro-beryllate (KBBF)) crystal as a prism coupled device (PCD) between  $\text{CaF}_2$  prisms. Active feedback control for output stabilization is implemented via piezo elements (PZT). Adapted from [17]. (b) Beam profile measured 200 mm behind the laser output.

Reprinted with permission from [KVO<sup>+</sup>18a] ©The Optical Society.

Figure 4.2a shows a schematic of the laser. It consists of three stages: first a CW frequency-stabilized open-cavity-type diode laser emitting at 772 nm, with a linewidth of less than 10 kHz (which is equal to  $\Delta\lambda = 1.24 \text{ \AA}$ ) [17]. This diode laser (TOPTICA *DL pro*) operates based on the master oscillator power amplifier (MOPA) principle. A highly stabilized diode seed laser (the

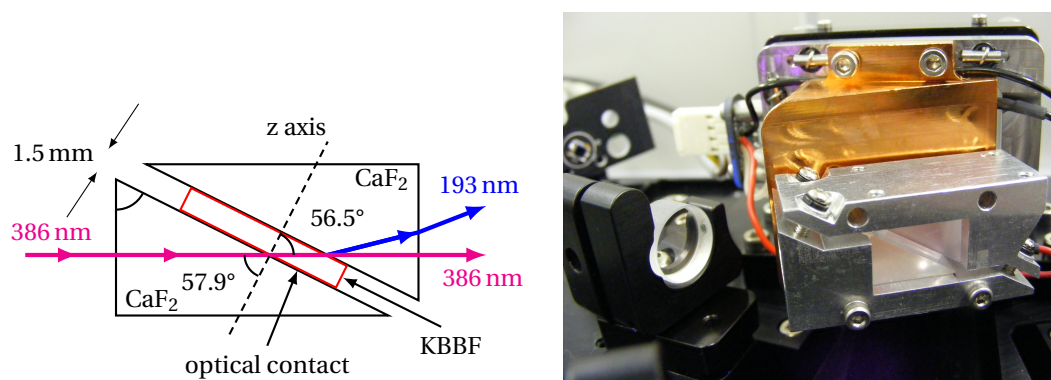


Figure 4.3 – Left side: schematic view of the mechanical mount for the KBBF crystal between two CaF<sub>2</sub> prisms, optimized for frequency-doubling from 386 nm to 193 nm. Right side: picture of the mechanical mount for the prism-coupled KBBF crystal. Reprinted with permission from [OSG<sup>+</sup>18].

master oscillator) is subsequently boosted by an amplifier, another semiconductor element similar to the seed laser, capable of much higher powers, to CW power >2 W. In a first second harmonic generation stage this output is up-converted to 386 nm in a LBO crystal. The shorter wavelength laser light is then up-converted in a second second harmonic generation (SHG) stage, featuring a KBBF crystal, emitting at 193 nm.

Faraday insulators around the power amplifier prevent back reflection both into the seed laser and the amplifier itself. The second harmonic generation cavities are both realized in bow-tie configuration which are stabilized with piezo-electronically actuated mirrors using the Pound-Drever-Hall scheme [118]. The optical output power at the final wavelength depends most sensitively on the beam position in the KBBF crystal, and is typically 7 mW CW, with a maximum of 10 mW for the crystal in use.

Only recently KBBF crystals of sufficient quality became available [119–121]. The implementation of this material into SHG cavities is challenging. As the crystal direction under which the non-linear upconversion takes place is below the angle of total internal reflection it is necessary to optically bond a KBBF crystal between two CaF<sub>2</sub> prisms, forming a prism-coupled device. This is not trivial with KBBF as it is a soft material which needs to be polished to optical quality. Figure 4.3 shows the bonded KBBF crystal slab, which has a thickness of 1 mm to 2 mm, between two CaF<sub>2</sub> prisms. The maximum output power of the KBBF SHG stage depends on the bond quality between the KBBF crystal and the CaF<sub>2</sub> prisms. The bonding process is an ongoing work at TOPTICA and the output power is expected to reach 50 mW to 100 mW in the near future.

The output beam exhibits a distorted Gaussian profile, imposed by the second second harmonic generation stage. The ellipticity of the beam profile, visible in fig. 4.2b, stems from the DUV output direction not being parallel to the pump laser direction [17] (skew projection of the Gaussian profile of the pump laser, into the new propagation direction).

Depending on the desired output power, the lifetime of a single spot in the bonded KBBF crystal varies. The continued use of a spot in the KBBF crystal for frequency upconversion causes the optical bond to the  $\text{CaF}_2$  prisms to deteriorate. To maintain a stable output the pump power is gradually increased. TOPTICA has conducted longterm measurements for different output powers. They demonstrated crystal spot lifetimes of up to 200 h for 10 mW of optical output at 193 nm, and over 500 h for 1 mW output [OSG<sup>+</sup> 18].

After the frequency quadrupling, the output beam still possesses a spectral linewidth of  $<500$  kHz [17], which is by far superior compared to standard high-pressure mercury arc lamps, and even superior compared to a linewidth of 2.5 GHz for latest DUV front-end lithographic systems with excimer sources [54]. For mask aligners this represents a challenge, as a high degree of coherence in the illumination can lead to unwanted and, worse, uncontrolled interferences in the illumination path. These manifest as optical speckle and interference fringe patterns from reflections off optical elements in the beam path. Both effects cause non-uniformities in the intensity in the photomask plane and, consequently, in the exposed photoresist. To suppress the visibility of interference fringes in the photoresist, the spatial degree of coherence has to be controlled to a length-scale shorter than the smallest Fabry-Pérot cavity in the illumination path in beam direction. In our case this is the exposure gap<sup>3</sup>. Additional measures have to be taken to suppress the visibility of optical speckle in the exposure field.

The following section discusses ways to transform the monomodal laser beam with Gaussian profile into a flat-top intensity profile and how to mitigate the visibility of coherence effects for mask aligner photolithography with the presented 193 nm CW source.

### 4.3 Illumination system for mask aligner lithography with a coherent source

Beam-shaping for mask aligner lithography with coherent laser light sources needs to address two main aspects: the transformation of the source beam profile into a flat-top in the mask plane and dealing with the coherence of the source.

In this section we review two illumination systems with beam-homogenizer setups featuring microoptical multi-aperture elements for beam mixing. Both reshape an arbitrary input irradiance profile to a flat-top profile. A rotating diffuser is introduced into the beam path to suppress the visibility of optical speckle, a typical problem with coherent illumination, in the exposed photoresist. We discuss the implementation of these beam-shaping systems and present incoherent ray-tracing simulations to demonstrate and evaluate their expected performance.

---

<sup>3</sup>We neglect here the resist layer height as a potentially smaller layer. It has to be noted that standing waves inside the photoresist layer is always a problem in photolithography that has to be addressed for smooth sidewalls. For this reason usually bottom anti-reflective layer and/or top anti-reflective layer are added. These coatings also help in mitigating interference fringes from the exposure gap Fabry-Pérot response.

Then, to take the coherence of our desired source into account, we discuss interference effects like fringe patterns and optical speckle. We present, investigate and validate a novel approach to coherently simulate not only optical speckle, but the entire illumination systems for mask aligner lithography with coherent sources and diffusers in the beam path. This simulation allows us to engineer the required speckle size to suppress the visibility of Fabry-Pérot responses from optical interfaces in the beam path. It enables the successful implementation of mask aligner photolithography with the 193 nm CW laser light source from TOPTICA.

#### 4.3.1 Beam-shaping with array optics

Mask aligner lithography relies on uniform illumination of the entire exposure field, or, in other terms, the whole active area of the photomask. Especially with the Gaussian beam profile of laser light sources, beam-shaping is required to transform the source irradiance profile into a flat-top profile<sup>4</sup> in the mask plane. For this reason we investigate non-imaging and imaging homogenizer beam-shaping setups [104, 105].

For the moment we ignore the coherence of the source, as the reshaping of light from an arbitrary profile into a flat-top profile works with the same optical setup for both coherent and incoherent sources. The source coherence, and the effects it causes, will be taken into account starting in the following subsection, section 4.3.2. For now, it suffices to know that a rotating diffuser setup is implemented prior to either homogenizer setup to suppress the visibility of speckle in the mask plane via temporal integration in the detector, in our case the photoresist. This also enables the use of incoherent simulation to investigate the behavior of the beam-shaping setup in this subsection.

As described in literature [105], non-imaging beam homogenizers usually are used for monomodal laser applications, as they are sensitive to the angle of incidence of the illumination. In our case we deal with a monomodal laser that passes an optical diffuser setup. This means that the laser beam is split into a multitude of beamlets, each with individual phase delay. These manifest as a transformation of the collimated laser beam into an uncollimated, or spreading, wavefront with varying phase. So theory suggests to deploy an imaging homogenizer setup [105]. We investigated both non-imaging and imaging approaches, also to compare different technologies of micro-optical mixing elements. Figure 4.4 shows the two setups we realized and implemented into the experimental mask aligner setup.

The non-imaging homogenizer setup, shown in fig. 4.4a, relies on a single-sided MLA as mixing element. A Fourier Lens ( $L_{FT}$ ) superimposes the fields of the individual lenslets in the mask plane, and a Field Lens ( $L_{FL}$ ) ensures illumination telecentricity in the mask plane. A mechanical iris aperture acting as illumination filter plate<sup>5</sup> is used to control the irradiated

---

<sup>4</sup>*Flat-top profile*, also known as top-hat profile, describes a distribution with rectangular cross-section. The center region has a uniform value  $> 0$  up to a certain field extent, at which the function value drops to zero. Ideally this transition is instantaneous, whereas in reality as sharp a transition as possible is aspired.

<sup>5</sup>We refer to the naming scheme introduced with MOEO [51], describing the state-of-the-art mask aligner exposure optics featuring microoptical Köhler integrators.

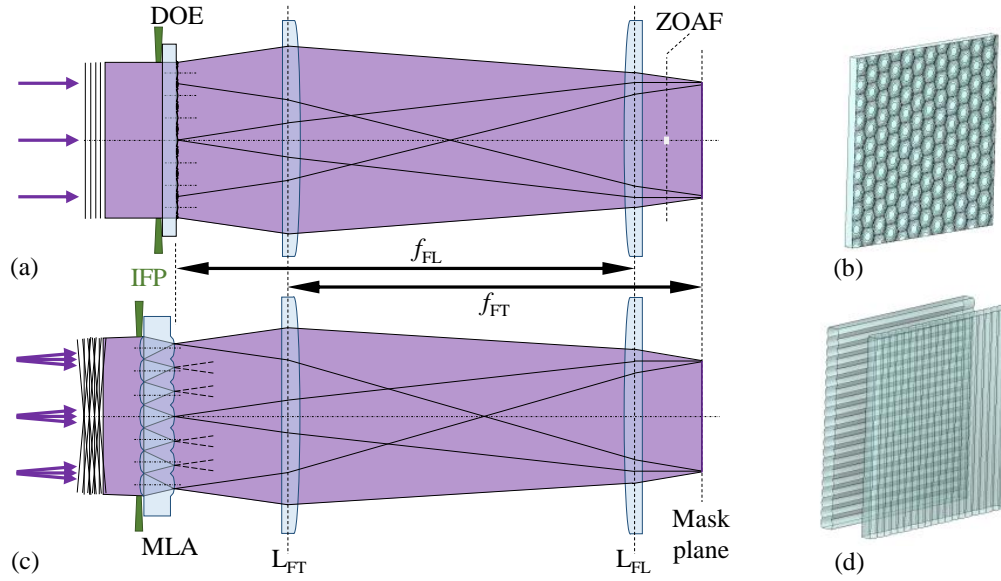


Figure 4.4 – Two-dimensional schematics of beam-homogenizer setups and their beam mixing elements. (a) Non-imaging homogenizer with single-sided diffractive optical element (DOE) as mixing element and zero order attenuation filter (ZOAF). Illumination by a plane wave to indicate its sensitivity to the illumination angle of incidence. (b) Schematic 3D rendering of the DOE. (c) Imaging homogenizer with Köhler integrator realized with a MLA (MLA). Multi-angle illumination to indicate its tolerance against a broader illumination angular spectrum. (d) Schematic 3D rendering of the Köhler integrator, realized as crossed double-sided cylinder MLAs.

Common features in (a) and (c): Fourier lens ( $L_{FT}$ ) for channel superposition in the mask plane; Field lens ( $L_{FL}$ ) to ensure illumination telecentricity in the mask plane; Mechanical aperture "illumination filter plate" (IFP) to control the irradiated area of the mixing element, thus controlling the angular spectrum in the mask plane.

area on the mixing element, thus controlling the angular spectrum in the superposition plane.

The mixing element, shown in fig. 4.4b, consists of a hexagonal arrangement of Fresnel lenslets with half-axis of 1.9 mm and 2.2 mm. It is realized as eight-level diffractive optical element and optimized for 193 nm [KVO<sup>+</sup> 18a]. It possesses a theoretical maximum diffraction efficiency of 95 % [122], which the element in use does not reach. Manufacturing errors in the production of diffractive optical elements lead to non-ideal performance [123]. Mainly etch-depth errors cause non-diffracted light to simply pass the the element and cause a strong zero order in the superposition plane. A small circular aperture, named zero order attenuation filter, is introduced into the beam path to mitigate this effect. It has the diameter of the zero order and is positioned on the optical axis, but outside the superposition plane. This allows to only attenuate the zero order instead of completely blocking it. This is necessary as otherwise the intensity in the center of the mask plane would reach zero, equally destroying the desired illumination uniformity.



### 4.3. Illumination system for mask aligner lithography with a coherent source

---

The imaging homogenizer setup, drawn in fig. 4.4c, features a microoptical Köhler integrator instead of a single-sided MLA. It is followed by a Fourier lens ( $L_{FT}$ ), again to superimpose the individual channels in the mask plane, and a field lens ( $L_{FL}$ ) to ensure telecentric illumination in the mask plane. The mixing element consists of two crossed double-sided cylinder MLAs, as shown in fig. 4.4d. The lenses on both sides of each element share the same focal length, and are separated by the same distance (element thickness chosen accordingly). This is the so-called Köhler integrator arrangement [124]. It realizes Köhler illumination [47, 103] for every channel of the microoptical integrator. This arrangement renders the integrator tolerant to the direction of incident light for illumination angles inside the acceptance angle of the element. The Köhler integrator in our case is realized with two crossed cylinder MLAs, enabling a fill-factor for the MLAs >98 %, and offering nearly square subapertures per channel. The channels are slightly rectangular due to the distance of approx. 2 mm between both cylinder MLA elements.

To simulate such beam-shaping systems, independent of the source, incoherent ray-tracing is the tool of choice for system investigation. This is also true for systems with coherent laser illumination, when they possess means to suppress speckle in the output plane, like a rotating diffuser.

Beam-shaping systems require the simulation of non-imaging optical systems, where the entrance pupil is usually imaged to infinity, to achieve good illumination uniformity and to suppress a direct representation of the source in the illumination plane. Additionally, beam-shaping systems are usually quite long (in mask aligners in the region of 1 m in length), and they can feature multi-aperture elements for beam mixing. In our case, with microoptical mixing elements, the count of parallel channels in these elements can easily reach several thousands<sup>6</sup>.

The exit pupil located at infinity and the presence of parallel channels prevent the use of classical sequential, incoherent optical simulation, where the system under consideration is analytically described via its transfer function in the exit pupil, with subsequent propagation of this function to the image plane. Numerical solvers could handle multi-aperture elements (also coherently), but quickly reach their limits when tasked with simulating large and/or long systems. Incoherent ray-tracing allows to combine all of the mentioned characteristics into one simulation model. Both, imaging and non-imaging systems have been simulated with ZEMAX<sup>7</sup>, in non-sequential mode, with general simulation settings as listed in table 4.2. *Non-sequential mode* in the context of ZEMAX refers to incoherent ray-tracing, as opposed to *sequential mode*, ZEMAX' basic mode of operation following the aforementioned analytical approach.

The results of these incoherent ray-tracing simulations are shown in fig. 4.5 for the non-imaging homogenizer, and in fig. 4.6 for the imaging homogenizer.

---

<sup>6</sup>For example the microoptical mixing element in our imaging beam homogenizer: circular illuminated area, 20 mm diameter, square microoptical channels, 350  $\mu$ m side length, i.e. > 2500 channels in parallel.

<sup>7</sup>Zemax OpticStudio®, by Zemax LLC, V19.4 SP1

## Chapter 4. Mask aligner photolithography at 193 nm

Table 4.2 – Simulation parameters for incoherent ray-tracing simulation in ZEMAX of non-imaging and imaging homogenizer setups for mask aligner lithography with 193 nm CW laser. Source shape is circular.

Description	Parameter	Value		Unit
		N.-imag.	Imag.	
Source diameter	$D$	20		mm
Source wavelength	$\lambda$	193		nm
Number of rays		$1 \cdot 10^7$		1
Angular spectrum <sup>1</sup>		0.1	2.5	°
Sub-aperture shape		hexagonal	square	
Sub-aperture size <sup>2</sup>		1.6	0.3	mm
Fourier lens focal length	$f_{FT}$	200		mm
Field lens focal length	$f_{FL}$	200		mm

<sup>1</sup> Uniform distribution.

<sup>2</sup> N.-imag: inscribed diameter; Imag.: side length.

The non-imaging homogenizer clearly exhibits a strong zero order (see center of fig. 4.5a), as well as the hexagonal shape of the illuminated area on the detector, which is located in the mask plane. This hexagonal shape stems from the hexagonal sub-apertures in the mixing element, the one-sided diffractive optical element. The zero order attenuation filter attenuates the zero order, as is shown in fig. 4.5b. Figure 4.5c depicts the angular spectrum in the mask plane, exhibiting the contribution of every illuminated Fresnel lenslet on the diffractive optical element. The entrance pupils of this mixing elements are underfilled, which is visible in the simulation as the angular spectrum is no uniform surface, but consists of discrete spots.

The results for the imaging homogenizer show the square illumination area, caused by the crossed microoptical cylinder lenses, which yield nearly square subapertures, compare fig. 4.6a. The cross-shaped artifact visible in this figure is caused by a small plane area in between lenslets in the simulational model of the MLA, which is not present in reality. In reality the inter-lens areas are not flat, but concave, due to the manufacturing process. As this area is not specified, though, and thus not measured, for the simulation it was assumed flat. The extent of the angular spectrum is continuous, and can be set with a mechanical aperture, the illumination filter plate, as shown in figs. 4.6b and 4.6c.

When comparing both approaches, non-imaging and imaging homogenizer, three points are immediately obvious: the irradiated area depends on the shape of the subapertures of the mixing element, the overall irradiance uniformity is better for the imaging homogenizer, and the border of the irradiated area of the imaging homogenizer is much sharper. The first point, the shape of the irradiated area, is no criterion for discussing superiority of either design; the shape should be chosen according to the desired geometry of the exposure field. Both other points, the steepness of the border of the intensity distribution in the exposure field and its uniformity over the field strongly influence the quality of photolithographic prints. Yet another

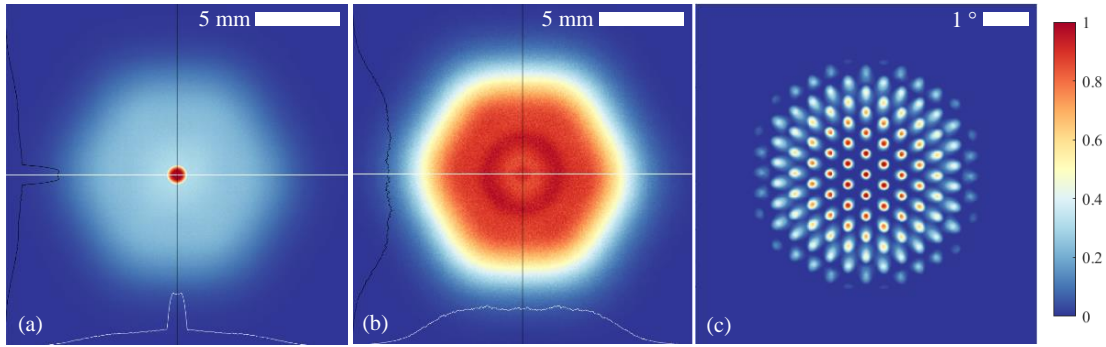


Figure 4.5 – Ray-tracing simulation of non-imaging homogenizer setup illumination in the mask plane, compare fig. 4.4a. Normalized intensity is shown.

(a) Intensity profile in the mask plane without zero order attenuation filter (ZOAF), (b) intensity profile with ZOAF. (c) Angular spectrum in the mask plane, without illumination filter plate (IFP) (thus showing maximum angles). Discrete angular channels are caused by underfilling the aperture of the individual microlens on the mixing element.

Reprinted with permission from [KVO<sup>+</sup> 18a] ©The Optical Society.

point to compare is the number of optical elements in the beam path required to realize either homogenizer. Every optical interface leads to losses, thus the less the better. Even though the non-imaging homogenizer setup has one optical element less for beam mixing, it requires the ZOAF, thus introducing those two optical interfaces elsewhere in the beam path.

From theory, non-imaging homogenizers are suggested for coherent laser beam shaping, as a highly directional input like a plane wave will illuminate the same area in the superposition plane [105]. But for a finite angular spectrum, as for example introduced by a diffuser, different angles illuminate slightly different fields in the mask plane, thus causing the large, slow slope at the border of the irradiated area. This is visible when comparing the inscribed cross-sections of figs. 4.5a and 4.5b and fig. 4.6a.

This means that we found, in agreement with expectation from theory, the imaging homogenizer setup in conjunction with a rotating diffuser as the best beam shaping setup for our application.

#### 4.3.2 Coherent sources and interference effects

When using coherent light sources like lasers one has to take into account their coherence, and the related effects. For illumination systems, where a certain intensity distribution is desired in the output plane, interference effects tend to cause trouble by introducing deviations from the desired output intensity. The detrimental interference phenomena present in our case can be arbitrarily differentiated in interference fringes and, a special case thereof, optical speckle. This differentiation is made based on the origin or cause of the effects, and will be discussed in the following. It has to be noted, though, that both are a result of the same underlying

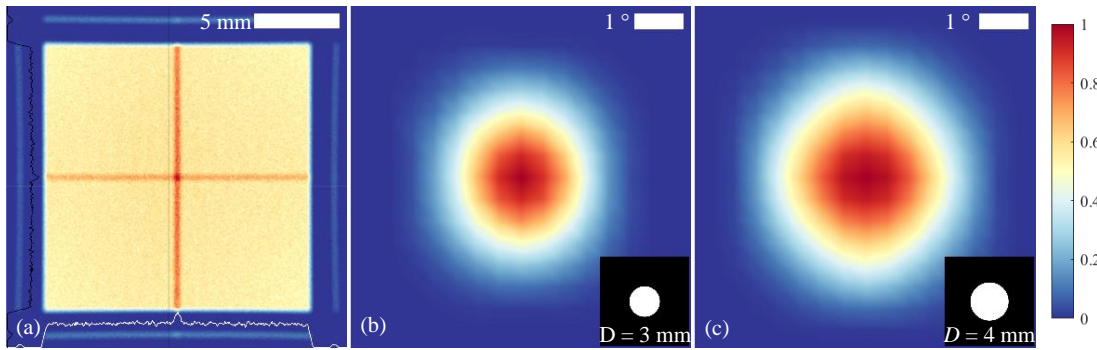


Figure 4.6 – Ray-tracing simulation of imaging homogenizer setup illumination in the mask plane, compare fig. 4.4b.

(a) Intensity top-hat profile in the mask plane. The simulation shows a cross-shaped artifact from the numerical representation of the area between individual microlenses of the MLA. (b,c) The angular spectrum for two illumination filter plates with different clear diameter. The insets schematically show the respective IFP, the white part being transmissive; respective diameters given in the insets.

principle.

Interference fringes are caused by the superposition of mutually coherent wavefronts propagating under two different angles, and are a result of the complex sum of those wavefronts. In the scope of illumination systems as discussed in this chapter interference fringes might originate mainly from two situations in the beam path, Fabry-Pérot type cavities or and Fizeau thin-film situations.

Fabry-Pérot cavities are formed between plane-parallel optical interfaces in the beam-path [125] [47, Chapter 7.6.2]. Well-known for their use as *etalon*, where their excellent wavelength-selectivity or finesse is used in the context of laser sources [126, 127] or spectroscopy [127], they pose a potential problem to our beam-shaping setups as they also present an angle-dependent transmission filter [128].

Fizeau fringes originate from similar situations, again from cavities formed between two interfaces in the beam-path, but in this case there is a (small) angle between the two interfaces [47, Chapter 7.6.7]. This interferometric setup is usually employed to gauge the flatness of optical surfaces [129]. A special case, with very little separation between the interfaces, yields co-called *Newton's fringes*. This also finds its main field of use in testing of optical surfaces [130].

In the beam-shaping setup for our exposure system we have to ensure that no interference fringes occur in the mask plane, or rather in the aerial image formed on the photoresist. They would modulate the exposure intensity over the field and thus decrease the uniformity of the exposure. If we consider the whole exposure system, including photomask and substrate, we can find the smallest separation of optical interfaces in the exposure gap  $g$ , compare figs. 4.1a

and 4.4. This is true for both homogenizer types previously discussed. The exposure gap is formed between the bottom-side of the photomask and the top-side of the photoresist on the substrate, and is usually in the range of  $20\mu\text{m}$  to  $50\mu\text{m}$  in mask aligners. We ignore here the cavity formed inside the photoresist itself, as standing waves formation in the photoresist layer is a large topic in and of itself in photolithography [4], as already mentioned in footnote 4 in section 4.2. To avoid aerial image intensity modulation from interference fringes, we have to ensure that no visible interference will occur caused by the cavity formed around the exposure gap.

The interference of two mutually coherent wavefronts with different propagation directions gives rise to periodic intensity variations, which can be observed as interference fringes when projected onto a screen or detector. If the number of interfering wavefronts becomes large, and if the wavefronts have mutually random phase differences, the resulting intensity variation due to interference is in turn random. This phenomenon is referred to as optical speckle, or simply speckle in this context [131, Chapter 1.2] [88, Chapter 7.7]. These random phase differences can be introduced for example by a diffuser. A diffuser can be implemented as a planar phase plate with random phase steps throughout its surface, as an element introducing randomized angles at different locations throughout its surface, or a mix between these two mechanisms.

Speckle offers some insight into the coherence properties of the underlying electromagnetic field. The average lateral and longitudinal speckle size of a speckle field equals the *ensemble average coherence*, as named by Goodman [88, Section 5.9]. This can be understood as the length-scale over which interference effects in addition to the speckle themselves will be visible. This means, as long as a superposition of the speckle field with a version of itself happens with a mutual displacement  $\leq$  the average speckle size, then interference effects like fringes will modulate the visible intensity of the speckle field. If the optical path distance between the two partial fields is bigger than the speckle size, no additional intensity modulation besides speckle can be observed. This is true in all three spatial dimension [132–135].

How can we find the speckle size<sup>8</sup> for a given speckle field? In comparison to measuring the longitudinal speckle size, for which one would need to take multiple pictures of a speckle field along its propagation direction and map the speckle throughout this volume, it is straightforward to measure the lateral speckle size by capturing a speckle field on a detector with sufficient resolution normal to propagation direction. The mean lateral speckle size  $\sigma_{x,y;m}$  in an image of a speckle field  $I_m(x, y)$  can be found as the width  $W_h$  at height  $h$  of the autocorrelation peak of said image, [88, Chapter 7.7] and [136]:

$$\sigma_{x,y;m} = W_h\left(C_I(I_m(x, y))\right), \quad (4.1)$$

with the autocorrelation function  $C_I$  as described in [136]. As is directly visible, the lateral

---

<sup>8</sup>If we talk about speckle size in this work, we usually refer to the mean or average speckle size of the speckle field under discussion, except for where specifically noted differently.

speckle size thus calculated depends on the criterium one applies to finding the width of the autocorrelation peak. An obvious choice might be the full width at half maximum (FWHM), but  $1/e$  or  $1/e^2$  might be sensible choices depending on the situation<sup>9</sup>.

The lateral speckle size is connected to the longitudinal speckle size, as speckle exhibit a grain-like granularity when investigated in three dimensions [136]. For the longitudinal speckle size  $\sigma_z$  one can find values from  $\approx 20\sigma_{x,y}$  to  $\approx 35\sigma_{x,y}$  times the lateral speckle size  $\sigma_{x,y}$  in literature [132, 134] for speckle in Fresnel regime (free-space propagation after a diffuser). Thus capturing a speckle field in a plane normal to its propagation direction allows for a good understanding of three-dimensional properties.

This range of values for the longitudinal speckle size depends on the one hand on the type of source chosen in a given publication (plane wave, Gaussian beam,...), hence on the lateral power distribution in the source plane. On the other hand, for speckle behind a Fourier lens as considered in this thesis, the speckle size also depends on the f-number<sup>10</sup> of the Fourier lens [135, 137, 138].

For practical purposes, in this work we worked with a first estimation of  $\sigma_z = 20\sigma_{x,y}$  for quick consideration. We used coherent simulation to evaluate the expected speckle contrast in the mask aligner setup under consideration, and verified these simulations with test prints in the mask aligner.

When we combine what we learned above, we can state:

- The formation of interference fringes from optical cavities in the beam path has to be suppressed, otherwise the aerial image intensity and thus the exposure dose will be modulated and the exposure non-uniform.
- Speckle have to be suppressed as well, as they form a chaotic interferogram equally disturbing the exposure uniformity.
- Speckle reduce the ensemble average coherence, thus the length-scale over which interference effects are visible.

This can be rephrased to: if we can control the speckle size<sup>11</sup>, we can engineer a situation where the presence of sufficiently small speckle will indicate a sufficiently small ensemble average coherence in the field to suppress visible interference fringes of the exposure gap in our exposure system.

One widely adopted approach to suppressing speckle is surprisingly simple. Due to their nature of being an interference effect yielding a random intensity distribution with unity

---

<sup>9</sup>For example: is the source a plane wave or has a Gaussian distribution? In case of a Gaussian distribution, the  $1/e$ -size might be more representative. We will see this in section 4.3.4.

<sup>10</sup>The *f-number* describes the ratio of the focal length to the diameter of the clear aperture of an optical system.

<sup>11</sup>By controlling the speckle size we refer to controlling the optical system causing the speckled field, with the speckle size as visible indicator of our doings.

### 4.3. Illumination system for mask aligner lithography with a coherent source

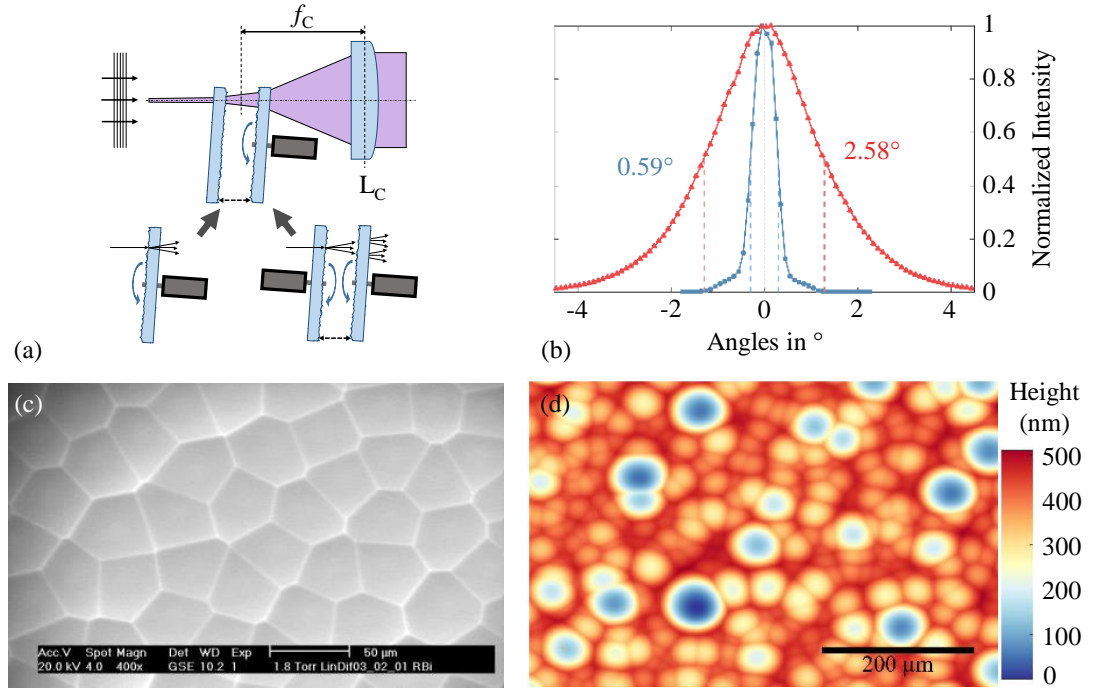


Figure 4.7 – Optical diffuser setups for beam-shaping applications. (a) A diffuser in the beam path is rotated to cause a time-varying speckle pattern. If necessary, it can be combined with a second, static diffuser, to further decrease the obtained speckle size. A condenser lens  $L_C$  is used to quasi-collimate the propagating speckle field. (b) Goniometric measurements of static (blue dots) and rotating (red triangles) diffusers. The full width at half maximum (FWHM) is denoted. (c) SEM micrograph of a shaped random diffuser. (d) White light interferometric image of a shaped random diffuser. Adapted with permission from [KVO<sup>+</sup>18a] ©The Optical Society.

contrast on a detector in the speckle field, the superposition of the intensity distribution of  $N$  statistically unrelated speckle fields of equal average intensity reduces the overall contrast by  $N^{-1/2}$  [88, Section 7.7.4]. Thus by integrating over a sufficiently large number of statistically unrelated speckle fields the overall speckle contrast asymptotically approaches zero. In mask aligner lithography this can be realized as temporal integration over different speckle fields in the photoresist. Here the resist behaves as analog sensor integrating over all irradiation of exposure wavelength. One only has to ensure that enough statistically unrelated speckle fields arrive on the photoresist during the exposure time interval.

A practical implementation of this approach is the introduction of an actuated diffuser into the illumination beam path. Optical diffusers are elements with a known roughness, either on a surface (surface height and shape variation) or in their volume (variation in the refractive index, i.e. the optical path length). They introduce random phase variation over the full interval of  $[-\pi; \pi]$ . It can be shown that a lateral displacement of the diffuser by more than the lateral speckle size it causes will cause a statistically unrelated speckle field [88, Section 7.7.4].

The diffuser actuation can for example be implemented as a rotation of the diffuser.

Figure 4.7a shows the diffuser setup as implemented for this work. A rotating diffuser, paired with a second, static diffuser, is introduced into the illumination laser beam path [139]. A condenser lens  $L_C$  with focal length  $f_C = 200$  mm quasi-collimates the propagating speckle field, also transforming the speckle into fully developed speckle by transferring them into the Fraunhofer domain. Figure 4.7b shows goniometric measurements of the angular characteristics of both the rotating (FWHM =  $2.58^\circ$ ) and the static (FWHM =  $0.59^\circ$ ) diffusers. In this work we use shaped random diffusers [139, 140], manufactured by *SUSS MicroOptics SA*. Figures 4.7c and 4.7d show a scanning electron microscope (SEM) micrograph and a white light interferometric height measurement of the surface of such a diffuser. The multi-faceted surface composed of a random arrangement of concave lenslets with uniform curvature is visible. The pairing of two diffusers was used in this work mainly to increase the angular spread behind the diffuser setup, to enlarge the central section of the Gaussian profile of the illumination. This was used to decrease the speckle size after the collimator lens. An interesting side-effect is that with this setup the speckle field behind the second diffuser changes even quicker than with a single rotating diffuser. The mechanics of this effect are interesting but outside the scope of this work. Please turn to Goodman's book on the matter, in case of interest [131]. The laser source used in this work facilitates this intensity homogenization. For a CW source, the rotation speed of the diffuser is not an important parameter, as long as the integration time comprises at least one full diffuser revolution.

### 4.3.3 Ray-tracing of coherent sources: Gaussian-beam decomposition

In section 4.3.1 we introduced ray-tracing as a means to simulate beam-shaping systems containing multi-aperture elements. What standard ray-tracing can not simulate, though, is the effects we expect from coherent sources, as discussed in the previous section 4.3.2.

In classical ray-tracing an optical source is composed out of single rays (encoding direction, wavelength, power, propagation distance, possibly polarization), and each ray is traced individually, and a simple addition of ray intensities in a detector. This can be made arbitrarily complex by adding means of simulating partial reflections at interfaces, or stray light, to only name two possibilities. What is not possible in classical ray-tracing, though, is the simulation of coherent light, where the wavefront information of the source is maintained while propagating.

To enable coherent simulation of an optical system the information of the initial wavefront needs to be conserved throughout propagation. In the detector plane this information is required to find the coherent response of the simulated optical system. One way to implement this is Gaussian beam decomposition (GBD). In this model, a source is now represented by a set of Gaussian beamlets instead of simple rays. Each beamlet consists of a principal ray representing the local part of the wavefront in direction, power and, most important, phase. The principal ray is supported by a bundle of secondary rays representing beam waist and



divergence, which enable the simulation of the propagation of the wavefront<sup>12</sup>. GBD can be understood as a simulation implementation of Huygens's principle, only with Gaussian beams instead of spherical wavelets. To retrieve the coherent response of an optical system which is simulated with this approach it suffices to calculate the coherent sum over all Gaussian beamlets on the surface of interest [141, 142]. In this work we use the ray-tracing software FRED<sup>13</sup>, and discuss GBD as implemented there.

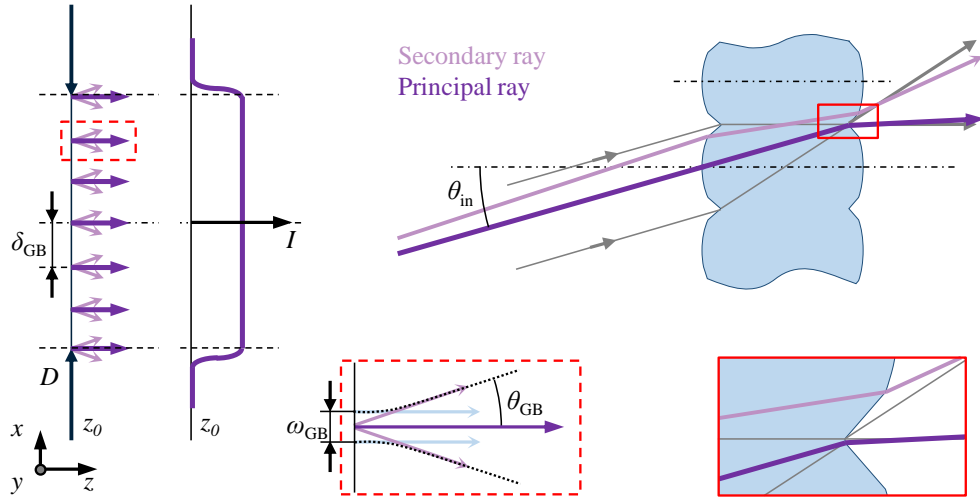


Figure 4.8 – GBD, schematically shown for a plane wave source of diameter  $D$ , see area on the left. The source is sampled by Gaussian beamlets. Each beamlet consists of a primary ray, which stores the direction, wavelength and phase information, and up to 8 secondary rays, modeling the individual waist ( $\omega_{GB}$ ) and divergence ( $\theta_{GB}$ ), as shown in the inset with dashed circumference. A coherent sum over all Gaussian beamlets on a detector plane yields the coherent system response on this plane, in good approximation, here shown for the source plane  $z_0$ .

The upper right area shows a difficulty in simulating microlens arrays: if one secondary ray hits a surface other than the principal ray (here: two different microlenses), then this Gaussian beamlet is discarded from simulation.

We review some aspects of the implementation of GBD in the following as it is central to understanding the limitations of this technique. Figure 4.8 shows a 2D representation of GBD. Obviously the simulation result largely depends on source representation. The implementation requires that lateral Gaussian beamlet spacing in the source plane has to be  $\delta_{GB} \geq 10\lambda$  or larger to enable correct wavefront representation<sup>14</sup>, compare fig. 4.8, left hand drawing. Beam waist and divergence of each beamlet are anti-proportional parameters - this is both required by the decomposition algorithm as well as it is central to a Gaussian distribution / representation of a beamlet [142]. The beam waist is set by the beamlet spacing (a certain

<sup>12</sup>Minimum two secondary rays, one for beam waist, one for divergence. Typically, if not for specific reasons, 8 secondary rays are used, 4 each for beam waist and divergence. This helps in ensuring integrity of the mathematical model in more directions during propagation, four in this specific case.

<sup>13</sup>FRED Optical Engineering Software, by PhotonEngineering LLC, v.18.14

<sup>14</sup>Value taken from the documentation of FRED. For mathematical background please refer to [141, 142]

overlap of beamlets is necessary), and the divergence is in turn given by the beam waist - the bigger the waist the smaller the divergence. This means that for wavefronts with high phase gradients small beamlets have to be used for wavefront representation. And, logically, this representation then has a large divergence.

The divergence of the individual beamlet plays an important role in a second requirement of the GBD algorithm: the *mathematical integrity* of the individual beamlet. This means that in GBD all rays of a single beamlet are required to intersect the same surfaces in the same order during propagation. If, for example, a single secondary ray intersects an aperture at the border of a lens instead of the lens surface itself, where the rest of the beamlet's rays intersect, the whole beamlet is discarded by the GBD algorithm. This causes the loss of this individual part of the source wavefront together with the attributed power for the computation. The more beamlets are discarded the more the result of the simulation deviates from the expectancy. This statement is quite vague, but it is difficult to give actual numbers for the amount of discarded beamlets to render a simulation invalid. It is important to analyze a given simulation model and the surfaces where beamlets are discarded, to understand what is happening if beamlets are discarded. In general the best case, and what should be aspired to achieve, is integrity of all beamlets.

GBD as simulation approach is limited by several boundary conditions. First, the lateral spacing of beamlets in the source has to be  $\geq 10\lambda$ , with the source wavelength  $\lambda$  [142], limiting the source resolution. Second, as already mentioned, as soon as beamlets lose their mathematical integrity, they are discarded. This is especially challenging when simulating multi-aperture elements, as in this case apertures are distributed throughout the simulated domain. This significantly increases the chances of beamlets partially hitting different surfaces. This case is drawn in the upper right part of fig. 4.8. And third, as the last limit mentioned here, GBD is usually applied in cases with low wavefront gradients, like for astronomical telescopes. There, techniques like wavefront resampling<sup>15</sup> are applied to trace coherent wavefronts over long distances (low beam-count necessary, thus low divergence), then pass limiting apertures (wavefront resampling with higher spatial resolution, to capture diffraction effects at the aperture), and continue propagation afterwards (again potentially with resampling to reduce ray count). For our application we have to first ensure that GBD is a viable approach also for the simulation of randomized coherent wavefronts as caused by optical diffusers.

### 4.3.4 Simulation of randomized sources and validation of approach

To investigate the viability of using GBD for simulating optical propagation of a randomized wavefront behind a diffuser we first start with a simple example with known properties.

For an ideal diffuser behind an ideal coherent light source (plane wave), which is then imaged onto a screen in focal distance behind the projection lens, the average lateral speckle size

---

<sup>15</sup> *Wavefront resampling* describes a technique in GBD where a coherent wavefront is captured on a detector, and then re-synthesized with a different beamlet spacing.

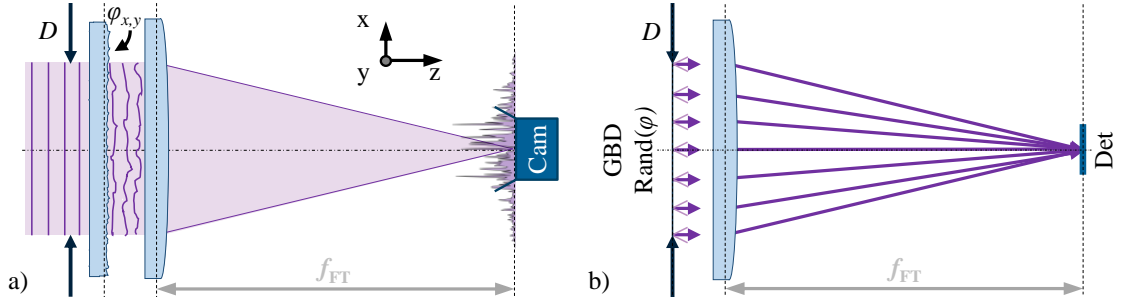


Figure 4.9 – Simulation of a single lens imaging system with randomized source. (a) Realistic setup with a diffuser randomizing the plane wave illumination, with a local phase distribution  $\phi_{x,y}$ . (b) Simulated equivalent with a Gaussian beam decomposed source, where a random phase value  $\phi$  between 0 and  $2\pi$  is added to every Gaussian beamlet. For evaluation in both cases a detector is placed in focal distance to the imaging lens. A circular area of diameter  $D$  is illuminated in both cases.

$\sigma_{x,y;a}$  can be found as the diffraction limited spot size [143]:

$$\sigma_{x,y;a} \approx 1.22 \frac{\lambda f}{D}, \quad (4.2)$$

with the wavelength  $\lambda$ , the focal length of the projection lens  $f_{FT}$  and the diameter of the projection lens exit pupil  $D$ . This is true for so-called fully developed speckle [88, 144], which are speckle in the Fraunhofer regime<sup>16</sup>. We compare this to the simulated lateral speckle size, calculated following eq. (4.1), as the autocorrelation of the simulated intensity distribution in the focal plane of the Fourier lens. This setup is shown for an experimental setup in fig. 4.9a as realized for example by Li *et al.* [136], and fig. 4.9b depicts the equivalent for simulation.

To test the validity of GBD for simulating optical speckle we realized the described setup in FRED. We simulated the randomized circular source of diameter  $D$  by initializing a coherent source to which we applied a random phase between 0 and  $2\pi$  per beamlet. The source was then traced through a lens with focal length  $f_{FT} = 100$  mm onto a detector in focal distance behind the lens. The mean speckle size on the detector was calculated in MATLAB<sup>17</sup> as the autocorrelation of the detector image. To find the peak-width of the autocorrelation function three different criteria have been tested: the FWHM, the width at  $1/e$  and the width at  $1/e^2$ . This is shown in fig. 4.10a, for the clear aperture  $D = 2$  mm to 20 mm. We found that the  $1/e^2$ -width corresponded best to analytical expectation  $\sigma_{x,y;a}$ , calculated as the diffraction limited spot size. But FWHM as criterion for the lateral speckle size delivered a more stable result, as it had a bigger distance to the noise floor of the autocorrelation. As this value was only offset from analytical expectation by a constant factor of  $\approx 0.54$ , compare fig. 4.10b, we chose this criterion, FWHM, as the one to use in the following considerations.

<sup>16</sup>In the case of illumination systems as discussed here, where there are always Fourier lenses employed to transform illuminated area into angular spectrum and vice versa, we only deal with fully developed speckle.

<sup>17</sup>MATLAB by MathWorks®, version R2019a.

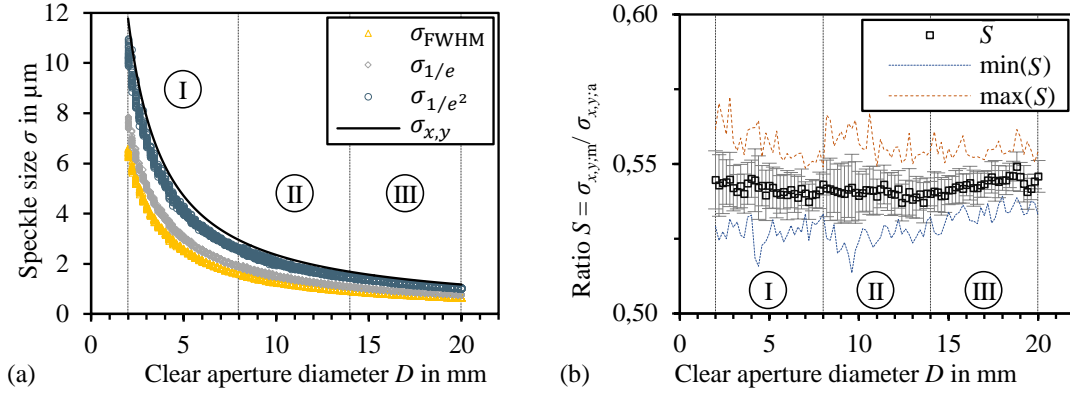


Figure 4.10 – Comparison of the ratio  $S$  of measured simulated lateral FWHM speckle size  $\sigma_{x,y,m}$  to theoretical lateral speckle size  $\sigma_{x,y,a}$  as function of the clear aperture  $D$ . Error bars show the standard deviation of variable source sampling (10...250  $\lambda$  beamlet spacing). Dashed lines show local minimum and maximum values of  $S$ .

When comparing a real diffuser to an ideal diffuser, one major difference is the direction-dependency of the speckle field. Real diffusers never reach true randomness, and will always allow some directional information to pass, which can be found in the speckle field forming/propagating behind them. This information content is used for example in speckle tomography for medical applications to measure the blood-flow in living tissue [145], or in related approaches to reconstruct information of hidden objects solely by investigating light scattered by this object [146]. In total we found that GBD with randomized sources represents a viable approach to coherently simulate an ideal diffuser. In the frame of this work this is sufficient, as in the Fraunhofer regime we typically deal with fully developed speckle. And the collimator lens  $L_C$  takes care of the transformation of all speckle in our system into this regime.

#### 4.3.5 Coherent simulation of beam-shaping systems with temporal averaging

Based on the coherent simulation of a randomized source using GBD, the next step is to simulate a beam-shaping setup in its entirety. Following fig. 4.11, we implemented the imaging homogenizer setup in FRED starting directly behind the diffuser setup with a randomized source. The two crossed double-sided cylinder microlens-arrays (Fly's eye) were implemented next to the source, followed by the Fourier and Field lenses  $F_{\text{FT}}$  and  $F_{\text{FL}}$ . A detector was situated in the mask plane. The first result we expected was a speckle field inside the area defined by the imaging homogenizer setup. Figure 4.12a shows this field, perfectly meeting our expectations. It is slightly oblong (stretched in vertical direction), which is caused by the spacing between the two cylinder MLA (horizontal MLA before vertical MLA in propagation direction, thus the vertical angular spread is slightly higher due to longer propagation). The high contrast of the speckle is illustrated by the large variation of the intensity throughout the

### 4.3. Illumination system for mask aligner lithography with a coherent source

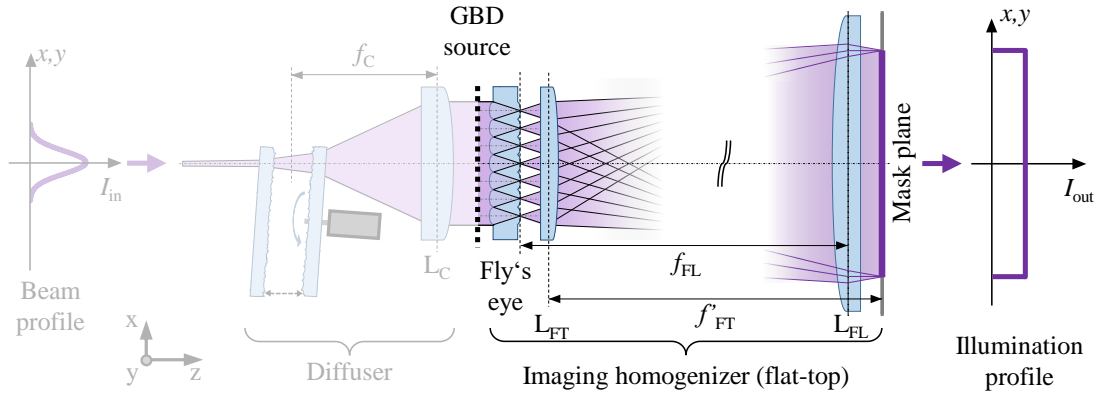


Figure 4.11 – Schema of the imaging homogenizer setup as coherently simulated in FRED. On the input side, the diffuser setup with its collimation lens  $L_C$  is replaced with a randomized GBD source, as described in section 4.3.4. The imaging homogenizer consists of two crossed cylinder-lens Fly's eye MLA elements, with a subsequent Fourier lens  $L_{FT}$ . A field lens  $L_{FL}$  ensures telecentricity in the mask plane, where the detector surface in the simulation is located.

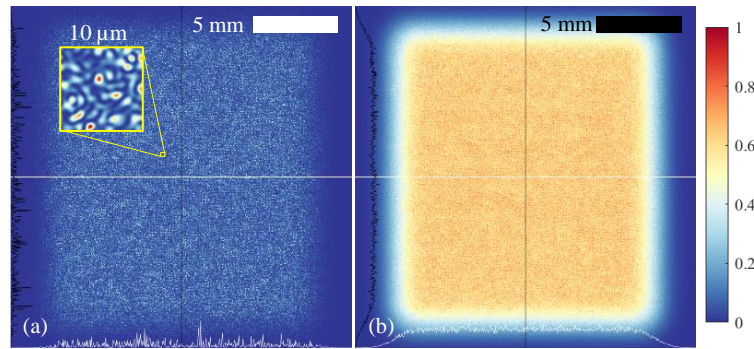


Figure 4.12 – Coherent simulation of the imaging beam homogenizer setup (normalized intensity plotted) as shown in fig. 4.11. (a) Simulation of a single static speckle field in the mask plane; the inset shows a zoom into the field. (b) Incoherent superposition of 100 independent speckle fields, to simulate time averaging during exposure. Field cross-sections shown as black and white plots near the bottom and left border, with straight lines marking the respective field position.

field, as can also be seen in the cross-sections, plotted close to the border of the graph. The inset in this figure shows a magnification of the speckle field. The source diameter was set to  $D = 20$  mm, resulting in lateral average speckle size of  $1.4 \mu\text{m}$ , compare fig. 4.10a.

To simulate the temporal averaging we would obtain using a rotating diffuser in conjunction with a photolithographic exposure in photoresist (temporal integration) we calculated the incoherent sum over 100 statistically uncorrelated speckle fields simulated after the same method<sup>18</sup>, shown in fig. 4.12b. The flat-top profile of the irradiation becomes clearly visible as

<sup>18</sup>This was achieved in simulation by using different seeds for the randomization of Gaussian beamlets in the source for each simulation run.

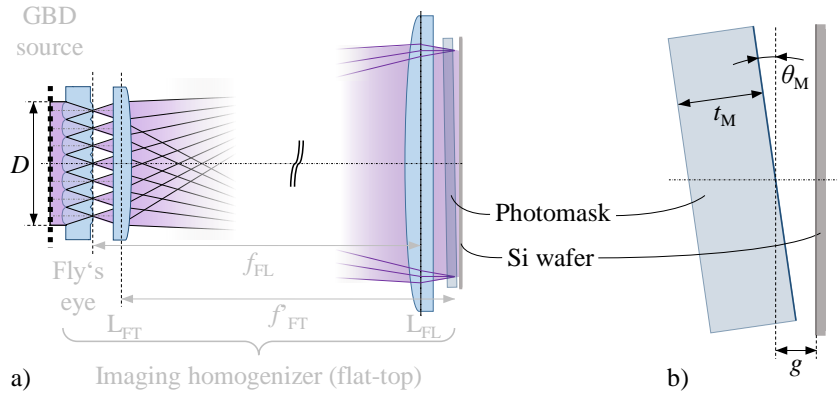


Figure 4.13 – Schema of the imaging homogenizer setup with photomask and substrate, as coherently simulated in FRED. (a) The simulation setup, modified from fig. 4.11, with source diameter  $D$ . (b) Exaggerated schematic depiction of the photomask of thickness  $t_M$  and Silicon substrate, separated by the exposure gap  $g$ . The photomask is inclined to the optical axis by  $\theta_M$ . The two interfaces of interest for interference fringe simulation are highlighted by bolder lines.

the slightly rectangular irradiated area. Also the smoothing effect of the time average can be clearly seen when comparing the field cross-sections of figs. 4.12a and 4.12b. For both graphs in this figure the cross-sections through the center of the field in both directions are plotted in black and white at the border of both graphs, with the straight lines corresponding to the position of the respective cross-section.

This result, the time-averaged intensity distribution shown in fig. 4.12b, also compares very well to the result obtained from incoherent ray-tracing simulation, as shown in fig. 4.6a.

To fully simulate the exposure in a mask aligner with the illumination beam-homogenizer setup, as described in figs. 4.11 and 4.12, the representation of a photomask and a Silicon substrate were included in the simulation, as shown in fig. 4.13. In the mask plane a fused silica slab of  $t_M = 2$  mm thickness is positioned, with an inclination of  $\theta_M = 0.002^\circ$ <sup>19</sup> against a Silicon substrate (rotation around y-axis), to simulate misalignment, or even surface warp in either photomask or substrate. Their respective distance, the exposure gap  $g$ , and the free diameter of the randomized source,  $D$ , were varied by  $20\ \mu\text{m}$  and  $30\ \mu\text{m}$  and  $10\ \text{mm}$  and  $20\ \text{mm}$ , respectively. The two closest interfaces in the optical path of the exposure systems are the surfaces of photomask and substrate facing each other, as highlighted in fig. 4.13b. They form the smallest optical cavity from which interference fringes might originate.

Figure 4.14 shows the result of these simulations, where, once again, an incoherent average over 100 simulation runs was taken to simulate the temporal averaging in photoresist. As expected, with increasing exposure gap  $g$  and increasing source diameter  $D$  the visibility

<sup>19</sup>This inclination ensured that the photomask was not touching the substrate over a field extent of  $10\ \text{mm}$  in  $x$ , with a minimum gap of  $20\ \mu\text{m}$  in the center.



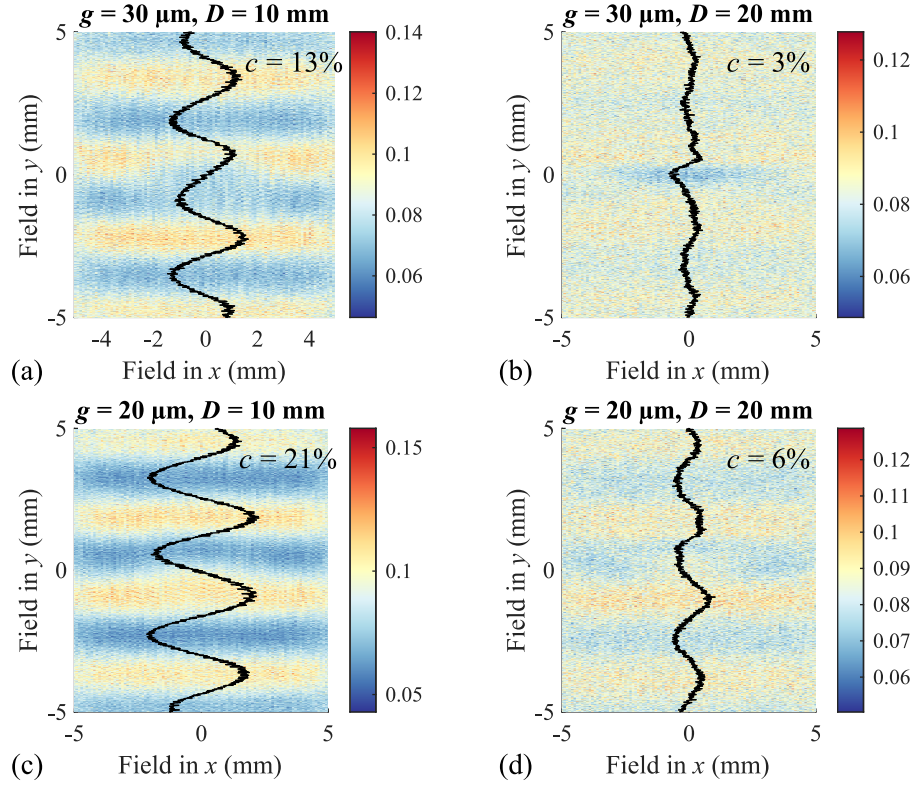


Figure 4.14 – Coherent simulation of the Fabry-Perot response of the optical cavity formed between photomask and a substrate during exposure. The flat-top irradiance profile from the beam-homogenizer setup described in fig. 4.12 served as illumination. The photomask is inclined  $0.002^\circ$  against the substrate. The figures show the incoherent superposition of 100 individual speckle fields. The mean exposure gap  $g$  and the free source diameter  $D$  were varied: (a)  $g = 30 \mu\text{m}$ ,  $D = 10 \text{ mm}$ . (b)  $g = 30 \mu\text{m}$ ,  $D = 20 \text{ mm}$ . (c)  $g = 20 \mu\text{m}$ ,  $D = 10 \text{ mm}$ . (d)  $g = 20 \mu\text{m}$ ,  $D = 20 \text{ mm}$ . The interference fringe contrast is calculated for the sum over all pixel columns in x-direction as inset  $c$ , this sum is drawn as black line.

of interference fringes decreases. The contrast  $c$  of the interference fringes was calculated and can be found in the individual subfigure. With the inclination of  $0.002^\circ$  the interference fringes formed by the air gap at an exposure wavelength of  $193 \text{ nm}$  should be spaced  $2.77 \text{ mm}$  (thin-film interference, or Newton fringes). The simulated results perfectly agree with this expectation.

The slightly higher fringe contrast visible in the center region in all four subfigures of fig. 4.14 are seen as an artifact of the simulation. There are two possible explanations. They might be caused by different coherence lengths in the speckle field, as can be found for imaging systems [136]. Or we can attribute them to an artifact of the simulation, the fact that in the center region all beamlets of the source contribute significantly, whereas in the outer regions

of the mask plane their number decreases. This small difference in contrast does not change the overall findings, which correspond very well to the expectation discussed in section 4.3.2.

The contrast requirement for visible interferences from the exposure gap should meet the uniformity requirement of usual mask aligners. MO EXPOSURE OPTICS [51], a state-of-the-art mask aligner illumination system featuring an imaging beam-homogenizer setup similar to the one discussed here, is specified to deliver a illumination uniformity of typically  $\leq \pm 2\%$  [24]. Following our results we could achieve this for  $D = 20$  mm and  $g = 30$   $\mu\text{m}$ .

With the simulation shown here we could show that we not only can coherently simulate the imaging beam-homogenizer system together with a randomized source, but also that this method has significant value for the design of such illumination systems when it comes to the suppression of visible interference effects in the photolithographic print.

In general it has to be noted, though, that while coherent ray-tracing simulation using GBD enables the coherent simulation of beam-shaping systems featuring multi-aperture elements, it compares poorly to incoherent ray-tracing of the same system in terms of computation time (a single coherent run took approx. 190 s, whereas an incoherent run with  $5 \cdot 10^7$  rays took approx. 16 min. This high number of rays was only needed for the graphs shown in this work; useful results can already be obtained with  $5 \cdot 10^5$  to  $1 \cdot 10^6$  rays). And, if only the overall intensity distribution in the superposition plane is of interest, and coherence effects in the beam-path are either neglected or excluded, incoherent ray tracing presents the tool of choice for the simulation of beam-shaping systems like the presented ones.

### 4.4 Mask aligner lithography with DUV CW light source

As discussed in section 3.4.1, the goal of this implementation of a CW 193 nm laser light source is to improve the resolution of a mask aligner by reducing the exposure wavelength. As shown in the previous section from a simulation point of view we are positive that this is possible, especially with the highly coherent source we want to use.

In the following we present results of photolithographic prints realized with the different beam-shaping setups previously examined, and discuss results.

#### 4.4.1 Methods

For the characterization of the illumination at different positions throughout the illumination path a beam-profiler was constructed. It consisted of a Silicon photodiode (Hamamatsu S1226-18BQ) sensitive to the DUV wavelength of 193 nm. It was outfitted with a laser-cut square aperture of  $300 \mu\text{m} \times 300 \mu\text{m}$  to define the active area, and mounted on an automated precision XY-stage. The system was piloted with a software routine implemented in MATLAB.

As the description already shows the beam profiler had a central limitation: the size of the



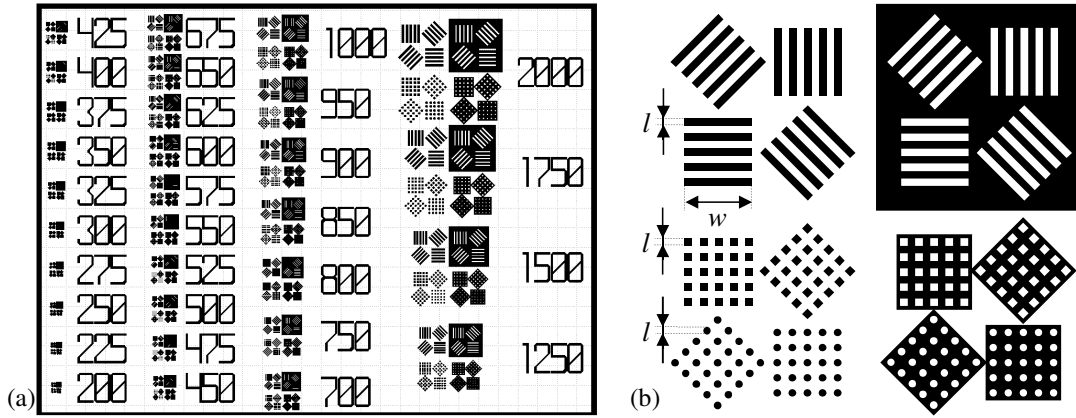


Figure 4.15 – Test-pattern as used to evaluate the print resolution of mask aligner photolithography at 193 nm, black represents the light blocking chrome layer on the photomask. (a) View of one cell of test patterns on the test mask. The numbers represent the critical dimension of the respective feature group to the left in nm. (b) Schematic drawing of one feature group, featuring lines and spaces, squares and circles. All features are present both as bright- and dark-field variants side by side. Groups of 5 lines and 4 spaces with 50 % duty-cycle are arranged in the shown fashion. Critical dimension was the line-width  $l$ , and the line-length  $w = 9l$ . Squares and circles have the critical dimension as side-length or diameter, respectively. They are arranged with the same spacing as the lines and space.

aperture was very large in comparison to the features we wanted to resolve, the speckle size. We could not circumvent this problem as higher source power and / or photodiodes with higher efficiency were not available, thus smaller apertures on the photodiode would have increased the measurement time to impracticable duration. The measured beam profiles presented in the following are all smoothed by a convolution with this square aperture.

Photolithographic test prints were made on 100 mm Silicon wafers, which were spin-coated with the chemically amplified DUV photoresist TOK TARF-P6239 ME; this resist is optimized for lines and spaces patterns. After spin-coating the wafers were subject to a soft-bake at 110 °C for 60 s, resulting in a layer thickness of 120 nm. Dose test exposure series have been made to establish exposure doses for each given print, with usual doses around 45 mJ cm<sup>-2</sup>. The exposure intensity in the mask plane was measured with a THORLABS Photodiode S120VC and was typically set to 5 mW cm<sup>-1</sup> over the total exposure field of 10 mm x 10 mm. A post-exposure bake of 60 s at 110 °C was conducted on a hotplate. The exposed wafers were developed in a puddle-process in AZ MIF 327 for 60 s. The developed prints were characterized using optical microscopes as well as scanning electron microscopes.

The exposure field, while being small, was sufficient for our proof of principle. For a larger field a light source with higher total optical power would be necessary, as otherwise the exposure irradiance would drop to values where printing no longer is practically possible.

Our mask-aligner features an ETEL<sup>20</sup> high-precision movement stage with 6 degrees of freedom to position the photoresist-covered wafer relative to the photomask. The exposure gap is measured with an AVANTES<sup>21</sup> spectroscopic reflectometry setup at three positions, enabling leveling of mask and wafer with sub-micron precision.

A Fused Silica amplitude mask with test structures was acquired to evaluate the print resolution in test exposures. Lines and spaces patterns as shown in fig. 4.15 were investigated, and compared between different tool configurations. These patterns consist of groups of 5 lines with 4 spaces in between with 50 % duty cycle. Line-widths as critical dimension were available from 200 nm up to 2  $\mu\text{m}$ . Line-length was 9 x line-width. Both dark and bright field structures were available for all features.

### 4.4.2 Results

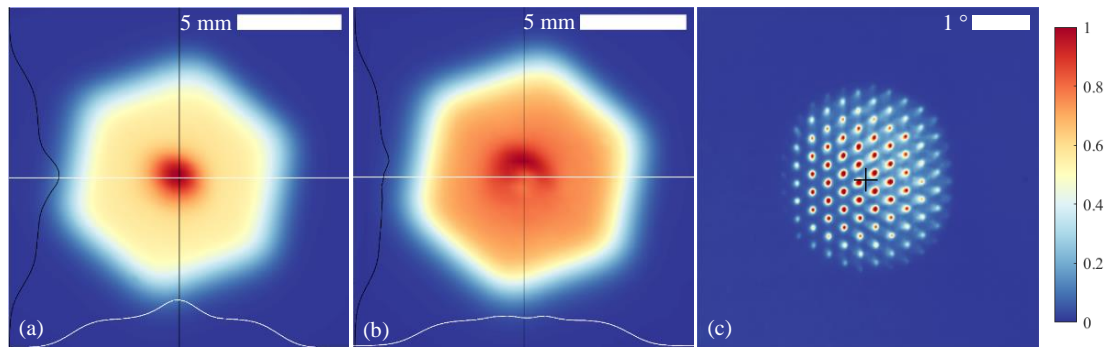


Figure 4.16 – Measurement of non-imaging homogenizer setup illumination in the mask plane, compare fig. 4.4a. Optical axis is marked by a black cross.

(a) Intensity profile in the mask plane without zero order attenuation filter, (b) intensity profile with zero order attenuation filter. (c) Angular spectrum in the mask plane, without illumination filter plate (thus showing maximum angles). Discrete channels are caused by underfilling the aperture of the individual microlens on the mixing element.

Adapted with permission from [KVO<sup>+</sup>18a] ©The Optical Society.

First, let us review the quality of the simulations conducted for this chapter. As discussed in section 4.3.4, standard incoherent ray-tracing simulation is the tool of choice for simulating beam-shaping applications. And even more so, if multi-aperture optical elements like MLA are involved in the beam path.

Measurements of the beam profile for the non-imaging homogenizer setup with the single-sided diffractive optical element as beam mixing element are presented in fig. 4.16. Figure 4.16a shows the beam profile without zero order attenuation filter, clearly exhibiting the

<sup>20</sup>ETEL S.A., CH-2112 Môtier, Switzerland, Sarigan motion system

<sup>21</sup>AVANTES BV, NL-7333 NS Apeldoorn, The Netherlands, AvaSpec-ULS2048CL-EVO spectrometer with AvaSoft-Thinfil software.

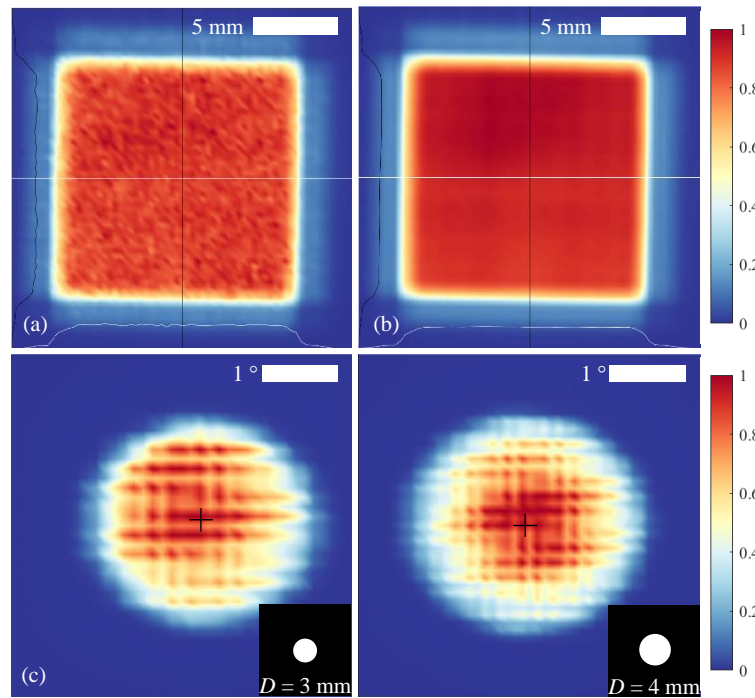


Figure 4.17 – Measurement of imaging homogenizer setup illumination in the mask plane, compare fig. 4.4b. Optical axis is marked by a black cross.  
(a,b) Intensity top-hat profiles in the mask plane for static and rotating diffuser, respectively.  
(c,d) Angular spectra in the mask plane for different IFP, see insets.

strong zero order peak in the center of the irradiated area. The hexagonal shape, expected from the individual hexagonal subaperture of the mixing element is visible as well. The slight rotation of the hexagonal is caused by a small misalignment between the orientation of the diffractive optical element and the overall  $y$ -axis. This was not an issue, as a square print field of 10 mm x 10 mm was used. Figure 4.16b shows a beam profile with the zero order attenuation filter. The still visible annular spike in intensity around the center of the irradiated area is a part of the zero order which was not blocked by the zero order attenuation filter. It has to be noted that while generally working as expected, the zero order attenuation filter turned out to be quite difficult to position, also because the zero order peak was not perfectly round. This measurement represents one of the best zero order attenuation filter placement configurations we could achieve. Figure 4.16c shows the angular spectrum without illumination filter plate before the diffractive optical element, hence the maximum available angular spectrum. All three pictures show a very good agreement to expectation from simulation, compare fig. 4.5.

Figure 4.17 shows measurements of the beam profile for the imaging homogenizer setup with double-sided cylinder lens MLA as mixing element, compare fig. 4.4b. Figures 4.17a and 4.17b show beam profiles of the intensity top-hat profile in the mask plane for static and rotating diffuser, respectively. The smoothing by temporal averaging over multiple, statistically

uncorrelated speckle fields becomes visible in fig. 4.17b when compared to fig. 4.17a. It has to be noted that this effect even becomes visible with the comparatively large photodiode aperture of  $300\text{ }\mu\text{m} \times 300\text{ }\mu\text{m}$  compared to the average lateral speckle size in the single micron range. This underlines once more the necessity as well as demonstrates the effectiveness of temporal averaging over multiple speckle fields. Figures 4.17c and 4.17d show measurements of the angular spectrum for illumination filter plate of different clear aperture  $D$  as illustrated by the insets in the respective pictures. The regular horizontal and vertical linear artifacts are caused by underfilled apertures of the individual channels of the mixing elements. In comparison to fig. 4.16c they are not clearly separated, as the individual aperture of the channels is smaller for the imaging homogenizer. All pictures very well conform to expectation from simulation, when compared to fig. 4.6.

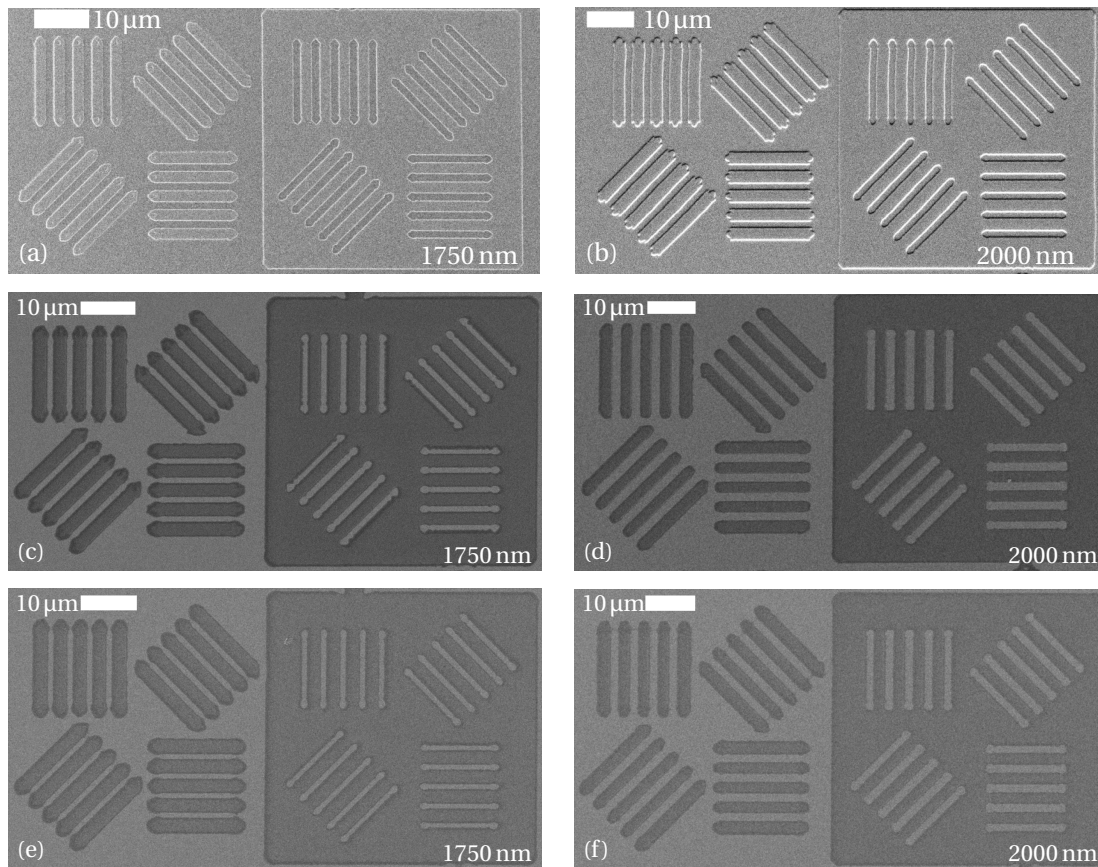


Figure 4.18 – Micrographs of test prints showing lines and spaces resolution structures printed into 120 nm TOK TARF-P6239 photoresist with  $20\text{ }\mu\text{m}$  proximity gap using an amplitude mask. Structures with critical dimension  $\leq 2\text{ }\mu\text{m}$  have been printed with all illumination setups. (a,b) non-imaging homogenizer illumination setup, 4 mm illumination filter plate. (c-f) imaging homogenizer illumination setup, (c,d) 3 mm illumination filter plate, (e,f) 4 mm illumination filter plate. The text in the lower right corner indicates the critical dimension (linewidth) of each group of lines and spaces. Every row of pictures has been taken from the same wafer. (a,b) Reprinted with permission from [KVO<sup>+</sup>18a] ©The Optical Society.

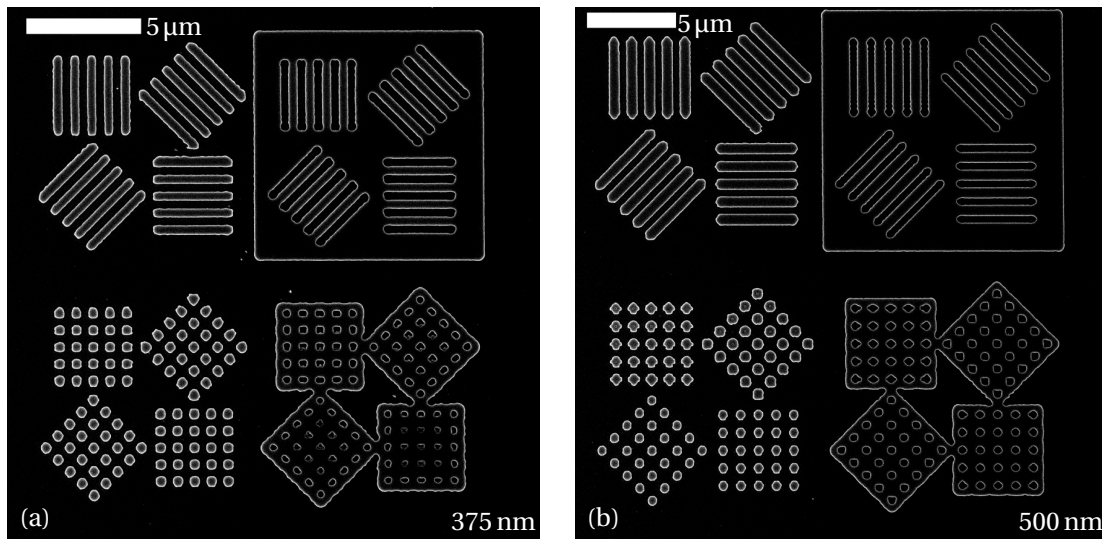


Figure 4.19 – SEM micrograph of resolution structures in photoresist, patterned in soft contact between mask and wafer. The lines and spaces have critical dimensions of (a) 375 nm and (b) 500 nm.

Photolithographic test-prints have been realized with both illumination setups. An amplitude mask with test structures has been used. Figure 4.18 shows SEM micrographs of lines and spaces structures for different illumination setups. Figures 4.18a and 4.18b were exposed using the non-imaging homogenizer setup with a 4 mm illumination filter plate. Figures 4.18c to 4.18f were exposed using the imaging homogenizer setup, also demonstrating the influence of different angular illumination spectra on the print; Figure 4.18d used a circular 3 mm illumination filter plate, while Figures 4.18a, 4.18b, 4.18e and 4.18f used a circular 4 mm illumination filter plate.

It is clearly visible from all pictures in fig. 4.18 that proximity printing with the 193 nm CW laser light source is feasible, and also yields resolution below  $2\text{ }\mu\text{m}$ , as expected from eq. (3.2). None of the structures are optimized in terms of exposure dose, therefore the duty cycle of the printed structures is not 50 %. Test prints were made such that the dose would enable printing of all structures we expected to be seen for a certain situation, i.e.  $2\text{ }\mu\text{m}$ ,  $1.75\text{ }\mu\text{m}$  and  $1.5\text{ }\mu\text{m}$  for proximity prints with  $20\text{ }\mu\text{m}$  gap. The goal of the presented work was to demonstrate the fundamental assumption and not to deliver a production-ready process.

In all presented pictures in fig. 4.18 line-end problems are present, as well (the least in fig. 4.18d, but still present). These are common problems in proximity printing, and could be reduced by applying resolution enhancement techniques like optical proximity correction (adding sub-resolution assist features (SRAF) like serifs and similar to mask structures) or, also involving the illumination, source-mask-optimization (SMO), where the illumination angular spectrum is tuned in conjunction with the SRAF on the photomask itself [89, Chapter 10].

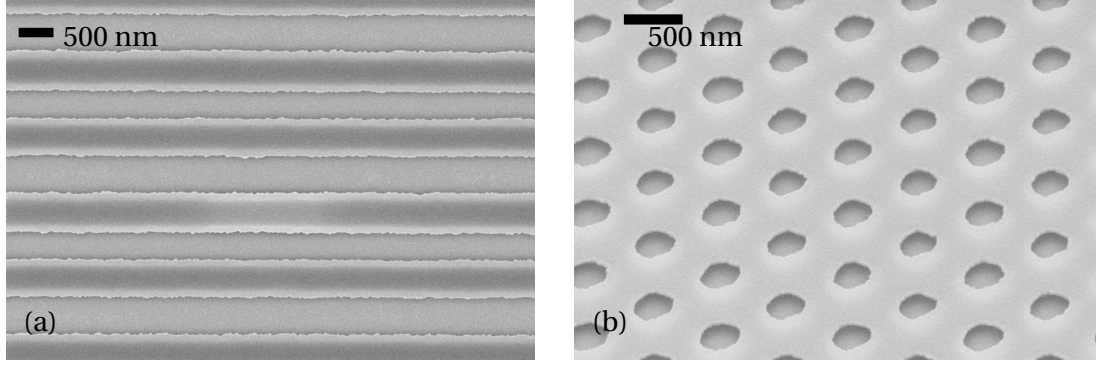


Figure 4.20 – Periodic structures in photoresist using a phase mask with one phase step of  $\pi$ , patterned with a proximity gap of  $20\mu\text{m}$  between mask and wafer. The grating period in (a) amounts to  $1\mu\text{m}$ , and the center-to-center distance in (b) is  $650\text{ nm}$ .  
Reprinted with permission from [KVO<sup>+</sup> 18a] ©The Optical Society.

#### 4.4.3 Outlook on other mask aligner printing techniques

For the sake of completeness, and also to illustrate the broader possibilities of mask aligner (MA) lithography, figs. 4.19 and 4.20 show results taken with the non-imaging homogenizer illumination setup, but with different exposure techniques. Figure 4.19 illustrates the resolution one can expect from soft contact exposure, where the exposure gap is set to  $0\mu\text{m}$  (soft contact does not rely on additional force or vacuum support to ensure good contact [89, Chapter 1]). We were able to demonstrate lateral resolution of down to  $375\text{ nm}$  critical dimension. Figure 4.20 shows a print result for a proximity print with  $20\mu\text{m}$  gap of a binary phase mask with a single step of  $\pi$ , featuring regular periodic structures. Figure 4.20a shows a linear grating with a grating period of  $1\mu\text{m}$ , Figure 4.20b shows a regular hexagonal hole pattern with grating period  $650\text{ nm}$ .

Talbot lithography represents another possible application. This work has been realized with Andreas Vetter, a fellow PhD-student, in the frame of European Project "NOLOSS", with funding from the European Union's Horizon 2020 research and innovation programme under the Marie Skłodowska-Curie grant agreement No 675745. It is enabled by the mask aligner setup developed in this chapter.

The Talbot effect, first described by H. F. Talbot in 1836 [147], describes a phenomenon that the superposition of diffraction orders behind a periodic structure of period  $\Lambda$  leads to self-imaging in discrete distances. The distance in which the first self-imaging occurs is the so-called Talbot length or distance  $z_T$  of

$$z_T = \frac{m \cdot \lambda}{1 - \sqrt{1 - (\lambda/\Lambda)^2}} \quad m \in \mathbb{N}, \quad (4.3)$$

with  $m$  denoting the Talbot plane behind the periodic structure and the the illumination wavelength  $\lambda$ . Talbot lithography exploits this effect in a proximity lithographic setup, with precise



control of the exposure gap, to achieve a considerably improved resolution over conventional proximity lithography. For a comprehensive treatment of the theoretical background we would suggest turning to A. Vetter's publication on the matter [VKO<sup>+</sup>18].

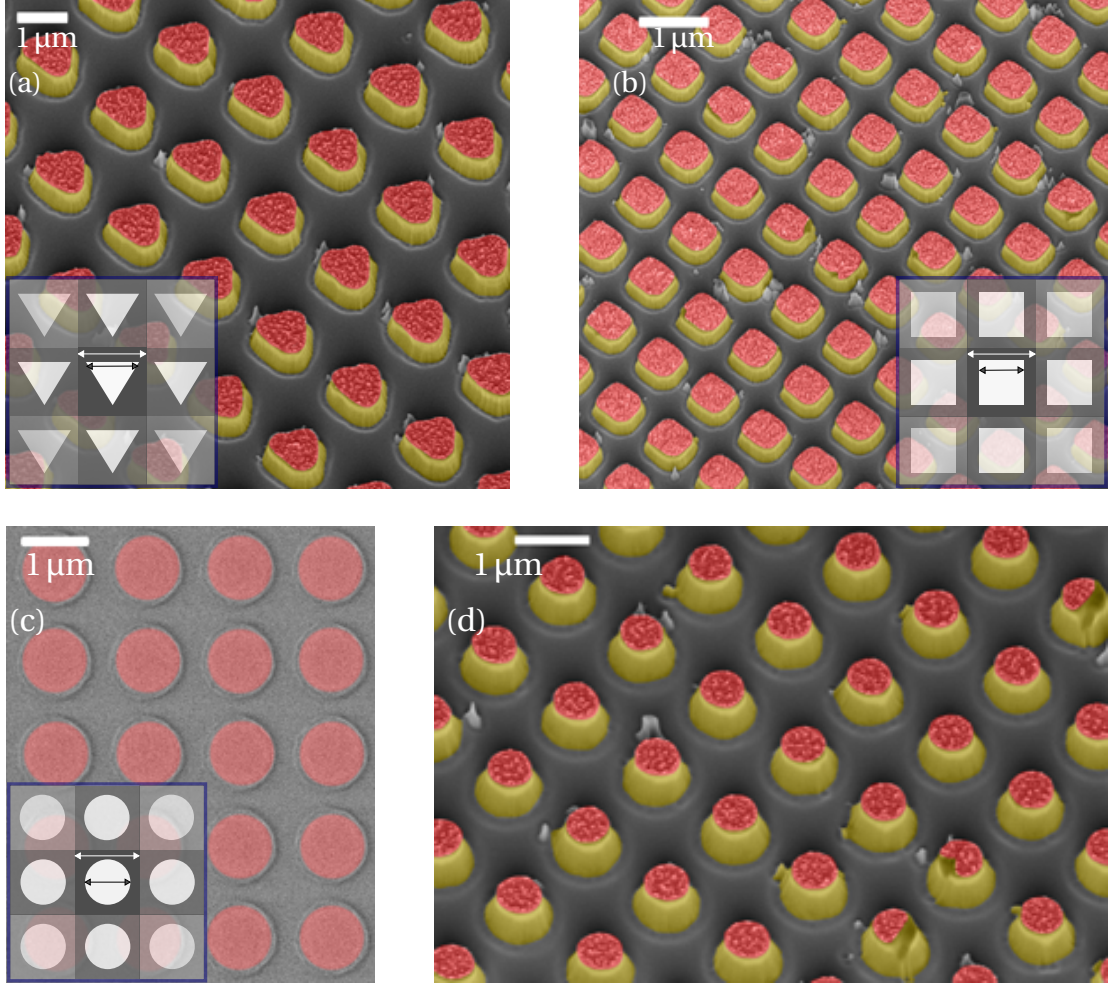


Figure 4.21 – Colorized SEM images of (a) triangular and (b) quadratic structures (yellow), etched into Silicon. The images are taken under an angle of 30°. The chromium hardmask (dyed in red) used for etching is not yet removed, and the etch depth amounts to about 800 nm. The insets show a sketch of the structures on the amplitude mask, with the white areas transparent to the illumination. The size of one unit cell is  $\Lambda = 1.97 \mu\text{m}$  (white arrows), and the side lengths of the triangles and squares are  $1.20 \mu\text{m}$  (black arrows).

Colorized SEM micrographs of (c) resist and (d) etched silicon micropillars, taken under an angle of 30°. The resist openings in (a) (dyed in red) correspond to the chromium hardmask in (b). The inset in (a) shows the design of the unit cell of the amplitude mask, with a period  $\Lambda = 1.4 \mu\text{m}$  (white arrow) and a diameter of  $0.8 \mu\text{m}$  (black arrow).

Reprinted with permission from [VKO<sup>+</sup>18] ©The Optical Society.

What we would like to show here are the results of photolithographic prints realized in the

mask aligner setup described in this chapter. Sub-micron feature sizes were printed with this technique of Talbot lithography, and, to increase the visibility of the structures, a layer of metallic chromium was deposited on the developed photoresist pattern, and structured with a lift-off process. The patterned chromium layer was then used as hardmask for subsequent reactive-ion etching. Figure 4.21 show results achieved with Talbot lithography.

### 4.5 Discussion of mask aligner lithography at 193 nm

The main goal of this chapter was to investigate the first suggested approach for improving the resolution of large-field photolithography: leveraging the wavelength-dependency of proximity mask aligner photolithography by introducing a novel 193 nm CW laser light source. Mask aligners, especially used in proximity printing mode, are a tool which is fit for one-shot exposure of substrates. Yet currently they are limited to lateral resolutions in the range of 3  $\mu\text{m}$  to 5  $\mu\text{m}$  for exposure gaps of 20  $\mu\text{m}$ <sup>22</sup> with their standard high-pressure mercury arc lamps with UV emission lines at 436 nm, 405 nm and 365 nm.

The implementation of the presented DUV laser light source posed several problems: While being advantageous for efficient beam shaping, the monomodal and thus highly coherent laser beam posed some serious challenges on the beam shaping. To achieve the required flat-top intensity distribution in the mask plane both non-imaging and imaging beam homogenizer setups have been investigated using ray-tracing simulation, and implemented in our experimental mask aligner setup (see section 4.3). A rotating diffuser setup with shaped random diffusers was used to limit the visibility of interference effects from the highly coherent source in the photoresist, section 4.3.2. A ray-tracing technique, relying on GBD for the simulation of coherent light, was developed to simulate optical speckle as caused by the diffuser setup, section 4.3.4. This technique was then combined with the simulation of the imaging homogenizer setup, which features two crossed cylinder lens microlens arrays as mixing elements, to fully simulate the whole illumination beam path. This simulation helped to show the Fizeau response from the smallest optical cavity in the illumination beam path, the exposure gap. We showed that by introducing optical speckle with the diffuser we could limit the visibility length scale for interference fringes from small misalignments between photomask and wafer to below the exposure gap, section 4.3.5.

The simulations were tested and verified against measurements taken on the realized beam shaping setups in the lab. Photolithographic testprints with a DUV photoresist were conducted, not only confirming the expectations from simulation but also demonstrating mask aligner photolithography with a novel CW laser light source at 193 nm. It has to be noted, though, that the light source currently is far away from being strong enough for large-field photolithography. The current exposure field is 10 mm x 10 mm, whereas state-of-the-art mask aligners are

---

<sup>22</sup>In production environments the exposure gap is seldom set to below 30  $\mu\text{m}$ . We use 20  $\mu\text{m}$  to demonstrate the working principle, which also confirms theoretical expectation, as the largest test structures on the available DUV photomask had a critical dimension of 2  $\mu\text{m}$ .



available for circular substrate sizes of 200 mm diameter and bigger.

We can thus answer the questions raised in the introduction to this chapter: In general, it is possible to use the presented, novel CW deep ultra-violet laser light source for mask aligner lithography with superior printing resolution compared to standard mask aligners. But, with the currently available optical power output from this source, large-field exposure is not yet possible.

The best beam shaping system for mask aligner lithography with the investigated light source was identified to consist of a diffuser setup featuring at least one rotating diffuser, possibly with a second, static one behind the rotating diffuser, followed by an imaging homogenizer setup featuring crossed cylinder microlens arrays as mixing element.

And we were able to not only incoherently simulate the homogenizer setup, as is state-of-the-art with standard ray-tracing simulation. We could also show that with a novel approach, using GBD in an unusual way, we can simulate optical speckle, as introduced by the optical diffusers, and use this approach to then simulate the whole beam shaping system with coherent ray-tracing.



## 5 Microlens projection lithography

Besides shorter exposure wavelengths, as discussed in the previous chapter, the other approach to increase the photolithographic resolution identified in section 3.4.2 is the introduction of a projection system between photomask and wafer. This means a departure from the shadow-printing approach from mask aligners. As introduced in section 3.4.4, realizing a 1X projection system as massively parallelized and integrated microoptical system can offer certain advantages. This chapter describes the implementation of an microlens projection lithography (MPL) system. It begins with the optical design of its heart, the projection optics, and its technical implementation. Then we look into the design and realization of the scanner mechanics required for the MPL approach. It closes with the implementation of optics and scanner mechanics with a wafer positioning stage and a light source into a complete prototype system.

At this point, the author of this thesis would like to point out that the MPL (MPL) system realized in the course of CTI project MURMELi was a collaborative work as already mentioned in section 2.3.2. The author of this thesis was tasked with realizing the overall system, comprising the technical implementation of the optical system, its integration into a scanner, developed by the author, and the evaluation of the overall system. The optical design of the MPL optics was the result of ongoing, profound and iterative discussions, where the author of this thesis contributed to the realization of the optical system, hence on the tolerancing process and the feasibility of the system. Nevertheless, the actual optics design is original work by K. Müller<sup>1</sup>. Furthermore, the author would like to point out the cooperation with J. Béguelin<sup>2</sup> on the improvement of microlens uniformity, as described in section 5.4.1.

### 5.1 Design of a multi-aperture imaging system for photolithography

Before diving into the design process for a multi-aperture imaging system for photolithographic application we introduce the MPL system in general, and discuss its components.

---

<sup>1</sup>Kevin Müller, SUSS MICROOPTICS SA, Hauterive, Switzerland. Email: kevin.mueller@suss.com.

<sup>2</sup>Jeremy Béguelin, SUSS MICROOPTICS SA, Hauterive, Switzerland. Email: jeremy.beguelin@suss.com.

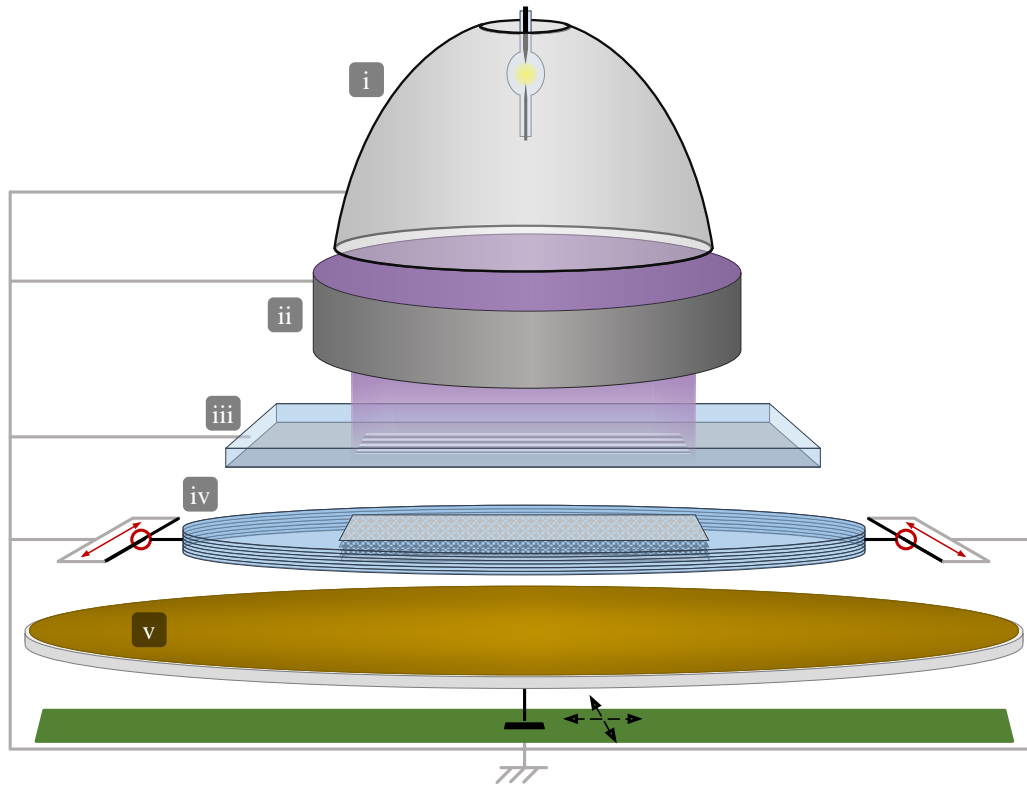


Figure 5.1 – Schematic drawing of a MPL system, highlighting the different components. **i** Exposure light source; **ii** Exposure optics; **iii** Photomask; **iv** MPL optics, mounted in linear in-plane scanner (highlighted in red); **v** Photoresist-coated wafer, mounted on a stepping stage (highlighted in green; dashed arrows signify stepping). The overall mechanical structure is indicated by the gray connecting lines.

The design of a multi-aperture imaging system for photolithography is the search for a compromise in a highly constrained solution space. This section aims at introducing these constraints to prepare a base for the optical design as this compromise. We introduce the constraints in a causal fashion that does not necessarily coincide with the order in which they have been identified and added to the design process.

### 5.1.1 Microlens projection lithography: a sum of many parts

The intended use-case for MPL is large-field 1X photolithography similar to proximity printing in a mask aligner [49], but with superior working distance. Being a photolithographic system, a MPL system aligns a photomask to a photoresist-coated substrate. In between those an integrated microoptical projection lens is located, which images the photomask onto the substrate during exposure. A light source supplies the irradiation for the exposure. The integrated microoptical lens requires an in-plane displacement during exposure to achieve uniform image transfer. Figure 5.1 shows a schematic representation of a typical MPL system, highlighting the individual components. The heart of a MPL system is its integrated microoptical projection

## 5.1. Design of a multi-aperture imaging system for photolithography

---

optics. It is mounted in a scanner that allows linear in-plane displacement of the optics during exposure, relative to a photomask and a substrate, here shown as wafer. This movement and why it is needed will be discussed in section 5.1.3. The photomask is positioned in the object plane of the projection system. The photoresist-coated substrate is (partially) positioned in its image plane. The substrate is mounted on a stepping stage, allowing it to be laterally displaced between exposures to enable sequential exposure of the whole surface. Above the photomask, a light source with suitable exposure optics ensures uniform illumination of the full active area of the photomask during exposure. Here, a high-pressure mercury arc lamp is drawn inside a hyperbolic mirror, which is a common source in back-end-of-line photolithography, and typically used in mask aligners [51, 108].

Not shown in fig. 5.1 are the degrees of freedom between individual components required in a MPL tool, to allow adjustments and enable to successfully implement an exposure process. These degrees of freedom include an in-plane rotation of the projection lens and leveling capabilities of photomask and substrate. Exhaustive investigation and discussion of the individual parts and their requirements is described in the following sections.

A major challenge for the whole project was the mechanical realization of a wafer gap of 500  $\mu\text{m}$ , a design requirement by CTI project MURMELi.

### 5.1.2 Microlens array technology for UV applications

The intended use-case, photolithography, imposes two requirements on the MPL optics. These are the choice of photoresists available for the application and the exposure wavelength. The exposure wavelength, or rather spectral range (g-, h-, i-line, 436 nm, 405 nm and 365 nm, respectively), requires the use of lens material transparent for these wavelengths.

The optical design of the MPL lens, which will be introduced in section 5.1, relies on the stacking of multiple MLAs with uniform lens dimensions over each array. In addition the arrays have an identical geometrical layout. This allows for individual lenses to line up with lenses in adjacent MLAs, to form many imaging systems in parallel. To achieve the highest density of integration the microlenses are arranged in regular hexagonal patterns inside the arrays.

For applications in the UV there are mainly two materials available: calcium fluoride and fused silica. While there exist processes for manufacturing concave microlenses [148], a stable and well-understood process for industrial production of fused silica microlens arrays on wafer-level exists for convex lenses [51, 70, 75]. This process is widely used at SUSS MICROOPTICS SA, where the experimental implementation was carried out. Therefore the MPL optics was designed with and constructed of such microlenses.

Fused silica microlenses and microlens arrays are produced on wafer-level using a molten-resist reflow with subsequent RIE process (also called dry-etching) [14]. The process is detailed in fig. 5.2. It starts with applying a layer of positive photoresist to a fused silica wafer in a

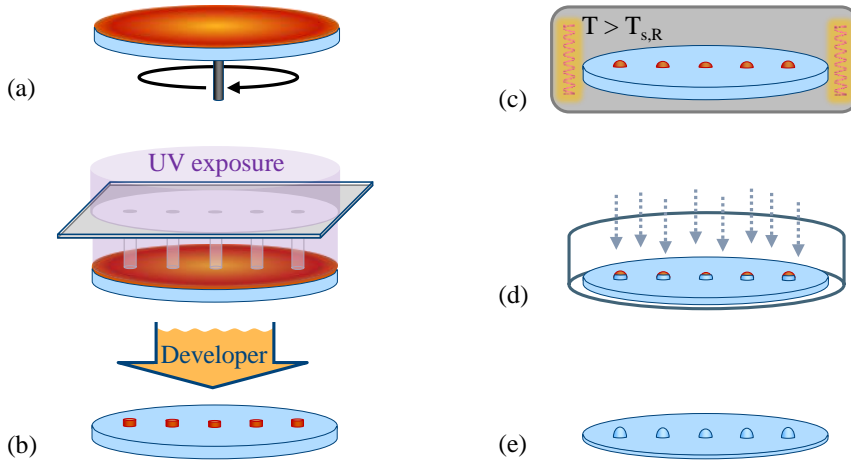


Figure 5.2 – Fused silica MLA production process: molten-resist reflow and reactive ion etching (RIE). (a) A fused silica wafer is spin-coated with positive photoresist. (b) Photolithographic patterning using a mask aligner leaves resist pillars at the position of microlenses. (c) Heating the wafers in an oven to slightly above the softening point of the photoresist  $T_{s,R}$  allows the resist to reflow to spherical lens caps. (d) These then serve as etch mask in a reactive ion etching (RIE) step. Control of the etch selectivity throughout the etching process enables the production of aspherical lens profiles. (e) Finished microlens array.

spin-coating process, fig. 5.2a. Layer thickness variation of spin-coated photoresist is typically  $< 1\%$  [149].

Then, the photoresist layer is structured in a photolithographic exposure in proximity printing in a mask aligner. A photomask blocks the exposure light at the position of lenses. After development, photoresist pillars remain at desired lens positions, with the same diameter as intended for the lens, see fig. 5.2b.

In the next step, fig. 5.2c, the wafer with resist pillars is heated in an oven to a temperature slightly above the softening point of the resist  $T_{s,R}$ . This temperature is held for some time, typically in the range of 1 h to 1.5 h, to allow surface tension in the liquid resist drops to reach an equilibrium state by reflow. This shape is nearly perfectly spherical for the lenses of interest for this work [150].

After the resist droplets have cooled down, the wafer can be placed in a RIE tool. Here, the resist lenses are transferred into the substrate material. By precise control of the etch selectivity, the differential etch rates for photoresist and substrate material, one can not only modify the radius of curvature of the etched lens, but also add an asphericity to the lens profile. To achieve this, the etch selectivity has to be controlled and gradually changed throughout the etching process. Once the photoresist has been completely etched away, thus the shape being transferred into the substrate material, the process is finished and the MLA can be removed from the etching tool. Table 5.1 shows a compilation of limits on the lens shape imposed by

## 5.1. Design of a multi-aperture imaging system for photolithography

Table 5.1 – Process limitations on the production of fused silica MLAs with a molten-resist reflow and RIE process.

Parameter	Limitation
Wafer material	Fused Silica
Wafer size	150 mm and 200 mm in diameter
Wafer thickness $t_W$	$0.4 \text{ mm} \leq t_W \leq 2.25 \text{ mm}$
Individual lens shape	Convex, circular footprint
Individual lens spacing	Non-touching, minimum distance $5 \mu\text{m}$
Individual lens height	Typically $100 \mu\text{m}$
Lens profile	Spherical and aspherical possible

the manufacturing process.

### 5.1.3 Image formation and achieving uniform dose and resolution

As briefly mentioned in section 2.3, photolithography relies on a photosensitive polymer, the photoresist, to capture the image of the photomask. These resists act as analog sensor, that means they require a uniform exposure dose to achieve uniform imaging over the whole exposure field [89, Chap. 5]. There is no means for localized post-processing like in pictures taken with digital cameras. This adds additional constraints, like a requirement for uniform brightness, to achieve constant exposure doses throughout the whole exposure field, and distortion-free imaging. Overall this means that the optical system needs to be very close to its design with little room for tolerances. Furthermore, to enable successful photolithographic prints, the requirement from CTI project MURMELi was an aerial image contrast of  $0.3^3$  for structures of  $2 \mu\text{m}$  critical dimension.

For multi-channel exposure systems like MPL this analog behavior poses several problems which need to be taken into account in the design of the system. First, uniform resolution over the whole field of view of each channel has to be realized. This implies for the optical design an optimization of the field, and/or a restriction of the field size to where this can be guaranteed.

Second, no inter-channel cross-talk is allowed. Identified as a problem in earlier versions of MPL [72], the participation of adjacent channels on common imaging leads to unwanted interference effects limiting both the resolution and the contrast due to the partial coherence of the source. In addition, cross-talk between adjacent channels leads to ghost images, decreasing the contrast. This is shown in fig. 5.3a, where the red hue on the white channel illustrates an unwanted contribution by an adjacent imaging channel.

<sup>3</sup>The contrast  $c$  is calculated as  $c = (I_{\max} - I_{\min}) / (I_{\max} + I_{\min})$ . This contrast is required to achieve a sufficient dose difference between exposed and unexposed regions of the photoresist required for feature registration in the resist. This is a strongly simplified approach, yet it has been defined in this way for project MURMELi. For a comprehensive treatment of this topic, the author suggests to turn to [4, Sec. 7.2], [49, Cha. 1]

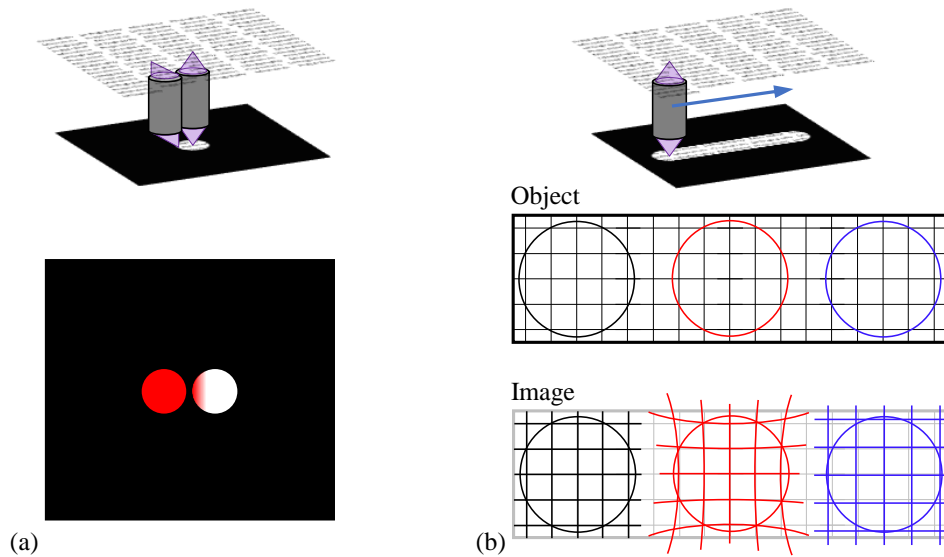


Figure 5.3 – Typical image formation errors in a microlens projection lithographic system. Upper row: depiction of the optical setup. Lower row: illustration of the impact.

(a) Inter-channel cross-talk. An adjacent channel images parts of the object to an image position where it is not supposed to be (large angles). (b) Optical aberrations prohibiting successful image recombination. Ideal imaging in black (to the left): the image (black grid) lines up with the desired image position (grey grid). Distorted imaging in red (center): the magnification changes over the field, leading to a distorted representation in the image. Magnification  $\neq 1$  in blue: the image (blue grid) has a different scale than the object.

Third, 1X imaging has to be realized by every imaging channel. If the individual image were inverted, a lateral displacement of the imaging system would lead to a displacement of the image in the opposite direction. Thus the object information would be spread over a distance twice the clear diameter of each imaging channel, instead of being recorded at the object-conjugate position.

Fourth, the recombination of single channel images to a unified image requires distortion-free 1X imaging. Otherwise the individual images do not line up correctly at the transition points from one channel to the next [151]. Figure 5.3b illustrates these aberrations. Ideal 1X imaging is shown in black, where the image lines up with the conjugated object position (shown as gray grid). In contrast, distortion (in red) or magnification  $\neq 1$  lead to a change of the image scale. Both aberrations lead to a misrepresentation or displacement of field points in the image. Now let us consider a lateral displacement of the respective imaging lens (the respective circles in fig. 5.3b). Only in the non-distorted case two overlapping images will line up properly. Any misalignment leads to blur in the image. This remains true for both the line a single channel will image during scan, and for the superposition of images of two different channels.

Fifth, achieving a uniform exposure dose over multiple adjacent channels.



## 5.1. Design of a multi-aperture imaging system for photolithography

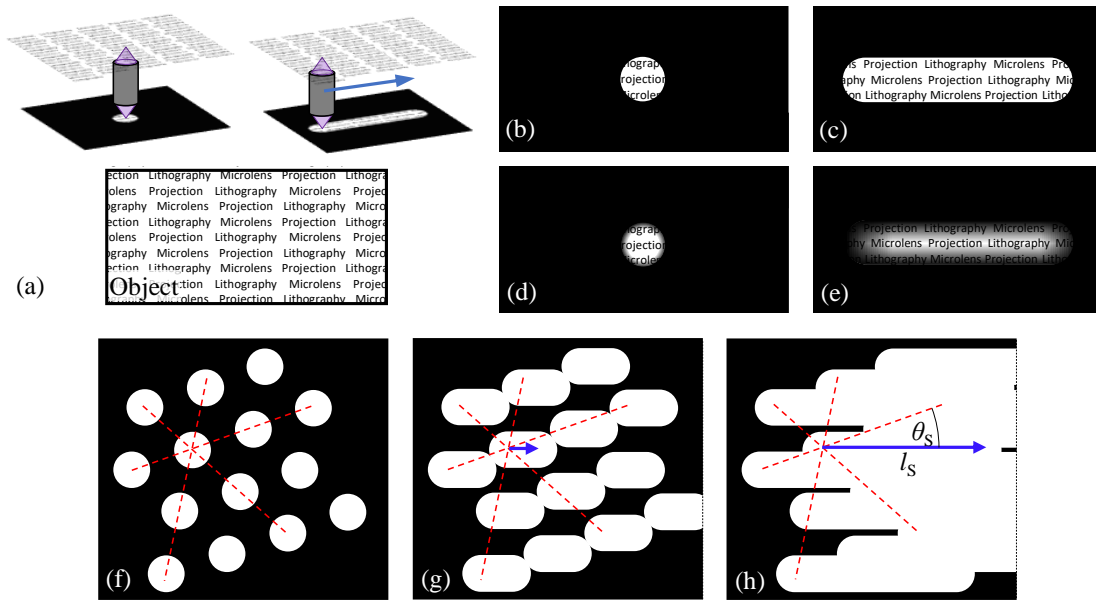


Figure 5.4 – Image formation in a microlens projection lithographic system. (a) Upper row: Single channel imaging, with scan during exposure, depicted by blue arrow. A view of the object is shown in the lower row (object does not have to be periodic). (b,c) Top view of the areas imaged in (a). (d,e) Top view of the images formed in (a), taking into account vignetting (exaggerated) (d) and intensity integration during the line scan(e). Image formation for a hexagonal array of imaging channels, following the same scheme: (f) Every channel transports a partial image. (g,h) These images overlap as a function of scanning distance  $l_s$  and scanning angle  $\theta_s$ . The main axis of the hexagonal array are indicated by dashed lines in red.

These requirements can only be fulfilled for small, isolated fields. To achieve uniform imaging with uniform dose an in-plane scan of the whole imaging system is required during exposure. This scan realizes the superposition of the images of the individual channels. At the same time it introduces a different challenge, the arrangement of imaging channels.

Figure 5.4 schematically shows the scanning image formation of a MPL system. Figure 5.4a shows an isometric rendering (top line) of a single imaging channel. A static exposure (upper left) images the corresponding field of view of the imaging channel. A line scan of the imaging channel (upper right) enables the transmission of a larger part of the image in case a 1X system, when the photoresist integrates over the total exposure time. The bottom line shows the object for the following subfigures. Figure 5.4b and fig. 5.4c show the results described for the isometric views in fig. 5.4a, only as top-view on the photoresist. If the vignetting of a realistic system is taken into account, as well as the temporal integration in case of the line scan, the corresponding pictures will look like figs. 5.4d and 5.4e. Figure 5.4e is rendered with a constant scan speed.

In case of multiple imaging channels under hexagonal arrangement, as is the case for MPL,

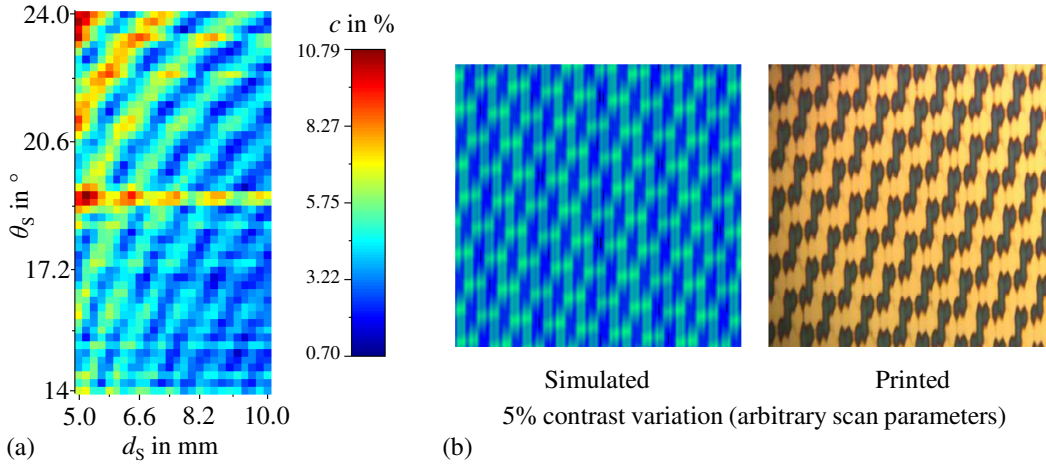


Figure 5.5 – Simulation of dose uniformity for a scanning superposition of a hexagonal arrangement of imaging channels, as function of scan distance  $d_s$  and angle  $\theta_s$  inside the hexagonal layout. (a) Contrast variation for a range of scan parameters, lower contrast is better. (b) Comparison between an underexposed test print with arbitrary scan parameters and a dose uniformity simulation with similar parameters. Reprinted with permission from [KMM<sup>+</sup>16].

static imaging will result in an image plane layout as shown in fig. 5.4f. Here each white area represents where information is imaged onto the photoresist, whereas the black area signifies the non-imaged area. The dashed red lines represent the main axis of the regular hexagonal array of imaging channels. Figures 5.4g and 5.4h show the image channel superposition for a scan of the imaging system with temporal integration in the photoresist for different scan lengths  $l_s$  (blue arrow) under an arbitrary scan angle  $\theta_s$ , measured to the closest symmetry axis.

A uniform scan speed was chosen, as a variation would render the whole problem a lot more complex. Figure 5.5a depicts the results of a simulation<sup>4</sup> of the dose uniformity one can expect from a scanning superposition of a hexagonal arrangement of circular channels, as function of scan distance  $d_s$  and angle  $\theta_s$ . The clear aperture  $D_C$  of a single channels was chosen as 93 % of the hexagonal array pitch  $p_C$ , in accordance to the lens design implemented later-on. In this graph, lower contrast is better, as it means less dose fluctuations over the exposure field. Figure 5.5b compares a testprint without mask and intentionally underexposed with  $d_s = 8.2\text{ mm}$  and  $\theta_s = 21.7^\circ$  to a simulation of the dose distribution with the same scan parameters. A close agreement can be observed.

The dose uniformity for any given combination of  $d_s$  and  $\theta_s$  was calculated as the maximum

<sup>4</sup>Channel superposition simulation implemented in SCILAB 5.5.2, [www.scilab.org](http://www.scilab.org), a numerical computation software similar to MATLAB, by Pauline Malaurie, based on imaging channel simulation in FRED, obtained by Kevin Müller.

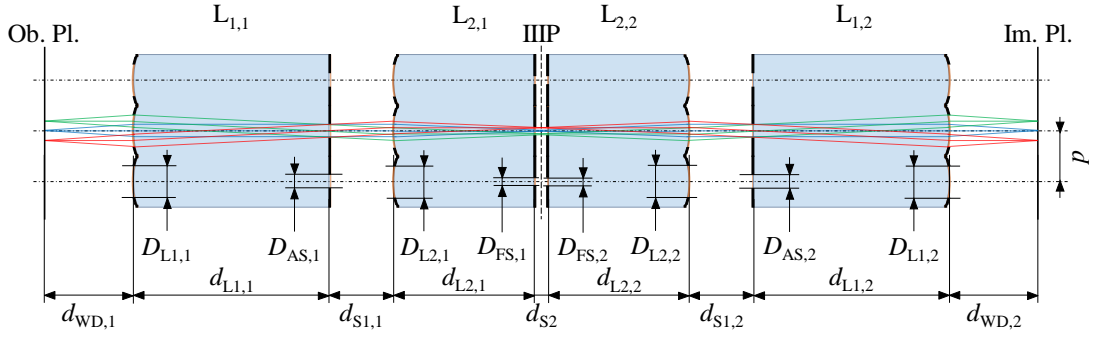


Figure 5.6 – Optical design of the MPL system as found by Kevin Müller and as realized in this thesis. The system consists of a pair of identical Kepler-type telescopes, each consisting of two lenses  $L_{1,n}$  and  $L_{2,n}$ , mirrored at the interior inverted image plane (IIIP) in the center of the system. An object on the object plane (Ob. Pl.) is imaged with 1X magnification on the image plane (Im. Pl.). Optical apertures are applied to all interfaces, with  $D_{Lm,n}$  denoting clear lens apertures,  $D_{AS,n}$  and  $D_{FS,n}$  denoting aperture and field stops, respectively. Object and image side working distances are denoted by  $d_{WD,n}$ , lens substrate thicknesses are denoted by  $d_{Lm,n}$ , the spaces in between are denoted by  $d_{Sm,n}$ . Element indices  $m, n \in [1, 2]$  refer to the respective lens element, compare lens names.

contrast  $c$  in integrated intensity  $I$  found in the field:

$$c = \frac{I_{\max} - I_{\min}}{I_{\max} + I_{\min}}. \quad (5.1)$$

A maximum scan distance  $d_C$  of 10 mm was chosen. We had to find a trade-off between the minimum scan distance required for uniform image formation and the maximum size of MLA, limited by the production process. The maximum scan distance was set also based on the results from scan simulations like shown in fig. 5.5 and similar, indicating that a scan for more than 10 mm would not lead to major gains in the exposure dose uniformity.

### 5.1.4 Optics design and tolerancing

The work presented in this subsection has been carried out by Kevin Müller, a fellow PhD-student at SUSS MICROOPTICS. The author of this thesis contributed in many discussions to the design process, while the simulations have been implemented and run by the aforementioned colleague. Parts of the presented work are submitted for publication [MKN<sup>+</sup>19]. The main design is reviewed for completeness, as it has been realized on wafer-level by the author of this thesis.

Figure 5.6 schematically depicts a cross-section through three adjacent imaging channels of the MPL system. We describe the design for one single channel, as all channels are identical. The system consists of two identical Kepler-type telescopes, mirrored at the interior inverted image plane. The inverted image at this plane is slightly demagnified to minimize

## Chapter 5. Microlens projection lithography

Table 5.2 – Parameters of the optical design of the MPL system realized in this thesis, compare fig. 5.6.  $D$  denotes the clear diameter of apertures,  $d$  axial distances throughout the optical system.

Description	Element	$R_C$ in $\mu\text{m}$	$\kappa$	Clear aperture $D_{Lm,n}$ [ $\mu\text{m}$ ]
Lens 1	$L_{1,1} = L_{1,2}$	285.1	-1.34	315
Lens 2	$L_{2,1} = L_{2,2}$	251.8	-1.02	315
Parameter		[ $\mu\text{m}$ ]		
Aperture stop	$D_{AS,1} = D_{AS,2}$	-	-	144
Field stop	$D_{FS,1} = D_{FS,2}$	-	-	218
Working distance	$d_{WD,1} = d_{WD,2}$	-	-	524.2
Thickness Lens 1	$d_{L1,1} = d_{L1,2}$	-	-	1012
Thickness Spacer 1	$d_{S1,1} = d_{S1,2}$	-	-	445.9
Thickness Lens 2	$d_{L2,1} = d_{L2,2}$	-	-	843
Thickness Spacer 2	$d_{S2}$	-	-	40
MLA pitch <sup>1</sup>	$p$	-	-	350

<sup>1</sup> Center-to-center distance of microlenses in all arrays; hexagonal arrangement.

inter-channel cross-talk. The overall symmetry of the systems not only realizes the required 1X imaging, that means upright imaging with unity magnification, it also brings certain benefits. Asymmetrical wave-aberrations introduced by the lenses cancel each other out, eliminating coma, distortion and chromatic magnification error [85, Sec. 31.1.16]. Symmetric wave-aberrations like spherical aberration are doubled due to the system symmetry. They are minimized by the use of aspherical lens profiles throughout the design [85, Sec. 31.1.13], compare the lens parameters for all four lenses in table 5.2. All lenses share the same substrate material, fused silica, thus there is no material correction for chromatic errors due to dispersion. The system has been designed for 390 nm, the center wavelength of the typical mask-aligner illumination spectral range (g-, h-, i-line; 365 nm, 405 nm and 436 nm).

Aperture layers on the lens surfaces exclude the lens borders, limiting the clear diameter to the specified region. This topic will be discussed in section 5.2.2. Additional aperture layers (aperture stop and field stop) define the numerical aperture ( $NA = 0.12$ ) and field extent of each imaging channel. The field stop, ideally positioned in the interior inverted image plane, has been split and positioned slightly off-center, compare fig. 5.6. This is due to the requirement of maintaining a certain gap size between any two optical interfaces, to avoid intensity modulations due to interference fringes between the interfaces. The mechanism of this effect has been discussed in section 4.3.2.

A slight image demagnification is realized on the center plane to minimize inter-channel crosstalk. The system symmetry also implies both object- and image-side telecentricity, ensuring constant magnification for out-of-focus positions both for the photomask placement in the object plane and the substrate placement in the image plane. This represents a major

## 5.1. Design of a multi-aperture imaging system for photolithography

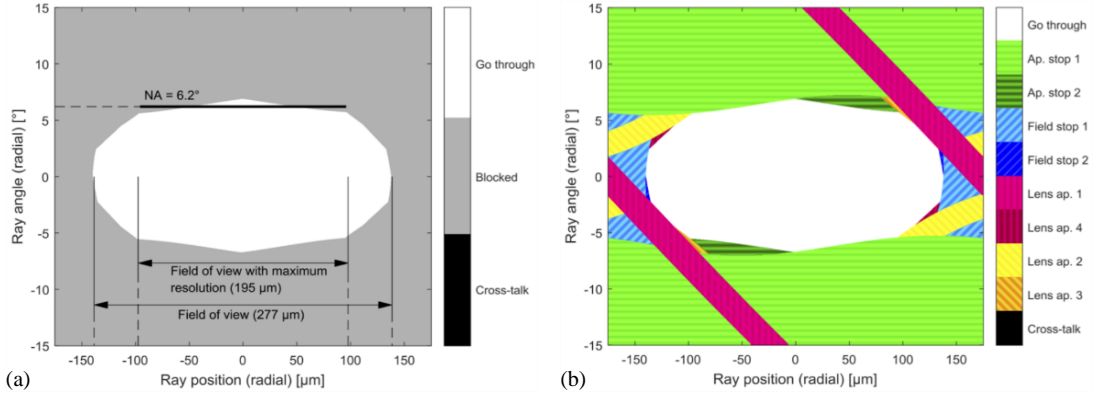


Figure 5.7 – Phase space diagram of the MPL system fig. 5.6 for a single channel. Center region: light passing the system. (a) Depiction of the system-side space-bandwidth product of a single channel; no cross-talk is visible. (b) Depiction of the limiting contributions of apertures in the beam path, compare fig. 5.6. Submitted for publication [MKN<sup>+</sup> 19].

feature for the system robustness towards mechanical displacements in application.

The substrate thickness of the lenses was adapted to existing wafer-thicknesses and chosen such that all aperture layers could be applied to existing interfaces in the system to minimize the required number of elements and interfaces in the optical path. This constraint was introduced to facilitate production.

To visualize the information transfer for image formation through one imaging channel one can plot the system in phase space, see fig. 5.7a, similar to the phase-space window proposed by Ozaktas *et al.* [91]. If in addition the contributions of individual apertures are marked, compare fig. 5.7b, one can learn several things about the optical system.

Figure 5.7a illustrates the information transmission capacity of a single channel of the MPL system. The center clear area equals the system-side space-bandwidth product, as introduced and discussed in chapter 3. This represents the range of spatial frequencies the system can transmit. As highlighted by the black arrows, the system has a field of view with very little loss of information transport capacity over 195 μm in diameter. The specification numerical aperture is  $NA = \sin(6.2^\circ) = 0.108$ . This allows for the design resolution of 2 μm critical dimension. The maximum field of view is 277 μm in diameter. The system has been designed such that no inter-channel cross-talk is present for a maximum illumination angle of  $\pm 8.2^\circ$ .

To learn more about the optical system, fig. 5.7b color-codes the aperture layers where rays are stopped in optical simulation of the system. This allows for a detailed analysis of the system behavior. The aperture stop is limiting the field angle over most of the field of view, as is to be expected. The border of the delimiting area imposed by the aperture stop is slightly inclined, because the stop is positioned slightly outside its ideal plane, the entrance pupil. This is a deliberate choice by the designer for balancing vignetting over the channel as well as to not

Table 5.3 – Tolerances on parameters of the optical design of the MPL system, fig. 5.6. The channel-to-channel tolerances of all microlens arrays as well as aperture arrays were assumed to be perfect, in comparison to the rest. This assumption was made on the basis of these tolerances relying on the accuracy of photomasks produced with e-beam lithography, with overall maximum lateral tolerances of 50 nm.

Parameter	Variation	Unit
Lens $\Delta R_C$ <sup>1</sup>	$\pm 2.5$	%
Lens $\Delta \kappa$ <sup>1</sup>	$\pm 0.5$	-
Lens RMS shape deviation <sup>1</sup>	100	nm
Aperture layer $\Delta x, y$ <sup>2</sup>	$\leq 1$	$\mu\text{m}$
Layer alignment $\Delta x, y$ <sup>3</sup>	$\leq 1$	$\mu\text{m}$
Wafer-to-wafer alignment $\Delta x, y$	$\leq 1.5$	$\mu\text{m}$
Wafer thickness error $\Delta d_{L,S1}$	$\pm 2$	$\mu\text{m}$
Center space error $\Delta d_{S2}$	$\pm 1$	$\mu\text{m}$

<sup>1</sup> Identical tolerances for all 4 microlens arrays.

<sup>2</sup> All aperture layers, including apertures limiting the clear lens diameter.

<sup>3</sup> Aperture layers to respective substrate.

having an intermediate focus coinciding with an optical interface in the beam path (the flat back surface of  $L_{1,n}$  in fig. 5.6). This also leads to a pit in the functionality of the aperture stop by relying on the second aperture stop in the symmetric system to block a part of the light passing the first one, due to its out-of-pupil-placement.

A similar behavior can be observed for the field stop, laterally limiting the field of view. As can be seen in the schema drawn in fig. 5.6, the position of the field stop, located on the back-side of  $L_{2,n}$ , is also slightly out of its ideal plane, which would be the inverted interior image plane (IIIP). The necessity to maintain a minimum air-gap between those two interfaces causes this behavior, and thus the slight inclination.

The clear lens diameters, denoted as Lens apertures in fig. 5.7b, slightly clip the outmost corners of the space-bandwidth product. This illustrates the presence of vignetting in the system, for fields larger than  $193\mu\text{m}$  in diameter. For field points further out from the optical axis the angular spectrum is clipped, leading to a loss in resolution together with loss in transmitted power.

Tolerancing the optical design turned out to be difficult. In contrast to the presentation in this subsection, compiling constraints and the accompanying tolerances has been the precondition for designing the system. Section 5.1.3 can be understood as a discussion of these constraints. A comprehensive list of tolerances has been compiled, see table 5.3. In addition, it has been found that a mix-and-match approach is necessary to assemble a symmetric system. A batch of minimum 10 wafers each has been manufactured for both lens types  $L_1$  and  $L_2$ , to increase the chance of finding lens wafers with similar radius of curvature.

This number represents a compromise between usual production spread, necessity of lens similarity and cost per wafer. Based on average lens shape and RMS shape deviations similar wafers were chosen. For this selection process a simulation has been run permuting through different possible combinations of wafers to identify the best combination. Additionally, the distances between lens wafers  $d_{sm,n}$  have been adapted to the actual manufactured lens parameters as additional degrees of freedom to achieve overall best system performance.

## 5.2 Implementation of a prototype system

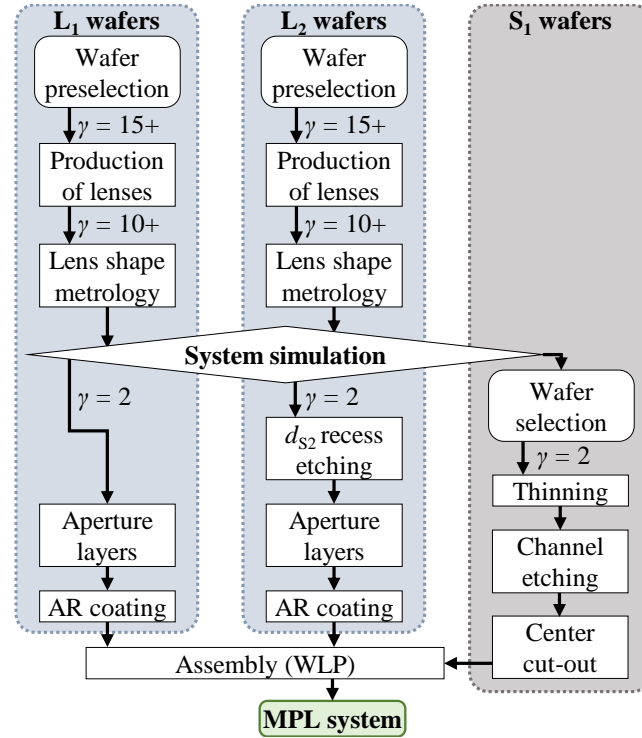


Figure 5.8 – Flow-chart of the manufacturing process of an MPL system. The batch size  $\gamma$  for the different types of wafers is denoted throughout the manufacturing process.

In this section a MPL system is implemented, following the design outlined in section 5.1.4. Figure 5.8 illustrates the steps required in producing a MPL optics. It starts with the selection of wafers for microlens production for both types of lens wafers. After the production of microlenses, as described in section 5.2.2, on a sufficient number of wafers (highlighted by  $\gamma$  in fig. 5.8), the MLAs were characterized. This information was fed into a simulation to find the best combination of wafers for a complete MPL system, as well as the best spacing of these lens wafers, compare fig. 5.6. In system assembly, or packaging, these distances between the lens wafers were set using spacers. Therefore wafers close to the required spacer thicknesses  $d_{s1,n}$  were selected, and thinned to the final thickness by full-face etching in a RIE etching step. Then, venting channels were etched into one surface and the center was cut out. These feature will be discussed in section 5.2.4. For the inner lens wafers  $L_{2,n}$  a recess was etched on



the opposite side of the MLA, to form distance  $d_{S2}$  when assembled. The lens wafers identified by the system simulation were then finished by applying aperture layers and anti-reflective (AR) coatings on all surfaces.

In addition to the optics a mechanical scanner system is required to enable full-field exposure with the MPL optics. This system has been developed and implemented as part of the presented work, and is also discussed in detail.

### 5.2.1 Mask design

The mask design for this project, as well as for any other mask drawn for this thesis, has been carried out with SILVACO EXPERT<sup>5</sup> photomask design software.

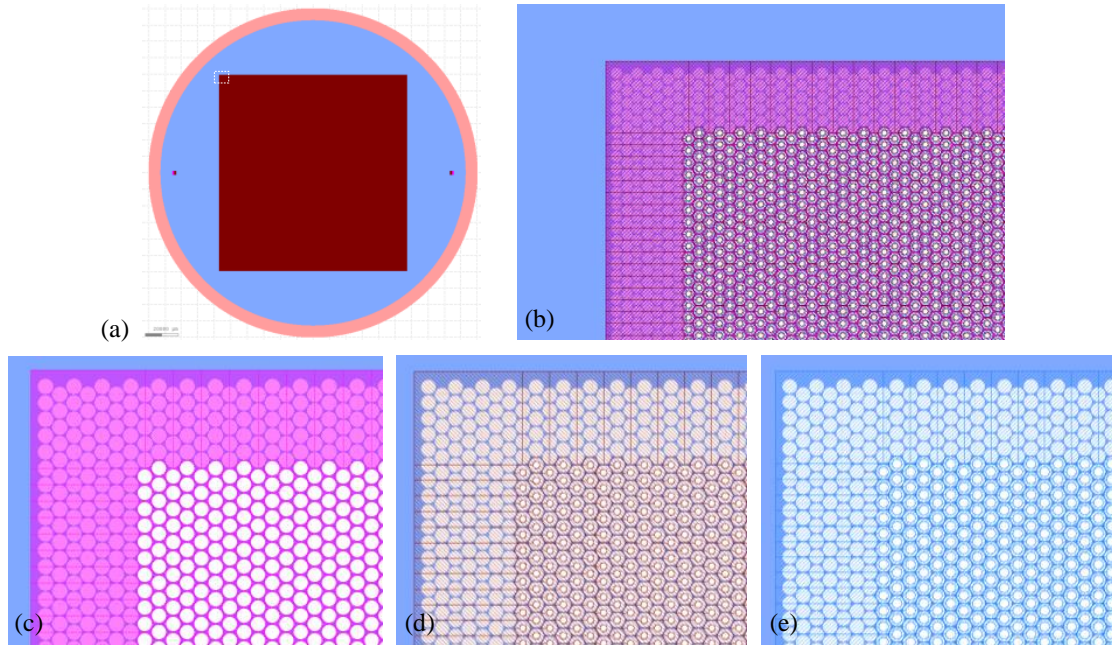


Figure 5.9 – Mask design for the MPL optics lens wafers. (a) Overall layout of a wafer, the orange ring represents the 200 mm wafer extent and at the same time the edge exclusion zone. The red area is populated with structures. (b) Zoom in on the hatched area from (a). All layers visible: microlens layer in light blue (outmost lenses used only for process stabilization), lens clear aperture layer in pink (c), aperture stop layer in brown (d) and field stop layer in hatched blue (e).

Figure 5.9 shows the mask design for the lens wafers  $L_1$  and  $L_2$ . Figure 5.9a shows an overall view of the layout, with the orange ring representing the 200 mm wafer diameter (outer diameter) and the edge exclusion zone (inner diameter) which cannot be used. Figure 5.9b shows a zoom in on the dashed orange rectangle in fig. 5.9a. Here all possible layers for lens wafers

<sup>5</sup>SILVACO Inc., California, USA. Photomask design software EXPERT in Version 4.16.6.



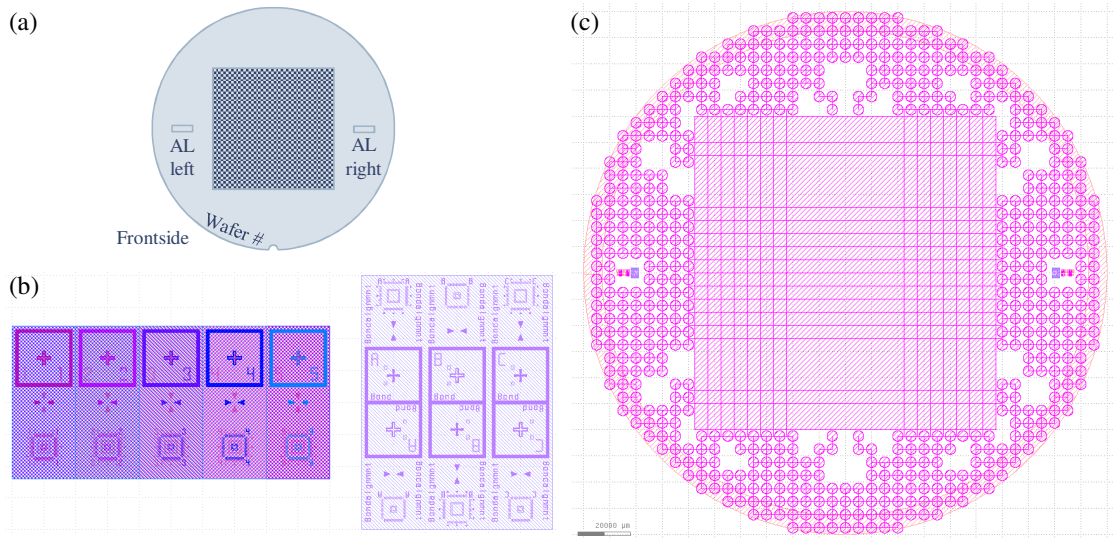


Figure 5.10 – Mask design for the MPL optics wafer-level packaging. (a) Wafer orientation convention, to differentiate the left and right groups of alignment marks (AL). (b) Alignment mark stack for the entire MPL optics production. Left group: lens wafer alignment marks, for the production of microlens arrays and respective aperture layers. Right group: wafer-level packaging alignment marks for wafer stacking. All marks come with lateral precision gauges in form of Vernier scales to assess the alignment. (c) Wafer-level packaging structures. The regular circles represent pouches to accept glue in the stacking process.

are shown in superposition. The light blue bottom layer is used for lens fabrication, the white circles will yield one lens each. On top of the lenses an aperture layer limiting the individual lens' clear aperture is applied, shown in fig. 5.9c. Figures 5.9d and 5.9e show the aperture stop and field stop layers, respectively, which will be applied to the backside of the respective lens wafers.

To mutually align the individual layers, each wafer gets a zero layer with alignment marks in the first production step. These marks are shown in fig. 5.10b. Each wafer has two groups of these alignment marks, see the small rectangular specks on the horizontal axis left and right to the central array in fig. 5.9a, and compare fig. 5.10a for naming convention of "left" and "right" alignment marks. The marks consist of 2 groups each. The first group, shown on the left side of fig. 5.10b, is used to align the lens array and aperture layers on the lens wafers  $L_1$  and  $L_2$ . They are also used to align the wafer-level packaging structures, shown in fig. 5.10c, to the respective layers. The wafer-level packaging structures consist of circular features of 4 mm diameter, which are etched for about 20 μm into the substrate, thus forming cylindrical pouches. All pouches are connected by channels of the same depth and 200 μm width. These channels also connect to the center area as well as to the outside. Thus ventilation of the central area can be assured. This is important so that the optics does not deform when air trapped in the central volume gets heated up during use of the optics due to absorbed exposure irradiation.

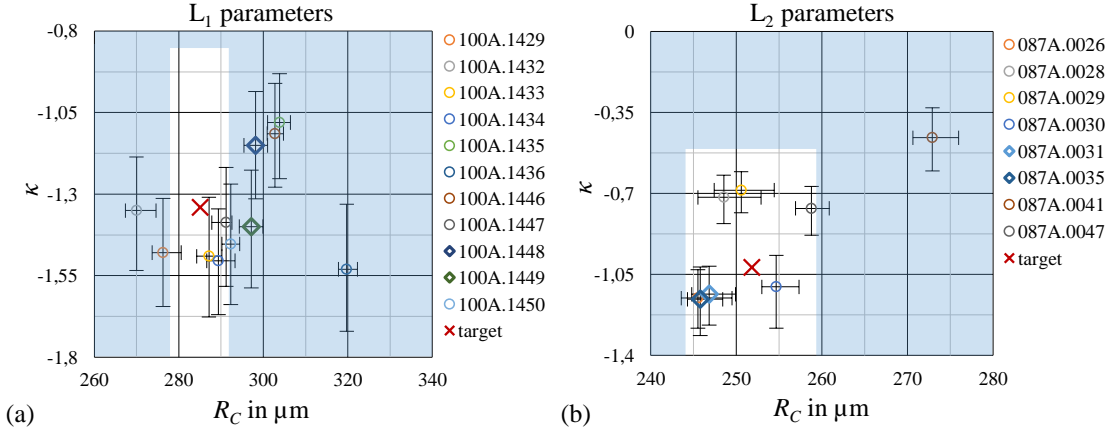


Figure 5.11 – Lens parameter distribution of the produced fused silica microlens arrays. The tolerance window of  $\Delta R_C = \pm 2.5\%$  and  $\Delta \kappa = \pm 0.5$  is drawn as white rectangle in the plot area. A large spread between individual wafers can be observed, and especially for the  $L_1$  wafers, most wafers just missed the actual tolerance window. This underlines the difficulty in manufacturing these microlens arrays. (a)  $L_1$  lens layout. (b)  $L_2$  lens layout.

Wafers used in system assembly have diamond marker.

The right group of features in fig. 5.10b is used for wafer-level packaging. Please note that all marks are present twice, mirrored along the horizontal axis. This feature, together with the axial symmetry of the overall wafer layout, enables wafer stacking with  $0^\circ$  or  $180^\circ$  mutual orientation between each adjacent wafer. This represents one additional degree of freedom for the mix-and-match approach in system assembly.

### 5.2.2 Production of microlens array wafers in fused silica

For the MPL system an exposure field size of 100 mm by 100 mm was chosen. A square field was implemented to facilitate stitching of the exposure field for the patterning of larger substrates. This field size represents a compromise between wafer-level exposure and the largest MLA we were able to fabricate. Fused silica microlens production at SUSS MICROOPTICS SA relies on 200 mm wafers. The MLAs for the MPL optics finally had a lateral extent of 110 mm by 115 mm, in anticipation of the scan.

All measurements of microlenses manufactured for the presented work have been performed on NANOFOCUS<sup>6</sup>  $\mu\text{surf}$  confocal microscopes with subsequent data fitting, according to the aspheric surface equation [152].

Figure 5.11 shows the average lens parameter distribution for all manufactured wafers both for the  $L_1$  and  $L_2$  layouts, compare fig. 5.6. Especially for the  $L_1$  wafers (fig. 5.11a) the difficulty in manufacturing these wafers becomes visible, as most of the wafers just barely missed the

<sup>6</sup>NANOFOCUS AG, Oberhausen, Germany.

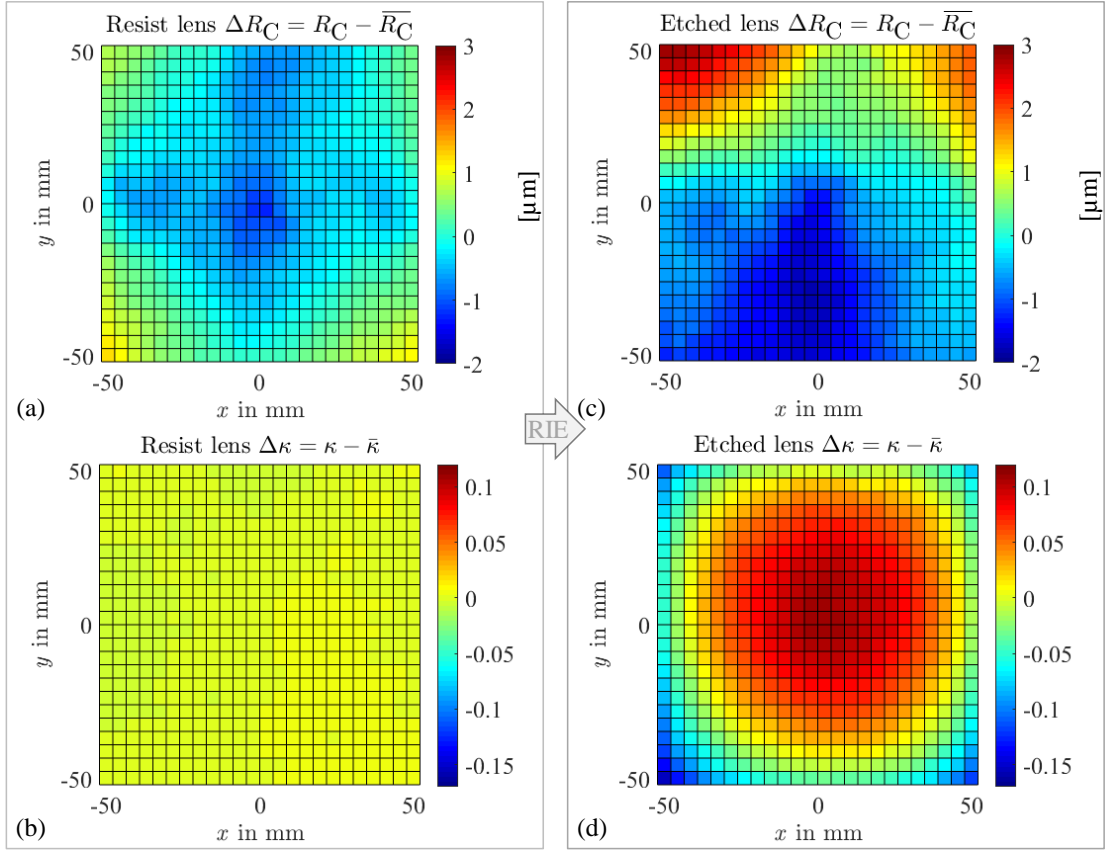


Figure 5.12 – Illustration of lens parameter variation throughout the production process for lenses on a field of 105 mm by 105 mm by plotting the deviation from the mean parameter value. (a) Radius of curvature  $\Delta R_C$  deviation of the photoresist lenses. (b) Conic constant deviation  $\Delta \kappa$  of the photoresist lenses. (c) Radius of curvature deviation  $\Delta R_C$  of the etched lenses. (d) Conic constant deviation  $\Delta \kappa$  of the etched lenses. Reprinted with permission from [KBN<sup>+</sup> 19].

tolerance window (the white rectangle in the graph). The wafers were tested anyhow with the mix-and-match simulation, as the etching of one wafer took typically about 8 h. The wafers chosen for system assembly are highlighted with a diamond marker. For both types of wafers more similar pairs of wafers exist (markers closer together in fig. 5.11). As three wafers broke during handling, they were deleted from the list of available wafers for the mix-and-match simulation.

The microlens arrays for MPL were produced in the standard production of SUSS MICROOPTICS SA. Figure 5.12 shows measurements taken on one of the  $L_1$  wafers. When comparing the evolution of radius of curvature and conic constant, it becomes immediately clear that the photoresist lenses after the reflow process are nearly perfect spherical caps you see in fig. 5.12b as is practically zero. The asphericity is introduced only by etching, compare fig. 5.12b (before etching) to fig. 5.12d (after etching). The radii of curvature changed after etching in compari-

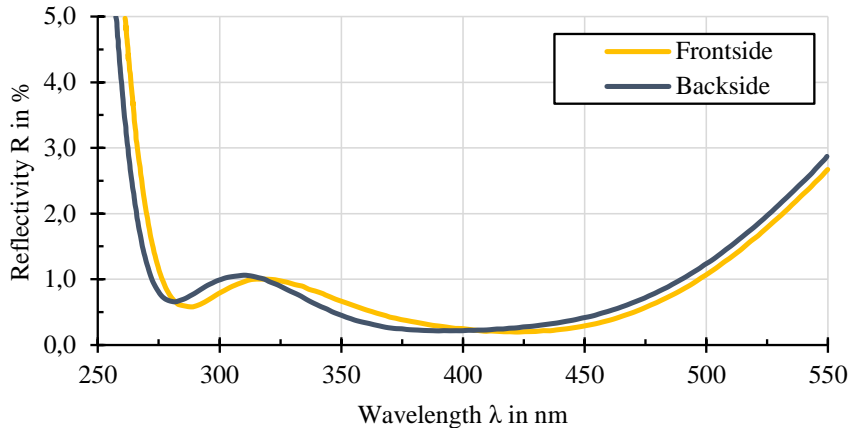


Figure 5.13 – Measurement of the reflectivity of one AR coating as applied to all MPL microlens arrays. The coatings were specified to a reflectivity below 1 % for a wavelength range of 350 nm to 450 nm.

son to the resist lenses, compare fig. 5.12a (before etching) to fig. 5.12c (after etching). The distribution of change in radius of curvature as well as of asphericity was found to be stable for the production process of either design  $L_1$  and  $L_2$ , even if the average parameters differed slightly between wafers of the same design.

The preparation of the microlens arrays then continued with the application of aperture layers. These apertures are required by the optical design and serve as aperture and field stop as well as to limit the free diameter of the individual channels, as discussed in section 5.1.4. The aperture layers were made of metallic chromium (lens-side apertures on the  $L_1$  wafers), or black chromium [153] (back-side of  $L_1$  and both sides of  $L_2$  wafers). All metallic coatings have an optical density (OD) of 3 [154, Sec. 5.5.1]. The aperture layers are structured using a lift-off process. The photolithographic structuring of a photoresist film and final lift-off was conducted at SUSS MICROOPTICS. The metallic layer deposition was done at by supplier. All wafers were finished with the application of AR coatings with a reflectivity below 1 % for a wavelength range of 350 nm to 450 nm, as shown in fig. 5.13.

### 5.2.3 System simulation

To prepare the system assembly, the best fitting MLAs had to be identified. A system simulation<sup>7</sup> has been set up, compare fig. 5.8. This simulation is described in detail in [MKN<sup>+</sup>19]. All manufactured wafers have been measured on multiple positions throughout the active area, and this data has been fed to the simulation. A permutation table was used to define allowed system combinations. For example all  $L_1$  wafers could be used as either  $L_{1,1}$  or  $L_{1,2}$ , but not at both positions at the same time. All lens wafers were manufactured symmetrical to

<sup>7</sup>The simulation is based on the optics design by Kevin Müller and was implemented by him. It was run for the system assembly by Bahareh Ghadiani, a student intern at SUSS MICROOPTICS at that time, under supervision of the author of this thesis.

## 5.2. Implementation of a prototype system

Table 5.4 – System parameters of the assembled MPL optics. The average lens parameters (marked by a bar) and the respective peak-valley variation (marked by  $\Delta_{PV}$ ) are listed.

Element	Wafer no.	$\overline{R_C}$ in $\mu\text{m}$	$\Delta_{PV}R_C$ in %	$\overline{\kappa}$	$\Delta_{PV}\kappa$	$\overline{d_S}$ in $\mu\text{m}$
L <sub>1,1</sub>	100A.1448	298.2	1.85	-1.151	0.33	500
S <sub>1,1</sub>	SE-SQ-051-0001	–	–	–	–	
L <sub>2,1</sub>	087A.0035	245.8	1.68	-1.157	0.3	40
S <sub>2</sub> *	–	–	–	–	–	
L <sub>2,2</sub>	087A.0031	245.5	2.4	-1.152	0.25	499
S <sub>1,2</sub>	SE-SQ-051-0023	–	–	–	–	
L <sub>1,2</sub>	100A.1449	297.3	1.89	-1.3995	0.36	

\* Distance S<sub>2</sub> is distributed equally on both wafers L<sub>2</sub> and etched into their respective back surfaces.

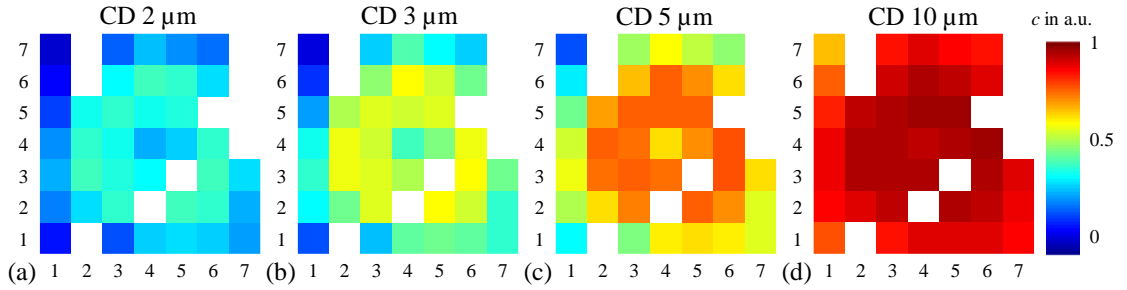


Figure 5.14 – Illustration of the simulated performance for the manufactured MPL system for 7 by 7 field points, regularly spanning an area of 100 mm by 100 mm. The MLAs chosen for the system were measured at positions throughout the active area, which allowed to simulate the expected imaging performance at multiple field positions of the optical system. The performance was simulated as the expected contrast for lines and spaces patterns with a given minimum feature size, described by the individual critical dimension. The results shown are for critical dimensions of (a) 2  $\mu\text{m}$ , (b) 3  $\mu\text{m}$ , (c) 5  $\mu\text{m}$ , (d) 10  $\mu\text{m}$ .

the horizontal axis defined by the alignment marks on both sides of the wafer. This allowed for an additional degree of freedom, where every lens wafer could be used in two orientations.

Table 5.4 lists the result of this simulation, or rather optimization, the wafer numbers of the manufactured MLAs and the best spacing of these wafers. Additionally, the wafer numbers of the wafers used to realize the spaces  $d_{S1,1}$  and  $d_{S1,2}$ ,  $S_{1,1}$  and  $S_{1,2}$  are listed. To characterize the lens wafers, the average lens parameters per wafer  $\overline{R_C}$  and  $\overline{\kappa}$  are listed, together with the peak-to-valley interval of these parameters per wafer,  $\Delta_{PV}R_C$  and  $\Delta_{PV}\kappa$ .

To visualize the result of the combination, the expected imaging performance of this system has been simulated. Here, the scanning superposition was taken into account. The simulation yields an expected value for the contrast obtainable for a certain structure size. As multiple positions distributed over the active area have been measured for each MLA, the performance

## Chapter 5. Microlens projection lithography

Table 5.5 – Dispensing parameters for the wafer-level packaging UV-curing glue dispense process using a BIOFLUIDIX PIPEJET P9 dispenser, mounted on a custom three-axis positioning stage from TETRAEDRE.

Parameter	Type / Value	Comment
Dispensing Tube	S200	200 $\mu\text{m}$ inner diameter
Dispensing frequency	10 Hz	Due to viscosity of DELO GB310
Dispensing velocity	250 $\mu\text{m ms}^{-1}$	Velocity of piezo hammer
# of droplets per position	5	Repetition to increase dispensed volume
Dispensed volume per position	$2.5 \times 10^7 \mu\text{m}^3$	Total droplet volume

at the respective positions could be simulated. The results of this simulation are shown in fig. 5.14. Not all measurements of all positions were successful, in which case the data of this position was discarded after metrology. The superposition of 4 wafers with incomplete data-sets led to the suppression of simulation positions where at least one data point was missing. Thus, for the total system, there are several positions without simulation data. These are visible in fig. 5.14 as blank squares.

In total, 49 positions have been measured on the MLAs, evenly spaced over 100 mm by 100 mm. The colored squares in fig. 5.14 represent a simulated contrast value for the respective field position. It can be seen from fig. 5.14a that the goal of CTI project MURMELi, a minimum contrast of  $c = 0.3$  for structures with 2  $\mu\text{m}$  feature critical dimension is expected to be partially achieved by the presented system. The annular resolution distribution visible throughout fig. 5.14 can be attributed mainly to a circular distribution of  $\kappa$  exhibited by all microlens arrays, as visible in fig. 5.12d. We expect this to be visible in the performance of the system once it is assembled and its performance can be experimentally evaluated.

### 5.2.4 Wafer-level packaging for microlens projection lithography

The MPL optics is assembled with wafer-level packaging. This describes typically the stacking of structured wafers to assemble many elements in one go, with subsequent separation of the full stack. Instead of separating the stack after assembly, the stack represents the final system in case of MPL. Thus we realize a monolithic system, facilitating mechanical integration in the scanner. For system assembly we relied on a mask aligner. This means we can use existing and established technology to enable the system assembly with sub-micron precision.

Another beneficial aspect of assembling the MPL optics on wafer-level is the stability we gain from this approach: the entire remaining wafer surface around the active area of each element adds stability to the system. This also helps towards minimizing wafer deflection as the suspended active area of the lens elements is minimized, as well as clamped on all sides.

To integrate the system we used DELO PHOTOBOND GB310 [155]. This is a single-component, solvent-free acrylic UV-curing polymer with low viscosity (100 mPa at 23 °C), enabling both

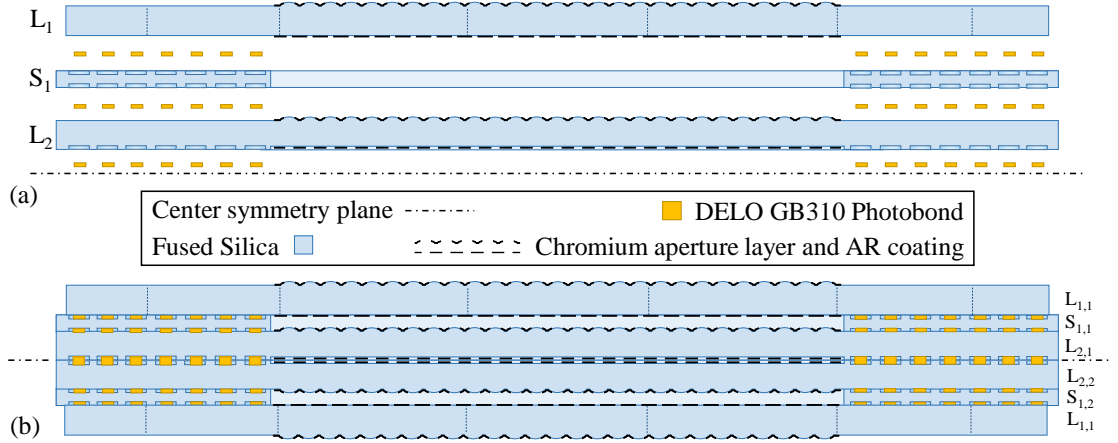


Figure 5.15 – Illustration of a cross-section of the MPL optics (not to scale). (a) Depiction of the individual layers, up to the center symmetry plane. The UV-curing adhesive is shown where it connects the wafers during assembly. Pouches are drawn where the glue will reside inside. (b) Depiction of the assembled system, with two identical halves, bonded at the common center interface.

spin-coating deposition of thin layers (used in a former MPL prototype) as well as dispensing with a BIOFLUIDIX PIPEJET P9<sup>8</sup> dispenser [156], as realized for this thesis. This dispenser uses a piezo-driven hammer to compress a silicon-rubber capillary tube, which is filled with the working fluid. The fast compression of a length of capillary tube leads to a rapid displacement of the liquid inside, parts of which is jetted from the front end of the tube. The other end is connected to a reservoir, refilling the tube due to capillary forces once the hammer has been pulled back. This system enables the precise and non-contact dispensing of nano-liter volumina (depending on the inner diameter of the capillary tube), with a lateral precision of 50  $\mu\text{m}$ , and a repetition rate of up to 100 Hz. The dispenser has been mounted into a three-axis positioning system manufactured by TETRAEDRE<sup>9</sup>, also with lateral positioning accuracy of 50  $\mu\text{m}$ . This meant the total dispensing system had a lateral accuracy of 100  $\mu\text{m}$ . The dispenser has been used with the parameters detailed in table 5.5. These parameters were mainly influenced or governed by the viscosity of the employed UV-curing glue DELO GB310.

Figure 5.15a illustrates process-related details on the elements for the wafer-level packaging approach realized in this work. The outer lens wafers  $L_1$  are structured only on one side, and possess aperture layers and AR coatings on both sides. Their circumference is diced, though, in the shape of a regular hexadecagon (16-sided polygon), with a circumscribed diameter of 199 mm and an inscribed diameter of 195.15 mm. The projection of this hexadecagon is indicated by the dashed vertical lines. Reason for this dicing is the mechanical integration of the optics in the scanner mechanics: the working distance of the system is  $\approx 500 \mu\text{m}$ , which equals the free distance between the lens apex of  $L_1$  and either photomask or substrate,

<sup>8</sup>BIOFLUIDIX GmbH, Freiburg, Germany.

<sup>9</sup>TETRAEDRE SARL, Auvernier, Switzerland.

depending on the side. And to mechanically mount the system a support has to be devised on which the optics can be posed. With the dicing of  $L_1$  it is possible to manufacture a sheet-metal plate with a cut-out in the same shape and size. The optics can now be posed on the spacer wafer  $S_1$ , while  $L_1$  protrudes. This aspect is discussed in the context of the construction of the mechanical scanner in section 5.2.5.

The next layer visible in fig. 5.15a is the spacer  $S_1$ . It possesses a cut-out or window in the center, which is slightly larger than the MLAs of the lens wafers. Thus it can accommodate the lenses of  $L_2$  while ensuring full surface contact on the outer area. For system assembly both surfaces of  $S_1$  are structured with circular pouches with 4 mm diameter and 20  $\mu\text{m}$  depth, compare fig. 5.10c. These pouches are positioned on a regular square grid with 5 mm side-length. For system assembly droplets of DELO GB310 will be dispensed into them, such that the droplet volume is smaller than that of a pouch, but with a droplet sag higher than 20  $\mu\text{m}$ . Then, when brought in contact to a neighboring wafer, the droplets will connect both surfaces and form a bond after curing. In addition, the chosen glue has a shrinkage of 10 % during curing, which translates into a force pulling both surfaces together, supporting good contact between adjacent wafers.

The third layer in fig. 5.15a is the inner lens wafer  $L_2$ . It contains lenses on one side, and a recessed area on the opposite surface. This recess is etched in the same step as gluing pouches and venting channels similar to the ones on  $S_1$  are applied to this surface. The depth of this recess is used as one degree of freedom in system assembly, and set by the system combination simulation. A thickness of 20  $\mu\text{m}$  per side has been realized for the presented system.

The wafer-level packaging of the MPL optics was carried out on a SUSS MA8GEN3 mask aligner with SMILE (SUSS MicroTec Imprint Lithography Equipment) tooling. This tooling mainly introduces a transparent vacuum chuck replacing the mask chuck compared to the standard mask aligner setup. This transparent chuck allows to load 200 mm wafers on both top and bottom chucks, and hence align for example two 200 mm wafers to each other. The UV lamp of the mask aligner then allows to cure UV glue after alignment for wafer-level packaging processes.

One difficulty encountered during wafer-level packaging is the cleanliness of the contact surfaces on all wafers in the final system. As aperture layer and AR coating has been carried out by a subcontractor, while the structuring of the aperture layers has been done in-house at SUSS MICROOPTICS, each lens wafer made three round-trips. In addition, wafers  $L_1$  were diced, and wafers  $L_2$  were etched on the backside. And the spacer wafers were first etched on both sides and then handed over to a mechanical shop<sup>10</sup>, where the center window has been milled out. We found minor particle pollution on all surfaces, which could be mostly, but unfortunately not entirely, removed by manual cleaning. The AR coating prohibited the application of stronger methods.

---

<sup>10</sup>IDONUS SARL, Hauterive, Switzerland



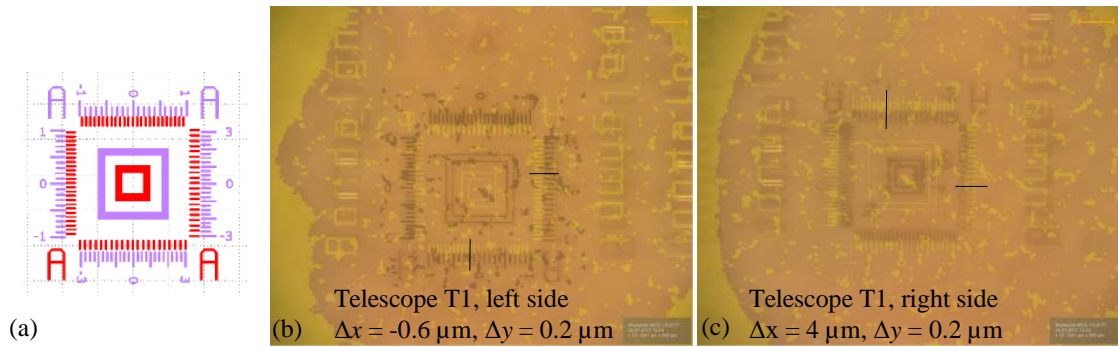


Figure 5.16 – Illustration of the alignment accuracy assessment for the wafer-level packaging of the MPL optics. (a) Superposition of two parts of a Vernier feature included on all alignment marks, compare fig. 5.10b. (b,c) Superimposed and edited microscopic pictures of the alignment marks on  $L_{1,1}$  and  $L_{2,1}$ . The contrast was enhanced and both pictures got colored differently in post-processing. The alignment values found are indicated in the pictures. Compare table 5.6 for the complete picture.

The milling of the window in  $S_1$  lead to a special case: glass debris bonded to the surface close to the milling lane, despite the full wafer being covered by a thick sacrificial layer ( $\approx 80 \mu\text{m}$ ) of MICROCHEMICALS AZ9260 photoresist. Mechanical cleaning was unable to remove them, as they usually form glass bonds, thus chemically attaching themselves to the glass surface directly after etching. To remove these particles a wet-etching step in hydrofluoric acid (10 % in aqueous solution, diluted MERCK SUPRAPUR®) for typically 15 min was applied. The surface of the wafer, except for the area close to the milling lane was covered with AZ9260 photoresist for protection against the wet etching attack [157].

To assess the achieved lateral alignment between the different layers in the MPL optics stack, the Vernier features located at the alignment marks (compare fig. 5.10b) were evaluated. Figure 5.16a shows the corresponding parts of the Vernier of two layers superimposed in the mask design. Two different scales,  $1 \mu\text{m}$  and  $3 \mu\text{m}$  are provided. Figures 5.16b and 5.16c show an example of how the wafer-level packaging alignment assessment was carried out. Microscopic pictures were taken of the alignment marks. To photograph one stack of alignment marks, the microscope was focused to different levels and a picture was taken. The microscope parallax error is here assumed to be insignificant. Pictures of corresponding layers were then post-processed, where the contrast was enhanced and different layers were colored differently. The processed pictures were then superimposed, and the lateral alignment error was recorded, as indicated by the black lines in figs. 5.16b and 5.16c. This was repeated for all layers.

Figure 5.17 shows the completed MPL optics. In contrast to the inner aperture layers, which are made from black chromium, the aperture layer around the lenses on the surface of wafers  $L_1$  is made of metallic chromium. This was intentional to minimize absorption during exposure in the inter-lens area, to minimize heating. Inside the system the aperture layers should absorb stray-light. The metallic chromium layer can be seen at the border of the MLA in

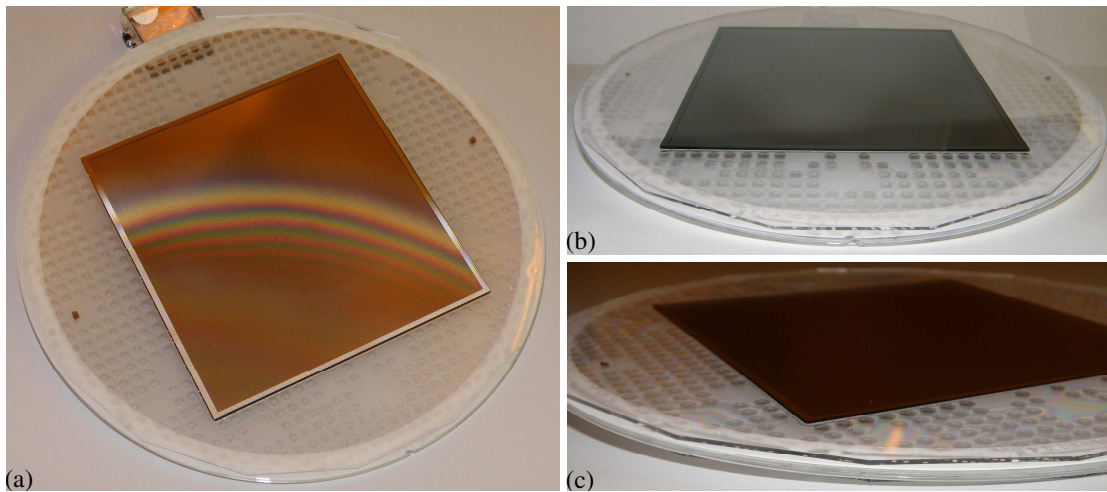


Figure 5.17 – Photographs of the assembled MPL optics. (a) Top view of the system. In the center the optically active area can be recognized from the reddish color of the AR coating over the different aperture layers. The outmost aperture layer is made from metallic chromium, resulting in a silvery reflective surface, visible at the border of the active area. (b,c) Close-up views on the lower border of the optics. The hexadecagonal shape of the outmost wafer is clearly visible. Inside the circular wafer-level packaging structures the droplets of photobond used for system assembly can be seen.

fig. 5.17a. The major part of the MLA here has a reddish tone which comes from the AR coating applied to all surfaces in the active area, over the aperture layers. Figures 5.17b and 5.17c show close-up views on the border of the assembled optics, highlighting the wafer-level packaging structures, in which the droplets of photobond used for system assembly are visible. Also the hexadecagonal shape of the outside wafers  $L_1$  is visible.

Accuracy measurements for the assembled MPL optics are compiled in table 5.6. The system assembly took place in three stages: first, both halves have been assembled separately, in identical fashion. First  $L_1$  to  $S_1$ , and then  $L_2$  was added. To mount  $L_1$  onto a vacuum chuck a jig was manufactured to enable clamping of the wafer only on the flat outside area. This jig was an unstructured wafer of  $500\mu\text{m}$  thickness with a center window, similar to the window in  $S_1$ . The spacer wafers  $S_1$  could not be clamped on a vacuum chuck, due to their venting channels and the center window. Thus they were fixed on the bottom chuck with blue tape<sup>11</sup> in the mask aligner. In the second bonding step  $L_2$  was aligned to  $L_1$ , as the alignment of  $L_1$  to  $S_1$  was not ideal.  $L_2$  could be vacuum-clamped on the chuck in the mask aligner, once the vacuum-quality-threshold value for this chuck was modified in the mask aligner control software.

The lateral alignment of the final assembly step, the combination of both system halves, could

<sup>11</sup> Blue tape is a term locally used at SUSS MICROOPTICS SA for a polytetrafluoroethylene (PTFE) adhesive tape with a silicone-based adhesive, which allows residual-free removal.

## 5.2. Implementation of a prototype system

Table 5.6 – Measured alignment precision for the wafer-level packaging process of the MPL optics. The identical systems' halves have been assembled first ( $T_1$  and  $T_2$ ) before mating them to form the complete optics. Vertical alignment was measured with Heidenhain tactile sensors in the SUSS MA8GEN3 mask aligner, used to control the layer parallelism (MT1-3, short for German "Messtaster", tactile sensor). Lateral alignment has been measured on the Vernier marks close to the alignment marks on the wafers.

Element	Wafer	Wafer number	Orientation (notch)		vertical alignment in $\mu\text{m}$			lateral alignment in $\mu\text{m}$			
			Wafer on chuck	Wafer to wafer	MT1	MT2	MT3	left x	left y	right x	right y
Telescope T1	L1,1	100A.1448	↑↑					Alignment values between L1,1 and L2,1			
				↑↑	5,1	3,7	-1,4				
	S1,1	SE-SQ-051-0001	↑↑								
				↑↑	10,3	5,5	-0,5	1	0,8	5	-1,25
System	L2,1	087A.0035	↑↑					-0,6	0,2	4	0,2
	T1 – L2,1	087A.0035									
				↑↑	15,34	12,9	-2,3	measurement not possible			
	T2 – L2,2	087A.0031									
Telescope T2	L2,2	087A.0031	↑↑					0,2	-0,4 < 1	< 1	
				↑↑	5,2	9,3	0,7	0,2	-2,8	0,2	1,8
	S1,2	SE-SQ-051-0023	↑↑								
				↑↑	7,3	5,1	3,1				
	L1,2	100A.1449	↑↑					Alignment values between L1,2 and L2,2			

not be measured. The total optics was too thick to achieve a sufficiently high contrast for imaging of the center plane in the light microscopes used for this task. Multiple microscopes were tested, each with similar, negative result.

In general we could achieve a lateral alignment better than  $\pm 4 \mu\text{m}$ . We expect that this misalignment will affect the achievable performance only in a minor way. In contrast, the vertical alignment was quite bad, with wedges present of about  $10 \mu\text{m}$  and worse over the full wafer extent. These misalignments will deteriorate the optical performance, compared to the simulation. Also the distribution of optical performance (resolution as function of field position) will change. This will be shown in the practical evaluation of the system in section 5.3.3.

### 5.2.5 Mechanical scanner for microlens projection lithography

The mechanical scanner enables full-field imaging during exposure with the MPL optics consisting of many parallel but separate channels. The MPL optics is a monolithic stack of fused silica wafers with a diameter of 200 mm and a total height of 5.7 mm. It has a design working distance of  $524.2 \mu\text{m}$ , and a clearance of  $\geq 500 \mu\text{m}$ . The optically active area measures 105 mm by 115 mm. For the prototype scanner system we did not want to limit the scan parameters, thus the scanner was designed to allow a maximum scanning distance  $d_{S,\text{max}} = 10 \text{ mm}$  with

0.1 mm precision and an arbitrary scanning angle with a setting precision of  $0.1^\circ$ , compare section 5.1.3.

The scanner to implement the scanning displacement for full-field imaging or recombination during exposure (compare section 5.1.3) has been developed as part of this thesis. Figure 5.18 shows renderings from the SOLIDWORKS 3D construction model, highlighting the main aspects.

Figure 5.18a shows an isometric view from above on the scanner assembly without holder for the photomask. The center part, tinted yellow, is the optics carriage, capable of linear movement. Two high-precision linear crossed-roller bearings, tinted red, custom-built NIPPON BEARING products, are mounted in parallel. The optics carriage is mounted stiffly to the long bearing, which defines the scanning direction. The other side is mounted laterally floating to the short bearing. Both sides are connected to synchronized linear spindle-driven actuators (tinted turquoise), PBC LINEAR CS COMPACT SERIES linear axis, with point-contact attachment. This attachment is realized as crossed-cylinder-pairing supported by a sheet-metal spring, as shown in the magnification view. The actuator on the side of the longer linear bearing is configured as master actuator, while the opposite actuator is configured as slave. This plays a role in the control schema, discussed at the end of this subsection.

Figures 5.18b and 5.18c show top and bottom views of the scanner assembly, respectively. The three attachment points, where the scanner is connected to the overall prototype machine, realized as angular brackets with micrometer screws for leveling, are clearly visible in both views, protruding the external boundaries of the frame top and bottom. To hold the optics while maintaining a clearance of  $500\text{ }\mu\text{m}$  towards the wafer positioned below the scanner, the outermost wafer of the wafer stack forming the MPL optics is diced into a regular hexadecagon. This allows the optics to be held inside a hexadecagonal aperture with similar dimensions. The optics stack is then mounted on the second wafer in the stack, the spacer  $S_1$ . This hexadecagonal aperture is nicely visible in the center of fig. 5.18c.

Figure 5.18d shows a cross-section view of the scanner mechanics, along cut-line A-A in fig. 5.18b. The optics carriage is the lowest point of the whole system, enabling the exposure of substrates larger than the active area of the optics (100 mm by 100 mm). The magnified views (i) to (iv) detail key features of the scanner mechanics. (i) Shows the micrometer screw in one of the angular brackets, allowing for a precise leveling of the total scanner mechanics in the overall exposure tool. (ii) shows one sidewall of one of the V-grooves where the mask-chuck is positioned (shown in fig. 5.19). Here the sapphire window is visible, which has been implemented to ensure precise and deformation-free contact with the ball-headed micrometer screws used to position the mask-chuck. The MPL optics itself is held in an assembly of 3 concentric rings. The outermost ring is connected to the linear bearings. The middle ring is connected to the outermost ring with three flexible arms, one of which is highlighted in (iii). A stack of disk spring washers was used to make the connection free of play. They allow to level the MPL optics to the movement plane, a crucial degree of freedom for

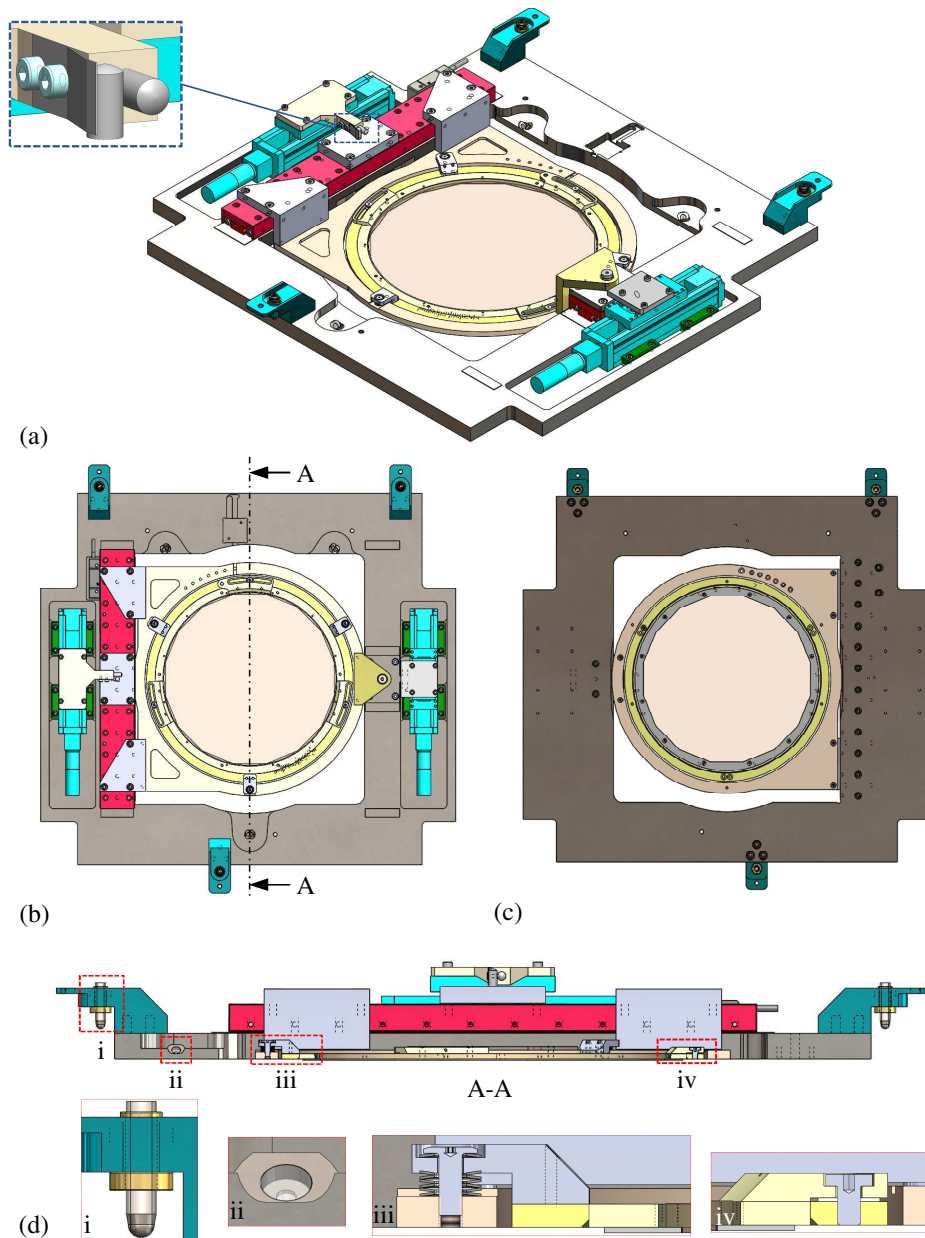


Figure 5.18 – Rendering of the MPL scanner. (a) Isometric view from above. The yellow tinted center parts are the optics mount. Tinted in red are two linear crossed-roller-bearings for precise linear motion (one short, one long). Two linear actuators are mounted parallel to the linear stages (turquoise). The scanner is connected to the overall machine via the three angle brackets featuring micrometer screws for levelling, tinted in darker turquoise. The point-pairing connector coupling linear actuator to optics carriage is shown in detail. (b) Top view of the scanner. (c) Bottom view of the scanner. Hexadecagonal shape of the optics mount visible as innermost aperture in the center. (d) Cross-section view along line A-A. Details provided for the micrometer screw in the angle bracket (i), the V-groove, where the photomask holder is positioned, compare fig. 5.19, realized with sapphire windows (ii), one tip-tilt-leg of the optics mount (iii), and one angular adjustment slider and fixator (iv).



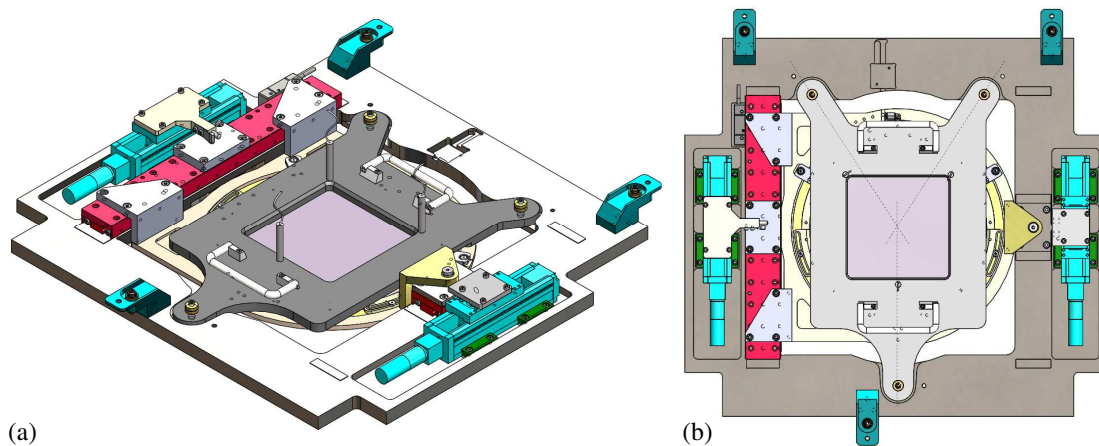


Figure 5.19 – Rendering of the MPL scanner mechanics with mask-chuck in place. (a) Isometric view from above. The mask chuck frame (gray) is positioned with 3 ballheaded micrometer adjustment screws fitting into V-grooves on the scanner frame to the scanner. It features two folding grips for handling. It is implemented as bottom-loading vacuum chuck. The clear aperture is 105 mm by 105 mm. The vertical zylinders around the central mask opening are fiber ends of the AVANTES gap sensor system. (b) Top view of the scanner with mask chuck, highlighting the connection and positioning system. The V-grooves on the scanner frame are arranged following the dash-dotted lines which intersect in the mask center.

successful printing. Finally the innermost ring, where the optics is held on and protruding the hexadecagonal aperture, is connected to the middle ring via an in-plane sliding mechanism, enabling angular adjustments against the scanning direction (iv). This enables the precise setting of the scanning angle  $\theta_s$ . For this reason, the connection between the inner and middle ring is constructed as a screw clamping through a curved slot, enabling rotation of the inner ring when the screw is not tightened. To facilitate sliding, a Teflon washer is located between the curved slot and the middle ring surface.

To enable precise scan angle setting a Vernier scale is implemented on the inner and middle ring, visible in fig. 5.18b at the 5-o'clock position. Together with an attachable push-screw (not shown) angular adjustment with  $0.1^\circ$  precision is possible.

The photomask is positioned above the MPL optics mounted on a bottom-load vacuum chuck, shown in fig. 5.19. It allows to position the mask in working distance over the optics, which is identical to the  $500\mu\text{m}$  working distance to the substrate below the optics. The mask chuck, drawn in gray in fig. 5.19a, has a distinct shape. This shape is governed by the functional necessity to enable vertical adjustment of the mask without changing the mask position laterally. Thus a three-point mount has been implemented, where ball-headed micrometer adjustment screws are located in V-grooves on the scanner frame. These V-grooves are aligned such that their center-lines intersect in the mask center, as highlighted in fig. 5.19b. The legs of the mask-chuck have to span the opening in the scanner frame necessary to contain the

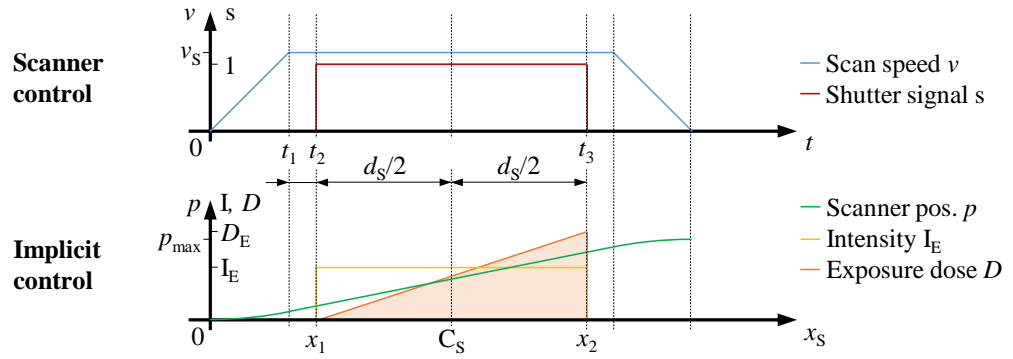


Figure 5.20 – Control schema of the MPL scanner. The scanner electronics directly controls the speed  $v$  of the linear actuators, and effects the shutter opening signal  $s$ . During exposure the scanner moves with a constant speed, thus has a linear change of the scanner position  $p$ . The photoresist integrates over the exposure intensity  $I_E$  resulting in an exposure dose  $D_E$ , illustrated by the tinted triangle. The scanner is controlled such that the exposure over scan distance  $d_s$  is centered on  $C_s$ , the center of the total scanner movement range.

optics carriage plus the scanning range, hence the elongated shape. To set the exposure gap, or rather the object side working distance between mask and MPL optics, the interferometric gap-measurement system from AVANTES, as also used in section 4.4.1, can be mounted in the mask chuck. This is visible in fig. 5.19a, where the three sensors can be found as the vertical cylinders around the clear aperture of the mask-chuck. The three micrometer adjustment screws are then used to both set the mask-chuck in the correct distance to the scanner for arbitrary mask thicknesses from 3 mm to 12.5 mm, and also to set the mask parallel to the optics.

The scanner has been implemented on the ETEL SARIGAN high-precision stepping stage, introduced in section 4.4.1. A 1 kW high-pressure mercury arc lamp lamp-house from a SUSS MA150 mask aligner has been installed to provide standard mask aligner illumination. It features MOEO EXPOSURE OPTICS [51] to ensure illumination uniformity  $\leq 2\%$  and enable adjusting the illumination angular spectrum to the acceptance angle of the MPL optics. The total system has been implemented and installed in the clean-room facilities of SUSS MICROOPTICS SA.

To control the scan distance and exposure time, the shutter of the lamp house is controlled by the electronics that also control the scanner actuators. A schema of the scanner control is drawn in fig. 5.20. Directly controlled are the scan speed  $v$  and the shutter "open" signal  $s$  as functions of time. The maximum scanner movement range is known as well as the starting position (defined by sensors on the master actuator). Thus by controlling the scan speed  $v$  as function of time the scanner position  $p$  can be controlled implicitly. The shutter of the exposure light source is opened symmetrically to the center of the scanner movement range  $C_s$ , which is set to coincide with the center of the photomask. As the exposure intensity  $I_E$  is constant, the exposure dose  $D_E$  can be controlled by choosing the corresponding scan speed  $v_s$ .

### 5.3 System evaluation

As the MPL system consists of different components, each with distinct functionality, an evaluation of the total system should first investigate the individual components before looking at the overall performance.

In this section we will thus first discuss methods of evaluation, then investigate the mechanics of the scanner system and their performance, before discussing the evaluation of the optical system and integrating it into the scanner. Finally we will investigate the total system performance.

#### 5.3.1 Mechanical system evaluation

The scanner mechanics has to fulfill several functions: it has to hold the MPL optics, allow for precise setting of the scan distance  $d_s$  and scan angle  $\theta_s$  and enable linear and in-plane displacements of the optics during exposure. Figure 5.21 shows a compilation of photographs of the overall system as well as details on some functional aspects. Figure 5.21a shows a picture of the scanner system integrated with the ETEL SARIGAN high precision wafer positioning stage with its 300 mm wafer chuck visible in the left center part under the horizontal frame bar. The scanner is located in the upper right quadrant. Figure 5.21h shows a zoom on the scanner itself. In the center the optics carriage, here without optics, can be recognized by its circular aperture. Under closer examination the hexadecagonal inner aperture becomes visible in the center opening. In this picture parts of an ATTOCUBE FPS3010 linear displacement sensor are positioned on the scanner (in the kinematic mounts indicated by the white rectangles). These are discussed in the following. Figure 5.21b shows the Vernier scale that has been added to two rings of the optics mount to allow setting of the scanning angle  $\theta_s$  in combination with the curved slot hole clamps, one of which is shown in fig. 5.21g. Figure 5.21c zooms in on one of the V-grooves for mask chuck positioning with sapphire windows in its walls. These windows prohibit an indentation of the ball-headed micrometer screws of the mask chuck in the frame material. Figure 5.21d shows one flexible ring connector of the scanner carriage. These connectors allow to set the optics parallel to the movement plane defined by the linear bearings, to account for wedge errors in the optics stack as well as positioning tolerances of the optics in the scanner carriage. Figure 5.21e zooms in on the point-contact connection between the master linear actuator (coming from the left) and the long linear bearing (vertical pin). Figure 5.21f shows a close-up on the laterally floating connection of the scanner carriage (the angle bracket on the left side) to the short linear bearing. This feature is implemented to minimize the impact of non-linear mounting of both linear bearings. The angle bracket is forced onto the surface of the linear bearing with a compression spring under the screw visible in the edge of the angle bracket. A Teflon washer between angle bracket and linear bearing surface ensures lateral sliding with minimum friction for  $\pm 0.5$  mm.

The linearity of the linear crossed-roller bearings was not tested directly. Instead, the motion



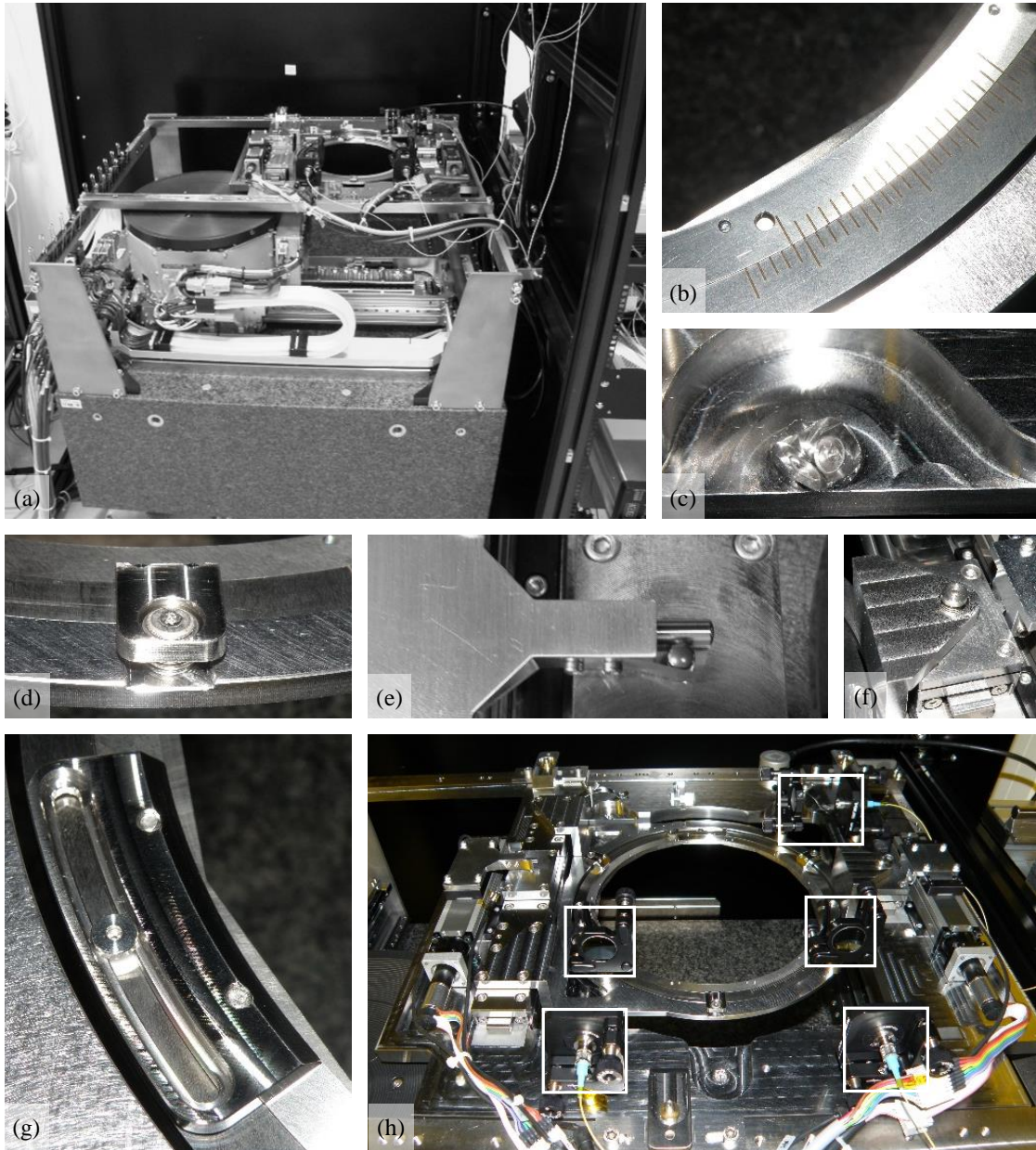


Figure 5.21 – Photographs of the MPL scanner mechanics as realized. Compare fig. 5.18. (a) Total system, with the scanner integrated on the ETEL SARIGAN high precision wafer positioning stage. (b) Detail on the scanning angle  $\theta_S$  control Vernier. (c) Detail on one V-groove for mask chuck positioning with sapphire window. (d) Detail on one flexible ring connector leg for scanning plane adjustment. (e) Point-contact connector of the actuator (from the left) to the scanner carriage (vertical pin). (f) Floating attachment point of the scanner carriage to the short linear bearing. (g) A curved slot connection point between two rings to enable adjustment of  $\theta_S$ . (h) View of the complete scanner, with both actuators mounted. In addition, the ATTOCUBE displacement sensors are set up (in white rectangles), compare fig. 5.22.

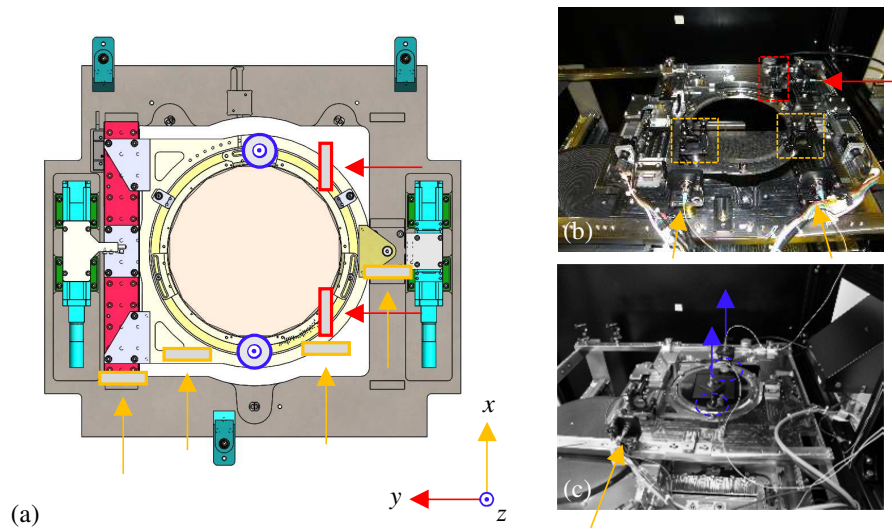


Figure 5.22 – Investigation of the scan linearity and smoothness of the MPL scanner carriage movement. (a) Top view rendering of the scanner, exhibiting possible measurement position for measurements in  $x$ -,  $y$ - and  $z$ -direction. (b) Photograph of the scanner (without optics) with two sensors in  $x$ - and one sensor in  $y$ -direction. (c) Photograph of the scanner (with optics) with one sensor in  $x$ - and two sensors in  $z$ -direction.

of the assembled optics carriage was investigated with an ATTOCUBE FPS3010<sup>12</sup> laser interferometric linear displacement measurement system with three measurement channels. With this system the displacement of the optics carriage has been captured in different directions during scan, as shown in fig. 5.22. The fiber-coupled sensor heads were mounted with magnetic mounts to the positions indicated by the arrows, and mirrors were positioned where indicated by the rectangular and round boxes, also with magnetic mounts. This enabled a comprehensive investigation of movements of the scanner carriage during exposure.

For treatment of the measurement data a routine in SCILAB<sup>13</sup>, has been set up. It allowed to import the raw displacement data. A manual lookup of the linear scanning movement in the collected data was performed and the constant speed (for  $x$ -direction measurements) was calculated. A position deviation assuming a constant speed was computed. An additional Fourier transform allowed to analyze the frequency spectrum of the deviations. For  $y$ - and  $z$ -direction measurements the same routine was applied, with the difference that the non-parallelism of the target mirror to the movement plane was eliminated instead of the constant speed. An exemplary measurement is shown in fig. 5.23. Figure 5.23a shows the result of an entire measurement. Axis 1 and 2, the green and blue lines (blue hidden behind green), illustrate the total displacement of the scanner carriage during one scan. Starting around 3 s the scanner accelerates to maximum speed. Just before reaching the designated scan starting

<sup>12</sup>ATTOCUBE SYSTEMS AG, Haar, Germany

<sup>13</sup>SCILAB 5.5.2, [www.scilab.org](http://www.scilab.org)

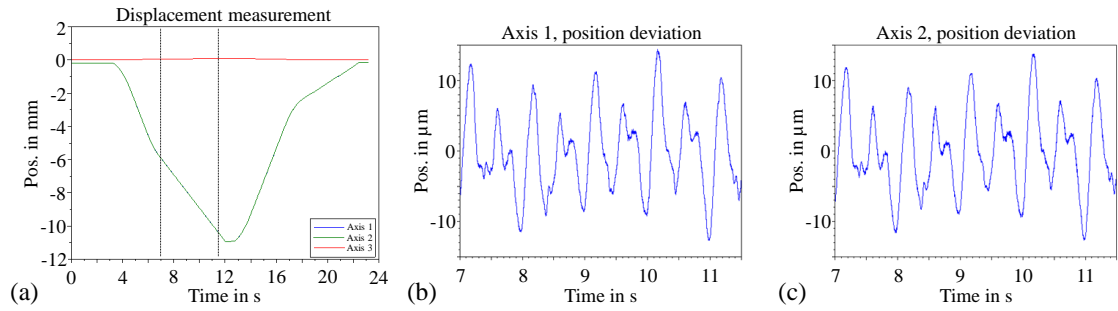


Figure 5.23 – Exemplary measurement of vibrations with the setup shown in fig. 5.22b. Axis 1 and 2 measure displacement along the scan direction, while axis 3 measures the in-plane perpendicular displacement. (a) Complete measurement data. The dashed vertical lines represent the actual constant scan interval which has been chosen manually for further investigation. (b,c) The manually selected interval of constant scan speed for axis 1 and 2.

point it decelerates to the designated scan speed, a time of about 6.5 s. Then the actual scan is performed, here a 5 mm scan with  $1 \text{ mm s}^{-1}$  constant scan speed. After the scan the scanner continues a small safety distance before it is accelerated to maximum negative velocity and returned to zero. Before reaching the original "home" position it slows down to not overshoot the "home" reference sensor implemented in the master actuator.

Figures 5.23b and 5.23c show the relative position deviations of the scanner during the constant scan part of fig. 5.23a for axis 1 and 2. What is immediately visible from these graphs is a harmonic oscillation of the position deviation with a frequency of 1 s, or 1 mm, if the scan speed is taken into consideration. This fluctuation could be traced back to manufacturing tolerances on the spindle in both linear actuators. The spindles have a pitch of 1 mm. The effect of both spindles having similar linearity errors of  $10 \mu\text{m}$  to  $15 \mu\text{m}$ , which were not synchronized, lead to a rocking motion of the scanner carriage in  $z$ -direction (not shown). An blur in photolithographic prints due to image shift caused by this tilt was the consequence. To improve this situation the slave actuator was disconnected, and the scanner was used only with the master actuator. Thus the rocking motion in  $z$ -direction was limited over the full extent of the scanner carriage to  $\pm 2 \mu\text{m}$  to  $3 \mu\text{m}$ . This translates into an image blur of  $\approx \pm 50 \text{ nm}$ , a value that was found acceptable for successful printing. The remaining rocking motion was attributed to a combination of tolerances in the linear bearings, the coupling points between linear bearings and the scanner carriage and the non-linear force input due to the pitch error of the linear actuator.

The position deviation in  $x$ -direction was not improved by this measure, as it did not address the pitch error of the actuator spindle. But this position deviation was deemed non-critical, as it represented a placement error in scanning direction. And subsequent tests showed that the exposure uniformity was much more susceptible to the scanning angle, rendering this actuator spindle error acceptable for the overall tool.

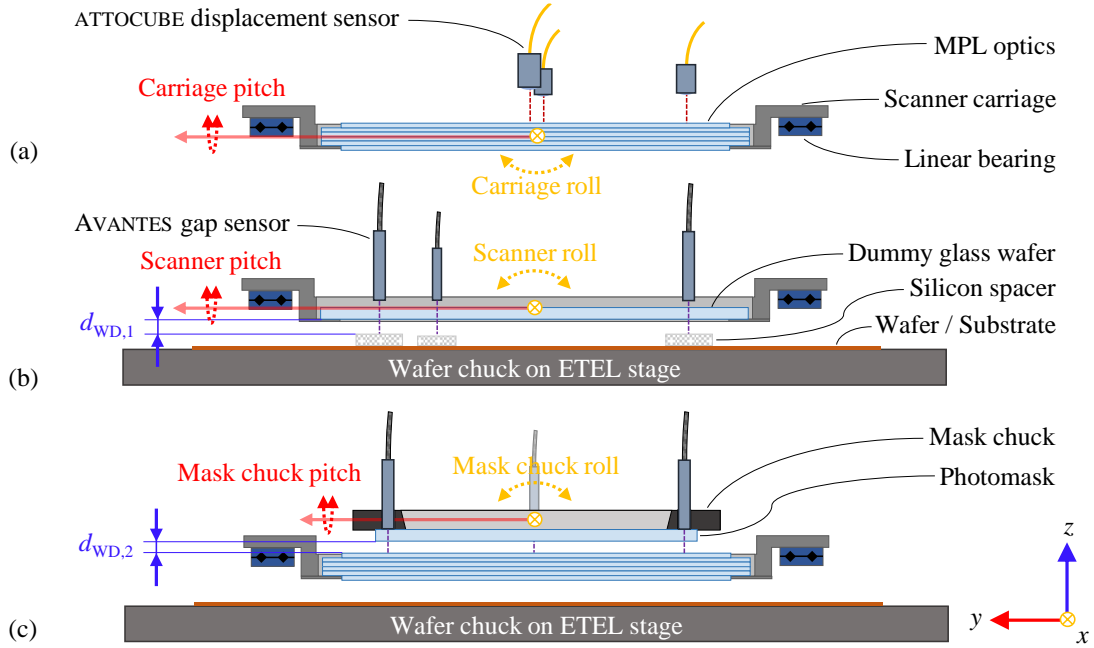


Figure 5.24 – Schematic of the procedure to install the MPL optics in the scanner. (a) The optics is placed in the scanner. The ATTOCUBE displacement sensors are used to align the optics to the movement plane. (b) The optics is replaced by a dummy wafer, and the scanner is aligned to the wafer chuck with the AVANTES gap sensors. Also the distance is measured to allow for indirect control of  $d_{WD,1}$  later on. (c) Finally, the optics is placed back in the scanner, and the mask chuck is loaded. The AVANTES gap sensors are used to align the mask chuck to the top surface of the optics.

### 5.3.2 System integration and operation

The installation of the MPL optics in the scanner required a complex procedure to align the different components. This procedure was complicated by the fact that areas in the optics stack without wafer-level packaging structures (glue pouches) were not transparent, as anticipated, but some of the surfaces had a matte finish. Hence it was impossible to install the optics and set the wafer-side working distance  $d_{WD,2}$ , measuring through the optics stack. Instead, the procedure shown in fig. 5.24 had to be followed. In a first step, the optics was placed in its mount in the scanner carriage. The ATTOCUBE displacement sensor, previously used for vibration investigation of the mechanics, was employed to align the optics mount to the scanning plane, see fig. 5.24a. This was enabled by the flexible connections between the middle and the outer ring of the optics mount, compare figs. 5.18d and 5.21d. In the next step, the optics was taken out and replaced by a dummy wafer, an unstructured glass wafer. Now the AVANTES gap sensors were used to align the scanner to the wafer chuck, compare fig. 5.24b. The dummy wafer did not protrude the hexadecagonal aperture of the optics carriage, and the total distance to another dummy wafer, placed on the wafer chuck, was too high for the AVANTES system. Additional silicon spacers of known thickness were placed on the lower wafer



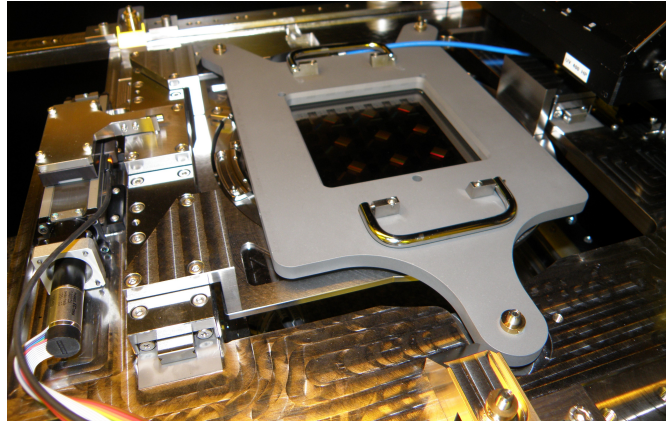


Figure 5.25 – Picture of the mask chuck, mounted on the MPL scanner.

as measurement targets. With this approach the scanner could be aligned to the wafer chuck, enabling wafer gap control later in the process by relying on the repeatability and stability of the ETEL SARIGAN movement stage. This proved to work out reliably. One drawback was that the dummy wafer did not possess the same weight as the MPL optics. We feared that the higher weight of the MPL optics would lead to additional deformation or displacement due to gravitational pull, but we found this to not present a problem in application. The wafer-side working distance had to be found through empirical testing later-on in any case, so any error in height here only added a constant offset to this empirical value. In the final step, drawn in fig. 5.24c, the MPL optics was placed again in its mount, and fixed in place this time by small sheet-metal springs, not shown here, pressing on the top. Only little force was applied, as these springs served mainly as security measure against the optics being pushed out of the carriage vertically for any unforeseen reason. Thus their influence was neglected in the initial setup step. This final setup step continued then by placing the photomask, clamped on its vacuum chuck, on the scanner assembly, as shown in fig. 5.25. The AVANTES gap sensors were placed in the mask chuck in mounts prepared for this application, and the mask was aligned to the surface of the MPL optics.

The mounted optics in the scanner can be seen in fig. 5.26, with a top- and bottom-view. In the top-view (fig. 5.26a) the regular arrangement of wafer-level packaging structures (compare fig. 5.10c) can be seen on the optics (round shape in the center) around the optically active area, the darker rectangle in the center of the optics. In addition, the matte parts between the wafer-level packaging features can be seen. They were intended for through-optics alignment to the wafer chuck. But the photoresist cover during etching of the wafer-level packaging structures proved to be too thin so that stochastic etching of the surface occurred, leading to the matte finish. On the left part of the bottom view, fig. 5.26b, the bottom wafer of the optics can be seen protruding through the hexadecagonal aperture of the optics mount in the scanner carriage.

Setting the scan angle  $\theta_S$  was initially thought to be possible with the optics in place. We found,

though, that as the whole alignment procedure had to be repeated once the scanning angle was changed. Hence the optics was usually taken out prior to changing the scanning angle, to minimize the risk of damaging it. Besides that, setting this scan angle proved to be as precise as planned. A comparison of the scan direction and simulation was already shown earlier, in fig. 5.5b. A good agreement was found.

The indirect setting of the wafer-side working distance  $d_{WD,2}$  as implemented relied on the machine accuracy and repeatability of the ETEL SARIGAN wafer positioning stage. We found that this was sufficient to repeatably print with constant quality. Nevertheless, this represents a shortcoming of the realized setup.

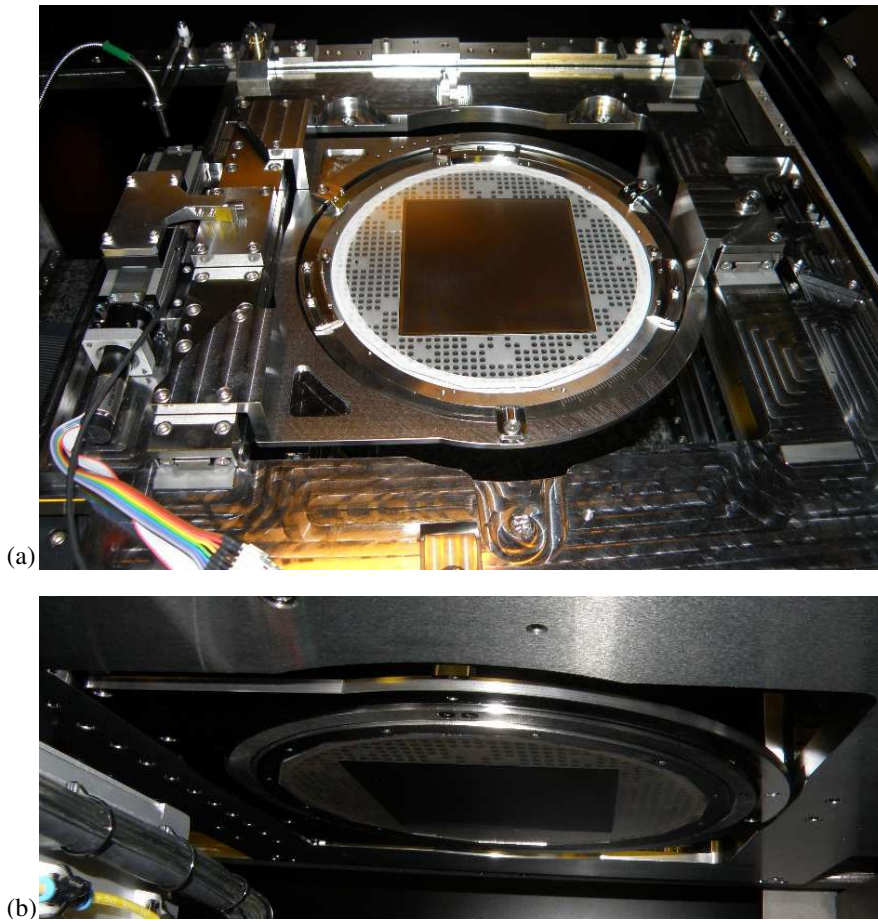


Figure 5.26 – Photographs of the MPL optics integrated in the scanner. (a) Top view, with the optics in the center, mounted in the scanner carriage. On the left side the master actuator is visible. (b) Bottom view, highlighting the hexadecagonal aperture of the inner ring of the scanner carriage and the fitting diced shape of the outer lens wafer, protruding through the aperture.

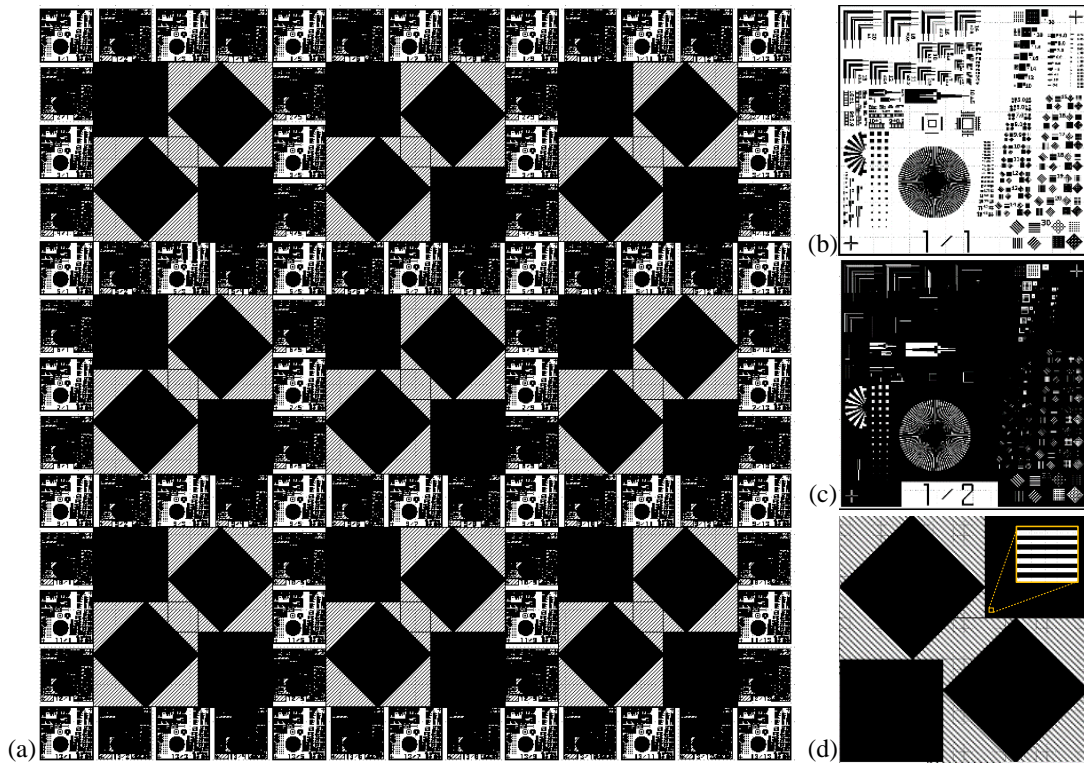


Figure 5.27 – Layout of the test-mask designed and acquired for MPL system evaluation. (a) Overall layout, showing the checkerboard arrangement of test-structure unit cells (bright- and dark-field) and the intermediate fields of lines and spaces under different angles. (b,c) Close-up of one bright- and dark-field unit cell, respectively. (d) Close-up of one lines and spaces test field, with the inset showing a magnification of the pattern; 1  $\mu\text{m}$ , 2  $\mu\text{m}$ , 3  $\mu\text{m}$ , 5  $\mu\text{m}$  and 10  $\mu\text{m}$  line-widths available in each field.

### 5.3.3 System verification

To evaluate the printing performance of the MPL system in total an electron beam-written 6" photomask with test-structures over the whole printing field of 100 mm by 100 mm was designed and ordered. Figure 5.27a shows an overall layout of this mask. The checkerboard arrangement of 13 rows and columns of the same unit cell of test-structures in bright- and dark-field variety is visible. A close-up view on these unit cells can be found in figs. 5.27b and 5.27c. In addition, the 3 by 3 matrix of lines and spaces patterns can be seen. They are intended to provide easy access to structure cross-sections when breaking a patterned wafer, with line-lengths of 5 mm. A close-up of these structures can be found in fig. 5.27d. The evaluation of the MPL system relies mainly on lines and spaces patterns present in all test-structure cells, similar to fig. 4.15b with feature sizes from 1  $\mu\text{m}$  to 30  $\mu\text{m}$ .

All photolithographic prints performed to assess the system performance were carried out using 200 mm polished Silicon wafers of 660  $\mu\text{m}$ , 690  $\mu\text{m}$  and 725  $\mu\text{m}$  thickness. The thickness

## Chapter 5. Microlens projection lithography

Table 5.7 – Varying Parameters of the MPL test prints shown in the following. All testprints were made in 0.73  $\mu\text{m}$  AZ1512 photoresist on 200 mm polished silicon wafers. After exposure the wafers were developed for 60 s in 1:4 diluted AZ400K developer in DI- $\text{H}_2\text{O}$  in a manual submersion process.

Print no.	Testprint	Mask gap $d_{\text{WD},1}$ [ $\mu\text{m}$ ]	Wafer gap $d_{\text{WD},2}$ [ $\mu\text{m}$ ]	Illumination -	Angular spectrum [ $^\circ$ ]	Dose <sup>+</sup> [mJ cm <sup>-2</sup> ]	Scan distance $d_s$ [mm]	Scan angle $\theta_s$ [ $^\circ$ ]
<b>MPL-TP1</b>	MPL2017-034	509	461	broadband	$\pm 3.7^*$	60	6.58	20.5
<b>MPL-TP2</b>	MPL2017-036	509	461	broadband	$\pm 3$	60	3.29	20.5
<b>MPL-TP3</b>	MPL2017-037	509	461	broadband	$\pm 3$	60	9.87	20.5
<b>MPL-TP4</b>	MPL2017-028	499	471	i-line	$\pm 2.3$	140	6.58	20.5
<b>MPL-TP5</b>	MPL2017-027	509	461	i-line	$\pm 2.3$	140	6.58	20.5
<b>MPL-TP6</b>	MPL2017-031	519	451	i-line	$\pm 2.3$	140	6.58	20.5

<sup>+</sup> Dose measured at i-line (365 nm), thus value differs for i-line (365 nm) and broadband (365 nm, 405 nm and 436 nm) illumination.

\* Without illumination filter plate (IFP) in the illumination path

did not influence the result and is only mentioned for completeness. The positive photoresist AZ1512 by MICROCHEMICALS GMBH was spincoated on the substrates with a layer thickness of 0.73  $\mu\text{m}$ . After exposure the wafers were developed for 60 s in a manual submersion process in a 1:4 dilution of AZ400K developer in deionized water.

The MPL system is able to resolve structures with 2  $\mu\text{m}$  critical dimension, conform to the stated goal for this work. Figure 5.28 shows photographs of resolution test structures taken with a light microscope with 50X magnification under bright field illumination. In fig. 5.28a the photolithographic print of lines and spaces with 2  $\mu\text{m}$  and 2.25  $\mu\text{m}$  line-width can be seen. The structures are not fully developed, as the dose was not optimized for these small features. All subfigures in fig. 5.28 are taken from the same field, R13C3 (read: row 13, column 3), from testprint MPL-TP1, compare table 5.7. The dose has been optimized rather for 5  $\mu\text{m}$  critical dimension.

However, the required resolution of 2  $\mu\text{m}$  was not achieved over the full exposure field of 100 mm by 100 mm. Figure 5.29 shows charts representing the full exposure field. The checker board structure represents the test mask layout, compare fig. 5.27a. For all testprints listed in table 5.7 the corresponding resolution chart can be found in fig. 5.29. The numbers in the cells of the charts represent the minimum resolved critical dimension for the respective cell on the test mask. In case of cell R13C3 of test print MPL-TP1 the best resolution is 2  $\mu\text{m}$ , as



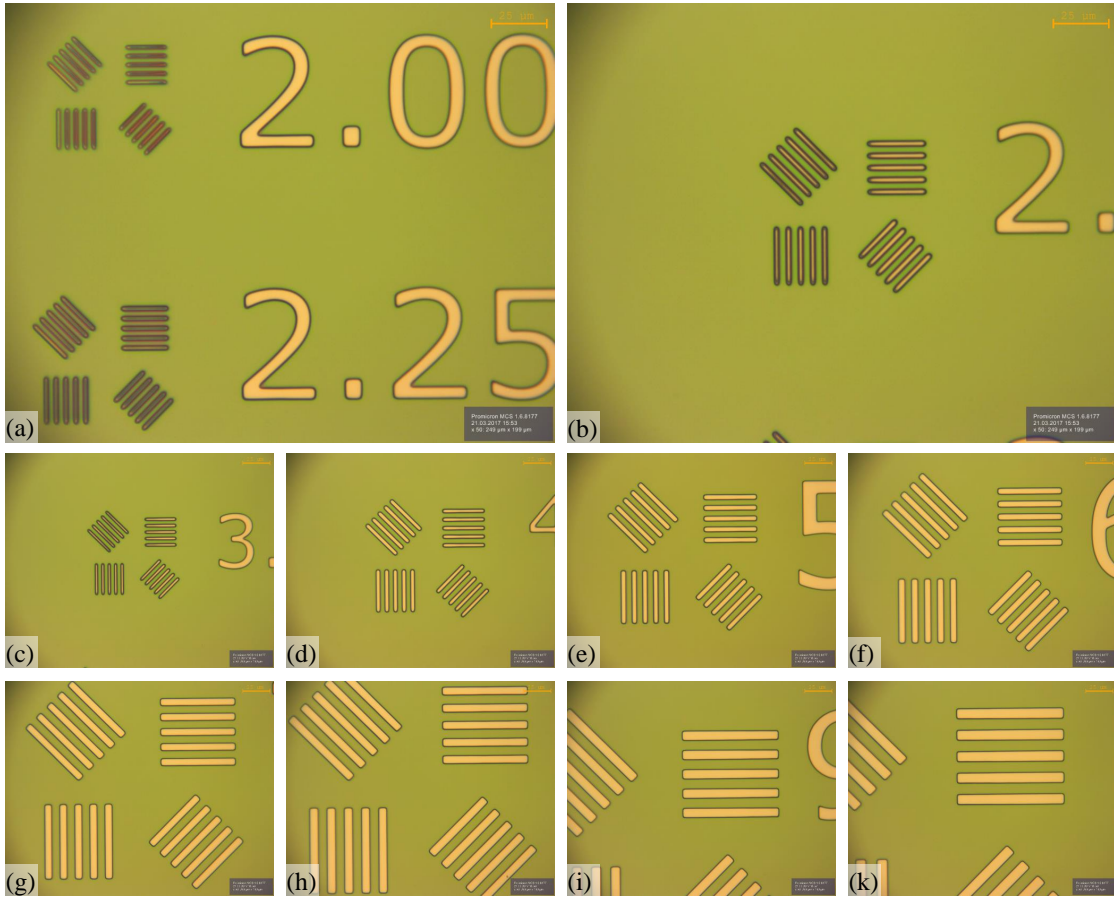


Figure 5.28 – Test print MPL-TP1, field R13C3, with the MPL system showing a series of resolution structures as evaluated in compiling data for the resolution charts fig. 5.29. Micrographs taken with 50X objective with bright field illumination. The subfigures show lines and spaces patterns with critical dimension of (a)  $2\mu\text{m}$  and  $2.25\mu\text{m}$ , (b)  $2.75\mu\text{m}$ , (c)  $3\mu\text{m}$ , (d)  $4\mu\text{m}$ , (e)  $5\mu\text{m}$ , (f)  $6\mu\text{m}$ , (g)  $7\mu\text{m}$ , (h)  $8\mu\text{m}$ , (i)  $9\mu\text{m}$ , (k)  $10\mu\text{m}$ . The dose is optimal for  $5\mu\text{m}$  line-width, hence the smaller features are underexposed.

shown in fig. 5.28a. All other fields have been populated similarly.

The missing fields in the corners have not been printed. The large scanning angle  $\theta_s$  of  $20.5^\circ$ , see table 5.7, leads to clipping of the outmost field points, in conjunction with the scanning length  $d_s$ . This can be seen in the resolution charts of MPL-TP2 and MPL-TP3, which differ only in  $d_s$  ( $3.29\text{ mm}$  versus  $9.87\text{ mm}$ , respectively). The influence of these different scan lengths can also be seen in the prints. Figure 5.30 shows micrographs from one of the regular lines and spaces pattern fields, compare fig. 5.27d, with  $45^\circ$  line inclination. The short scan length for fig. 5.30a manifests in non-uniform dose distribution, visible in the partially not fully developed structures. The longer scan, fig. 5.30b, in comparison exhibits uniform structures.

The lower row of prints in fig. 5.29 is part of a series of exposures to investigate and demonstrate

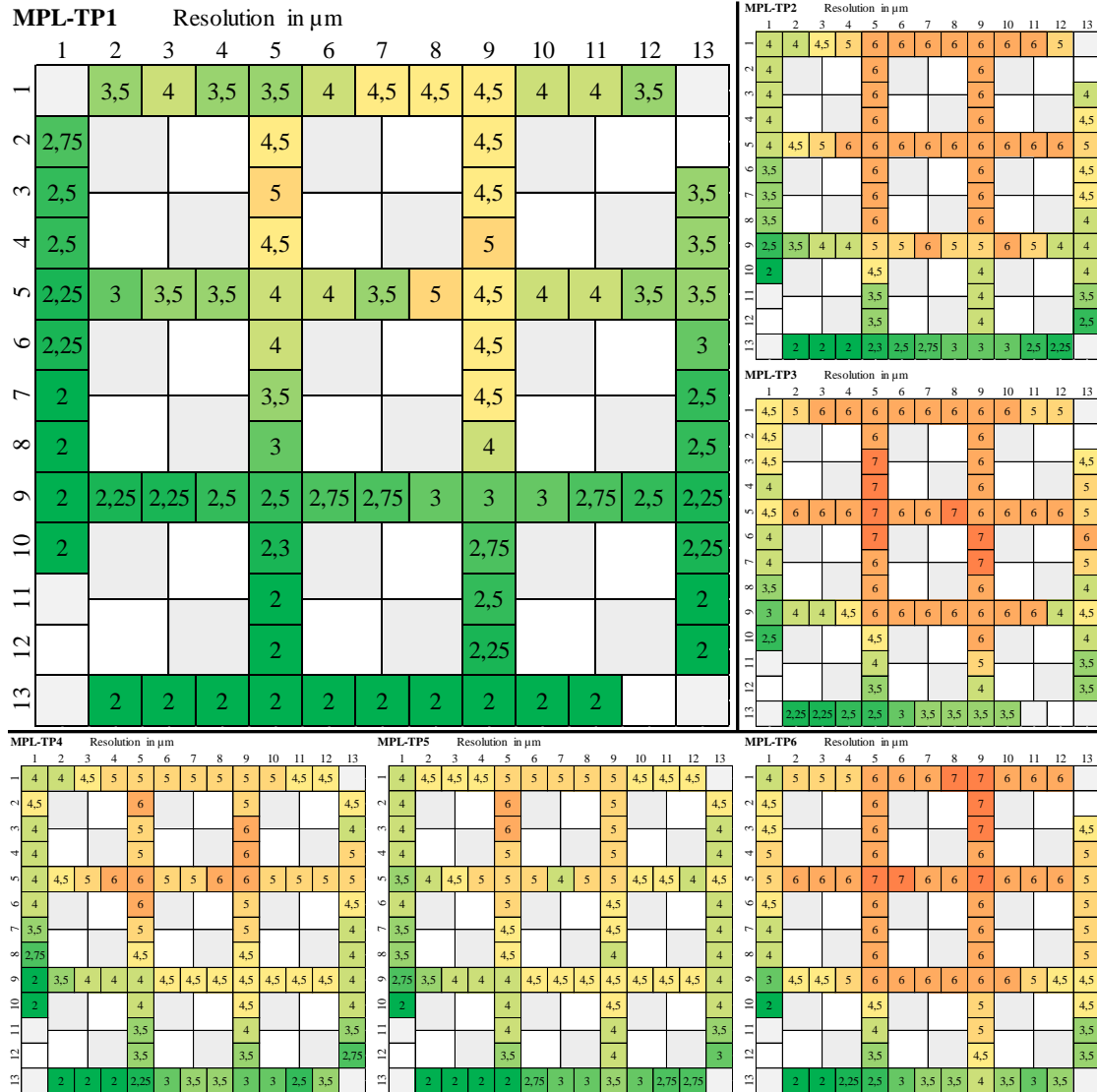


Figure 5.29 – Full-field resolution charts for the test prints listed in table 5.7. The individual cells in each chart represent the resolution structure cells on the MPL test mask, fig. 5.27a. The value in each cell is the smallest printed critical dimension in  $\mu\text{m}$  for the respective cell. The color coding is the same for all charts, with 2  $\mu\text{m}$  in dark green and 7  $\mu\text{m}$  in red.

the tolerance of the MPL optics, and system in general, against vertical displacement of the optics. This is similar to a depth of field investigation, but aims at highlighting another strength of the MPL approach. To take these prints the sum of mask and wafer gap ( $d_{WD,1}$  and  $d_{WD,2}$ ) was kept constant, but the relative vertical position of the optics in between was varied over a vertical range of 20  $\mu\text{m}$ , compare prints MPL-TP4 to MPL-TP6 in table 5.7. When comparing the achieved print resolution for the three charts shown in the lower row of fig. 5.29, two tendencies can be identified. First, the overall distribution of print resolution does not change (which is a trivial), and second, we can find a constant print resolution in the lower

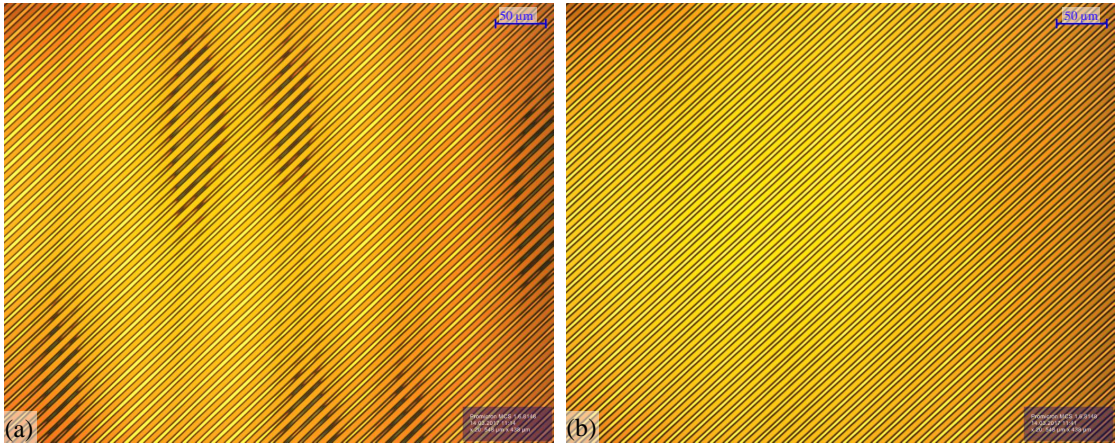


Figure 5.30 – Test prints with the MPL system demonstrating the influence of the scan distance  $d_s$  on the dose uniformity. Micrographs taken with 20X objective with bright field illumination. (a) Scan distance  $d_s = 3.29$  mm. (b) Scan distance  $d_s = 9.87$  mm.

left corner of the test prints over the total range. This area was where the assembled MPL optics performed to specification. In the remaining test field we could observe in general a degradation of  $1\text{ }\mu\text{m}$  to  $2\text{ }\mu\text{m}$  compared to the resolution for best vertical optics position.

Figure 5.31 shows the ends of lines and spaces patterns under  $45^\circ$  in the bottom left field of MPL-TP1. Line-end rounding is clearly visible in the case of  $3\text{ }\mu\text{m}$  critical dimension (fig. 5.31a), an effect already less pronounced for  $4\text{ }\mu\text{m}$  critical dimension (fig. 5.31b). This effect is expected, as it is caused by the low-pass characteristics of optical systems in general, blocking the transmittance of spatial frequencies above the system NA, causing resolution loss for sharp corners.

An interesting aspect of scanning imaging systems is visible in the Siemens star resolution feature shown in fig. 5.32. The rays of the star are discernible up to the resolution limit, a little below  $2\text{ }\mu\text{m}$ . Then the contrast drops to zero, as expected. Yet after the phase change structures are no longer visible. For static systems usually a phase shift of  $\pi$  can be observed below the resolution limit, manifesting as inversion of the dark and light rays. Yet for scanning systems a phase change leads to errors in image superposition during scan, resulting in complete contrast loss. This means that a scanning system is resistant against artifacts caused by structures at or just below the resolution limit.

In general, when comparing the achieved resolution of the different prints in fig. 5.29, the influence of the angular spectrum on the exposure resolution becomes clearly visible. For the angular spectrum values please consult table 5.7. The largest angular spectrum possible with the current illumination source was  $\pm 3.7^\circ$ , realized for print MPL-TP1, shown in the large chart in fig. 5.29. This angular spectrum also enables the highest resolution in the photolithographic prints realized for this work. From the optics design we know the systems



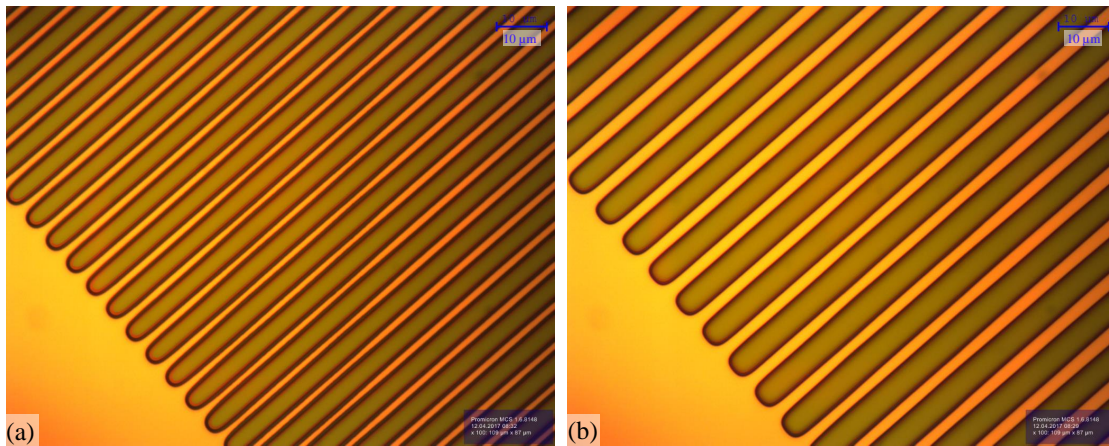


Figure 5.31 – Test print MPL-TP1, bottom left field, with the MPL system showing the lines and spaces pattern and line ends under 45°. Micrographs taken with 100X objective with bright field illumination. (a) 3  $\mu\text{m}$  critical dimension. (b) 4  $\mu\text{m}$  critical dimension. Dose not perfectly adapted for both feature sizes, both slightly underexposed.

allows angles of  $\pm 6.2^\circ$  to pass (see section 5.1.4). To successfully print structures we need at least two diffraction orders passing the imaging system, as introduced in section 3.1.4. For a structure of 2  $\mu\text{m}$  and at an exposure wavelength of 365 nm the diffraction angle of the first order is  $10.52^\circ$ , or  $\text{NA} = 0.1825$ . This means that only for off-axis illumination with sufficiently large angle both the 0<sup>th</sup> and the 1<sup>st</sup> orders will be transmitted, thus resolving the structure.

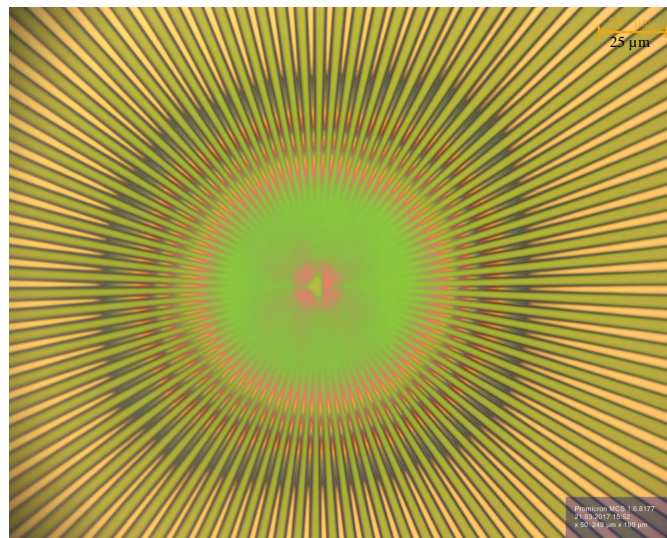


Figure 5.32 – Test print MPL-TP1, field R13C3, with the MPL system showing the center of a Siemens star. Micrograph taken with 100X objective with bright field illumination. The contrast drops to zero at the resolution limit. In contrast to static imaging systems no phase change inside the resolution limit is visible, which is a specific property of scanning systems.

From partial coherence theory we know that sources have to be treated as extended source [89, Sec. 2.3.2]. If we stick with this image to explain image formation for MPL, we can say that the 1<sup>st</sup> order is partially transmitted through the system, enabling image formation, even though the center of the 1<sup>st</sup> diffraction order lies outside the entrance pupil of an individual imaging channel. At the same time, this explains the loss in contrast for small feature sizes, leading to non-fully developed or exposed structures in the prints shown in fig. 5.28, when comparing the small features (2  $\mu\text{m}$  to 3  $\mu\text{m}$  critical dimension) to larger ones.

## 5.4 System improvements

The previous section showed the results we were able to obtain with the manufactured MPL optics. Conducting the tests we found the mechanics delivering up to expectation. The optics, however, had certain shortcomings, which prohibited full field printing with the desired resolution. This section addresses the main shortcomings we identified and discusses concepts we developed to improve the respective aspects.

### 5.4.1 Microlens array uniformity

One major factor influencing the printing resolution uniformity is the system uniformity. The more identical the individual imaging channels are throughout the whole active area, the more uniform the printing result will be. System uniformity can be separated into two subproblems: non-uniform axial spacing over the printing field extent and lens-to-lens uniformity of the MLAs themselves. Both points are connected to two aspects of MLA uniformity.

Non-uniform axial spacing besides wedge errors due to non-ideal wafer-level packaging processes, can be attributed to bow of the microlens arrays. The effect of wafer bow on the axial spacing is drawn in exaggerated manner in fig. 5.33. This deformation can have multiple influences. Fused silica wafers possess an intrinsic bow which comes from the polishing in their production. Hence wafer bow should be taken into account in MLA fabrication (processing of MLAs on both convex and concave sides of wafers). Together with the mix-and-match

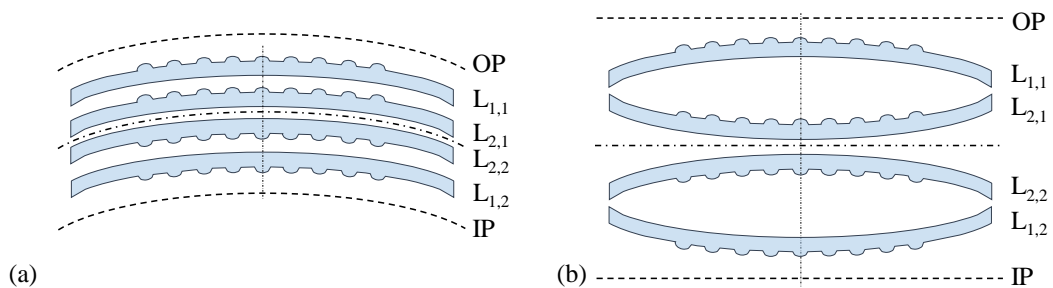


Figure 5.33 – Exaggerated schematics of wafer bow in MPL optics assembly. (a) Ideal wafer bow. (b) One worst case.

assembly process required for MPL, this signifies a major increase in wafer number necessary to achieve similar wafer bow in addition to similar MLA parameters for pairs of wafers chosen for system assembly. In addition, optical coating are a known source of induced stress, which can lead to additional wafer bow. In this work we tried to apply coatings in a symmetric way to minimize this effect. Yet during this project an exhaustive investigation of stress induced by the optical coatings was out of scope and has thus not been included. An attempt in taking intrinsic wafer bow into account for the production of the MPL optics was made, but had to be abandoned during system assembly. Initially, a system with wafers with similar lens parameters and fitting wafer bow was possible and planned for. Unfortunately, two of the wafers for this system were lost during shipping back from the optical coating supplier. The shipping conditions were improved after this incident, but we did not have replacement wafers for these two with fitting intrinsic bow.

Future MPL optics should take this fact into account, as we estimated the influence from opposite wafer bow to a difference in axial distance between two wafers to about  $5\mu\text{m}$  wafer displacement over the total field. Simulations showed an effective loss of contrast by several percent for variations of axial spacing of only  $10\mu\text{m}$ . Hence the influence of several misalignments in the  $5\mu\text{m}$  range is expected to cause severe loss of optical performance of the system. Appendix A lists some simulation results on the sensitivity of the MPL optical design to spacer thickness variation, illustrating this point.

Another way of decreasing the influence of bow on the performance of an MPL optics would be to decrease the size of the print field. A smaller field would mean less suspended area, thus less influence of the bow. This comes with the trade-off of decreased throughput, as more prints would be required to expose the same area. Yet this is more of an economical factor.

The other aspect previously mentioned is the lens-to-lens uniformity of the MLAs themselves. On this topic the author of this thesis carried out some investigation together with Jeremy Béguelin. The results of this investigation have been published [KBE<sup>+</sup>19] and presented [KBN<sup>+</sup>19]. These lens-to-lens or intra-wafer non-uniformities of lens parameters are an accumulative effect caused by non-uniform contributions of all process steps in the MLA production. As all of these processes are already driven to their maximum in terms of process control, no improvements could be made here. Instead, we turned to an empirical approach investigating the overall effects and possible ways of compensation.

In investigating the total MLA production process step-by-step we found that the reflowed photoresist lenslets exhibited a certain, but stable distribution of radius of curvatures with nearly perfectly spherical shape. Only the dry-etching process introduced the lens asphericity, again with a stable distribution, while maintaining a stable distribution of radius of curvature. This can be seen in fig. 5.12.

An investigation of the shape description of aspherical surfaces conducted in the same context showed that the classical description with radius of curvature and conic constant is not very well suited for this task. For purely geometrical reasons there are a range of combinations of

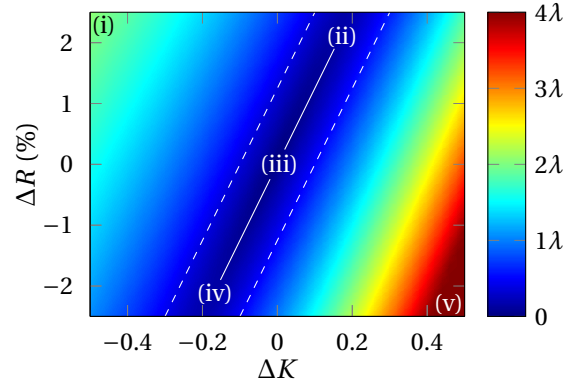


Figure 5.34 – Relative RMS wavefront error (with respect to the target lens) for a single plano-convex microlens with plane-wave illumination at  $\lambda=365$  nm. Lens target parameters:  $R_{C,t}=253\text{ }\mu\text{m}\pm 2.5\%$ ,  $\kappa_t=-1.02\pm 0.5$ , clear aperture  $2a=316\text{ }\mu\text{m}$ . The white solid line represents the target design (principle aberration component = 0) and the two dashed lines the respective tolerances. Reprinted with permission from [KBN<sup>+</sup>19].

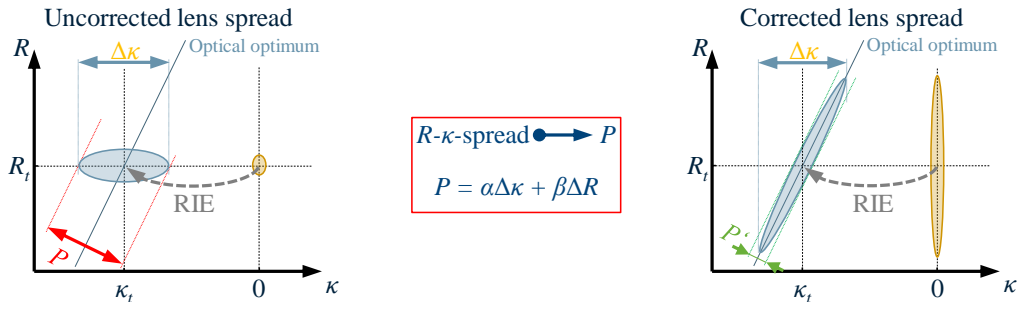


Figure 5.35 – Approach of the microlens uniformity improvement. The microlens radius of curvature  $R$  is adjusted prior to dry etching such that afterwards the lenses are aligned along the line of optimal performance, compare fig. 5.34. This represents an improvement over the current state, as the spread of  $R$  cannot be reduced within the manufacturing process.

radius of curvature and conic constant describing nearly the same lens shape, whereas other combinations yield completely different surfaces. As the optical function of a lens is governed by its surface profile, the problem this causes is immediately visible. When comparing the functionality of a lens throughout the defined tolerance space for production to the target lens, the difference between both can be plotted as the relative root-mean-square (RMS) error, see fig. 5.34. A positive diagonal can be found, drawn in white, along which the lens performance remains quasi-constant. While when moving perpendicular to this line through the parameter space, the performance of the lens quickly deviates strongly from the target performance, in the center of the graph. To increase the lens-to-lens uniformity one could now decrease the allowed parameter space, but this would mean to tighten the production tolerances. This is not possible in praxis, as the  $\pm 2.5\%$  used for this project are already at the limit for microlens production at SUSS MICROOPTICS SA, compare the manufactured wafers for this project in fig. 5.11.

Instead, we changed the description of microlenses by departing from the classical parameters  $R$  and  $\kappa$  [152], and transforming them to a parameter along the line of best performance, and a parameter perpendicular to this diagonal. The perpendicular parameter we called primary aberration component  $P$ , as we applied principle component analysis to perform this transformation [158, 159]. This allowed us to map the  $R - \kappa$ -spread on  $P$  in linear approximation, with the use of two constants  $\alpha$  and  $\beta$  provided by the principal component analysis. We thus had a means to describe the microlens with a parameter directly representative of the lens functionality. It has to be clearly stated that this approach relies on an optical figure of merit of performance of a lens, which requires access to the optical design of the respective lens. In addition, it requires an already stable manufacturing process on which this improvement can be based.

When we investigated the manufacturing process, we could only identify the photoresist volume of each microlens as single free parameter that we could adjust separately for each individual microlens. This can be implemented either by grey-tone lithography, or, as realized in our case, the variation of the size of the individual feature on the photomask used for the respective lithographic exposure. Upon investigation, we found that a small variation in photoresist volume per lens could be used to influence the radius of curvature of the photoresist lenses independently of other parameters. Together with a characterization of the production process for an MLA and the knowledge on how radius of curvature and conic constant develop throughout the process we could shift the lenses in the  $R$ - $K$ -parameter space in direction of the radius of curvature, such that they were aligned along the diagonal of best performance. This is schematically shown in fig. 5.35.

Relying on principal component analysis we found the means to mathematically describe this connection. We have demonstrated an improvement of the lens-to-lens uniformity for  $L_1$  wafers by a factor  $> 1.4$ , and for  $L_2$  wafers by a factor  $> 2$  with this approach [KBE<sup>+</sup>19, KBN<sup>+</sup>19]. Complementary data can be found in appendix B.

Unfortunately, at the time of writing of this document no MPL optics has been assembled relying on these wafers yet.

### 5.4.2 Wafer-level packaging process improvements

To render the wafer-level packaging process tolerant against particle pollution we suggest a different approach. The adhesive for the wafer-level packaging process could be filled with beads with precise diameters. Such beads are available of different materials and could act as spacers which get dispensed together with the adhesive material. Filled adhesives offer several advantages. The spacers can be applied throughout the adhesive layer, maintaining a stable layer thickness over large areas. The spacer beads act like the balls in a bearing, allowing lateral alignment with small forces even when both surfaces around the adhesive layer are in contact with the spacer beads. And the spacer beads can be chosen in size to enable a wide range of adjustable yet very precise layer thickness. This would make them ideal



for wafer-level packaging of MPL optics, as here large area gluing has to be combined with high lateral alignment precision requirements. Also the need to adjust the spacer thickness according to the lens parameters of the manufactured MLAs can be fulfilled with accordingly chosen bead sizes. Spacer beads of sufficiently precise grades could be acquired for example from COSPHERIC<sup>14</sup>.

The use of spacer-filled adhesives requires two additional competences for successful wafer-level packaging. One is the mixing of the beads into the adhesive, to achieve a bubble-free or de-gassed homogeneous suspension. The second is the dispensing of the filled adhesive, that means the suspension of spacer beads in the matrix of liquid adhesive. For the latter timing is critical if the density of the beads differs from the density of the adhesive, as sedimentation or buoyancy of the beads otherwise complicates the process. For both problems exist functioning solutions, though<sup>15</sup>.

Another point to improve the wafer-level packaging process for MPL is the clamping of the lens wafers on the mask aligner used for system assembly. For the realized systems, two blank wafers of 800  $\mu\text{m}$  thickness have been milled out in the center, similar to the spacer wafer  $S_1$ . They were placed as templates on the vacuum chuck, on which lens wafers were placed with the MLA projecting into the cut out. The contact between the flat area around the MLA and the template wafer was sufficient to achieve vacuum clamping of both wafers on either chuck of the SMILE tooling (compare section 5.2.4). In any case, the volume below the MLA was evacuated as well, and caused a deformation of the MLA. This deformation explains to large parts the lateral mismatch between the alignment marks of  $L_1$  and  $S_1$ , compare table 5.6.

One possibility to improve this point would be the acquisition of custom vacuum chucks with vacuum grooves only in areas with flat wafer surface, and a center pouch to accommodate protruding MLAs.

### 5.4.3 Additional concepts for further improvement

The following completes the list of possible improvements we identified during system production, assembly and testing.

First and foremost of importance for a MPL system optimized towards actual deployment in any kind of production environment, the scan angle  $\theta_s$  has to be fixed. Then the mask layout of the MLA wafers has to be adapted accordingly, to enable true full-field printing of the overall exposure field of 100 mm by 100 mm.

A major point for system application is to improve the transparency of the windows in the MPL optics stack to allow *in-situ* setting of the wafer gap  $d_{WD,2}$ . This would not only greatly simplify

<sup>14</sup>COSPHERIC LLC, Santa Barbara CA, USA. [www.cospheric.com](http://www.cospheric.com).

<sup>15</sup>One obvious solution for the sedimentation problem is the use of spacer beads with similar density to the adhesive, or vice versa. The dispensing of filled adhesives can be accomplished for example with the DISPENSEJET DJ-9500 dispenser series by NORDSON ASYMTEK, according to the manufacturer.

the initial setup-procedure, as the optics could be placed in the scanner, fixed in place and all adjustments could be made with the optics in place. It would also mark a major improvement in system reliability and accuracy, as the wafer gap could be continuously monitored and corrected during exposures.

Another point is the adaptation of the exposure light source, to enable printing of  $2\text{ }\mu\text{m}$  structures with the same contrast as larger structures. The light source's angular spectrum needs to be enlarged to enable full passage of the 1<sup>st</sup> diffraction order together with the 0<sup>th</sup> order.

And finally, as a minor detail, the linear actuator of the current scanner mechanics could be replaced against one with less linearity error. Still, the system has proven tolerant towards these scan-speed variations, hence this represents not a critical problem.

### 5.5 Conclusion on microlens projection lithography

To draw a conclusion on MPL, let us revisit the major points of this chapter. Building on the previous work on MPL, outlined in section 2.3.1, we set out to implement a system addressing two key points, realizing photolithographic print resolution of  $2\text{ }\mu\text{m}$  and to enable printing on substrates of arbitrary size. To achieve this goal we had to

- develop a new design for the MPL optics,
- implement (manufacture and assemble) this optical system,
- build a mechanical scanner to realize scanning imaging channel superposition, capable of handling the optics and with sufficient precision
- and implement a complete prototype system relying on a high precision wafer positioning stage to enable printing on arbitrary substrate sizes.

To realize the optical design we compiled a comprehensive list of limitations on the optical system, constraining the optical design. In cooperation with Kevin Müller we found an optics design fulfilling all requirements, and implemented simulation to enable system production (mix-and-match), because of the tight tolerances.

The MLAs and spacer wafers for the optical system were manufactured by SUSS MICROOPTICS under supervision of the author of this thesis, and a working combination of wafers was identified.

Then we assembled the system relying on a specifically developed wafer-level packaging process for this optics, realizing large-area contact between the wafers, to achieve a stable and monolithic system. This served two purposes, wafer bow was minimized to the suspended active area of the MLAs, and mechanical integration in the scanner was simplified. The outmost wafers were diced to a hexadecagon. This allowed mounting the system in the scanner carriage with access to the image plane for printing on arbitrarily sized substrates. In addition, the wafer-level packaging process relies on structures featuring channels connecting the air volumes inside the optical system between the MLAs to the outside. This avoids the

formation of barometric pouches inside the system. Heating of the system during exposure thus does not lead to a build-up of pressure in the system, which would lead to deformation of the MLAs.

A scanner was designed, manufactured and assembled, tested and debugged. We found the scanner capable of precise linear scans with scan plane rocking so small that a lateral displacement of the individual image per channel was limited to 50 nm. This was found acceptable for the application.

The MPL optics was integrated in the scanner. The scanner in turn was implemented into a system comprising a high precision wafer positioning stage and a mask aligner light source. An alignment procedure for system setup was developed and implemented. This was complicated by an undesired side-effect in the production of the wafer-level packaging structures, rendering designated windows in the wafer-level packaging structures opaque for optical metrology to set the wafer gap, the distance between MPL optics and the to-be-patterned substrate. A work-around was found and implemented, enabling test prints with the prototype tool. A wafer-side working distance  $d_{WD,2}$  of 461  $\mu\text{m}$  was found for the manufactured optics, slightly less than the desired design goal of  $\geq 500 \mu\text{m}$ . We attribute this shorter working distance to misalignments in wafer-level packaging, which should be addressed for future system generations. Anyhow we realized an operational prototype system.

The print field of the system was designed to be 100 mm by 100 mm, with the scanner being designed to print on arbitrarily sized substrates. Test prints were typically conducted on 200 mm silicon wafers in 0.73  $\mu\text{m}$  layers of AZ1512 positive photoresist. We could demonstrate a printed resolution of 2  $\mu\text{m}$ , as per design, for a working distance of approximately 500  $\mu\text{m}$ . We could furthermore demonstrate the relative robustness of the system towards vertical displacement of the optics between photomask and wafer over a range of 20  $\mu\text{m}$ .

A performance investigation of the total system, and the MPL optics in particular, showed that the optical system possesses certain flaws, limiting the designed performance to a small part of the overall print field. In addition, the layout of the MLAs was not optimized for the print angle  $\theta_s$  under which the prints were finally performed. This caused a clipping of the corners of the print field, without limiting the general performance of the system. Another limit was imposed by the light source, as it was not capable of delivering the full angular spectrum required by the optical design.

Steps for improving the system have been discussed and developed to different degrees of completion. For issues with the scanner mechanics paths forward have been identified and presented. For the integration of the MPL optics a different wafer-level packaging approach has been laid out, relying on filled adhesives, where precise beads, for example glass beads, are in suspension in the liquid adhesive during dispensing, to act as mechanical spacer over the entire gluing area. This process will render the wafer-level packaging process immune against particle pollution of the involved wafer surfaces if spacer beads with diameters bigger than the expected particle size are deployed. Only minor development effort would be required to

realize this process.

A large study to improve the lens-to-lens uniformity of MLAs was undertaken. We developed a process to improve this uniformity for individual lens designs with stable production process. This process can also be used to increase the yield of other products relying on the same microlens production technology, as the lens-to-lens uniformity of large (full-surface) MLAs is equivalent to the yield of a full wafer populated with many repetitions of the same element.

## 6 Conclusion and Outlook

In this thesis we investigated possible improvements for large-field photolithographic systems. To define such systems and to evaluate their requirements we started with an analysis of large-field photolithographic applications, typically referred to as BEOL. We investigated existing photolithographic systems in this field and their suitability for large-field printing. Proximity printing offers the simplest approach for photolithographic patterning of large substrates. This method is typically limited to substrate sizes slightly smaller than the photomask. Also the achievable resolution in the photolithographic print is typically limited to  $3\mu\text{m}$  to  $5\mu\text{m}$  minimum feature size, which is no longer sufficient for many BEOL applications. The beauty of mask aligners, the tools used for proximity printing, lies in their simplicity. To maintain their competitiveness in today's market both of the previously identified issues need to be addressed. The presented work has been carried out in this context, to investigate possible paths ahead for MAs, or closely related systems.

The substrate size limit in mask aligners is a mechanical problem. These systems typically rely on mechanical spacers to set the substrate parallel to the photomask. To overcome this problem we developed a prototype tool based on a high-precision positioning stage for substrate handling. We integrated this stage with a photomask holder and an optical metrology system that allows to measure the gap between photomask and substrate *in situ*. Thus we could eliminate the need for mechanical spacers, and we enabled large-field substrate handling on this tool.

To overcome the resolution limit on mask aligners, we investigated photolithographic systems in phase-space. This allowed us to identify two approaches for improvements, which are subsequently investigated in this thesis. First, we looked into classical proximity printing. Its resolution dependency on the exposure wavelength lends itself to the option of using non-standard light sources. With the recent development of a novel semiconductor CW laser by TOPTICA, which emits at 193 nm, we identified a possible source for this purpose. Its wavelength is shorter by a factor of 2 compared to the canonical g-,h-,i-line illumination based on high-pressure mercury arc lamps (436 nm to 365 nm). From theory this should allow to decrease the printed resolution by a factor of  $\sqrt{2}$ . The wavelength of 193 nm is

favorable as photoresist chemistry for this exposure wavelength is readily available from FEOL photolithography.

To enable proximity printing with this novel laser light source, a beam-shaping system was required. It has to ensure uniform intensity over the entire exposure field. The high coherence of the source represented a challenge, which was overcome by the combination of rotating diffusers and an imaging homogenizer setup. This beam-shaping system was validated with coherent simulation. We could demonstrate for the first time proximity printing of minimum feature sizes of  $1.75\mu\text{m}$  with an exposure gap of  $20\mu\text{m}$  with this source. This result also compares favorably to the attempt of using an ArF excimer source for proximity printing [24]. In combination with the optical gap-setting approach and the high-precision substrate positioning stage we demonstrated a large-field capable mask aligner system. Furthermore, the suitability of this setup for advanced mask aligner printing approaches like Talbot lithography, realizing sub-micron structures with similar proximity gaps, has already been demonstrated [VKO<sup>+</sup>18]. It has to be stated that the optical output power of the novel laser light source is not yet fit for industrial application. But as the source is topic of ongoing development at the manufacturer this can be considered only a question of time.

In the other approach towards modernizing mask aligner-like systems investigated in this thesis we implemented the latest generation of microlens projection lithography. The heart of the system is a highly integrated microoptical multi-aperture projection lens. It was designed to enable a minimum feature size of  $2\mu\text{m}$  in the photolithographic print with a working distance, or distance from the substrate to the lens, of  $500\mu\text{m}$ . This design was implemented in an optical system with an exposure field of  $100\text{ mm}$  by  $100\text{ mm}$ . Its realization relied on the integration of four microlens arrays with two spacer layers in a custom-developed wafer-level packaging (WLP) process, resulting in a monolithic lens. A mechanical scanner, required to enable uniform printing of the entire exposure field, was realized as well. Both, scanner and projection system, were then integrated with the high-precision substrate positioning stage and an advanced mask aligner illumination system.

With this system we could validate the optical design by demonstrating minimum feature sizes of  $2\mu\text{m}$  in photolithographic exposures. Furthermore, we could demonstrate a minimum resolution of  $5\mu\text{m}$  over the whole exposure field, which represents a new milestone for this technology. We investigated remaining shortcomings of the implementation of the optical systems and presented and discussed ways to address them. We thus paved the way for future implementations of this approach with full specified performance. Furthermore, with the presented system we were able to demonstrate a nearly diffraction-limited optical performance with a comparatively small NA. To achieve higher resolution towards  $1\mu\text{m}$  minimum feature size or below, the NA of the individual channels has to be enlarged. Without changing the microlens production technology (in respect to the lens height), this would imply to decrease the working distance of the MPL optics. This could be a topic of future work.

## A MPL optics sensitivity to axial misalignment

The tolerancing of the MPL optics relied on simulation. To simulate the system sensitivity on the different parameters of the optical design the system simulation implemented by Kevin Müller was used. The system was simulated with variations of different parameters, and the expected contrast in the aerial image after scan was computed. As we found in section 5.2.4, the axial spacing of the system achieved in wafer-level packaging was not as good as intended for the reasons discussed there. Thus an investigation of the system sensitivity to these misalignments is especially of interest.

Figure A.1 shows the result of several runs of the simulation, where one of the spacer thicknesses, that means the distances between the lens wafers, have been varied. This was done individually to also find out about the impact of each misalignment. The spacer thicknesses were varied by  $\pm 10\mu\text{m}$  around the design value.

Figures A.1a and A.1b show the results for spacers  $S_{1,1}$  and  $S_{1,2}$ , respectively. They exhibit similar behavior, or performance loss. This is expected as the MPL optics is symmetric to the center plane. Figure A.1c shows the result for a variation of the center distance between the inner lens wafers,  $S_2$ . We find a misalignment of this distance to have a higher impact as for  $S_{1,n}$ . In summary, fig. A.1d shows a comparison of the weight of misalignments of all axial distances in the MPL optical design. Weight is defined here as the relative impact for a similar variation. It can be seen that the overall system is most sensitive to an error of the center spacing between the two system halves,  $d_{S2}$ . This is not unexpected, when we consider the setup of the system. Both system halves are telescopes, which are connected via their common image plane, the center plane. A relative misalignment between both halves leads thus to defocus, directly diminishing the system performance.

At the same time, this sensitivity also represents the strongest correction factor we have in system assembly. This can be exploited because the recesses in the  $L_2$ -wafers are etched with RIE, offering a precise depth-control.

## Appendix A. MPL optics sensitivity to axial misalignment

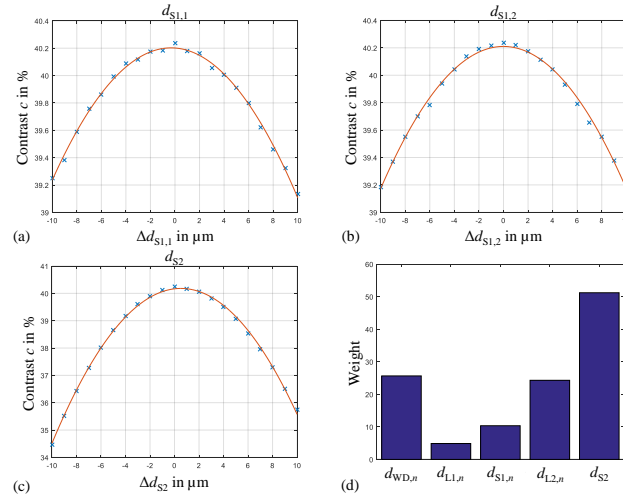


Figure A.1 – Simulated sensitivity of the MPL optics to axial misalignment, mainly in respect to spacing of the lens arrays. System performance evaluated as contrast in the aerial image after an ideal scan. (a) Variation of spacer thickness  $d_{S1,1}$  over  $\pm 10 \mu\text{m}$ . (b) Variation of spacer thickness  $d_{S1,2}$  over  $\pm 10 \mu\text{m}$ . (c) Variation of spacer thickness  $d_{S2}$  over  $\pm 10 \mu\text{m}$ . (d) Comparison of the weight of thickness errors for the different distances in the system, compare table 5.2



## B Improving the wafer-level microlens array uniformity

As published in [KBE<sup>+</sup>19, KBN<sup>+</sup>19], we applied the intra-wafer MLA uniformity improvement approach to the production of additional microlens arrays for a future microlens projection lithography optics. This appendix compiles additional results and information on the topic, to complete and complement section 5.4.1.

Figure B.1 shows the relative distribution of lenses for non-optimized and optimized microlens array wafers, produced for microlens projection lithography optics. Each dot in the four

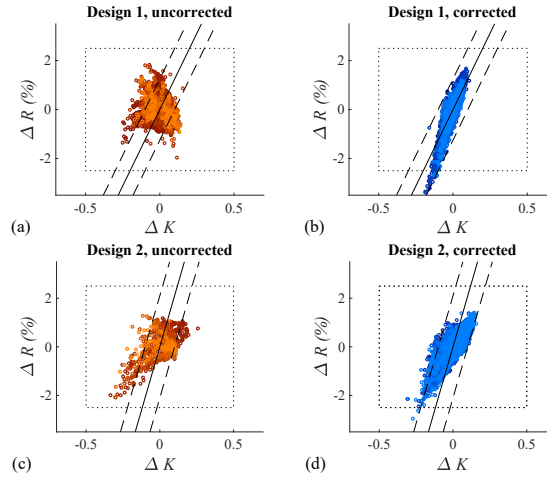


Figure B.1 – Measured  $\Delta R_{FS}/\Delta K_{FS}$  distribution ( $\Delta$  with respect to the average parameters  $\bar{R}_{FS}$  and  $\bar{K}_{FS}$ ) before and after correction for production runs of two designs: (a) 16 non-optimized MLA of Design 1 ( $L_2$ ). (b) 14 optimized MLA of Design 1 ( $L_2$ ). (c) 4 non-optimized MLA of Design 2 ( $L_1$ ). (d) 14 optimized MLA of Design 2 ( $L_1$ ).

Before correction the lenses are grouped in terms of  $R$ , especially for Design 1 ( $L_2$ ). After correction they are distributed along the minimum  $P$  line, as shown in fig. 5.35. The black lines correspond to the lines drawn in fig. 5.35, the dotted rectangle marks the typical classical tolerance space for these lenses. Reprinted with permission from [KBN<sup>+</sup>19].

## Appendix B. Improving the wafer-level microlens array uniformity

graphs represents one measured lens of the produced microlens arrays. The realignment or regrouping of individual lenses is obvious for both different lens designs  $L_1$  and  $L_2$ .

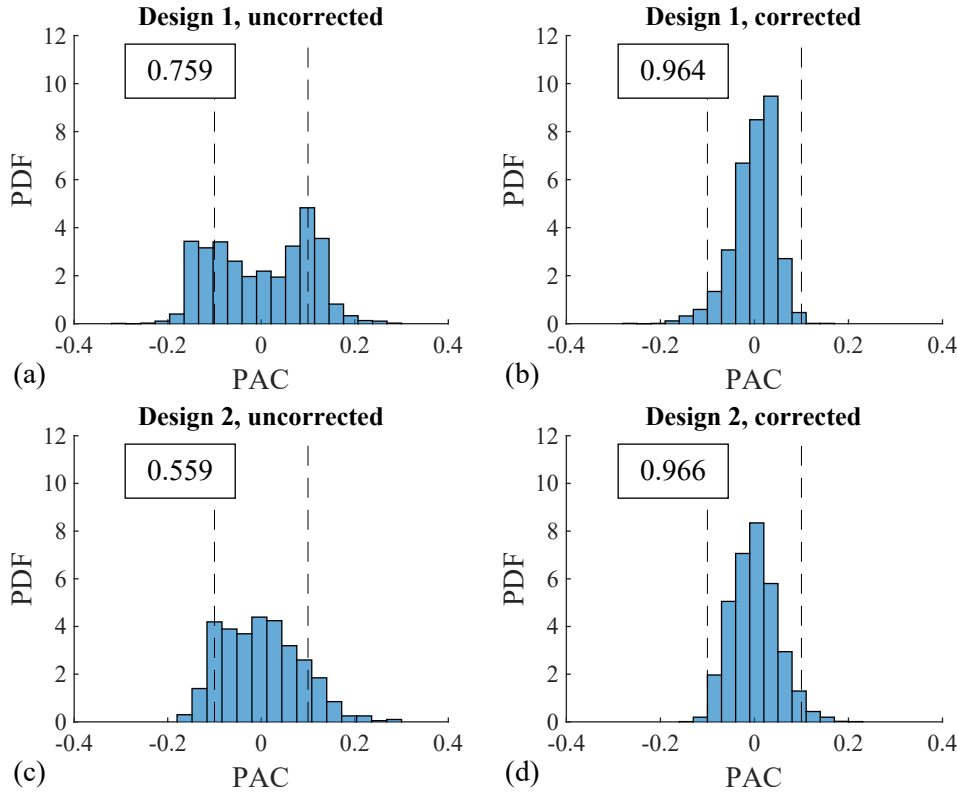


Figure B.2 – PDF of the relative PAC ( $P$ ) for production runs of two designs: (a) 16 non-optimized MLA of Design 1 ( $L_2$ ): standard deviation = 0.100, Peak-to-Valley = 0.592. (b) 14 optimized MLA of Design 1 ( $L_2$ ): standard deviation = 0.045, Peak-to-Valley = 0.439. (c) 4 non-optimized MLA of Design 2 ( $L_1$ ): standard deviation = 0.069, Peak-to-Valley = 0.463. (d) 14 optimized MLA of Design 2 ( $L_1$ ): standard deviation = 0.048, Peak-to-Valley = 0.368. Before correction, 76 % and 56 % of the lenses lie within the tolerance for Designs 1 ( $L_2$ ) and 2 ( $L_1$ ), respectively (dashed lines, as shown in fig. 5.35). This value increases to 96 % and 97 % in the optimized cases (see inset numbers). Reprinted with permission from [KBN<sup>+</sup>19].

A statistical investigation is more significant. Figure B.2 shows probability density plots of the lenses from fig. B.1 in function of their distance to the optical optimum line or  $P$ . The non-optimized spread for both designs exhibits a grouping around the  $P$ -limits, drawn by the dashed lines, (fig. B.2a) or at least a broad distribution over the whole  $P$  tolerance (fig. B.2c), with significant quantities of lenses outside the limits (the inset number in the square in each of the graphs). In comparison, the optimized distributions exhibit a clear regrouping around the center of the  $P$  tolerance space, with hardly any lenses outside the tolerance limits (figs. B.1d and B.2b). When comparing the standard deviations of the distributions, it can be found that for the  $L_1$  wafers an average improvement of  $> 1.4$  was achieved (non-optimized

---

st.dev.: 0.069, optimized st.dev.: 0.048), and for  $L_2$  the improvement was even bigger with a factor  $> 2$  (non-optimized st. dev.: 0.1, optimized st. dev.: 0.045).



# List of Figures

2.1	Comparison of BEOL exposure optics . . . . .	6
2.2	MPL Alpha system . . . . .	11
3.1	Propagating plane waves in phase-space . . . . .	17
3.2	Plane waves passing an optical system in phase-space . . . . .	17
3.3	Diffraction at a single slit . . . . .	18
3.4	Near-field diffraction at a single slit in phase-space . . . . .	19
3.5	Fresnel diffraction at a single slit in phase-space . . . . .	19
3.6	Far-field diffraction at a single slit in phase-space . . . . .	20
3.7	Free-space propagation behind aperture, skew illumination . . . . .	22
3.8	Free-space propagation, skew illumination, cross-sections . . . . .	22
3.9	Rayleigh resolution criterion . . . . .	24
3.10	Space-bandwidth product . . . . .	25
3.11	Space-bandwidth diagram . . . . .	27
3.12	Space-bandwidth support . . . . .	28
3.13	Petzval curvature and depth of field in extended phase-space . . . . .	29
3.14	Explanation to curves in phase-space . . . . .	30
3.15	Mask aligner behavior in phase-space . . . . .	34
3.16	Projection system in phase-space . . . . .	36
3.17	Koehler illumination setup . . . . .	37

## List of Figures

---

3.18 Koehler illumination in phase-space . . . . .	38
3.19 Off-axis illumination in phase-space . . . . .	40
3.20 Comparison mask aligner litho. with i-line vs. 193nm . . . . .	41
3.21 Temporal superposition in phase-space . . . . .	42
3.22 Multi-channel systems in phase-space . . . . .	44
3.23 MPL in phase-space . . . . .	45
4.1 Mask-aligner setup with 193 nm CW laser . . . . .	49
4.2 TOPTICA's 193 nm UV MOPA semiconductor laser . . . . .	50
4.3 Second harmonic generation cavity for 193 nm . . . . .	51
4.4 Schematics of multi-aperture beam-homogenizer setups . . . . .	54
4.5 Ray-tracing simulation of non-imaging homogenizer setup illumination . . . . .	57
4.6 Ray-tracing simulation of imaging homogenizer setup illumination . . . . .	58
4.7 Optical diffuser setups for beam-shaping applications . . . . .	61
4.8 Gaussian beam decomposition, schematically shown . . . . .	63
4.9 Setup for verification of coherent simulation of randomized source . . . . .	65
4.10 Verification of coherent simulation of randomized source . . . . .	66
4.11 Schema of the imaging homogenizer setup as coherently simulated in FRED . . . . .	67
4.12 Coherent simulation of the imaging beam homogenizer setup, results . . . . .	67
4.13 Schema of the imaging homogenizer setup with photomask and substrate . . . . .	68
4.14 Coherent simulation of exposure gap interference fringes . . . . .	69
4.15 Mask test-pattern to evaluate photolithography at 193 nm . . . . .	71
4.16 Measurement of non-imaging homogenizer setup illumination in the mask plane . . . . .	72
4.17 Measurement of imaging homogenizer setup illumination in the mask plane . . . . .	73
4.18 Photolithographic proximity print results at 193 nm with binary amplitude mask . . . . .	74
4.19 Photolithographic contact print results at 193 nm and binary amplitude mask . . . . .	75

4.20 Photolithographic proximity print results at 193 nm and binary phase mask . . .	76
4.21 Microstructures fabricated with Talbot lithography . . . . .	77
5.1 Schematic drawing of a MPL system . . . . .	82
5.2 Molten-resist reflow and RIE . . . . .	84
5.3 Image formation errors in microlens projection lithography systems . . . . .	86
5.4 Image formation in a microlens projection lithographic system . . . . .	87
5.5 Scanning image superposition dose uniformity simulation . . . . .	88
5.6 Optical design of the implemented MPL system . . . . .	89
5.7 MPL phase space diagram . . . . .	91
5.8 MPL system production flow diagram . . . . .	93
5.9 MPL mask design: lens wafers . . . . .	94
5.10 MPL mask design: wafer-level packaging . . . . .	95
5.11 Lens parameter distribution for produced MLAs . . . . .	96
5.12 Microlens shape during production . . . . .	97
5.13 MPL lens wafer AR coating reflectivity measurement . . . . .	98
5.14 Simulated performance of manufactured MPL system . . . . .	99
5.15 WLP schema for MPL assembly . . . . .	101
5.16 WLP alignment accuracy assessment of MPL assembly . . . . .	103
5.17 Assembled MPL optics . . . . .	104
5.18 MPL scanner rendering . . . . .	107
5.19 MPL scanner rendering with mask-chuck . . . . .	108
5.20 Control schema of the MPL scanner . . . . .	109
5.21 MPL scanner mechanics, as realized . . . . .	111
5.22 MPL scanner linearity investigation setup . . . . .	112
5.23 MPL scanner linearity investigation measurement . . . . .	113

## List of Figures

---

5.24 MPL optics installation procedure . . . . .	114
5.25 MPL scanner with mask-chuck . . . . .	115
5.26 MPL optics mounted in scanner . . . . .	116
5.27 Test-mask layout for MPL evaluation . . . . .	117
5.28 MPL test prints: resolution series . . . . .	119
5.29 MPL test prints: Resolution charts . . . . .	120
5.30 MPL test prints: scanning distance and dose uniformity . . . . .	121
5.31 MPL test prints: lines and spaces . . . . .	122
5.32 MPL test prints: Siemens star . . . . .	122
5.33 MPL optics production: wafer bow . . . . .	123
5.34 Relative RMS wavefront error for a lens over its tolerance range . . . . .	125
5.35 MLA uniformity improvement: approach . . . . .	125
A.1 Sensitivity of the MPL optics to axial misalignment . . . . .	134
B.1 Measured microlens distribution before and after improving uniformity . . . .	135
B.2 Measured lens distribution in terms of optical function . . . . .	136



## List of Tables

4.1	Important wavelengths and corresponding light sources for photolithography .	48
4.2	Parameters for homogenizer simulation in ZEMAX . . . . .	56
5.1	Microlens array production process limitations . . . . .	85
5.2	Optical design parameters for the realized MPL system . . . . .	90
5.3	Tolerances for the realized MPL system . . . . .	92
5.4	MPL optics system parameters . . . . .	99
5.5	MPL WLP: Dispenser parameters . . . . .	100
5.6	MPL WLP alignment measurements . . . . .	105
5.7	Parameters of MPL test prints . . . . .	118



## List of abbreviations

**AR** anti-reflective.

**ArF** argon fluoride.

**BEOL** back-end-of-line.

**CaF<sub>2</sub>** calcium fluoride.

**CD** critical dimension.

**CW** continuous-wave.

**DUV** deep ultra-violet.

**EUV** extreme ultra-violet.

**FEOL** front-end-of-line.

**FOV** field of view.

**FWHM** full width at half maximum.

**GBD** Gaussian beam decomposition.

**IC** integrated circuit.

**IFP** illumination filter plate.

**KBBF** potassium fluoro-berylo-borate.

**KrF** krypton fluoride.

**L&S** lines and spaces.

**LBO** lithium triborate.

## List of abbreviations

---

**LD** laser diode.

**LED** light emitting diode.

**MA** mask aligner.

**MEMS** microelectromechanical system.

**MLA** microlens array.

**MOPA** master oscillator power amplifier.

**MPL** microlens projection lithography.

**NA** Numerical Aperture.

**OD** optical density.

**RIE** reactive ion etching.

**RMS** root-mean-square.

**ROC** radius of curvature.

**SBP** space-bandwidth product.

**SEM** scanning electron microscope.

**SHG** second harmonic generation.

**SMO** source-mask-optimization.

**SRAF** sub-resolution assist features.

**UV** ultra-violet.

**VIS** visible range.

**WLP** wafer-level packaging.

**ZOAF** zero order attenuation filter.

# Nomenclature

- $C_I$  The autorrelation function.
- $E$  The exposure dose.
- $F$  The stop number of a lens.
- $I$  An intensity distribution.
- $K$  The conic constant.
- $N_F$  The Fresnel number.
- $R$  The radius of curvature.
- $Res$  The lateral resolution.
- $SBPY$  The system-side, transmission space-bandwidth product.
- $W_h$  The width of the autocorrelation peak at height  $h$ .
- $\Lambda$  The period of a periodic structure.
- $\delta_{GB}$  The lateral spacing of Gaussian beamlets.
- $\lambda$  The exposure wavelength.
- $\nu$  The wavelength-normalized angular extent of a signal.
- $\phi_{x,y}$  A local phase distribution.
- $\sigma$  The degree of coherence of a source.
- $\sigma_z$  The longitudinal speckle size.
- $\sigma_{x,y}$  The lateral speckle size.
- NA** The numerical aperture.
- $\theta$  The object-side half-angle of a lens.
- $\theta_M$  The inclination of a slab of fused silica.

## Nomenclature

---

- $\theta_S$  The scan angle of an MPL system.
- $a$  The half-width of an aperture.
- $c$  The contrast.
- $f$  The focal length of a lens.
- $g$  The exposure gap.
- $h$  The height coordinate.
- $k$  An empirical resolution factor in photolithography.
- $l_S$  The scan length of an MPL system.
- $t_M$  The thickness of a slab of fused silica.
- $u$  The propagation angle to the optical axis.
- $x$  Lateral field dimension, typically in  $\mu\text{m}$ .
- $y$  Lateral field dimension, typically in  $\mu\text{m}$ .
- $z$  Propagation dimension and/or direction, typically in  $\mu\text{m}$ .
- $D$  A clear diameter.
- $dD$  A thickness in  $z$ .
- $p$  The pitch of a microlens array.
- $z_T$  The Talbot distance.
- DOF** The depth of field.

## Original Work

- [KBE<sup>+</sup>19] Raoul Kirner, Jeremy Béguelin, Martin Eisner, Wilfried Noell, Toralf Scharf, and Reinhard Voelkel. Improvements on the uniformity of large-area microlens arrays in Fused Silica. Optics Express, 27(5):6249, 2019.
- [KBN<sup>+</sup>19] Raoul Kirner, Jeremy Béguelin, Wilfried Noell, Martin Eisner, Toralf Scharf, and Reinhard Voelkel. Leveraging wafer-level manufacturing process limitations to increase large-scale fused silica microlens array uniformity. In Mark A. Kahan, Richard N. Youngworth, and José Sasián, editors, Optical Modeling and System Alignment, page 9. SPIE, aug 2019.
- [KMM<sup>+</sup>16] Raoul Kirner, Kevin Mueller, Pauline Malaurie, Uwe Vogler, Wilfried Noell, Toralf Scharf, and Reinhard Voelkel. Array imaging system for lithography. volume 9951, page 99510A, Sep 2016.
- [KNSV19] Raoul Kirner, Wilfried Noell, Toralf Scharf, and Reinhard Voelkel. Coherent Ray Tracing Simulation Of Non-Imaging Laser Beam Shaping With Multi-Aperture Elements. EPJ Web of Conferences, 215:01001, sep 2019.
- [KVN<sup>+</sup>] Raoul Kirner, Andreas Vetter, Wilfried Noell, Toralf Scharf, and Reinhard Voelkel. Presented at ODF18, Hiroshima, Japan.
- [KVO<sup>+</sup>18a] Raoul Kirner, Andreas Vetter, Dmitrijs Opalevs, Christian Gilfert, Matthias Scholz, Patrick Leisching, Toralf Scharf, Wilfried Noell, Carsten Rockstuhl, and Reinhard Voelkel. Mask-aligner lithography using a continuous-wave diode laser frequency-quadrupled to 193 nm. Optics Express, 26(2):730, 2018.
- [KVO<sup>+</sup>18b] Raoul Kirner, Andreas Vetter, Dmitrijs Opalevs, Matthias Scholz, Patrick Leisching, Toralf Scharf, Wilfried Noell, Carsten Rockstuhl, and Reinhard Voelkel. Enabling proximity mask-aligner lithography with a 193nm CW light source. In Jongwook Kye and Soichi Owa, editors, Optical Microlithography XXXI, number March, page 50. SPIE, March 2018.
- [KWNN] Raoul Kirner, Susanne Westenhöfer, Wilfried Noell, and Andreas Nagy. Gestell für eine Replikationsvorrichtung, sowie Verfahren zur Herstellung von nano-

und/oder mikrostrukturierten Bauteilen mittels einer Replikationsvorrichtung.  
NL2023051.

During the course of this thesis, the author published two peer-reviewed articles [KVO<sup>+</sup> 18a, KBE<sup>+</sup> 19], has filed one patent application [KWNN] and presented at several conferences [KMM<sup>+</sup> 16, KVO<sup>+</sup> 18b, KVN<sup>+</sup>, KNSV19, KBN<sup>+</sup> 19].



# Contributions

- [BSK<sup>+</sup>19] Johana Bernasconi, Toralf Scharf, Raoul Kirner, Wilfried Noell, Reinhard Voelkel, and Hans Peter Herzig. Spatial coherence properties of an LED-based illumination system for mask-aligner lithography. (March):48, 2019.
- [LSN<sup>+</sup>18] Patrick Leisching, Toralf Scharf, Wilfried Noell, Carsten Rockstuhl, Reinhard Voelkel, Raoul Kirner, Andreas Vetter, Dmitrijs Opalevs, and Matthias Scholz. Enabling proximity mask-aligner lithography with a 193nm CW light source. In Jongwook Kye and Soichi Owa, editors, Optical Microlithography XXXI, number March, page 50. SPIE, mar 2018.
- [MKN<sup>+</sup>19] Kevin Mueller, Raoul Kirner, Wilfried Noell, Toralf Scharf, and Reinhard Voelkel. Tools for the design of multi-aperture imaging systems. Optics Express, submitted, may 2019.
- [OSG<sup>+</sup>18] Dmitrijs Opalevs, Matthias Scholz, Christian Gilfert, Andreas Vetter, Raoul Kirner, Carsten Rockstuhl, Toralf Scharf, Reinhard Voelkel, Ru Kang Li, L. J. Liu, Xiao Yang Wang, Patrick Leisching, Wilfried Noell, Chuangtian Chen, and Juergen Stuhler. Semiconductor-based narrow-line and high-brilliance 193-nm laser system for industrial applications. In W. Andrew Clarkson and Ramesh K. Shori, editors, Solid State Lasers XXVII: Technology and Devices, page 83. SPIE, feb 2018.
- [VKO<sup>+</sup>18] Andreas Vetter, Raoul Kirner, Dmitrijs Opalevs, Matthias Scholz, Patrick Leisching, Toralf Scharf, Wilfried Noell, Carsten Rockstuhl, and Reinhard Voelkel. Printing sub-micron structures using Talbot mask-aligner lithography with a 193 nm CW laser light source. Optics Express, 26(17):22218, aug 2018.
- [VKS<sup>+</sup>18] Andreas Vetter, Raoul Kirner, Toralf Scharf, Wilfried Noell, Carsten Rockstuhl, and Reinhard Voelkel. Improving the Resolution in Mask-Aligner Lithography. In 2018 International Conference on Optical MEMS and Nanophotonics (OMN), volume 0, pages 1–5. IEEE, jul 2018.
- [VOS<sup>+</sup>18a] Andreas Vetter, Dmitrijs Opalevs, Matthias Scholz, Patrick Leisching, Raoul Kirner, Toralf Scharf, Wilfried Noell, Carsten Rockstuhl, and Reinhard Voelkel. Mask-aligner Talbot lithography using a 193 nm CW light source. In Jongwook Kye

## Contributions

---

and Soichi Owa, editors, Optical Microlithography XXXI, number March, page 33. SPIE, mar 2018.

[VOS<sup>+</sup> 18b] Andreas Vetter, Dmitrijs Opalevs, Matthias Scholz, Patrick Leisching, Raoul Kirner, Toralf Scharf, Wilfried Noell, Carsten Rockstuhl, and Reinhard Voelkel. Mask-aligner Talbot lithography using a 193 nm CW light source. In Jongwook Kye and Soichi Owa, editors, Optical Microlithography XXXI, number March, page 33. SPIE, mar 2018.

[VYK<sup>+</sup> 19] Andreas Vetter, Chen Yan, Raoul Kirner, Toralf Scharf, Wilfried Noell, Reinhard Voelkel, and Carsten Rockstuhl. A computational rule-based approach for corner correction of non-Manhattan geometries in mask aligner photolithography. submitted to Optics Express, jul 2019.

In addition, the author contributed to the work of peers [VKO<sup>+</sup> 18, VKS<sup>+</sup> 18, OSG<sup>+</sup> 18, VOS<sup>+</sup> 18a, VOS<sup>+</sup> 18b, LSN<sup>+</sup> 18, BSK<sup>+</sup> 19, VYK<sup>+</sup> 19, MKN<sup>+</sup> 19].

# Bibliography

- [1] M. Eifert, "The information age," Engineering Management Journal, vol. 8, no. 6, pp. 277–287, 1998.
- [2] J. H. Bruning, "Optical lithography: 40 years and holding," in Optical Microlithography XX, D. G. Flagello, Ed., vol. 6520, mar 2007, p. 652004.
- [3] M. P. Groover. Automation. Accessed 30.09.2019. [Online]. Available: <https://www.britannica.com/technology/automation>
- [4] C. Mack, Fundamental Principles of Optical Lithography: The Science of Microfabrication, 2007.
- [5] J. Nall and J. Lathrop, "Photolithographic fabrication techniques for transistors which are an integral part of a printed circuit," in 1957 International Electron Devices Meeting, IRE, 1957, pp. 117–117.
- [6] J. A. Hoerni, "US Patent 3025589," 1959.
- [7] K. Ronse, "Optical lithography-a historical perspective," Comptes Rendus Physique, vol. 7, no. 8, pp. 844–857, 2006.
- [8] D. Basting, K. D. Pippert, and U. Stamm, "History and future prospects of excimer lasers," in Second International Symposium on Laser Precision Microfabrication, I. Miyamoto, Y. F. Lu, K. Sugioka, and J. J. Dubowski, Eds., vol. 4426, no. May, feb 2002, p. 25.
- [9] F. Rayleigh, "XXXI. Investigations in optics, with special reference to the spectroscope," The London, Edinburgh, and Dublin Philosophical Magazine and Journal of Science, vol. 8, no. 49, pp. 261–274, oct 1879.
- [10] W. Ulrich, S. Beiersdoerfer, and H.-J. Mann, "Trends in optical design of projection lenses for UV and EUV lithography," in Soft X-Ray and EUV Imaging Systems, W. M. Kaiser and R. H. Stulen, Eds., vol. 4146, nov 2000, pp. 13–24.
- [11] C. Wagner and N. Harned, "Lithography gets extreme," Nature Photonics, vol. 4, no. 1, pp. 24–26, jan 2010.

## Bibliography

---

- [12] H. Jones. Semiconductor Industry from 2015 to 2025. Accessed 30.09.2019. [Online]. Available: <https://www.semi.org/en/semiconductor-industry-2015-2025>
- [13] M. Eisner and J. Schwider, "Transferring resist microlenses into silicon by reactive ion etching," Optical Engineering, vol. 35, no. 10, pp. 2979—2982, oct 1996.
- [14] P. Nussbaum, R. Völkel, H. P. Herzig, M. Eisner, and S. Haselbeck, "Design, fabrication and testing of microlens arrays for sensors and microsystems," Pure and Applied Optics: Journal of the European Optical Society Part A, vol. 6, no. 6, pp. 617–636, 1999.
- [15] R. Voelkel, "Natural optical design concepts for highly miniaturized camera systems," in Optical Systems Design and Production, F. Merkle, Ed. International Society for Optics and Photonics, aug 1999, pp. 548–556.
- [16] W. B. Hugle, R. Dändliker, and H. P. Herzig, "LENS ARRAY PHOTOLITHOGRAPHY," 1996.
- [17] M. Scholz, D. Opalevs, P. Leisching, W. Kaenders, G. Wang, X. Wang, R. Li, and C. Chen, "A bright continuous-wave laser source at 193 nm," Applied Physics Letters, vol. 103, no. 5, p. 051114, jul 2013.
- [18] M. Bastiaans, "The Wigner distribution function applied to optical signals and systems," Optics Communications, vol. 25, no. 1, pp. 26–30, apr 1978.
- [19] K. A. Reinhardt and W. Kern, Eds., Handbook of Silicon Wafer Cleaning Technology, 2nd ed. William Andrew Inc., 2008.
- [20] ASML. (2017) TWINSCAN NXE : 3400B. Technical Specifications. Accessed 28.09.2019. [Online]. Available: <https://www.asml.com/products/systems/twinscan-nxe/twinscan-nxe3300b/en/s46772?dfp{ }product{ }id=842>
- [21] O. Yildirim, E. Buitrago, R. Hoefnagels, M. Meeuwissen, S. Wuister, G. Rispen, A. van Oosten, P. Derks, J. Finders, M. Vockenhuber, and Y. Ekin, "Improvements in resist performance towards EUV HVM," in Extreme Ultraviolet (EUV) Lithography VIII, E. M. Panning and K. A. Goldberg, Eds., vol. 10143, mar 2017, p. 101430Q.
- [22] Freescale Semiconductor Inc. (2015) Wafer Level Chip Scale Package (WLCSP). Accessed 28.09.2019.
- [23] USHIO. (2014) Next-Generation Packaging Solutions, Datasheet. Accessed 28.09.2019. [Online]. Available: [https://www.ushio.co.jp/documents/NEWS/products/20140707/ushio\\_product\\_data\\_sheet\\_20140707\\_e.pdf](https://www.ushio.co.jp/documents/NEWS/products/20140707/ushio_product_data_sheet_20140707_e.pdf)
- [24] S. Partel, S. Zoppel, P. Hudek, A. Bich, U. Vogler, M. Hornung, and R. Völkel, "Contact and proximity lithography using 193nm Excimer laser in Mask Aligner," Microelectronic Engineering, vol. 87, no. 5-8, p. 936, may 2010.

- [25] R. Voelkel, U. Vogler, A. Bramati, A. Erdmann, N. Ünal, U. Hofmann, M. Hennemeyer, R. Zoberbier, D. Nguyen, and J. Brugger, "Lithographic process window optimization for mask aligner proximity lithography," in *Proc. of SPIE*, K. Lai and A. Erdmann, Eds., vol. 9048, mar 2014, p. 90520G.
- [26] NIKON Corporation. (2019) FX-103SH/103S Datasheet. Accessed 28.09.2019. [Online]. Available: [https://www.nikon.com/products/fpd/lineup/pdf/FX-103SH{}\\_103S{}\\_e.pdf](https://www.nikon.com/products/fpd/lineup/pdf/FX-103SH{}_103S{}_e.pdf)
- [27] SUSS MicroTec SE. (2018) SUSS DSC500 Datasheet. Accessed 28.09.2019. [Online]. Available: <https://www.suss.com/brochures-datasheets/projection-scanner-dsc500.pdf>
- [28] Canon Inc. (2018) MPAsp-E813 Flat-Panel Exposure Main Unit Specifications. Accessed 28.09.2019. [Online]. Available: <http://downloads.canon.com/nw/pdfs/industrial/mpasp-e813-flat-panel-exposure-system-specs.pdf>
- [29] Canon Inc. (2018) MPAsp-H803 Flat-Panel Exposure Main Unit Specifications. Accessed 28.09.2019. [Online]. Available: <http://downloads.canon.com/nw/pdfs/industrial/mpasp-h803-flat-panel-exposure-system-specs.pdf>
- [30] Canon Inc. (2018) Technology Used in Flat Panel Display (FPD) Lithography Equipment. Accessed 28.09.2019. [Online]. Available: <https://global.canon/en/technology/support25.html>
- [31] RUDOLPH Technologies. JetStep G45 System. Accessed 28.09.2019. [Online]. Available: <https://www.rudolphtech.com/products/jetstep-g45-system>
- [32] RUDOLPH Technologies. JetStep X500 System. Accessed 28.09.2019. [Online]. Available: <https://www.rudolphtech.com/products/jetstep-x500-system>
- [33] NIKON Corporation. (2019) MEMS Steppers. Accessed 28.09.2019. [Online]. Available: <https://www.nikon.com/products/customized/pdf/mems-stepper.pdf>
- [34] RUDOLPH Technologies. JetStep G35 System. Accessed 28.09.2019. [Online]. Available: <https://www.rudolphtech.com/products/jetstep-g35-system>
- [35] Canon Inc. MPAsp-H1003T / H803T. Accessed 28.09.2019. [Online]. Available: <https://global.canon/en/product/indtech/fpd/sph1003th803t.html>
- [36] SUSS MicroTec SE. (2017) SUSS MA / BA Gen4 Series Datasheet. Accessed 28.09.2019. [Online]. Available: <https://www.suss.com/brochures-datasheets/mask-aligner-ma-ba-gen4-series.pdf>
- [37] Heidelberg Instruments Mikrotechnik GmbH. (2019) MLA300 Fact Sheet. [Online]. Available: [https://heidelberg-instruments.com/files/downloads/fact-sheets/hi{}\\_factsheet{}\\_mla300.pdf](https://heidelberg-instruments.com/files/downloads/fact-sheets/hi{}_factsheet{}_mla300.pdf)

## Bibliography

---

- [38] Heidelberg Instruments Mikrotechnik GmbH. (2016) DWL Series Fact Sheet. [Online]. Available: [https://heidelberg-instruments.com/files/downloads/fact-sheets/hi\\_{ }fact\\_{ }sheet\\_{ }dwl-2000-4000.pdf](https://heidelberg-instruments.com/files/downloads/fact-sheets/hi_{ }fact_{ }sheet_{ }dwl-2000-4000.pdf)
- [39] Heidelberg Instruments Mikrotechnik GmbH. (2019) VPG+ 200 / 400 Fact Sheet. [Online]. Available: [https://heidelberg-instruments.com/files/downloads/fact-sheets/hi\\_{ }factsheet\\_{ }vpg-200-400.pdf](https://heidelberg-instruments.com/files/downloads/fact-sheets/hi_{ }factsheet_{ }vpg-200-400.pdf)
- [40] H. C. Pfeiffer, "Direct write electron beam lithography: a historical overview," M. W. Montgomery and W. Maurer, Eds., sep 2010, p. 782316.
- [41] Y. Chen, "Nanofabrication by electron beam lithography and its applications: A review," Microelectronic Engineering, vol. 135, pp. 57–72, 2015.
- [42] H. Ulrich, R. Wijnaendts-van Resandt, C. Rensch, and W. Ehrensperger, "Direct writing laser lithography for production of microstructures," Microelectronic Engineering, vol. 6, no. 1-4, pp. 77–84, dec 1987.
- [43] R. C. Auyeung, H. Kim, N. A. Charipar, A. J. Birnbaum, S. A. Mathews, and A. Piqué, "Laser forward transfer based on a spatial light modulator," Applied Physics A: Materials Science and Processing, vol. 102, no. 1, pp. 21–26, 2011.
- [44] L. Yang, A. El-Tamer, U. Hinze, J. Li, Y. Hu, W. Huang, J. Chu, and B. N. Chichkov, "Parallel direct laser writing of micro-optical and photonic structures using spatial light modulator," Optics and Lasers in Engineering, vol. 70, pp. 26–32, jul 2015.
- [45] S. Rizvi, Ed., Handbook of Photomask Manufacturing Technology. CRC Press, oct 2018.
- [46] NIKON Corporation. FPD Lithography Systems. Accessed 28.09.2019. [Online]. Available: <https://www.nikon.com/about/technology/product/fpd/index.htm>
- [47] M. Born and E. Wolf, Principles of Optics, 7th (expanded) ed, 1999.
- [48] J. Fischer and M. Wegener, "Three-dimensional optical laser lithography beyond the diffraction limit," Laser and Photonics Reviews, vol. 7, no. 1, pp. 22–44, 2013.
- [49] P. Rai-Choudhury, Ed., Handbook of microlithography, micromachining, and microfab. Bellingham, Wash.: SPIE Optical Engineering Pr., 1997.
- [50] L. Stürzebecher, F. Fuchs, U. D. Zeitner, and A. Tünnermann, "High-resolution proximity lithography for nano-optical components," Microelectronic Engineering, vol. 132, p. 120, jan 2015.
- [51] R. Voelkel, U. Vogler, A. Bich, P. Pernet, K. J. Weible, M. Hornung, R. Zoberbier, E. Cullmann, L. Stuerzebecher, T. Harzendorf, and U. D. Zeitner, "Advanced mask aligner lithography: new illumination system," Optics Express, vol. 18, no. 20, p. 20968, sep 2010.

- 
- [52] K. Jain, C. Willson, and B. Lin, "Ultrafast deep UV Lithography with excimer lasers," IEEE Electron Device Letters, vol. 3, no. 3, p. 53, mar 1982.
- [53] K. Jain, "Advances In Excimer Laser Lithography," p. 115, 1987.
- [54] T. Saito, T. Matsunaga, K.-i. Mitsuhashi, K. Terashima, T. Ohta, A. Tada, T. Ishihara, M. Yoshino, H. Tsushima, T. Enami, H. Tomaru, and T. Igarashi, "Ultrannarrow-bandwidth 4-kHz ArF excimer laser for 193-nm lithography," p. 1229, sep 2001.
- [55] T. Weichelt, Y. Bourgin, and U. D. Zeitner, "Mask aligner lithography using laser illumination for versatile pattern generation," Optics Express, vol. 25, no. 18, p. 20983, 2017.
- [56] J. S. Sanders and C. E. Halford, "Design and analysis of apposition compound eye optical sensors," Optical Engineering, vol. 34, no. 1, p. 222, jan 1995.
- [57] J. Duparr  , "Microoptical artificial compound eyes," Ph.D. dissertation, Friedrich-Schiller-Universit  t Jena, 2005.
- [58] A. Br  ckner, "Microoptical Multi Aperture Imaging Systems," Ph.D. dissertation, Friedrich-Schiller-Universit  t Jena, 2011.
- [59] J. Duparr  , P. Dannberg, P. Schreiber, A. Br  uer, and A. T  nnermann, "Artificial apposition compound eye fabricated by micro-optics technology," Applied Optics, vol. 43, no. 22, p. 4303, aug 2004.
- [60] A. Br  ckner, J. Duparr  , F. Wippermann, R. Leitel, P. Dannberg, and A. Br  uer, "Ultra-compact close-up microoptical imaging system," in SPIE Optical Engineering + Applications, R. B. Johnson, V. N. Mahajan, and S. Thibault, Eds., vol. 7786, aug 2010, p. 77860A.
- [61] J. Tanida, T. Kumagai, K. Yamada, S. Miyatake, K. Ishida, T. Morimoto, N. Kondou, D. Miyazaki, and Y. Ichioka, "Thin Observation Module by Bound Optics (TOMBO): Concept and Experimental Verification." Applied optics, vol. 40, no. 11, pp. 1806–1813, 2001.
- [62] R. H. Anderson, "Close-up imaging of documents and displays with lens arrays." Applied optics, vol. 18, no. 4, pp. 477–84, feb 1979.
- [63] M. Kawazu and Y. Ogura, "Application of gradient-index fiber arrays to copying machines," Applied Optics, vol. 19, no. 7, p. 1105, 1980.
- [64] R. W. Gundlach, "Lens Strip Optical Scanning System," 1971.
- [65] H. Kawano, T. Okamoto, H. Nakajima, S. Takushima, Y. Toyoda, S. Yamanaka, T. Funakura, K. Yamagata, T. Matsuzawa, T. Kunieda, and T. Minobe, "Practical design for compact image scanner with large depth of field by compound eye system," Optics Express, vol. 22, no. 15, p. 18010, jul 2014.

## Bibliography

---

- [66] D. J. Brady, M. E. Gehm, R. A. Stack, D. L. Marks, D. S. Kittle, D. R. Golish, E. M. Vera, and S. D. Feller, "Multiscale gigapixel photography," Nature, vol. 486, no. 7403, pp. 386–389, 2012.
- [67] G. Carles, J. Downing, and A. R. Harvey, "Super-resolution imaging using a camera array," Optics Letters, vol. 39, no. 7, p. 1889, apr 2014.
- [68] J. Johnson, "Selection of Materials for UV Optics," WCOS University of Arizona, Tech. Rep., 2008.
- [69] R. Daendliker, S. Gray, F. Clube, H. Herzig, and R. Voelkel, "Non-conventional techniques for optical lithography," Microelectronic Engineering, vol. 27, no. 1-4, pp. 205–211, feb 1995.
- [70] M. Eisner, K. J. Weible, and R. Voelkel, "Aspherical Microlenses Manufactured by Wafer-Based Technology," in Advanced Optics Using Aspherical Elements, spie press ed., R. Hentschel, B. Braunecker, and H. J. Tiziani, Eds. Spie Press Book, 2008, ch. 13.11, pp. 277–283.
- [71] R. Voelkel, P. Nussbaum, K. Weible, H. P. Herzig, R. Daendliker, S. Haselbeck, M. Eisner, and J. Schwider, "Fabrication of non-conventional microlens arrays," Microlens Arrays, vol. 5, pp. 116–120, 1995.
- [72] R. Voelkel, H. P. Herzig, P. Nussbaum, R. Daendliker, and W. B. Hugle, "Microlens array imaging system for photolithography," Society of Photo-Optical Instrumentation Engineers, vol. 35, no. 11, pp. 3323–3330, 1996.
- [73] R. Völkel, H. Herzig, P. Nussbaum, W. Singer, R. Dändliker, and W. Hugle, "Microlens lithography: A new approach for large display fabrication," Microelectronic Engineering, vol. 30, no. 1-4, pp. 107–110, jan 1996.
- [74] E. Cullman, R. Voelkel, and K. M. Wells, "LENS ARRAY PHOTOLITHOGRAPHY," 2000, u.S. Patent No. 6016185A.
- [75] M. Eisner, C. Ossmann, R. Voelkel, E. Feick, P. Kaiser, S. Seider, S. Week, and K. Weible, "Refractive microlens arrays for photolithography," in Diffraction Optics and Micro-Optics, no. Figure 1. Washington, D.C.: OSA, 2000, p. DTuD35.
- [76] R. Völkel, M. Eisner, and K. J. Weible, "Miniaturized imaging systems," Microelectronic Engineering, vol. 67-68, pp. 461–472, 2003.
- [77] C. Blöthner, "Microlens Projection Lithography," Bachelor Thesis, University of Applied Sciences Jena, 2007.
- [78] J. Bernasconi, "High power ultraviolet led illumination systems: coherence properties and applications in photolithography," Ph.D. dissertation, École Polytechnique Fédérale de Lausanne, Lausanne, 2018.



- 
- [79] M. Testorf, B. M. Hennelly, and J. Ojeda-Castaneda, Phase space in optics - Fundamentals and Applications, 2010.
- [80] A. W. Lohmann, R. G. Dorsch, D. Mendlovic, C. Ferreira, and Z. Zalevsky, "Space-bandwidth product of optical signals and systems," JOSAA, vol. 13, no. 3, p. 470, 1996.
- [81] H. M. Ozaktas and H. Urey, "Space-bandwidth product of conventional Fourier transforming systems," Optics Communications, vol. 104, no. 1-3, pp. 29–31, dec 1993.
- [82] W. Singer, M. Totzeck, and H. Gross, Eds., Handbook of Optical Systems, Volume 2. Wiley-VCH Verlag GmbH & Co. KGaA, 2005.
- [83] J. Babington, "Phase space aberrations in general imaging systems," in Optical Design and Engineering VII, L. Mazuray, R. Wartmann, and A. P. Wood, Eds., no. June 2018. SPIE, jun 2018, p. 11.
- [84] E. Wigner, "On the Quantum Correction For Thermodynamic Equilibrium," Physical Review, vol. 40, no. 5, pp. 749–759, jun 1932.
- [85] H. Gross, H. Zügge, M. Peschka, and F. Blechinger, Eds., Handbook of Optical Systems, Volume 3. Weinheim, Germany: Wiley-VCH Verlag GmbH & Co. KGaA, 2006.
- [86] J. W. Goodman, Introduction to Fourier Optics, 3rd ed. Roberts & Company Publishers, 2005.
- [87] J. W. Goodman, Introduction to Fourier Optics, 3rd ed. Roberts & Company Publishers, 2005.
- [88] J. W. Goodman, Statistical Optics, 2nd ed. Wiley, 2015.
- [89] C. Mack, Fundamental Principles of Optical Lithography. Chichester, UK: John Wiley & Sons, Ltd, nov 2007.
- [90] Q. Gu, J. Cao, and Y. Sun, "Lagrange invariant, interference invariant, and space bandwidth product," in International Conference on Holography and Optical Information Processing (ICHOIP '96), G. Mu, G. Jin, and G. T. Sincerbox, Eds., vol. 2866, no. December 1996, dec 1996, pp. 104–107.
- [91] H. M. Ozaktas and F. S. Oktem, "Phase-space window and degrees of freedom of optical systems with multiple apertures," JOSAA, vol. 30, no. 4, p. 682, apr 2013.
- [92] C. Shannon, "Communication In The Presence Of Noise," Proceedings of the IEEE, vol. 86, no. 2, pp. 447–457, feb 1998.
- [93] R. Castaneda, "Phase space representation of spatially partially coherent imaging," Applied Optics, vol. 47, no. 22, p. E53, aug 2008.

## Bibliography

---

- [94] D. Dragoman, "Wigner distribution function applied to third-order aberrations," Applied optics, vol. 34, no. 1, pp. 161–168, 1996.
- [95] T. Dietrich, W. Ehrfeld, M. Lacher, M. Krämer, and B. Speit, "Fabrication technologies for microsystems utilizing photoetchable glass," Microelectronic Engineering, vol. 30, no. 1-4, pp. 497–504, 1996.
- [96] D. Hülseberg, "Glasses for microsystems technology," Microelectronics Journal, vol. 28, no. 4, pp. 419–432, may 1997.
- [97] S. Etoh, T. Fujimura, R. Hattori, and Y. Kuroki, "Fabrication of on-chip microcapillary using photosensitive glass," Microsystem Technologies, vol. 9, no. 8, pp. 541–545, oct 2003.
- [98] L. Waller, G. Situ, and J. W. Fleischer, "Phase-space measurement and coherence synthesis of optical beams," Nature Photonics, vol. 6, no. 7, pp. 474–479, 2012.
- [99] SUSS MicroTec. (2013) SUSS Manual Mask Aligner MJB4 Datasheet. Accessed 28.09.2019. [Online]. Available: <https://www.suss.com/brochures-datasheets/mask-aligner-mjb4.pdf>
- [100] T. Weichelt, U. Vogler, L. Stuerzebecher, R. Voelkel, and U. D. Zeitner, "Resolution enhancement for advanced mask aligner lithography using phase-shifting photomasks," Optics Express, vol. 22, no. 13, p. 16310, jun 2014.
- [101] Y. Tanaka, "Full-field projection lithography, optimum for HVM of HB LEDs," iLED, vol. 2, no. October, p. 18, 2011.
- [102] Y. Shen, "Lithographic source and mask optimization with narrow-band level-set method," Optics Express, vol. 26, no. 8, p. 10065, 2018.
- [103] A. Köhler, "Ein neues Beleuchtungsverfahren für mikrophotographische Zwecke," Zeitschrift für wissenschaftliche Mikroskopie und für mikroskopische Technik, vol. 10, no. 4, pp. 433–440, 1893.
- [104] R. Voelkel, "Micro-Optics for Illumination Light Shaping in Photolithography," in Laser Beam Shaping Applications, F. M. Dickey and T. E. Lizotte, Eds. CRC Press, 2017.
- [105] D. M. Brown, F. M. Dickey, and L. S. Weichmann, "Multi-Aperture Beam Integration Systems," in Laser Beam Shaping: Theory and Techniques, F. M. Dickey, Ed. CRC Press, 2017, ch. 10.
- [106] D. Rausch and A. M. Herkommer, "Phase space approach to the use of integrator rods and optical arrays in illumination systems," Advanced Optical Technologies, vol. 1, no. 1-2, pp. 69–78, 2012.
- [107] A. W. Lohmann, "Scaling laws for lens systems." Applied Optics, vol. 28, no. 23, pp. 4996–4998, 1989.

- 
- [108] R. Völkel, U. Vogler, A. Bich, K. J. Weible, M. Eisner, M. Hornung, P. Kaiser, R. Zoberbier, and E. Cullmann, "Illumination system for a microlithographic contact and proximity exposure apparatus," Patent 47, 2009.
- [109] ASML. (2019) TWINSCAN NXT : 2000i Datasheet. Accessed 28.09.2019. [Online]. Available: <https://www.asml.com/-/media/asml/files/products/duv-immersion-nxt/twinscan-nxt2000i.pdf>
- [110] S. Tanaka, M. Arakawa, A. Fuchimukai, Y. Sasaki, T. Onose, Y. Kamba, H. Igarashi, C. Qu, M. Tamiya, H. Oizumi, S. Ito, K. Kakizaki, H. Xuan, Z. Zhao, Y. Kobayashi, and H. Mizoguchi, "Development of high coherence high power 193nm laser," p. 972624, 2016.
- [111] J. Hecht, "A short history of laser development," Applied Optics, vol. 49, no. 25, p. F99, sep 2010.
- [112] M. Wraback, "Semiconductor ultraviolet emitters and detectors with potential for wire-less communications," in 2012 IEEE Photonics Society Summer Topical Meeting Series, vol. 3. IEEE, jul 2012, pp. 134–135.
- [113] D. Basting and G. Marowsky, Eds., Excimer Laser Technology. Berlin, Heidelberg: Springer Berlin Heidelberg, 2005.
- [114] M. Mizuguchi, H. Hosono, H. Kawazoe, and T. Ogawa, "Color center formation and time-resolved photoluminescence for ArF excimer laser irradiation in CaF<sub>2</sub> single crystals," p. 60, sep 1998.
- [115] R. E. Schenker, L. Eichner, H. Vaidya, S. Vaidya, and W. G. Oldham, "Degradation of fused silica at 193 nm and 213 nm," p. 118, 1995.
- [116] J. M. Algots, R. Sandstrom, W. N. Partlo, P. Maroevic, E. Eva, M. Gerhard, R. Linder, and F. Stietz, "Compaction and rarefaction of fused silica with 193-nm excimer laser exposure," p. 1639, 2003.
- [117] G. Derra and W. Singer, "Collection Efficiency of EUV Sources," in EUV Sources for Lithography. 1000 20th Street, Bellingham, WA 98227-0010 USA: SPIE, 2010, no. June 2003, pp. 893–913.
- [118] R. W. P. Drever, J. L. Hall, F. V. Kowalski, J. Hough, G. M. Ford, A. J. Munley, and H. Ward, "Laser phase and frequency stabilization using an optical resonator," Applied Physics B Photophysics and Laser Chemistry, vol. 31, no. 2, p. 97, 1983.
- [119] C. Chen, Y. Wang, Y. Xia, B. Wu, D. Tang, K. Wu, Z. Wenrong, L. Yu, and L. Mei, "New development of nonlinear optical crystals for the ultraviolet region with molecular engineering approach," Journal of Applied Physics, vol. 77, no. 6, p. 2268, mar 1995.
- [120] D. Tang, Y. Xia, B. Wu, and C. Chen, "Growth of a new UV nonlinear optical crystal:," Journal of Crystal Growth, vol. 222, no. 1-2, p. 125, jan 2001.

## Bibliography

---

- [121] T. Kanai, X. Wang, S. Adachi, S. Watanabe, and C. Chen, "Watt-level tunable deep ultraviolet light source by a KBBF prism-coupled device," Optics Express, vol. 17, no. 10, p. 8696, 2009.
- [122] G. J. Swanson, "Binary optics technology: Theoretical limits on the diffraction efficiency of multilevel diffractive optical elements," M.I.T. Lincoln Laboratory, Tech. Rep., 1991.
- [123] M. Taghizadeh, P. Blair, B. Layet, I. Barton, A. Waddie, and N. Ross, "Design and fabrication of diffractive optical elements," Microelectronic Engineering, vol. 34, no. 3-4, pp. 219–242, dec 1997.
- [124] J. C. Miñano, M. Hernández, P. Benítez, J. Blen, O. Dross, R. Mohedano, and A. Santamaría, "Free-form integrator array optics," in Nonimaging Optics and Efficient Illumination Systems II, R. Winston and R. J. Koschel, Eds., vol. 5942, no. September 2005, aug 2005, p. 59420C.
- [125] C. Fabry and A. Pérot, "Théorie et Applications d'une Nouvelle Méthode de Spectroscopie Interférentielle," Ann. Chim. Phys., vol. 16, no. 7, p. 115, 1899.
- [126] H. M. Gibbs, S. L. McCall, and T. N. Venkatesan, "Differential gain and bistability using a sodium-filled fabry-perot interferometer," Physical Review Letters, vol. 36, no. 19, pp. 1135–1138, 1976.
- [127] G. W. Chantry, "The use of Fabry-Perot interferometers, etalons and resonators at infrared and longer wavelengths-an overview," Journal of Physics E: Scientific Instruments, vol. 15, no. 1, pp. 3–8, 1982.
- [128] S. A. Pollack, "Angular Dependence of Transmission Characteristics of Interference Filters and Application to a Tunable Fluorometer," Applied Optics, vol. 5, no. 11, p. 1749, 1966.
- [129] S. Kaiser, T. Maier, A. Grossmann, and C. Zimmermann, "Fizeau interferometer for phase shifting interferometry in ultrahigh vacuum," Review of Scientific Instruments, vol. 72, no. 9, pp. 3726–3727, 2001.
- [130] D. Malacara and A. Cornejo, "Testing of Aspherical Surfaces with Newton Fringes," Applied Optics, vol. 9, no. 4, p. 837, 1970.
- [131] J. W. Goodman, Speckle Phenomena in Optics : Theory and Applications. Roberts & Co, 2007.
- [132] L. Leushacke and M. Kirchner, "Three-dimensional correlation coefficient of speckle intensity for rectangular and circular apertures," Journal of the Optical Society of America A, vol. 7, no. 5, p. 827, may 1990.
- [133] Q. B. Li and F. P. Chiang, "Three-dimensional dimension of laser speckle," Applied Optics, vol. 31, no. 29, p. 6287, oct 1992.

- 
- [134] T. Yoshimura and S. Iwamoto, "Dynamic properties of three-dimensional speckles," vol. 10, no. 2, pp. 324–328, 1993.
- [135] H. T. Yura, S. G. Hanson, R. S. Hansen, and B. Rose, "Three-dimensional speckle dynamics in paraxial optical systems," Journal of the Optical Society of America A, vol. 16, no. 6, p. 1402, jun 1999.
- [136] D. Li, D. P. Kelly, R. Kirner, and J. T. Sheridan, "Speckle orientation in paraxial optical systems," Applied Optics, vol. 51, no. 4, p. A1, 2012.
- [137] G. Scarcelli, A. Valencia, and Y. Shih, "Experimental study of the momentum correlation of a pseudo-thermal field in the photon counting regime," Quantum Electronics and Laser Science Conference (QELS), vol. 2, pp. 1138–1140, 2005.
- [138] D. Li, D. P. Kelly, and J. T. Sheridan, "Three-dimensional static speckle fields Part I Theory and numerical investigation," Journal of the Optical Society of America A, vol. 28, no. 9, p. 1904, 2011.
- [139] R. Völkel and K. J. Weible, "Laser beam homogenizing: limitations and constraints," p. 71020J, sep 2008.
- [140] R. Bitterli, T. Scharf, H.-P. Herzig, W. Noell, N. de Rooij, A. Bich, S. Roth, K. J. Weible, R. Voelkel, M. Zimmermann, and M. Schmidt, "Fabrication and characterization of linear diffusers based on concave micro lens arrays." Optics express, vol. 18, no. 13, pp. 14 251–61, 2010.
- [141] J. Arnaud, "Representation of Gaussian beams by complex rays," Applied Optics, vol. 24, no. 4, p. 538, feb 1985.
- [142] A. W. Greynolds, "Vector Formulation Of The Ray-Equivalent Method For General Gaussian Beam Propagation," R. E. Fischer, J. E. Harvey, and W. J. Smith, Eds., vol. 0679. International Society for Optics and Photonics, dec 1986, p. 129.
- [143] M. Sjodahl, L. R. Benckert, M. Sjödahl, and L. R. Benckert, "Systematic and Random Errors in Electronic Speckle Photography," Applied Optics, vol. 33, no. 31, pp. 7461–7471, 1994.
- [144] J. W. Goodman, Speckle phenomena in optics: theory and applications, R. & Company, Ed., Englewood, CO, 2005.
- [145] H. M. Varma, C. P. Valdes, A. K. Kristoffersen, J. P. Culver, and T. Durduran, "Speckle contrast optical tomography: A new method for deep tissue three-dimensional tomography of blood flow," Biomedical Optics Express, vol. 5, no. 4, p. 1275, apr 2014.
- [146] P. Rangarajan and M. P. Christensen, "Imaging hidden objects by transforming scattering surfaces into computational holographic sensors," Optics InfoBase Conference Papers, pp. 4–6, 2016.

## Bibliography

---

- [147] H. Talbot, "LXXVI. Facts relating to optical science. No. IV," Philosophical Magazine Series 3, vol. 9, no. 56, pp. 401–407, 1836.
- [148] P. Ruffieux, T. Scharf, I. Philipoussis, H. P. Herzig, R. Voelkel, and K. J. Weible, "Two step process for the fabrication of diffraction limited concave microlens arrays," Optics Express, vol. 16, no. 24, pp. 19 541–19 549, 2008.
- [149] C. T. Wang and S. C. Yen, "Theoretical analysis of film uniformity in spinning processes," Chemical Engineering Science, vol. 50, no. 6, pp. 989–999, 1995.
- [150] S. Abe and J. T. Sheridan, "Curvature correction model of droplet profiles," Physics Letters A, vol. 253, no. 5-6, pp. 317–321, mar 1999.
- [151] M. A. van den Brink, H. Jasper, S. D. Slonaker, P. Wijnhoven, and F. Klaassen, "Step-and-scan and step-and-repeat: a technology comparison," in Optical Microlithography IX, G. E. Fuller, Ed., vol. 2726, no. June 1996, jun 1996, pp. 734–753.
- [152] ISO 10110-12:2007, Std., 2007, Optics and photonics – Preparation of drawings for optical elements and systems – Part 12: Aspheric surfaces.
- [153] J. C. C. Fan and S. A. Spura, "Selective black absorbers using rf-sputtered Cr<sub>2</sub>O<sub>3</sub> /Cr cermet films," Applied Physics Letters, vol. 30, no. 10, pp. 511–513, may 1977.
- [154] J. X. Zhang and K. Hoshino, "Optical transducers: Optical molecular sensing and spectroscopy," in Molecular Sensors and Nanodevices. Elsevier, 2019, pp. 231–309.
- [155] D. I. Adhesives, "DELO PHOTOBOND GB310," 2019. [Online]. Available: [https://www.delo.de/fileadmin/datasheet/DELOPHOTOBOND\\_GB310\\_%28TIDB-D%29.pdf](https://www.delo.de/fileadmin/datasheet/DELOPHOTOBOND_GB310_%28TIDB-D%29.pdf)
- [156] BioFluidix, "BioFluidix PipeJet P9," 2017. [Online]. Available: [http://www.biofluidix.com/produkte/downloads.html?file=files/data/downloads/DownloadsEN/2017\\_PipeJet\\_Datasheet.pdf](http://www.biofluidix.com/produkte/downloads.html?file=files/data/downloads/DownloadsEN/2017_PipeJet_Datasheet.pdf)
- [157] M. GmbH, "COMPOSITION AND PROPERTIES OF AZ® AND TI PHOTORESISTS." [Online]. Available: [https://www.microchemicals.com/technical\\_information/photoreists\\_composition\\_properties.pdf](https://www.microchemicals.com/technical_information/photoreists_composition_properties.pdf)
- [158] K. Pearson, "LIII. On lines and planes of closest fit to systems of points in space," The London, Edinburgh, and Dublin Philosophical Magazine and Journal of Science, vol. 2:11, pp. 559–572, nov 1901.
- [159] H. Abdi and L. J. Williams, "Principal component analysis," WIREs Comp Stats, vol. 2, no. 4, pp. 433–459, 2010.

# Acknowledgements

First of all I would like to thank Dr. Toralf Scharf, the supervisor of my thesis. His advice and support towards, but not limited to, realizing this thesis helped me to adopt different perspectives on my work and gave valuable impulses.

Similarly, this work would not have been possible without the support of Dr. Reinhard Völkel. He has been a mentor to me throughout the last five years. On his invitation I decided to pursue my graduate studies in industry at SUSS MICROOPTICS SA (SMO). The welcoming and open-minded atmosphere at SMO made it easy to find a comfortable place for realizing this work.

Writing a doctoral thesis is inherently a solitary endeavor. Yet the preparation does not have to be, and so I am deeply grateful to my fellow PhD students Andreas Vetter, Jeremy Béguelin and Kevin Müller, to not only sharing parts of the way but also to the mutual support. I would like to point out Andreas' contribution to chapter 4, which is based on cooperative studies of the topic, Kevin's work on the optics design and the mix-and-match simulation of chapter 5, upon which the MPL implementation realized in this thesis is based to a good deal, and the cooperation with Jeremy on the topic of improving microlens array uniformity. Peer-reviewed papers have been published or are submitted for publication in scientific journals with all three of them.

As this thesis has been realized as industrial project, it would not have been possible without the support and facilities of SMO. I would like to express my gratitude to the whole staff at SMO for their warm welcome from the beginning and helpfulness in producing microoptical elements on my request, even in the face of full production capacities.

Specifically I would like to thank Dr. Wilfried Noell for his technical as well as personal support. I learned a lot from him over the course of this doctoral project, and I appreciate his willingness to share his knowledge and experience on topics ranging from optical simulation to improving scientific presentations.

I would also like to thank Dr. Martin Eisner for his support in developing the initial WLP process for the assembly of the MPL optics, and his help in pushing my projects through production at SMO. Special thanks to Cédric Droguet and Quentin Lohri, for without them

## Acknowledgements

---

controlling the MPL system would have been an enormous task by itself, and to Uwe Vogler for his support of the MPL project in the company.

I would like to express my gratitude to the photolithography, etching and metrology departments at SMO for producing the microoptical elements I needed to realize this thesis, especially Dr. Samuel Queste, Perric Weber, Serdar Ozveren and Lisa Leonini, to the R&D team for giving me a home in the company, here Sophiane Tournois has not been mentioned yet, and to all other colleagues who supported me in one way or another throughout the past five years. Some of whom have become dear friends to me, rendering the experience of working at SMO ever more pleasant.

Furthermore I would like to thank two student interns at SMO, Pauline Malaurie and Bahareh Ghadiani, whom I supervised during my doctoral studies, for running simulations and spending many hours in the cleanroom performing test-prints towards chapter 5.

Finally, I would like to thank my family and friends for their support, not only limited to this work. Profound gratitude goes to my parents Brigitte and Ulrich, and my siblings Bernadette, Marie and Vincent, for their lifetime support and love. I would like to close with thanking Anja, who supported me with emotional back up and a lot of patience, especially towards the end of this endeavor.

*Neuchâtel, 27 September 2019*

R. K.



# Raoul Kirner

## Personal information

Date of birth: 22. May 1989  
Place of birth: Ulm, Germany  
Nationality: German

## Professional affiliations

Since Jan. 2015 Optical Engineer in R&D at SUSS MicroOptics SA,  
Hauterive, Switzerland  
Q3/Q4 2014 Scientific Assistant at Ilmenau University of Technology,  
Ilmenau, Germany  
Q1, Q3 2012 Student internship at SUSS MicroOptics SA,  
Hauterive, Switzerland  
Q3 2007 – Q2 2008 Civil Service with Caritas Ostwürttemberg,  
Aalen, Germany

## Education

Since Jan. 2016 Doctoral studies at Photonics Doctorate School EDPO,  
École Polytechnique Fédérale de Lausanne, Switzerland  
Q3 2008 – Q3 2014 Undergraduate and graduate studies in Optronik  
at Ilmenau University of Technology, Germany  
Master of Science, 29. August 2014  
Bachelor of Science, 21. May 2012  
1999 – 2007 Theodor Heuss Gymnasium Aalen, Germany

Hauterive, 27. September 2019

Raoul Kirner